Håkon Viumdal

Dynamic Estimators Using Laser and Ultrasonic Instrumentation for Determining the Metal and Bath Heights in Aluminium Electrolysis Cells

A combination of hard/soft sensor approach

Thesis for the degree of Philosophiae Doctor

Trondheim, January 2015

Norwegian University of Science and Technology
Faculty of Information Technology, Mathematics and
Electrical Engineering
Telemark University College
Faculty of Technology

NTNU – Trondheim
Norwegian University of
Science and Technology

Høgskolen i Telemark

Preface

This thesis is submitted for the academic degree of Philosophiae Doctor (PhD) at the Department of Engineering Cybernetics, Faculty of Information Technology, Mathematics and Electrical Engineering at Norwegian University of Science and Technology (NTNU), in cooperation with Faculty of Technology, Telemark University College (TUC), and the national research institute Tel-Tek. The work was carried out at Tel-Tek as a part of the Strategic Institute Program MULTIPROCON (Multi-variable Process Control in High Temperature and High Pressure Environments using Multi Sensor Data Fusion), funded by the Research Council of Norway (project no 153958/420), and took place from August 2007 to August 2014. This is the forth and last thesis submitted in the MULTIPROCON program, with the mutual aim of improving measurements in harsh environments encountered in hydro-cyclones, under-balanced drilling and aluminium industries.

The main focus in this specific project has been on measuring the aluminium height in aluminium electrolysis cells, for improving its performance using improved measurement techniques and process control. The work consisted of two main sections;

- Physical sensors measuring the metal level. Ultrasonic time domain reflectometry in particular.

- Soft sensor approach, where the metal level is estimated, using sensor data fusion and inferential methods.

Although the work has not led to any new implementation in the aluminium industry, I think we have put focus on the problem with measurements in harsh environments, and have made contributions particularly in the field of using ultrasonic buffer rods, that could be interesting for various application, not only in the aluminium industry.

I wish to express my sincere gratitude to my supervisor Prof. Saba Mylvaganam at TUC, for all his advice and guidance throughout my research. His continuous support and knowledge have been of great importance to me. I would also like to thank my co-supervisors Prof. Tor Engebret Onshus at NTNU, Dr. Morten Liane at Norsk Hydro, Årdal, and Prof. Knut Arne Paulsen. I am thankful to Morten Liane for giving me the opportunity of running several valuable measurements in their aluminium cells at Årdal. These field tests in real industrial environment gave me good insight into the process and provided me highly valuable data for testing our measurement techniques and control.

Further, I am grateful to Prof. C.K. Jen, and Dr. Kuo-Ting Wu who invited me to the National Research Council of Canada, and spend several days giving

Overview

Various approaches, based on both modeling and monitoring, to estimate the metal height in aluminium electrolysis cells are studied in this dissertation. The thesis consists of four parts. The first part is an introduction to aluminium electrolysis cells, and the objective of this work. The second and third part are describing two different approaches to solve the measurement problem identified in the introduction. The second part deals with physical (hard) sensors for bath/metal height measurements in the electrolysis cells. Bath and metal height measurements were performed using ultrasonic time domain reflectometry including buffer rods and LASER Vibrometry. In the third part the height is estimated using soft sensors. The forth part draws the large lines with control strategies and future work, and concludes the thesis.

This thesis also includes five individual publications, that have been published during this work. They are referred to in the text, and hence arranged in a thematic order at the end of this thesis. The two first papers introduce the reader to the present situation of height measurements in aluminium electrolysis cells, and provides an overview of recent research and developments of the topic. Metal and bath height measurements and estimations are especially emphasized. The third and fourth paper cover topics of ultrasonic height measurements in molten metals, with specific focus of improving the signal to noise ratio in ultrasonic buffer rods, by fine tuning their geometrical parameters. In the last paper system identification algorithms are considered for estimation of the metal height in aluminium electrolysis cells.

In the thesis, the papers are referred to as:

- **Paper A:** Multi Sensor Data Fusion for Aluminium Cell Health Monitoring and Control, by H. Viumdal, R. Yan, M. Liane, B. Moxnes, and S. Mylvaganam.

    Published in: *TMS (The Minerals, Metals & Materials Society) Annual Meeting and Exhibition, February 2010, Seattle, USA*, Supplemental Proceedings, Volume 3: General Paper Selections, pp. 149-159, ISBN Number 978-0-87339-753-7

- **Paper B:** Beyond the Dip Stick: Level Measurements in Aluminum Electrolysis, by H. Viumdal, and S. Mylvaganam.

    Published in: *Journal of Minerals, Metals & Materials Society (JOM)*, Vol. 62, No. 11, pp. 18-25, November 2010, ISSN 1047-4838.

- **Paper C:** Enhancing Signal to Noise Ratio by Fine-Tuning Tapers of Cladded/Uncladded Buffer Rods in Ultrasonic Time Domain Reflectometry in Smelters, by H. Viumdal and S. Mylvaganam.

- **Paper D:** Dependency of Signal to Noise Ratio on Transducer Diameter and Buffer Diameter in Guided Wave Time Domain Reflectometry, by H. Viumdal, K.-T. Wu, and S. Mylvaganam.

- **Paper E:** System Identification of a Non-Uniformly Sampled Multi-Rate System in Aluminium Electrolysis Cells, by H. Viumdal, S. Mylvaganam, and D. Di Ruscio.

Since this thesis consists of five self-contained papers, some of the information from the papers are to some extent repeated in the thesis. There are also some differences in the notation used in the papers. In the descriptive section of the thesis, for clarity and conformity, a set of symbols are used, which are somewhat different from the symbols used in the papers. The study is truly multidisciplinary and the selection of symbols and deciding on their coherence were hence challenging.

Both bath and metal height in aluminium electrolysis cells were initially on the agenda of this study, and hence described in Part 1, Paper A and Paper B. In the further work, except for the laser vibrometer measurements of the bath surface, the focus of this study was limited to estimating techniques and ultrasonic instrumentation to determining the metal height.

In this study some groups of students and individual students at TUC have been involved in different projects, both at bachelor and master levels, in conjunctions with project based learning tasks and final year projects. The tasks span from a large variety of subjects relevant for this study. The supervised projects are listed in Table 1 and some of the relevant results are described later in appropriate places of the thesis.

Table 1: Student projects involved in this study

Year	Student(s)	Title
2008	M.I. Olsen, T. Pettersen E. Samuelsen, H. Nilsen T.H. Notvik, B.H. Olsen	Energisparing i smelteverk (Energy saving in smelters) *Bachelor project*
2008	M.B. Myhre, R. Sahm C. Novy, T. Nordal A. Mohamed	Nivåmåling under aluminiumsproduksjon (Level measurements in the aluminium production). *Bachelor project*
2009	Kai Anders Refsahl	Ultrasonic level measurements in smelters using buffer rods for thermal isolation *Master thesis* (described in Part II)
2009	Ru Yan	Usage of laser vibrometry in monitoring surfaces and interfaces *Master thesis* (described in Part II)
2009	H.H. Arbabi, R. Xia, Z. Wenjing, W. Xuecheng,	Estimating heights of molten metal using ultrasonic transducer with buffer rods *Master project* (described in Part II)
2010	I. Andreassen, N. Sen R. Balasubramanian	Neural networks in aluminium industry *Master project* (described in Part III)
2010	Sandeep Kumar Gandluru Rabin Bilas Pant	Fuzzy logic based level measurement *Master project*
2010	Sandeep Kumar Gandluru Olena Manova	Ultrasonic time domain reflectometry in molten metals using various buffer rods *Master project*
2011	Sandeep Kumar Gandluru	Ultrasonic level measurements with buffer rods *Master thesis*
2011	T. Granerød, K.H. Andersen, K.D. Finmark, E. Gundersen, and E. Frøhaug	HMS i aluminiumsproduksjon (Health, environment and security in Aluminium production). *Bachelor project*
2012	A.N. Kløcker, M.B. Johansen, H. Jensen, P. Håndlykken, Å.H. Hilde, R. Karlsen	Måling av nivå i en pulversilo (Measuring the level in a powder silo) *Bachelor project*
2012	T.H. Bråthen, G.I. Bitar, T. Gåsdalen, Y. Hermansen, M. Henriksen, Ø. Guldberg	Nivåmåling i væsketank (Level Measurement of a fluid in vessel) *Bachelor project*
2014	Erihe	Fusing ultrasonic time domain reflectometric data for multi-level fluids in vessels *Master thesis* (described in Part II)

Nomenclature

Symbol	Quantity	Units
A	Relative amplitude of reflected pulse (Part II)	dB
A	Cross section of aluminium pad (Part III)	m^2
b_1 and b_2	Parameters of mechanistic model	
BW_{UT}	-6 dB bandwidth of UT	%
BW_F	-3 dB bandwidth of filter	Hz
CE	Current Efficiency	
d_{Be}	Diameter of buffer rod end	m
d_{Bm}	Maximum diameter of buffer rod	m
d_{UT}	Element diameter of transducer	m
dN	Near field distance	m
F	Faraday constant	C/mol
f	Frequency	Hz
f_{Fc}	Center frequency of filter	Hz
f_{Fp}	Peak frequency of filter	Hz
f_{Flc}	Lower cut-off frequency of filter	Hz
f_{Fuc}	Upper cut-off frequency of filter	Hz
f_{UTc}	Center frequency of UT	Hz
f_{UTp}	Peak frequency of UT	Hz
f_s	Sampling frequency	Hz
f_m	System frequency	Hz
h	Level of molten aluminium	m
$\Delta\widehat{h}$	Predicted change of Aluminium level	m
$\bar{h}$	Aluminium level prediction	m
$\widetilde{h}$	Aluminium level measurement	m
I	Line current	A
K	Kalman gain matrix	
k	Discrete time	
L	Length of buffer rod	m
LN	Lorentz number	V^2/K^2
M_{Al}	Molecular mass of aluminium	g/mol
M	Sampling difference factor between T_f and T_s	
m	Mass of molten aluminium	kg

N	Number of data samples	
n_i	Discrete sampling instant of the i-th output measurement	
P	Covariance matrix	
T	Temperature	K
T_f	Fast sampling time	s
T_s	Slow sampling time	s
t	Time	s
Δt	Time step	s
Q	Charge	C
V	Volume of aluminium	m^3
v_s	Shear velocity of sound	m/s
v_l	Longitudinal velocity of sound	m/s
V_t	Criterion function	
w_1	Weight factor used for the results from model	
w_2	Weight factor used for measurements	
z	Charge number of an ion	
α	Taper angle (Part II)	°
α	Forgetting factor (Part III)	
Δt	Sampling time of input measurements	s
ρ	Density	kg/m^3
ε	Grid space of simulation (Part II)	m
ε	Prediction error (Part III)	
η	Shear viscosity	Pa $\cdot$ s
θ	Half angle of divergence (Part II)	°
θ	Parameter vector of the OLS model (Part III)	
κ	Thermal conductivity	W/(K$\cdot$ m)
λ	Lame's 1st constant (Part II)	Pa
λ	Parameter weight in OLS model (Part III)	
μ	Lame's 2nd constant	Pa
π	Bulk viscosity	Pa $\cdot$ s
ρ	Density	kg/m^3
σ	Electrical conductivity	S/m
φ	-6 dB ultrasonic beam spread angle	°
Φ	Measurement vector for fast sampling	
ϕ	Element in the measurement vector	
ψ	Measurement vector for slow sampling	

ACD	Anode Cathode Distance
CCA	Canonical Correlation Analysis
CE	Current Efficiency
DSR	Deterministic and Stochastic system identification and Realization
MDSR	Multiple time series DSR
MSE	Mean Square Error
MVDA	Multi Variate Data Analysis
NMSE	Normalized Mean Square Error
NN	Neural Network
NRMSE	Normalized Root Mean Square Error
NUSM	Non-Uniformly Sampled Multi-rate syst.
OLS	Ordinary Least Squares
PEM	Prediction Error Method
ROLS	Recursive Ordinary Least Squares
SI	System Identification
SNR	Signal to Noise Ratio
SSM	State Space Model
TUC	Telemark University College
UTDR	Ultrasonic Time Domain Reflectometry

Contents

List of Figures

List of Tables

Part I

NECCESSITY FOR HEIGHT MEASUREMENTS IN ALUMINIUM ELECTROLYSIS CELLS

Chapter 1

Height Measurements in the Aluminium Electrolysis Process

Aluminium is the third most abundant element, and the most abundant metallic element in the earth's crust. Aluminium combines strongly with oxygen, silicon or other elements, hence proper processes to extract pure aluminium from its ore have been difficult to establish [60]. In contrary to iron oxides, which can be fairly easily reduced to iron in a reaction with carbon, the reduction of aluminium compounds requires more advanced methods and large amount of energy [2].

1.1 Historical aspects

In 1807 the British chemist Sir Humphrey Davy tried to extract a metal from fused alumina (aluminium oxide, Al_2O_3). The extraction was not successfully performed, but he concluded that alumina had a metallic base, and he named it alumium [54]. Later he changed the name to aluminium. Some years later, in 1825, the Danish physicist and chemist Hans Christian Ørsted managed to prepare anhydrous aluminium chloride, which was an important step in isolating metallic aluminium [60]. He also managed to isolate impure metallic aluminium by further reducing aluminium chloride with potassium amalgam [36]. Two years later, in 1827, the German chemist Friedrich Wöhler managed to produce the first sample of pure aluminium powder, based upon a reaction between potassium and anhydrous aluminium chloride. His process was further refined by the Frenchman Henri Sainte-Claire Deville, which led to the first commercially production of aluminium in 1854, and hence a drastically reduction of the metal price in the following years. However, it was not until 1886 by the invention of the Hall-Héroult process, that industrial production of aluminium became interesting. The two scientist Paul Louis Toussaint Héroult from France, and Charles Martin Hall

from USA, were unaware of each other's work as they simultaneously invented a new process of making aluminium [2]. This electrolysis process where alumina is dissolved in a molten bath mainly consisting of cryolite (Na_3AlF_6), constitutes the basis of the industrial aluminium production still today. In the wake of the invention of the Hall- Héroult process in 1886, aluminium production became really industrially interesting, although the access to pure alumina was restricted. Only a few years later, in 1892, the Austrian chemist, Karl Joseph Bayer invented an efficient process of extracting alumina from natural ores of bauxite. The invention of the Hall- Héroult process and the Bayer process, made the founding of the aluminium industry even more successful. Hence, the annual production rate of aluminium went from 15 tons in 1885 to 8000 tons in 1900 [54].Throughout the last century the exponential growth in the net production of the metal continued, and in 2006, the annual primary aluminium production rate world wide was about 34 million tones, and 16 million tones of secondary aluminium (recycled) [47]. Recent numbers from the World-Aluminium report that the annual production rate world wide of primary aluminium in 2013 was about 50 million metric tonnes [57].

1.2   Properties of aluminium

Aluminum is the 13th element in the periodic system, and is categorized in the group of light metals, together with beryllium, magnesium, and titanium. In addition to light weight, they all reveal high strength, which make them particularly suitable for constructions of buildings and vehicles. Light metals are reactive metals and difficult to produce, and are therefore quite new in metallic state [18].

Measured in volume, aluminum is today the most extensive non-ferrous metal, although the production of the metal started fairly late compared to a lot of other metals. Its unique properties have made it the most versatile metal worldwide [2]. The major part of the aluminum consumption relates to the transport and building marked, but considerable amounts are used for packaging, electrical components, machinery and others. Extreme high purity of aluminum can be achieved by repeatedly numbers of electrolysis processes. Aluminium with a purity higher than 99.9999% has been reported [36]. In very pure state aluminium is a relative soft metal and lacks strength. However, aluminum is mostly used in some kind of alloys, as even small amounts of other elements increase the mechanical strength considerably compared to aluminum with high purity [19]. In transportation and constructions where weight saving is decisive, aluminium with a density about 2698 kg/m^3 has a huge advantage over iron alloys with densities about 3 times that of aluminium. Aluminium reacts easily with oxygen, forming a stable adherent oxide surface that is very resistant to further corrosion, contrary to iron. Other

Table 1.1: Properties of Aluminium, based upon [60, 36, 5]

Property	Value
Atomic number	13
Atomic weight	26.9815
Density at 25°C, kg/m^3	2698
Melting point, °C	660.2
Boiling point, °C	2494
Electrical conductivity, S/m	$37.67 \cdot 10^6$
Electrical resistivity at 20°C, Ω·m	$2.6548 \cdot 10^{-8}$
Electrode potential ($Al^{3+} + 3e^- \leftrightarrows Al(s)$), V	-1.68
Young's modulus, Pa	$65 \cdot 10^9$
Tensile strength, Pa	$50 \cdot 10^6$

properties that makes aluminium so applicable and more utilized than any other nonferrous metals are high electrical conductivity, nontoxic, odorless, and non-magnetic [36]. Some physical and chemical properties of aluminium with 99.99 % purity are shown in Table 1.1.

1.3   The Hall- Héroult process

The prevailing aluminum production world wide still utilizes the principles developed by Hall and Héroult 125 years ago, i.e. the production is based upon an electrolysis process where the electrolyte consists of alumina dissolved in cryolite (Na_3AlF_6). Although much effort has been spent on developing new methods of producing aluminum, e.g. inert anodes and carbothermic reduction of alumina, the Hall- Héroult process is the only method of producing aluminum industrially today [59].

However, the production line is much more efficient today. The improvements relates to an optimization of the electrolyte composition, the inclusion of a control and monitoring system, and automation of the alumina feeding process. However, the prevailing electrolysis process requires considerable manual intervention. There is an incessant requirement of higher production rates, that makes the process more complicated to run, as undesirable variations of the process variables, e.g. temperature, bath and metal level might occur more rapidly with a high production rate. Therefore, there is a trade off between high production rate and energy efficient production.

Two different main methods within the Hall- Héroult process concept have been used to produce aluminum, i.e. the concept with the prebaked anodes and the

Søderberg process. The main difference of the two processes are how the anodes are constructed. Both utilize a paste of cole and pitch. In the former method the anodes are baked in separate furnaces ahead of the electrolysis process, whereas the paste is baked in situ in the electrolysis cell with the Søderberg process [59]. The prebaked anode method has been dominating the industry more and more the last decades, and will also be in focus in this thesis. Mainly, due to a lower production rate, lower Current Efficiency (CE), and more environmental pollution with the Søderberg method, more Søderberg cells are rebuilt to cells for prebaked anodes today.

The overall chemical reaction in the Hall- Héroult process is the electrolytic reaction, where the dissolved alumina reacts with the carbon anode producing aluminum and carbon dioxide [14]:

$$2Al_2O_3 \text{ (dissolved)} + 3C \text{ (s)} \rightleftharpoons 4Al \text{ (l)} + 3CO_2 \text{ (g)} \qquad (1.1)$$

At the cathode, dissolved aluminium fluoride ions are reduced to molten aluminium in two steps [58];

$$AlF_4^- \text{ (dissolved)} + 2e^- \quad \leftrightarrows \quad AlF_2^- \text{ (dissolved)} + 2F^- \text{ (dissolved)}$$
$$AlF_2^- \text{ (dissolved)} + e^- \quad \leftrightarrows \quad Al(l) + 2F^- \text{ (dissolved)}.$$
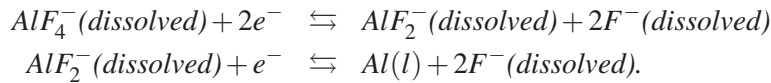
The anode reaction involves many complex reaction, and the details are still controversy. However, a likely reaction is described in [59], where the oxygen in a dissolved ion reacts with the carbon anode, producing carbon dioxide;

$$2Al_2OF_8^{4-} \text{ (dissolved)} + C \text{ (s)} \rightleftharpoons CO_2 \text{ (g)} + 4AlF_4^- + 4e^-.$$
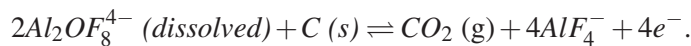
In real, the reactions are more complex, but these reactions demonstrate the overall redox reaction taking place at the anode and cathode.

Based upon Equation 1.1, and the molar mass of each element, theoretically 1889 kg of Al_2O_3 and 333 kg of C is needed to produce 1000 kg Al. Due to different kinds of losses, the actual numbers are a bit higher. A typical consumption for producing 1000 kg aluminium is shown in Table 1.2.

The original alumina reduction cell as drawn by Charles M. Hall in his patent "Process of reducing aluminium from its fluoride salts by electrolysis" , published in 1889 [21], is shown in Figure 1.1. Note that the two electrodes are vertically placed, and external heating is used to obtain and maintain the desired cell temperature.

Table 1.2: Materials and energy in producing 1000 kg aluminium [58]

Component	Consumption
Alumina (Al_2O_3)	1930 kg
Anode (C)	400 kg
Cryolite (Na_3AlF_6)	10 kg
Aluminium fluoride (AlF_3)	30 kg
Electrical energy	13 000-16 000 kWh
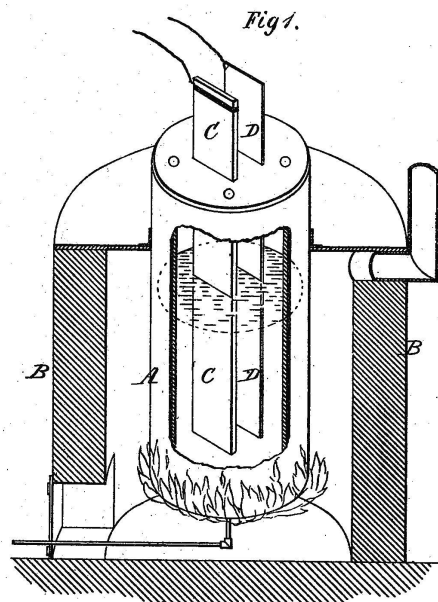
Figure 1.1: The original drawing of the alumina reduction cell patent, by Charles M. Hall, 1889, [21]. The essential parts of the cell are the crucible (A), the furnace (B), the anode (C) and the cathode (D).

Further improvements are seen in another patent publication from 1925 [25]. At that time the electrolysis cell, as shown in Figure 1.2 got a cell design, that is quite similar to prevailing cells. The cathode was placed underneath the electrolyte, whereas the anode is distributed into several anode blocks at the top of the cell. A thermal and electrically insulating side lining containing a frozen mixture of aluminium and sodium fluorides was introduced. A main difference to the prevailing alumina electrolysis cell is the size of the anode blocks, as they were much smaller at that time.
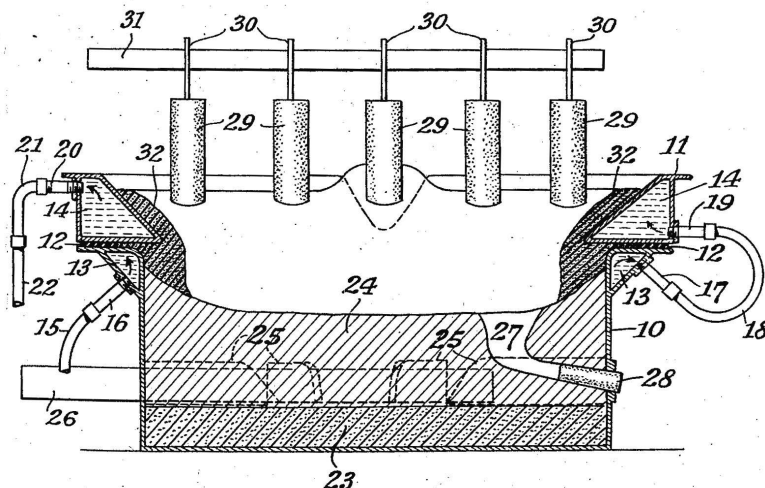
Figure 1.2: A novel alumina electrolysis cell in 1925, [25]. The essential parts of the cell are the bottom layer of heat insulating material (23), the bottom lining of conducting material, i.e. the cathode (24), the metal collector plates (25), the busbars (26 and 31), the carbonaceous anodes (29), conducting metal rods (30) and the thermally and electrically insulating lining (32).

A schematic drawing of a typical modern aluminium electrolysis cell is shown in Figure 1.3. Carbon anodes are connected to anode rods (iron stubs), that further are connected to the superstructure of the cell by a jack application to adjust the vertical position of the anodes. In each cell there are typically 20-30 anode blocks, although cells with 6 to 48 anodes are reported in the literature [56]. The anode blocks are partly immersed into the electrolyte which mainly consists of cryolite with about 2 to 3 wt % alumina (Al_2O_3). Throughout the electrolysis process alumina reacts with the carbon anode and molten aluminium is precipitated on top of the carbon cathode at the bottom of the cell. This molten metal pad is technically regarded as a part of the cathode; hence the aluminium precipitation is actually taking place at the metal/electrolyte interface indicated by h_1 in Figure 1.3. The electrolysis cell is incorporated in a steel container. Inside the steel shell, a refractory carbon lining is thermally insulating the cell and protecting the steel shell from corrosion. The carbon lining at the bottom of the cell is connected to thick current collector bars. The electrolysis process is taking place at about 970 °C, and has an extreme corrosive effect on most materials that is immersed into the cell. That is one of the reasons why the carbon side linings are covered with a layer of frozen electrolyte. In addition the bath or electrolyte surface h_3 is

covered with a electrolyte crust, reducing the heat loss from the cell. As alumina within the electrolyte is consumed during the electrolysis process, alumina powder has to be added regularly. In modern cells that is performed by a point feeder. A chisel shaped crust-breaker makes a hole in the crust, where a certain amount of alumina is poured into. The frequency of the feeding varies according to a feeding control strategy that will be explained later.

During the electrolysis process the carbon anodes are consumed as they take place in the electrolytic process, hence the anode rods have to be lowered to keep the Anode-Cathode Distance (ACD) as stable as possible. In Figure 1.3 the ACD=h_2-h_1. The height of the carbon anodes are typically reduced by 1.5 cm per day. Approximately every third week the carbon anodes are changed. At that moment about one-third to one-fourth of the anode is left, but further anode consumption will eventually cause corrosion of the iron stubs, that will again lead to impurity of the molten aluminium [17].
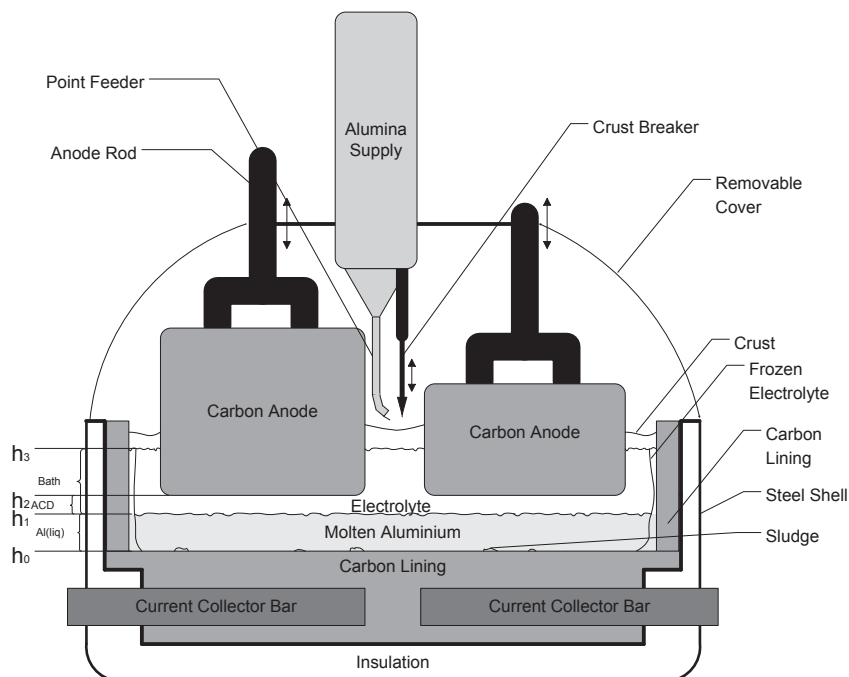
Figure 1.3: A schematic figure of a prebaked aluminium electrolysis cell showing essential features of the multi-level molten materials in the cell with the parameters under scrutiny in the present work h_1, h_2, etc. Movement up or down depending on the process state or crust breaker movement.

Also the cathode level varies with time, as the molten aluminium is regarded as a part of the cathode. The metal pad has normally a height of approximately 20 cm, and increases by about 2 cm per day, dependent of the production rate and cross-sectional area of the cell. The ACD, as shown in Figure 1.3, is one of the most important variables in the electrolysis cell. A small ACD is desirable to reduce the bath resistance to a minimum, particularly as modern cells use 300 kA or more.

Although the applied cell voltage is only between 4.0 and 4.6 V and the ohmic resistance constitute 1.3 to 2.0 V of this [17], the energy loss due to a to large ACD can be decisive to the aluminium plant. In contrast, too small an ACD will lead to more short circuits, and back reactions, where molten aluminium reacts with carbon dioxide generated at the anode, forming alumina and carbon monoxide. In this case the CE is reduced. Simultaneously, the thermal energy caused by the ohmic resistance of the electrolyte is used for keeping the cell temperature at steady state. Desired steady state of the cell temperature is only about 5-15 $^{\circ}C$ above the liquidus temperature [58]. This temperature difference between the liquidus temperature of the electrolyte or bath and the actual temperature of the electrolyte is called the super heat of the cell.

With a super heat within the narrow desired range, the electrolyte close to the wall and at the top of the electrolyte layer will be frozen. Both this side ledge and the crust have insulating effects of the cell. To some extent this phenomenon has an auto controllable impact of the temperature, as a high temperature will reduce the insulation, hence increase the heat loss. However, the side ledge has another very important function, by protection the carbon lining and the outer steel shell from corrosion. No other materials seems to be that resistant to the corrosion within the cell, hence its thickness has to be maintained The cell is normally designed to operate with a ACD about 4 -5 cm [58]. With a persistently higher ACD the super heat will increase causing the side ledge of frozen cryolite to melt, inducing a harmful corrosion of the carbon lining and eventually the steel shell. This may cause severe damage to the cell, which then has to be rebuilt before further operation.

Constantly demand of higher production rates have led to an increase in the line current through the cell, which makes the cell more complicated to run, as the process variables as the ACD are more rapidly changed. Hence, the need for proper measurement and control system is decisive.

Table 1.3: Measured process variables, based on [64]

Class	Measured variable	Purpose	Frequency
Automatic	Cell voltage	Process control	Continuously
Automatic	Line current	Process control	Continuously
Manual	Bath temperature	Process control and and cell monitoring	Daily to weekly
Manual	Bath composition	Process control and and cell monitoring	Daily or several times a week
Manual	Bath height	Process control	Daily to every second day
Manual	Metal height	Process control	Daily to every second day
Manual	Tapped metal weight	Process monitoring	Daily to every second day
Manual	Metal purity	Quality indicator	Daily to weekly
Manual	Cathode voltage drop	Monitoring the cathode aging	Occasionally
Manual	Anode Current	Monitoring anode conditions	Daily or when pots are unstable
Manual	Cathode Current	Monitoring cathode conditions	Occasionally
Manual	Freeze profile	Monitoring the side ledge condition	Occasionally or at anode change

1.4 Regular measurements in the aluminium electrolysis process

Although the Hall- Héroult process has been improved during the years since the invention in 1886, still manual intervention to monitor and operate the process is predominant in the aluminium electrolysis process. Table 1.3 displays an overview of the main measurements performed [64].

Pseudo-resistance is a very important variable, utilized for controlling the alumina feeding procedure of modern cells. It is not directly measured, but calculated based on cell voltage and line current [53];

$$R_{pseudo} = \frac{U - E}{I}, \tag{1.2}$$

where U is the measured cell voltage, and E is a theoretical constant of the zero current intercept of cell voltage versus line current linearized curve. There are

Table 1.4: Additional process variables

Class	Variable
Automatic/Manual	Alumina supply frequency
Automatic/Manual	Aluminium fluoride supply
Automatic/ Manual	Anode adjustment
Manual	Anode change
Manual	Metal tapping
Manual	Adding bath
Manual	Removing bath
Manual	Crust covering
Manual	Adding soda
Automatic/manual	Crust breaking
Automatic/manual	Anode effects
Automatic/manual	Anode defects

also additional process information that can not be categorized as measurements, but are still important to the process. Table 1.4 shows some of them.

The three first mentioned parameters in Table 1.4 are control outputs, i.e. process inputs. In modern cells more of the variables marked with "Automatic/Manual" are atomized, but still a lot of these variables are based upon manual intervention in older plants.

1.5   New technology and the continuous need for metal and bath height monitoring and control

The method of using a dip stick for measuring the bath height and metal height simultaneously, is still the prevailing method in the aluminium electrolysis process. Typically this manual measurement is performed once a day, or even every second day, as shown in Table 1.3. It is normal procedure to accomplish the measurements just before tapping of the molten aluminium. Unfortunately, the accuracy of the height measurement is probably about ± 0.5 to ± 1.0 cm, as the height is manually measured in steps of 0.5 cm. This is very poor as the metal height before and after the tapping varies by typically 2cm. Simultaneously, an increase in the frequency of the measurements would be desirable, but are demanding as it is fully manually performed. Although strict routines for the manual height measurement procedures are common, replacing this manual intervention with an automatically performed method, would reduce the exposure of unhealthy gases and possible accidents.

In addition to these, improved level measurements are important of several technological reasons;

1. Increased production rate

2. Reduced ACD and Maintaining a high CE

3. Smaller electrolyte volume

Each of the items will be discussed in the following subsections. Some relates only to the bath height, whereas other only the metal height.

1.5.1   Increased production rate of aluminium

During the years, the manufactures have been striving for and achieved increased production rate. The most important contribution factor has been the pot-line amperage (line current), that has increased from about 50 kA in 1940 to about 300 kA for the most advanced cells in 2000 [56]. Today even higher amperage is reported. Both the cell design and the cell operation have been adjusted to manage such high currents. To keep the current density at a sustainable level, the corresponding total anode area in the electrolysis cell have increased from 5 m^2 to 38 m^2 [56]. That implies actually a small decrease in average anode current density from 1.0 A/cm^2 to 0.8 A/cm^2. The Critical Current Density (CCD) varies from about 0.1 A/cm^2 in pure cryolite to more than 20 A/cm^2 for alumina-rich melts [59]. Typical values of the anode current density in alumina reduction cells are approximately 0.85 A/cm^2, but it is claimed that a current density of even higher values is possible with improved design and operation [1]. If the current density increases above the CCD, the normal anode reaction will be replaced by unwanted Anode Effects (AE). AE is characterized by a blockage effect of the current transport between the anode and the electrolyte, due to an electrical insulating gas film under the anodes [37], and emerge as a sudden increase in cell voltage. In addition to a high degree of energy loss, and possible melting of the side ledge of frozen bath, perfluorcarbon greenhouse gases, as CF_4 and C_2F_6, are emitted together with CO and CO_2 [59]. In the recent years, there has been an increased focus on reducing both the local pollution in the production hall and the environmental air pollution, hence limiting the AE has been a topic with high priority. In modern electrolysis cells an automated point feeder system of the alumina has been introduced. The feeding is performed through a hole in the crust automatically made by a crust braking chisel just before the feeding procedure. This in combination with improved control strategies where the pseudo resistance is utilized to estimate the alumina concentration has been the main contributes in successfully reducing the AE.

The cell voltage used to estimate the pseudo-resistance, and hence the alumina content in the bath, depends both on the bath concentration and on the ACD. By improving the metal height measurement, the uncertainty in the resistance estimation could be reduced. This is even more important now as the increased production rate induce more rapid variations in the bath and metal height.

1.5.2   Reduced ACD and maintaining a high CE

A large ACD will give a high ohmic resistance, that will cause a high energy loss, and also reduce the thickness of the side ledge and crust, as a result of an increased superheat. Therefore there has been a focus on reducing the ACD to an optimal level. Actually, Alcoa cells had a reduction of the ACD, leading to a reduction of the cell voltage from about 5.7 V in 1940 to 4.5 V in 1980 [37]. In 2000 Kvande and Haupin assumed that the optimal ACD for the prevailing cell technology was reached at a level of 4.1 V to 4.2 V for cells with line currents above 200 kA [37]. Further reduction of the ACD seems to be possible only with drained cathodes in combination with inert sidewalls. Hence, increased thermal insulation will be necessary.

Further reduction of the ACD without these improvements will cause reduced CE, due to increased back reaction. By improving the control and stability of the aluminium-bath interface the CE in the electrolysis cell will improve [48]. When reducing the ACD, the side-ledge will become too thick, affecting the electrolysis process in a negative way. Although, there is an optimal minimum level for each cell design, the operational ACD will in practice often be at a higher level, in order to compensate for heat loss through disturbing interventions as anode change etc. Hence, the ACD is considered as the main input to control the energy balance in the cell. Proper metal height measurements could make it easier to determine the ACD and maintain it at an optimal level.

1.5.3   Effects of smaller electrolyte volume

As already mentioned the total anode area in the electrolysis cell has increased dramatically during the recent decades. Yet, the total cell area has not had a similar increase during the years, i.e. the ratio between the total anode area and the cell area has increased considerably, inducing a relatively smaller electrolyte volume and horizontal cross sectional area of the electrolyte around the anodes. In addition to the increased production rate, this results in more rapid variations in the bath height. Improved and more frequent bath height measurements could make it easier to monitor and to maintain the bath height at a desired level. Proper bath height measurements will make it easier to determine when to replace the anodes. If the bath level flows over the anode blocks, the anode stubs will corrode,

Table 1.5: Overview of research on determining the bath and metal height in aluminium electrolysis cell

Method	Year	Metal height	Bath height	ACD	Ref.
Anode elevation	1985		√		
Electrical contact	1988		√		
Voltage drop (CMD)	1998	√	√		
Voltage drop and mechanical	2003	√		√	
Chisel contact	2009		√		[11]
Temperature gradients	2004	√			[66]
Ultrasonic measurements	1993	√			[49]
Dynamic nonlinear model	1980	√	√		[15]

resulting in an increased iron content in the molten aluminium in addition to the reduced lifetime of the anode stubs itself.

1.6 Research on height measurements in aluminium electrolysis cells

In [61] an overview of several researchers work of developing alternative methods to replace or to improve the measuring method is given. The methods are listed in Table 1.5. The optional methods of measuring the bath and metal height can be divided into two main categories. The first group is the direct measurements, where new hardware or instrumentation is introduced to measure the measurand, whereas the second group consists of indirect measurements, i.e. state estimation based upon a mathematical model and recent data from related/dependent variables.

Several possible measuring methods related to determining levels within the aluminium electrolysis cell have been developed, but still the use of a dip-stick is the industrial method used in regular cell operation. The main reason for not successfully involving any of these novel methods relates to technological challenges in this harsh environment, i.e. high temperature, extreme corrosion, opaque substance and strong magnetic fields. More details regarding R&D on measurements for determining the metal height and the bath height in aluminium electrolysis cells are given in Paper A and Paper B.

1.7   Abstract of Paper A

The prevailing aluminium electrolysis process demands steady-state conditions within narrow borders, to improve performance with respect to molten metal production per day, energy usage per kg of aluminium, current efficiency, CO_2 and flour-gas emissions etc. However, only the current and the cell voltage are obtained by on-line measurements. Many bath parameters are manually measured on a daily or even weekly basis. Innovating measurements of the bath temperature, the bath chemistry, the molten metal height and the height of the electrolyte would all be of substantial importance for the control regime. However, combining new measurements and soft sensors for estimating "'unavailable'" variables would improve both the monitoring and controlling tasks of the aluminium electrolysis process. This paper gives an overview of many online and off-line measurements and reports some new possible measurement scenarios with increasing potential for extensive, fast, efficient and even real-time data fusion. Finally some interesting examples of data fusion examples based on actual plant measurements covering many months are also included.

1.8   Abstract of Paper B

The "old fashioned" and imprecise approach of using a dip stick is still employed to measure the crucial level information in electrolysis baths in the aluminum industry. The dip stick method is based on manually immersing a metal rod into the cell and observing the marks left by the molten bath components to estimate the metal/electrolyte interface and the bath level. However, methods to improve height estimation have been developed in recent years, although none has yet been introduced as part of the routine measurement procedure in the aluminum manufacturing industries. An attempt is made here to give an overview of the promising methods for measuring or estimating the different levels of the bath constituents in an electrolysis cell. Broadly, these methods can be classified into two categories: methods based on innovative physical equipment with the necessary sensors and transducers, and inferential methods which exploit existing measurement data. The first category encompasses many physical and chemical disciplines, whereas the second relies on inferential methods employing approaches sometimes called soft computing or soft sensors. Both approaches are presented and discussed in this paper.

Part II

HARD SENSORS

Chapter 2

Ultrasonic Height Measurements

Ultrasonic measurements are widely used in industrial Non-Destructive Evaluation (NDE). The applications involve flowmetry, thermometry, interface sensing, density, porosity etc. A comprehensive scope of applications are provided by L. Lynnworth [42]. In the present work the main focus has been on height measurement in aluminium electrolysis cell, to detect the interface between the molten aluminium and the electrolyte. The measurement scenario builds upon the "time of flight" concept, mainly using "pulse echo" mode, often called Ultrasonic Time Domain Reflectometry (UTDR). To be able to use Ultrasonic Transducers (UT) in this application, some restrictive conditions have to be considered:

- It is not possible to use a noninvasive ultrasonic device, as the ultrasound will be reflected on top of the crust, if transmitted through air. The ultrasound has to travel through a *solid material* that is immersed into the molten bath to achieve a reflection of the ultrasonic signal at the interface of interest.

- The *solid material* must act as a buffer, and hence be able to withstand the harsh, hot and corrosive environments of the electrolysis cell, within acceptable lifetime. This *solid material* that acts as a wave guide is in general rod shaped, and therefore often called Buffer Rod (BR).

- The acoustic impedance of the BR material should be as close to the acoustic impedance of the molten bath as possible, to minimize the reflection at the interface between the BR and the molten bath. Simultaneously the wetting conditions of BR in the bath should be evaluated. There is a trade-off between enhancing the wetting to improve the transmitting of the signal, and reducing the wetting to reduce the corrosion of the BR.

- The BR should have acceptable ultrasonic wave guiding properties, and should be shaped to further improve these features. According to several

papers, e.g. [49, 28, 32], both cladded BRs, taper shaped BRs, BRs with threaded grooves at their surfaces, have the ability to improve the wave-guiding performance of BR, compared to straight cylindrical BRs. Also BRs with columnar grain structures and BRs where their radial acoustic velocity profile is graded are claimed to have the similar effect [33, 27].

• Ultrasonic transducers and ultrasonic transceiver system should "'match"' the wave-guiding properties of the BR.

These considerations and more are explained and discussed in Paper C.

2.1   Assembly of the experimental setups

This study has involved a large variety of experiments for detection of interfaces, and calculations of levels and heights in different applications, as itemized in the following:

• SNR measurements of BRs.

• Thickness measurements of different metal pieces.

• Height measurement of metal pieces in water, using BRs.

• Detection of a metal plate with angular adjustment in water, using BRs.

• Height measurement of metal pieces in molten tin, using BRs.

• Height measurement of metal pieces in molten lead, using BRs.

• Height measurement of metal pieces in molten zinc, using BRs.

• Height measurement of aluminium-cryolite interface in aluminium electro-lysis cell, using BRs with cooling pipes.

To be able to run all these tests, a lot of technical equipments and software were needed. Most of the hardware had to be specially designed by the under-signed, and manufactured at TUC or by external partners. The most important equipments are described in this section. During the study, several scripts and programs were generated, both in LabVIEW and MATLAB. Brief descriptions of some of them are also included in the following.

2.1.1 Ultrasonic transceivers

In this study the two following ultrasonic transceivers were utilized for UTDR:

- Panametrics-NDT Model 5900 PR in combination with a Tektronix TDS 2022B Oscilloscope and a laptop with installed LabVIEW software.

- Olympus EPOCH 1000i

The Olympus device is a fully integrated transceiver, made for industrial settings, and was used both in lab at TUC and in a real aluminium electrolysis plant at Hydro, Årdal. The device worked excellent both for determining the distance between transmitted and reflected signal peaks and for determining the SNR of the waveforms described both in Chapter 3 and later in this chapter. To be able to store and analyze the raw data representing the waveforms, the Panametric system had to be used in combination with an oscilloscope, and a laptop with specially designed LabVIEW programs. The Panametric device is mainly designed for labwork, but was also tested out in the real plant. Although covered up with μ-metal its relay was damaged by the high magnetic field present in the aluminium electrolysis plant.

2.1.2 Mounting UTs on to the BRs

As most of the experiments involved an UT in combination with a BR, an arrangement for mounting the UT in a fixed position on top of the BR had to be designed. Three different versions of an UT holder was constructed, as seen in Figure 2.1.
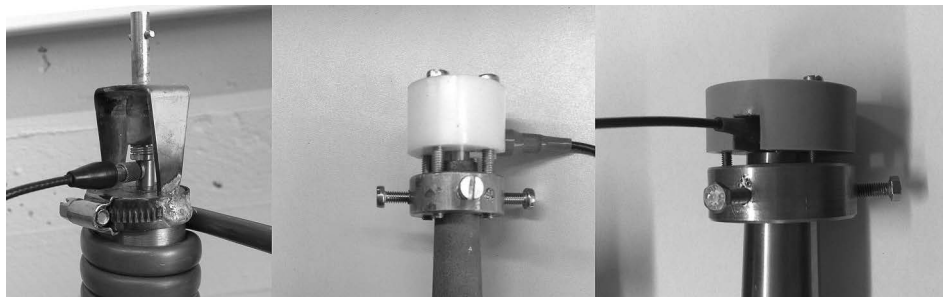
Figure 2.1: 3 different versions of the UT holder. Left: The first version used a spring for aligning the UT. Middle: The second version had a slot in a plastic structure for aligning the UT. Right: The third version had three replaceable plastic structures each with different slot size for fitting different UTs.

The first version utilized a spring to bring the UT into the right position (left part of Figure 2.1). The spring was attached to a bracket welded on a hose clamp. The hose clamp was easily fixed to one of the rod ends. The holder did work and made it very easy to change between different UT. However, this version had some severe limitations:

- The UT had a tendency of not remaining in the same fixed position, when moving the BR or the wire connecting the UT to the transceiver.

- When arranging the UT, misalignment of the centers of UT and BR was often a problem. A small deviation from the radial center positions of UT and BR could easily reduce the SNR drastically.

- The hose clamp gave little flexibility with respect to variations in diameter for different BRs.

In the second version these limitations were resolved, by using a thick cylindrical plastic disc with a slot fitting the size of the UT (middle part of Figure 2.1). The plastic structure was fixed to a metal cylinder with four screws. This cylinder was again fixed to the BR by four other screws. To avoid scratches on the BR and acoustic contact between the screws and the BRs, rubber was used as an intermediate damping structure. The result was a much more stable UT holder, providing stable and repeatable measurements. The main drawback of this UT holder was the time demanding work for changing the UT, and BR. A third version with more flexibility to change between different sizes of UTs and BRs was designed by using a larger metal cylinder and three exchangeable plastic discs with different slots for different UTs (right part of Figure 2.1).

2.1.3   Experimental rig for ultrasonic and laser systems

To perform reliable ultrasonic measurements in the aluminium electrolysis cells, a dedicated rig was necessary. The harsh and demanding environment in and around the aluminium electrolysis cell, causes several restrictions both on which equipment that can be used in its vicinity, and on selection of materials and design of new equipment;

- Electronic equipment are very sensitive in the vicinity of the electrolysis cells. Ordinary laptops cannot be used, as the mechanism behind the movement of the hard disc will break down due to the prevailing extremely high magnetic fields, caused by the high electric current passing through the electrolysis cells. Also ordinary laptop screens may get damaged for the same reason.

- Long electrical conducting structures are prohibited, as they can cause short circuits between serial connected electrolysis cells.

- Cooling pipes are needed for running the ultrasonic measurements, but cooling liquids represent a hazardous explosion risk in the vicinity of the molten electrolyte.

- Attention should be payed on selecting material with low thermal conductivity, and ability to withstand high temperature.

- Magnetic materials should be avoided, as the forces from the magnetic field can affect or obstruct the operation of the measurement equipment.

With these restriction in mind a wooden rig for operating the ultrasonic measurements was constructed, as seen in Figure 2.2. A cooling pipe was wrapped around the BR and compressed air was used as the coolant. The vertical position of the BR was adjusted by a sliding holder on top of the rig. The same rig was slightly modified for accommodating the laser vibrometer described in Chapter 5.
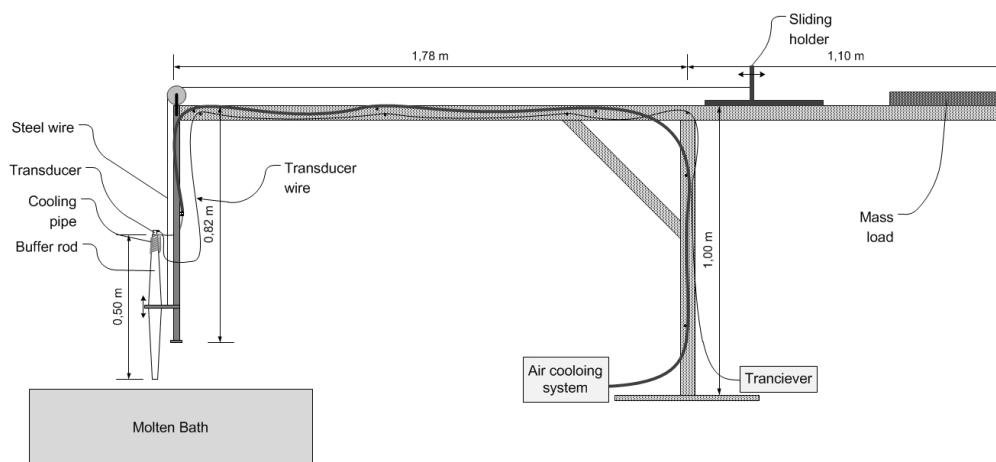
Figure 2.2: A schematic drawing of the wooden rig, due to safety aspects, used for ultrasonic measurements in aluminium electrolysis cells. Design and construction in collaboration with our late colleague Mr. Talleiv Skredtvedt, Telemark University College. Other measurement modalities can be easily incorporated in this design, see Figure 5.1.

2.2   Development of LabVIEW programs

LabVIEW based programs were created to store data sets representing time-domain waveforms, and for calculating actual heights. Several different approaches have been used to extract the peaks of interest (the interface reflection) from noisy waveforms often encountered in real measurements. The different approaches are:

- *Dual measurement*. The algorithm described in [49] has been implemented in a LabVIEW program [52]. Here two measurements are performed at two different altitudes, providing two different waveforms. By subtracting the second waveform from the first, a waveform representing the difference is created. In this difference waveform, the noise within the BR will be reduced to a minimum, as the noise signals will be at the same positions for the two measurements. All the samples in the difference waveform that are below a predefined level are assumed to be equal in both waveforms, hence these samples are given the value 0 in the resulting binary time series. Otherwise, sample values above the predefined level are assumed to be unique reflection, that are only detected by one of the waveforms, hence it is given the value 1 in the resulting binary time series. By calculating the time distance between the peaks in the resulting binary time series, and measuring the distance the BR has been moved between the two measurements, the sound velocity in the molten material is calculated. Knowing the velocity, the temporal positions of the peaks of the two reflections and the length of the BR, the distance between the BR and the interface of interest is easily calculated.

- *Fuzzy logic*. Fuzzy logic has been implemented in a LabVIEW program to detect the interface of interest [4]. The selected fuzzy variables were the amplitude of the signal, the reflection time, and deviation from the former measurement, with suitable membership functions.

- *Mean value*. The waveforms from the ultrasonic measurement system are usually unstable. To obtain a stable waveform representation a LabVIEW program was developed. By running online measurements of the system, new waveforms are generated at least every 5 ms. By taking the mean value of either 8 or 16 waveforms at a time, representative and more stable waveforms amenable for parameter evaluation were achieved.

2.3 Comparing the performance of different BRs

There is a diversity of factors to consider when selecting BRs for an application. The Signal to Noise Ratio (SNR) is considered to be the most important response or output variable to investigate when optimizing the wave guiding performance of BRs. Therefore the scope of this study regarding ultrasonic BRs for UTDR is mainly on improving the SNR. Both geometrical aspects of the BR and UT, acoustical aspects of the UT and filter properties of the transceiver system have been included in this study.

In the early stage of the present work, BRs with a variety of sizes, cylindrical or taper shaped (see Figure 2.4), were tested with respect to their SNR. Table 2.1 shows the geometrical parameters and the material of the BRs, the main ultrasonic transducer specifications, and their respective SNR. The measurements were made with "pulse echo" mode, with a "free" BR end.

Table 2.1: Experiment with respect to SNR, using different BRs and UTs

No	Material	Shape	Cladding	L (mm)	d_{Be} (mm)	α (°)	SNR UT_A^*	$UT_B^\star$	$UT_C^\diamond$
1	Aluminium	Cyl.	$\checkmark$	161	6.7	0.0	15.2	12.8	21.5
2	Aluminium	Cyl.	$\checkmark$	166	4.7	0.0	9.8	10.2	22.6
3	Aluminium	Cyl.	$\checkmark$	189	25.9	0.0	18.2	17.4	15.0
4	Alumina	Cyl.		152	20.0	0.0	11.4	9.7	7.9
5	Steel	Cyl.	$\checkmark$	305	19.6	0.0	19.9	17.1	18.8
6	Aluminium	S. taper	$\checkmark$	136	5.6	2.6	19.6	20.6	22.9
7	Steel	S. taper		299	21.0	2.9	6.7	6.5	0.4
8	Steel	S. taper		290	20.8	3.0	16.6	11.1	7.9
9	Stainless steel	S. taper		306	19.9	2.6	8.8	7.5	1.6
10	PEEK	S. taper		74.0	13.0	4.8	21.4	21.0	7.0
11	PEEK	S. taper	$\checkmark$	75.1	12.8	4.9	24.4	22.7	9.0
12	Steel	D. taper	$\checkmark$	140	5.8	4.4	40.3	39.9	28.9
13	Steel	D. taper	$\checkmark$	279	11.7	3.9	24.4	24.5	18.0
14	Steel	D. taper	$\checkmark$	541	13.6	3.1	28.2	26.6	27.0
15	Steel	D. taper	$\checkmark$	892	16.3	2.1	37.0	36.1	29.0

$^*\ UT_A : f = 5\,MHz,\ d_{UT} = 6.35\,mm$ $^\star\ UT_B : f = 10\,MHz,\ d_{UT} = 6.35\,mm$
$^\diamond\ UT_C : f = 20\,MHz,\ d_{UT} = 3.18\,mm$

The SNRs of the UT-BR combinations given in Table 2.1 are given as a bar chart in Figure 2.3, with respect to the BR number. There is a large variation in

the SNR between the poorest and best combinations.
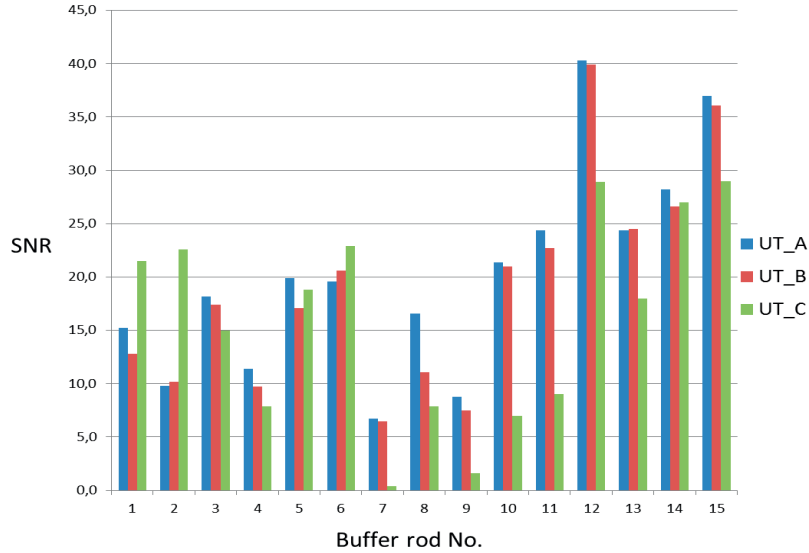
Figure 2.3:   Histogram of the SNR for the 15 different BRs tested in the initial experiment. Three UTs were used in combination with each of them. There are large differences in the SNR, both between the BRs and the UTs used. There is a tendency that the double-tapered and cladded BRs provides the best SNRs. The SNR is reduced with increased UT frequency for the high attenuating plastic material PEEK. For the thickest BRs, the SNR is relatively high with the low UT frequency, but small for the thin BRs, and vice a versa.

For the 5 first BRs, i.e. the *cylindrical BRs*, the BRs with cladding on the buffer walls are providing the best SNR. Using this arc-sprayed technique to improve the SNR on BRs has been introduced and documented by C.K. Jen [30, 31, 29]. The thinnest BRs in the cylindrical group (No 1 and No 2) provided the highest SNR with the smallest UT (UT_C), i.e. the UT with the highest resonant frequency (20 MHz). There is also a tendency that the BRs with the largest diameters (No 3 and No 4) in the same group had the opposite result, displaying the best SNR with lower frequencies (5 MHz (UT_A) and 10 MHz (UT_B)). As the resonant frequency f of the UTs and its element diameter d_{UT} are correlated variables in this data-set,

it is not possible to conclude whether the frequency or the diameter of the UT is the most important explanatory variable of the SNR.

Also in the group containing the *single tapered* BRs (No 6-11) (see Figure 2.4) the SNR is related to the diameter of the BRs, the frequency of UT transducer and its element diameter in the same manner as in the group of cylindrical BRs. BR No 7-9 are special as 2/3 of their BR length is tapered, and 1/3 is cylindrical. These BRs displayed poor wave-guiding performance, especially with the small UT, with high frequency (UT_C). The "plastic material" PEEK is represented by fairly good SNRs, especially for the cladded version. However, its low melting point and high ultrasonic attenuation, make it not suitable in hot environments or for long BRs.

Straight buffer

Single taper buffer

Double taper buffer

Multi taper buffer
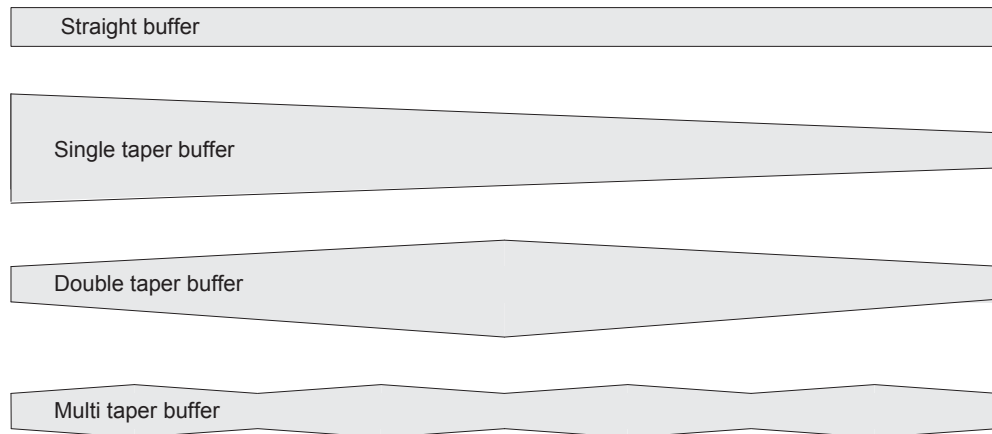
Figure 2.4: Schematic drawings of the most common BR shapes, with variations of degrees and number of tapers and their position along the BR.

All the SNR measurements of the *double-tapered* BRs (No 12-15) in the experiment were of a high or excellent level. Especially impressive is the SNR provided by the almost 90 cm long BR (No 15). Both the shape and the cladding of these BRs are designed to enhance the SNR. The BRs in this double-tapered group are designed and fabricated by the National Research Center of Canada.

BR No 7 to 9 were the first BRs that was made at Telemark University College in our study, and were tested out in an operating aluminium electrolysis cell at Hydro, Årdal, Norway. These measurements were unfortunately not successful, as it was not possible to distinguish the reflected signal from the metal-bath interface.

Another challenge was the powerful magnetic field generated by the high line current. The BRs made of steel were not possible to operate in a desired way, as the one made in stainless steel. Based on these experiences, we concluded to focus on how to improve the SNR of the BRs, as the SNR of these three BRs were insufficient. Further a replacement to the steel material, that could withstand the harsh conditions of the electrolysis bath, was on the agenda.

Chapter 3

Experimental study on the Waveguiding Performance of BRs

Although several publications involve ultrasonic BRs, a study on how all the main variables of the measurement system and their interactions (as considered in Table 2.1) are influencing the waveguiding performance, has not been found in the literature. In this chapter an experimental investigation with different combinations of BRs and UTs is presented. Similar simulations were performed for some of the combinations. The experiment was intended to decide the optimal combination of UT and BR to perform height measurements in smelters. An extensive experiment including 10 different BRs and 10 different UTs was designed in the present study. The experiment was performed in a structured way, and the results are presented and discussed in this chapter.

In particular there were few guidelines found in published literature on how to choose the geometrical variables of the BRs to optimize the SNR. As described in Chapter 2 and in Paper C, double tapered BRs are expected to have excellent waveguiding performance, but the optimal angle can be hard to find, and might vary with respect to end diameter etc. Hence, the main focus in this experimental study, has been on how geometrical variables as diameter and taper angle will influence the acoustical waveguiding properties of the BRs, in UTDR. Another important aspect is how different acoustical and geometrical properties of the UT will affect the waveguiding performance of the measuring system as a whole.

A set of titanium BRs has been tested with respect to the SNR and the amplitude of the received reflected signal, by employing different UTs with varying sizes and operating frequencies. The influence of variations of taper angle α, BR end diameter d_{Be}, UT element diameter d_{UT}, UT frequency f, UT bandwidth BW_{UT}, filter frequency f_F, and filter bandwidth BW_F have been tested out and their effects exploratory analyzed, using Principal Component Analysis (PCA).

The results of the experiment is further discussed and analyzed to extract

knowledge of how the BR geometry, the UT parameters and the parameters of the measuring system are influencing the SNR of the UTDR. Some of the results from this experiment are published in Paper C [62]and Paper D [61].

3.1   The experimental setup

The experimental setup used for this experiment is shown in Figure 3.1. The measurement system consists of an Olympus Epoch 1000i, which is a signal transceiver, with a display showing the UTDR waveforms. This is connected to a UT that is fixed to one end of a BR. In this study, a square pulse was transmitted from the UT, transmitted through the BR, and reflected at the BR-air interface at the other end of the BR. The measurements were performed in a pulse-echo mode, so the received signal had traveled twice the length of the BR, before it was detected by the same UT.
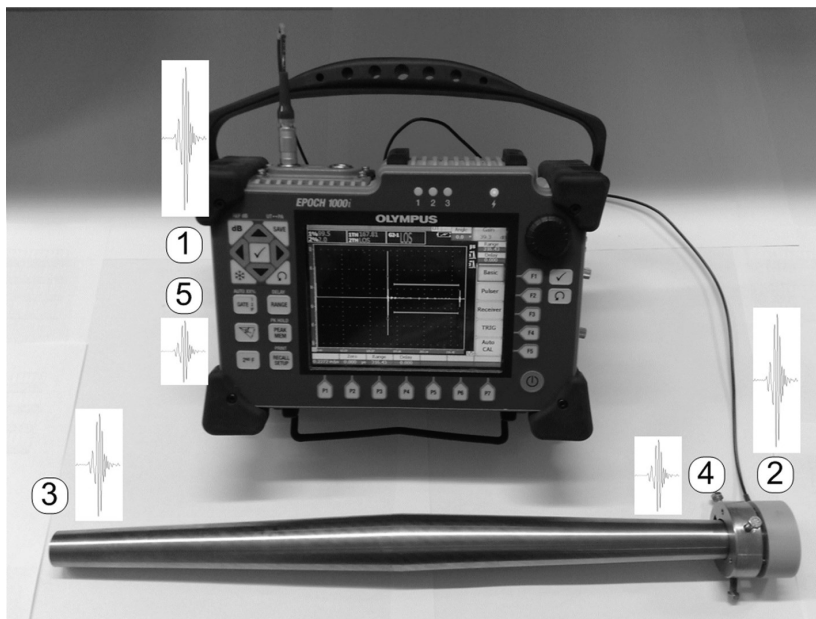
Figure 3.1: The signal-path for the experimental set-up: (1) an electrical pulse is generated, (2) the electrical pulse is transformed into an acoustic pulse in the UT, (3) the acoustic pulse is reflected at the buffer-air interface, (4) the reflected acoustic pulse is transformed into an electrical pulse in the UT, and (5) the electrical signal is received, amplified and displayed by the receiver.

The reflected signal was detected about 167 μs after the pulse had been transmitted. Its amplitude A_S was determined. The amplitude of the noise A_N was defined as the highest peak of the waveform located in the range between 15 μs after the first reflection, and the second reflection from the BR end. The SNR is given by:

$$SNR[dB] = A_S[dB] - A_N[dB] \qquad (3.1)$$

Proper alignment of the actual UT on top of the BR is achieved by specially designed UT holders for all the different UT sizes. The UT holder assembles the UT to a fixed and centered position at the BR end by three screws. The mounting of the UT is performed with high accuracy, as even small misalignment and improper contact of the UT will reduce the desired signal considerably. Regular ultrasonic couplant was used in the interface.

3.1.1 Main features of the BRs

444 measurements were performed on 10 different titanium BRs. The BRs were made of grade 2 material with a purity of 99.4 %. The BR parameters are shown in Table 3.1. All the first 9 BRs are with double-tapers, whereas the last is a multi-taper BR, as can be seen in Figure 3.2 and Figure 3.3.

Table 3.1: Ultrasonic titanium BRs used in the experiments

Group	Label	Length, L (mm)	End diameter, d_{Be} (mm)	Max. diameter, d_{Bm} (mm)	Taper angle, α (°)
G1, Ga	R1	500	8.9	16.8	0.9
G1, Gb	R2	500	8.9	20.2	1.3
G1, Gc	R3	500	8.9	23.7	1.7
G2, Ga	R4	500	17.8	25.7	0.9
G2, Gb	R5	500	17.8	29.1	1.3
G2, Gc	R6	500	17.8	32.6	1.7
G3, Ga	R7	500	25.4	33.3	0.9
G3, Gb	R8	500	25.4	36.7	1.3
G3, Gc	R9	500	25.4	40.2	1.7
	R10	500	17.8	25.2	1.7

For analyzing purpose, each of the BRs are given a label from R1 to R10, and are grouped into three different categories, according to the end diameter of the BR d_{Be}. BRs with $d_{Be} = 8.9$ mm are categorized into group G1, BRs with $d_{Be} = 17.8$ mm are categorized into group G2, whereas BRs with $d_{Be} = 25.4$ mm

are categorized into group G3. In a similar way the BRs are grouped into three categories, according to taper angle α. Group Ga, Gb, and Gc represent BRs with α = 0.9°, α = 1.3°, and α = 1.7°, respectively.
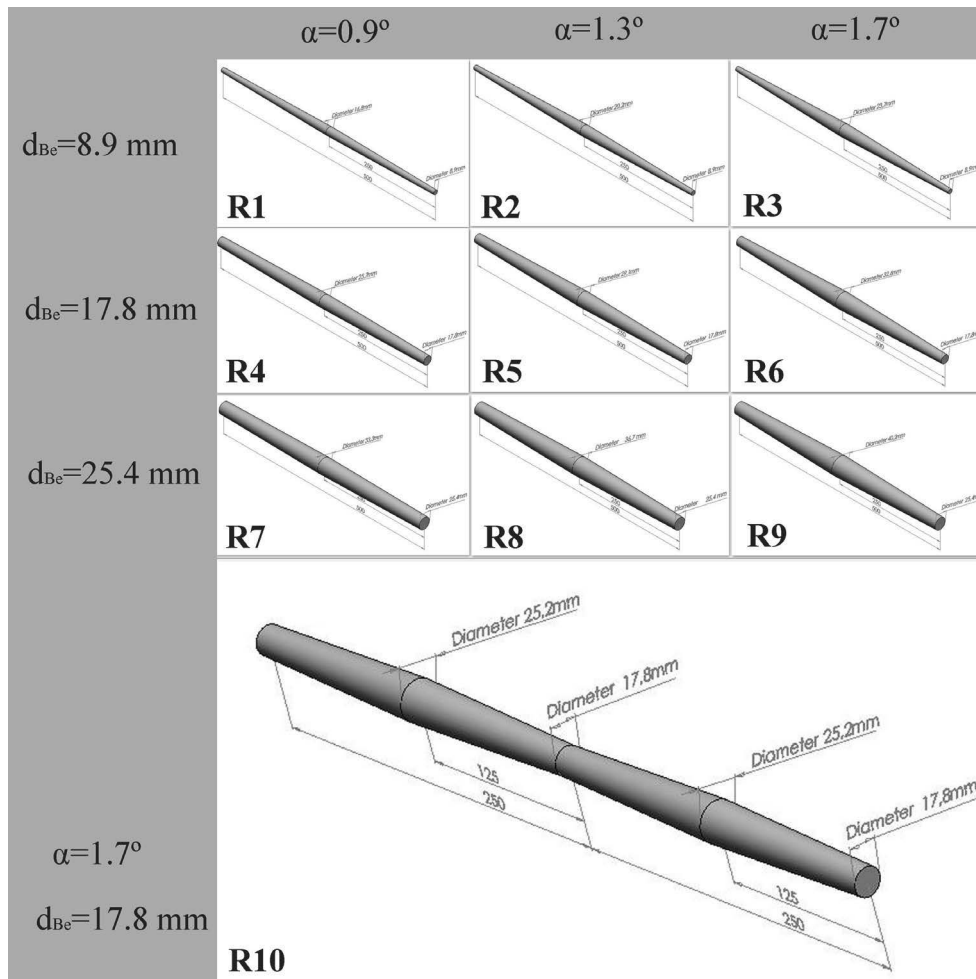
Figure 3.2: Sketches of the ten titanium BRs tested in the experiment. The taper angles α for the nine double-taper BRs are 0.9°, 1.3° and 1.7° for the three columns, respectively, whereas the end diameter d_{Be} of the BRs is 8.9, 17.8 and 25.4 mm for the rows, respectively. The taper angle α and the end diameter d_{Be} of the multi-taper BR is 1.7° and 17.8 mm, respectively.
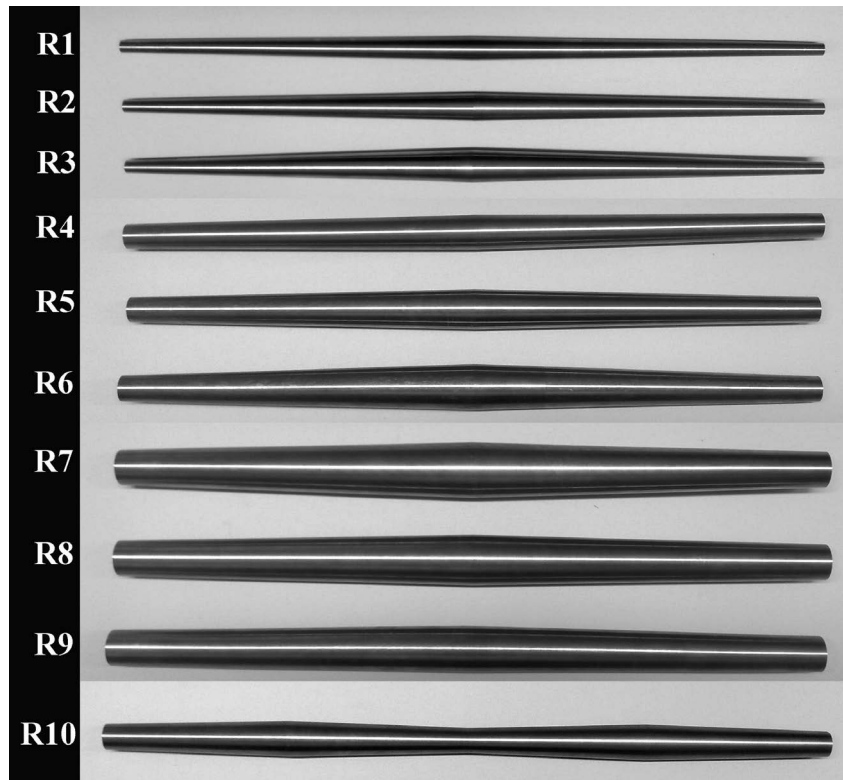
Figure 3.3: Pictures of the ten titanium BRs tested in the experiment.

The length of the BRs was chosen to be as long as 500 mm each, to better physically protect the UT from the molten metal in industrial smelters. The UT is also better protected against heat conduction from the molten metal through the BR compared to shorter BRs. This is specially an advantage when considering intermittent measurements in hot fluids. Even longer BRs were considered, but very long BRs may attenuate the signal considerably, and might be inconvenient from an industrial point of view.

The lower part of Figure 3.2 shows a drawing of a titanium BR with four tapered shapes (R10), called a multi-taper BR. This was also included in the experiment, to assess its impact on the SNR and the signal strength. Multi-taper BRs could be an alternative to large double-taper BRs if the performance is on par or better. The multi-taper BR has the advantage of having smaller maximum diameters for identical taper angles and lengths, i.e. the multi-taper BR provides a more convenient size for industrial applications.

3.1.2 Main characteristics of the UTs

Ten different UTs, as presented in Table 3.2, were used in the experiment. All the UTs are single element longitudinal wave transducers. The resonant frequencies of the UTs are 5 MHz and 10 MHz, and vary with three different UT element sizes: 6.35 mm (0.25 inch), 12.7 mm (0.50 inch) and 19.1 mm (0.75 inch).

Table 3.2: UTs used in the experiments. Based on data, courtesy of Olympus NDT.

Label	Type	Element diameter (mm)	Labeled frequency (MHz)	Peak frequency (MHz)	Center frequency (MHz)	-6dB bandwidth (%)
UT1	V	6.35	5	6.2	6.2	93.1
UT2	A	6.35	5	4.6	5.1	84.1
UT3	V	6.35	10	9.6	9.3	101.9
UT4	A	6.35	10	8.8	9.4	57.1
UT5	V	12.7	5	4.9	4.9	71.3
UT6	A	12.7	5	5.9	5.8	36.7
UT7	V	12.7	10	8.2	8.5	73.6
UT8	A	12.7	10	7.2	9.0	85.0
UT9	V	19.1	5	4.7	4.3	86.0
UT10	A	19.1	5	4.0	4.8	70.8

UTs operating with two categories of bandwidths are used, i.e. Videoscan (V) and Accuscan (A) UTs. Videoscan UTs are broadband transducers, whereas Accuscan are transducers with narrower bandwidths [50]. For the three small BRs (R1-R3, i.e. group G1) with end diameter d_{Be}=8.9 mm, only the four UTs with element size d_{UT}=6.35 mm (UT1-UT4, i.e.group G1) were used in the experiment, as the other UTs had larger housing diameter than the diameter of the BR ends. For the medium sized BRs (R4-R6, i.e. group G2 and R10), additionally four larger UTs with element size 12.7 mm but similar transducer specifications as the smaller ones were utilized (UT5-UT8). For the three largest BRs (R7-R9, i.e. group G3) all the ten UTs, included the two 5 MHz UTs with element size 19.1 mm were utilized.

All the combinations of UT and BRs utilized in the experiment fulfill the requirements of placing the BR end in the far field of the UT. The near field distance d_N, which describes the extent of the near field, and hence the beginning of the far field is given by [50]:

$$d_N = \frac{d_{UT}^2 f}{4c} \tag{3.2}$$

According to Eq.(3.2) the near field distances in titanium of the UTs used in this experiment vary from 8.3 mm to 74.4 mm.

3.1.3 The transceiver filters

Six different internal bandpass filters of the transceiver were also a part of the variables considered in this experiment. This was done to investigate the filtering properties of the different BRs. The main characteristics of these filters are displayed in Table 3.3.

Table 3.3: Bandpass filter used in the experiments

Label	-3dB lower limit (MHz)	-3dB upper limit (MHz)
F1	0.5	4.0
F2	1.5	8.5
F3	5.0	15.0
F4	8.0	26.5
F5	0.2	10.0
F6	2.0	21.5

3.2 Computer simulations of the UTDR System

Experimental investigations of different combinations of BRs and UTs are costly and time consuming. Computer simulations can help to circumvent these, if the results are consistent. Hence, the ultrasonic signal propagation was simulated for some of the most promising combinations of BR and UT, using the ultrasonic simulator Wave3000^{TM}. Results for BRs R7-R9, which are in group G3 were used in the simulation studies. These simulations are based on the following visco/elastic wave equation [8]:

$$\rho \frac{\partial^2 w}{\partial t^2} = \left(\mu + \eta \frac{\partial}{\partial t} \right) \nabla^2 w + \left(\lambda + \mu + \pi \frac{\partial}{\partial t} + \frac{\eta}{3} \frac{\partial}{\partial t} \right) \nabla (\nabla \cdot w) \tag{3.3}$$

where ρ is the material density, λ and μ are the first and second Lamé constants of the material, η the shear viscosity and π the bulk viscosity. *t* is time and *w* is the 3 dimensional displacement vector:

$$w(t) = \begin{bmatrix} x_1 & x_2 & x_3 \end{bmatrix}^T \tag{3.4}$$

The Equation 3.3 is solved at each grid point of the BRs, and the magnitude of the displacement vector is computed at each point and each step of the simulation. The grid spacing was set to about 1/30 of a longitudinal wavelength in titanium to obtain high accuracy, and the time step Δt was chosen to satisfy the Neumann stability criterion [3];

$$\Delta t \leq \frac{\varepsilon}{\sqrt{v_1^2 + v_s^2}} \tag{3.5}$$

where Δt and ε represent the time step and the grid spacing of the simulation, respectively, whereas v_l and v_s denotes longitudinal and shear wave velocities, respectively. Sine Gaussian longitudinal pulses of 5 MHz from the UTs with diameter of 6.35 mm, 12.7 mm and 19.1 mm were used for the simulation in this study. The ultrasonic simulator Wave3000 models only the linear propagation of ultrasound in a homogeneous medium comprised of an isotropic material with viscous loss [35]. The texture of the titanium may increase or decrease the ultrasonic velocity depending on the orientation of the grains in the BRs, but it is not considered in the simulation. In addition, the density and properties related to material's elasticity were assumed to be constant in the simulations of the waveforms.

3.3 Results and discussion

In this experiment data from 7 input variables and 2 output variables as shown in Figure 3.4, are sampled and analyzed. As the experiment is done by changing one by one of the input variables, a lot of variations are included, displaying a data-set of 444 different compositions. The measurements showed very good reliability. A random selected duplicate test set of 10 different measurements, the correlation with the previous measurements of SNR was 99.0 %.
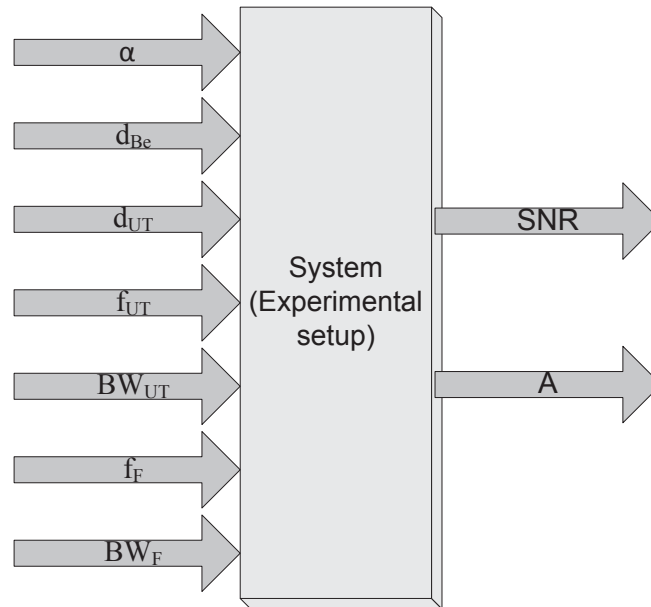
Figure 3.4: The inputs and outputs considered in the experimental setup and for the analysis done in this study. The inputs are representing the geometric properties of the BRs and the UTs, as well as the characteristics of the UTs and the internal filters of the transceiver. The symbols are in accordance with the *list of symbols and abbreviations* given in the front of the thesis.

3.3.1 Signal Waveforms

Figure 3.5 shows the experimental generated waveforms from the nine different double-taper BRs, whereas the waveform of the multi-tapered BR (R10) is shown in Figure 3.6. All the waveforms are representing the combination that resulted in the highest SNR for each BR. The BRs R1, R8 and R9 are providing very well defined reflected signal from the end of their BRs. On the other side, the waveform attained by R3 is rather noisy. The noise at the left side of the peak implies that there are a lot of reflections within the BR, which are reflected back to the UT, during the whole time span.
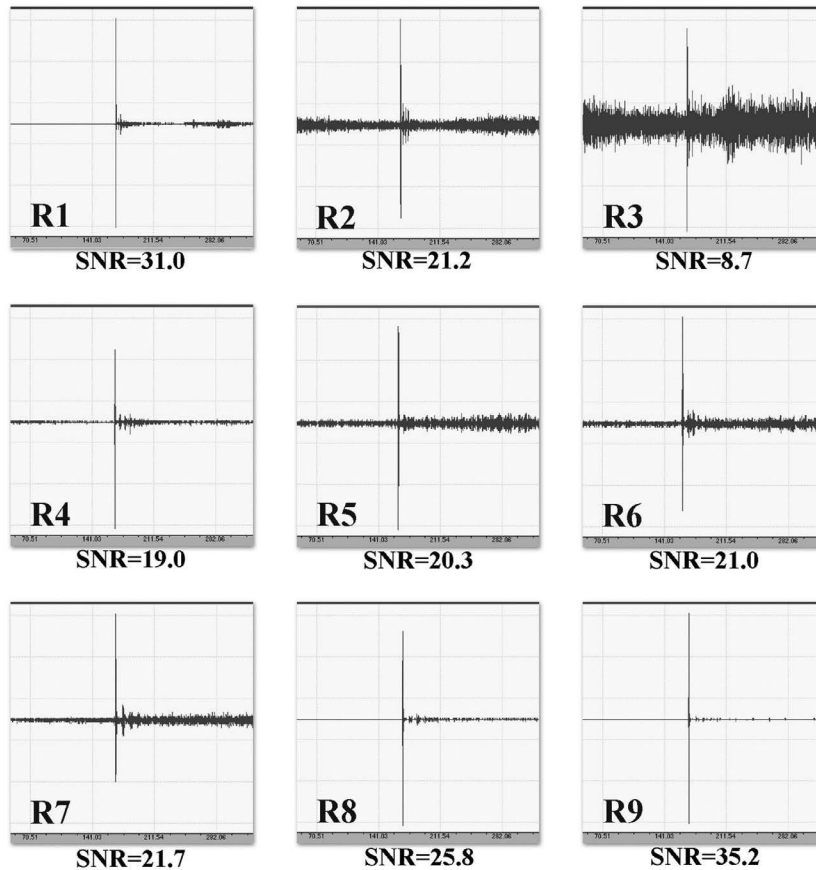
Figure 3.5: Waveform of nine BRs, where row number 1, 2 and 3 are representing the BRs with end radius 8.9 mm, 17.8 mm and 25.4 mm respectively, which are corresponding to group G1, G2, and G3. Column number 1, 2 and 3 are representing the BRs with taper angle $0.9°$, $1.3°$ and $1.7°$ respectively, corresponding to group Ga, Gb and Gc. The SNR decreases with an increased taper angle for the BRs with the smallest BR end, but increases with an increased taper angle for the BRs with thicker BR end.

The multi-taper BR R10 shows satisfactory results with respect to the SNR. The results are very similar to the results from the double-tapered BR with identical taper angle and diameter of the end, i.e. R6.
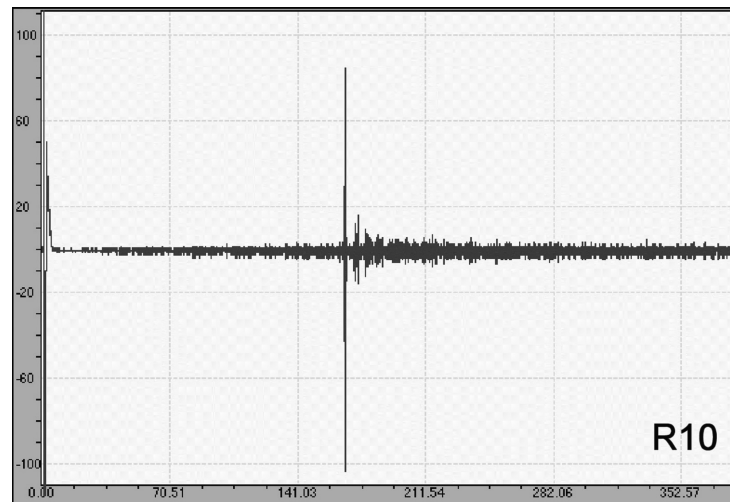
Figure 3.6: Waveform of the multi-tapered BR, R10 with end radius 17.8 mm and taper angle 1.7°. SNR=23.1 dB.

3.3.2 Principal component analysis

The results from the experiment are analyzed utilizing PCA, which is an explorative multivariate data analysis technique. PCA is a mathematical approach used to explore interrelationships among variables. With PCA, the most important information found in the original variables is condensed into a few latent variables [45]. These new variables contain the most "critical" information, as they are associated with maximum variance. Hence, the first latent variable, often called the first principal component (1PC) is constructed along the axis with highest variance. The second principal component (2PC) is orthogonal to the first principal component, and is defined along the axis with the second most variance in the multivariate space. It is possible to construct more principal components in the same manner, but normally most of the information is shown along the two or three first components. Both the objects/samples and the variables can be plotted in the new coordinate system, called score- and loadings-plots, respectively. In this paper the focus will be on loading plots. Each original variable is then represented by a vector or point in the new coordinate system. The loading plot illustrates how the different original variables contribute to the new principal components. Instead of analyzing how two and two variables are related, PCA offers a method that can be

used to display the relation between more variables in one single plot. Not only are the number of plots drastically reduced, interactions between more than two variables are more easily detected. For further studies on multivariate data analysis and PCA in particular, the reader is refereed to basic textbooks in multivariate data analysis, e.g. [45, 13, 20].

To get a first impression of how the different input variables shown at the left side of Figure 3.4 affect the SNR and amplitude A, a PCA was performed on the entire data-set. The two main principal components (PC1 and PC2) are plotted against each other in the loadings plot (Figure 3.7). These two components do only explain 26.2 % and 17.3 % of the variance in the data-set, respectively. In other words 56.5 % is not explained by these two main components, indicating that more complex information is hidden in the data-set. However, the amplitude A and the SNR are closely located and pulls in the same direction, i.e. they are fairly related. Calculations confirm a correlation coefficient between the SNR and A of 79 %.
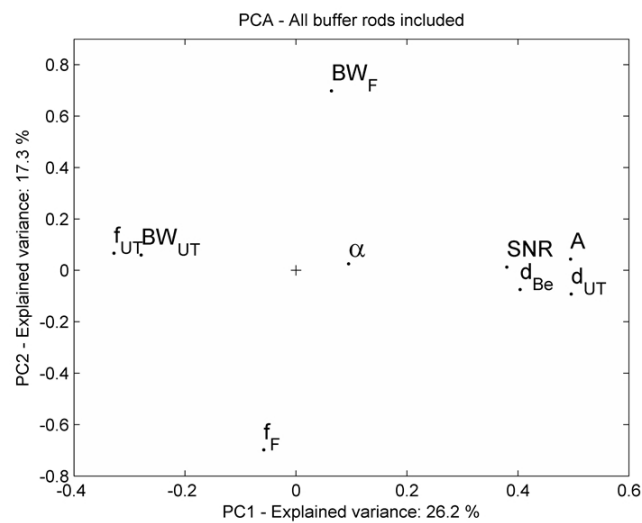
Figure 3.7: PCA loadings-plot using data from all ten BRs. The plot implicate improved SNR by increased diameter of the UT and the BR-end, whereas UT frequency and its bandwidth will have the opposite effect.

The amplitude of the reflected signal is an important variable to consider, when analyzing the waveguiding properties of a BR, but the SNR is perhaps even more important, as the amplitude often can be amplified to desired levels utilizing advanced ultrasonic measurement system, whereas the SNR is not straight forward

to improve. However, the results show that high SNR generally are correlated with high amplitude reflection.

The ultrasonic attenuation within the different BRs should be identical, since identical materials are used. Hence, in addition to properties of the UT, the variations in amplitude has to be related to mode conversions and reflections within the BRs, i.e. properties that reduce the SNR.

Based upon the PCA plot, the BR end diameter d_{Be} together with the UT diameter d_{UT} are closely related to a high SNR, whereas the ultrasonic frequency f_{UT} and bandwidth BW_{UT} pulls in the opposite direction. This would indicate that improved SNR would be gained by increasing the diameter of both the UT and the BR end, and simultaneously selecting an UT with low frequency and low bandwidth. The taper angle α is located close to the origin, indicating negligible influence on the SNR. However, a further investigation of the data-set reveals that the system is more complex.

By dividing the test sets into two times three groups, based upon the diameter of the BR end and the taper angle, according to Table 3.1, more information from the experimental data-set is exposed. Figure 3.8 shows the PCA loadings-plots for the groups G1, G2 and G3, i.e. each group correspond to a specific BR end diameter d_{Be}. Thus, G1, G2 and G3 represent the BRs with smallest, medium and largest end diameters, respectively. All the subgroups displays much more of the variance within each data-set, compared to the PCA performed on the entire data-set, showed in Figure 3.7.
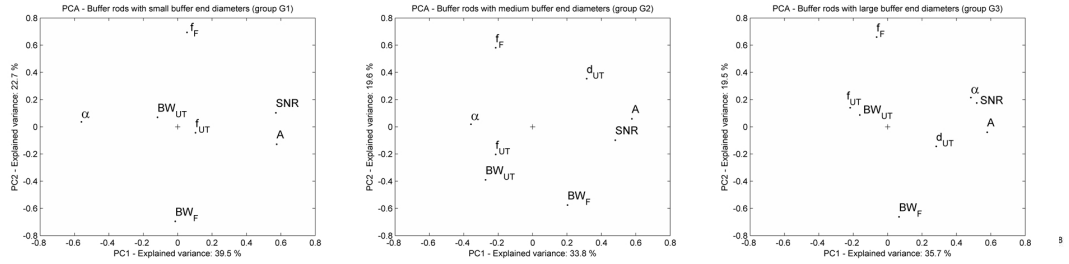
Figure 3.8: PCA-plots, based upon experimental setup, using data from subgroups with different end diameters d_{Be}. From left the sub-figures represent group G1, G2, and G3, with BR end diameter d_{Be} = 8.9 mm, d_{Be} = 17.8 mm and d_{Be} = 25.4 mm, respectively. There is a negative correlation between taper angle and the SNR for the thinnest BRs, but opposite for the thicker BRs.

In all three cases, the SNR and A are very closely located, confirming that a high amplitude of the reflected pulse is related to a high SNR, for all the three

groups with different BR end diameters. The PCA loadings-plots for each group (Figure 3.8), show that the taper angle α has a much more distinct impact on the SNR, than could be concluded from the main PCA-plot (Figure 3.7). The first sub-figure considers the BRs with the smallest end diameters, i.e. group G1, where d_{Be}=8.9 mm. The important impact of the taper angle α inside this group, is demonstrated by the large Euclidean distance from the origin, in almost the opposite direction as of SNR and A. Hence, α and SNR are antagonists, as they pull in opposite directions. In this group there is a high negative correlation coefficient between α and SNR (-86.6 %). This contrast is less distinct in the case of medium sized BRs (group G2 with d_{Be}=17.8 mm), as the Euclidean distance from origin is almost halved for α. Contrary to the two former groups, α and SNR are very closely located in the PCA-plot (Figure 3.8) representing the BRs with the thickest end diameter (group G3 with d_{Be}=25.4 mm). Hence, they are closely related. This is further confirmed by the distinct positive correlation coefficient between the SNR and α in group G3 (85.5 %). Similar results are attained for the correlation between α and A. The uppermost waveguiding properties for the thinnest BRs are accomplished by the smallest taper angles, whereas the best waveguiding properties with the thickest BRs are achieved with the largest taper angles. Hence, within the range of taper angels and BR thicknesses used in this experiment, the taper angle α should be "small" for "thin" BRs, and "large" for "thicker" BRs to obtain a high SNR.

The BRs were also grouped into three groups based upon the taper angles. Group Ga, Gb and Gc are representing taper angles α of 0.9°, 1.3° and 1.7°, respectively. The PCA-plots are shown in Figure 3.9.
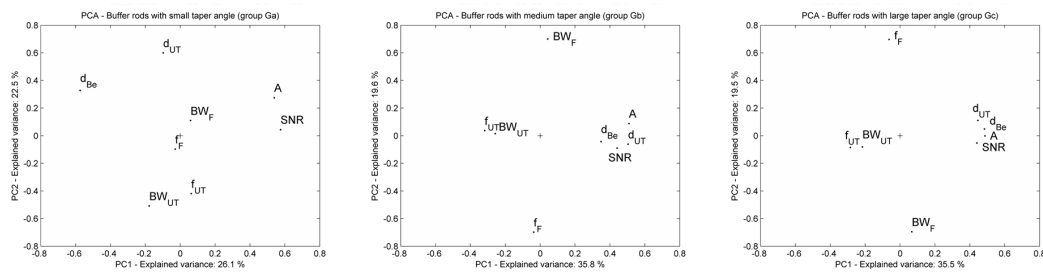
Figure 3.9: PCA-plots, based upon experimental setup, using data from sub-groups with different taper angles α. From left the sub-figures represent group Ga, Gb, and Gc, with taper angle $\alpha = 0.9$, $\alpha = 1.3$ and $\alpha = 1.7$, respectively. There is a negative correlation between BR-end diameter and the SNR for the BRs with small taper angles, but opposite for the BRs with larger taper angles.

The most distinct result that can be seen by comparing the three different PCA-plots in Figure 3.9 is that the end diameters of the BRs d_{Be} are important to the ultrasonic waveguiding properties. From the left sub-figure, i.e. group Ga (α=0.9°), d_{Be} and SNR work in opposite directions, and they are both having fairly large distances from the origin. There is a negative correlation coefficient of 66 % between those two variables, i.e. a "small" d_{Be} is preferably with respect to a "high" SNR for BRs with "small" taper angles (Group Ga). In the two other subgroups d_{Be} and SNR work in almost identical directions and extensions. For the group with highest taper angle, i.e. group Gc (α=1.7°), there is a positive correlation coefficient of 86 %, indicating that for BRs with "larger" taper angles, the thickest BRs will provide the best SNR.

Similar to the end diameters of the BRs d_{Be}, the PCA-plots show that large UT size d_{UT} is beneficial both for high SNR and A, for group Gb and Gc, i.e. BRs with taper angle 1.3° and 1.7°. In group Ga (α=0.9°), the UT size d_{UT} shows no systematic correlation with the SNR.

3.3.3 The impact of the taper angle

Figure 3.10 displays how the SNR of the reflected signal is influenced by the choice of different UTs for all the 10 BRs used in the experiment.

In group G1 (d_{Be}=8.9 mm), the highest SNR are always achieved for the BR with the smallest taper angle (R1), independent of the UT. Hence, the results from the PCA, where there is a negative correlation between the taper angle and the SNR, is confirmed for this group. In group G2 (d_{Be}=17.8 mm), there is no distinct relation between the taper angle of the BRs and the SNR. The highest SNRs for the BRs in group G3 are always achieved by the BR with the largest taper angle (BR9). This also confirms the results from the PCA, displaying a positive correlation between the taper angle and the SNR, for this group.

Earlier publications have concluded that increased taper angle will significantly reduce the trailing echoes in the taper angle range of $0.0° \leq \alpha \leq 2.0°$, but will have only minor influence on higher taper angles [7]. This observation has been confirmed both by simulation and measurements using a single taper steel BR with length 65 mm and large diameter 10.7 mm, with a 5 MHz 6.35mm UT.

In our experiments with 50 cm long BRs, the positive correlation between taper angle and SNR is only confirmed for BRs with end diameter 25.4 mm (Group G3) and the taper angles 0.9, 1.3 and 1.7, as seen in the lower part of Figure 3.10.

The multi-tapered BR is showing acoustic properties similar to the other BRs with end diameter 17.8 mm. There is no indications that the SNR will be reduced by a multi-tapered shape compared to a double-tapered shape, but more experiments should be performed to verify it more generally.
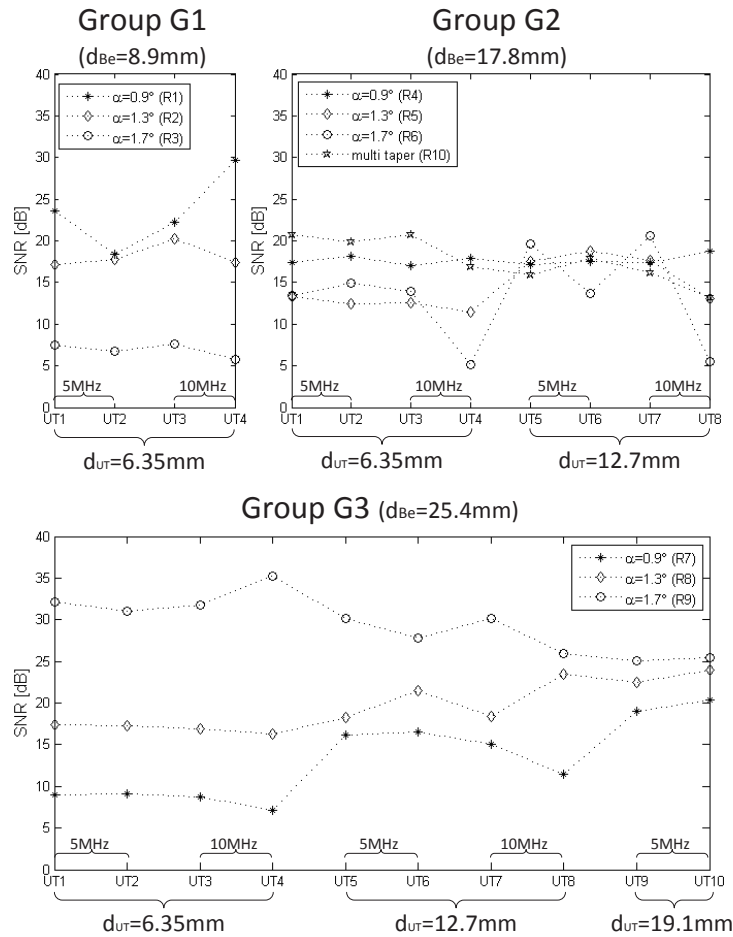
Figure 3.10: The SNR is changed by using different UTs. The element sizes of UT1-UT4 are 6.35 mm, UT5-UT8 are 12.7 mm, and UT9-UT10 are 19.1 mm. A 2.0-21.5 MHz broad-band filter is used to generate these SNR data.

Figure 3.11 displays how the relative amplitude of the reflected signal is influenced by the choice of different UTs for all the 10 BRs. There are similar relations between the taper angle and the amplitude, as was found between the taper angle and the SNR. This is also in accordance with the PCA-findings. Hence, the highest amplitudes in group G1 are found for the BR with the smallest taper angle,

regardless of the UT, whereas the highest amplitudes in group G3 are found for the BR with the largest taper angle, also regardless of the UT.
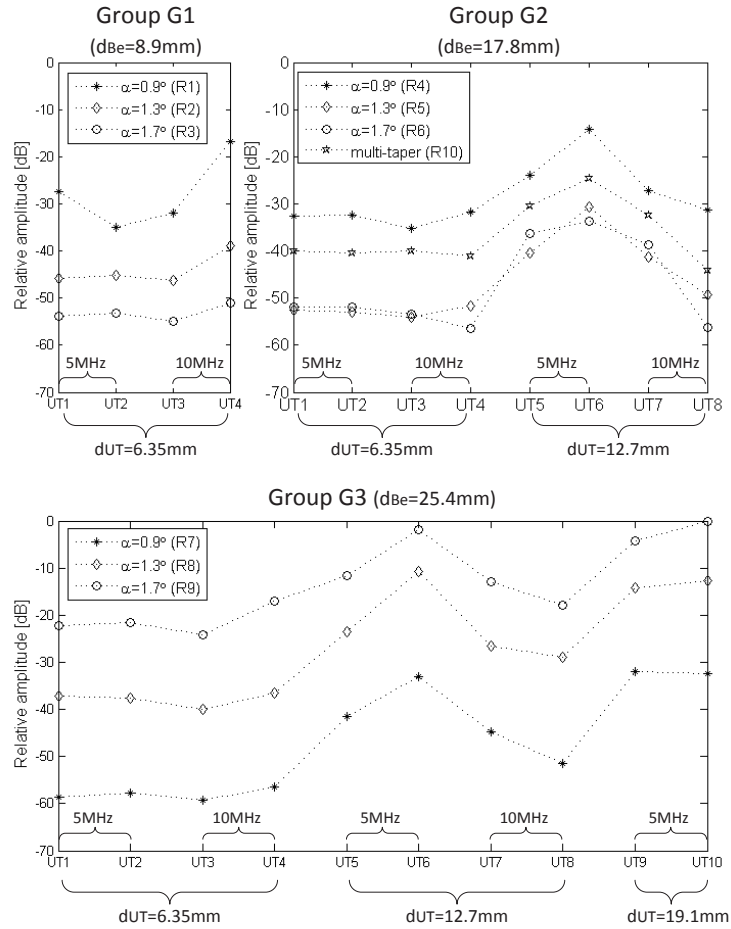
Figure 3.11: Displaying the relationship between the relative amplitude of the reflected signal and the different UTs used for the BRs with end diameter 8.9 mm (top left), 17.8 mm (top right) and 25.4 mm (bottom) respectively. The element sizes of UT1-UT4 are 6.35 mm, UT5-UT8 are 12.7 mm, and UT9-UT10 are 19.1 mm. The specifications of the UTs are shown in Table 3.2. A 2.0-21.5 MHz broadband filter is used to generate these SNR data.

Only, the BRs in group G3 are displaying properties reported also in earlier studies, where an increased taper angle correspond with increased waveguiding properties [26]. However, the results from our experiment disclose that an increased taper angle not always leads to increased waveguiding properties of BRs. Other variables of the BR shape and size have to be analyzed to get a more complete picture.

3.3.4 The impact of the UT

Figure 3.10 and Figure 3.11 show that the 10 MHz narrow-band transducer (UT4) provided the highest amplitude and SNR for BR R1, displaying excellent waveguiding properties. For the two other BRs in group G1 the differences in obtained amplitudes and SNRs are less significant for the different UTs. The high waveguiding performance of the 10 MHz UT in R1 can be related to a small angle of divergence of the ultrasonic beam. The formula of angle divergence for far-field region [46], shows that the beam spreading is reduced by an increased resonant frequency of the UT;

$$\varphi = sin^{-1}\left(0.7\frac{c}{f \cdot d_{UT}}\right) = sin^{-1}\left(0.7\frac{\lambda}{d_{UT}}\right) \tag{3.6}$$

The smaller spread of the beam is beneficial for all the BRs in group G1, by reducing the internal scatter within the BR, but especially for R1, having the smallest taper angle α, and hence the smallest maximum diameter d_{Bm}.

All the four medium sized BRs, i.e the three double-taper BRs in group G2, in addition to the multi-taper BR, all having d_{Be}=17.8 mm, gave the highest reflected amplitudes with UT 6 (Figure 3.11), which is a 5 MHz narrow-band transducer with element size d_{UT}=12.7 mm (see Table 4). According to the divergence formula, the beam divergence of this UT is similar to UT4, as the element size is doubled and the resonant frequency halved. The benefits of further reducing the beam divergence by increasing the resonant frequency to 10 MHz as achieved with UT8 seems to be suppressed by the reduced attenuation, compared to the 5 MHz transducer (UT6). The fact that the 6.35 mm UTs provided poorer reflected amplitudes compared to the UTs with element diameter of 12.7 mm is probably related to the larger beam divergence, as well as the larger UTs also have the advantage of possibly transmitting more energy. The drawback using UT6 in group G2 is seen in Figure 3.10, where all the UT are displaying similar results for this group. I.e. with the UT6 both the amplitude of the signal and noise are large.

Similar to the BRs in group G2, UT6 is also a preferred UT with respect to the amplitude of the reflected signal A, in group G3, i.e. the BRs with d_{Be}=25.4 mm. However UT10, which also is a 5 MHz narrow-band UT, but with an even

larger element diameter (d_{UT}=19.1 mm), also provides similar reflected amplitudes. According to Table 3.2 the bandwidth of UT 6 is much smaller than for UT10. If their bandwidths were more alike, even higher reflected amplitude could be expected for UT10, as the beam divergence should be smaller. Otherwise, this indicates that the beam spreading from the UT is less important for the larger BRs.

As also seen in group G2, an increased amplitude, does not always lead to an increased SNR. The size of the transducer elements is also an important factor when analyzing the SNR of the different BRs. For the BRs in group G3, which are having the largest end diameters ($d_{Be} = 25.4mm$), the smallest UTs (6.35 mm) (UT1-UT4) were providing the best SNR for the BR with highest taper angle, $\alpha = 1.7°$ (Figure 3.10). This is probably related to increased scatter at the BR-wall for this group, when using large UTs. The opposite is the case for the smallest taper angle, i.e. SNR is at the highest level for the largest transducer elements (19.1 mm) (UT9 and UT 10), as well as the SNR is reduced for the smaller UTs.

Whether small or large sized UTs are used on the largest BRs, increased taper angles α provides improved SNR, although an increased taper angle α, is most efficient on the UTs with the smallest element size. It should be noted that all the 6.35 mm UT provides SNR above 30 dB for BR R9, i.e. a BR with $\alpha = 1.7°$ and d_{Be}=25.4 mm. Although these SNR results are excellent, the signal strength provided by these small UTs could be too small in some industrial settings, depending on the ultrasonic device, but also the power limitation of the UTs. Larger UTs in general tolerate better higher pulse energy than the smaller one. There is no clear relationship between the UT size and SNR for group G2, i.e. BR with d_{Be}=17.8 mm (Figure 3.10). Only two different UT sizes were used for those BRs, whereas only one UT size was used for the smallest BRs. Note that the multi-taper BRs provide the best SNR results with the smallest UTs, and descend for the larger sized UTs. In general, the multi-taper BR provides similar or better SNR, compared to the other BRs with d_{Be}=17.8 mm.

3.3.5 BRs functioning as bandpass filters

Another approach to explain the phenomena of different reflected amplitudes achieved by different UT is related to the signal processing field and the equipment setup, and then in particular the filter properties of the BRs. It is well known that ultrasonic waveguides like these BRs, act as bandpass filters, hence the attenuation of the ultrasonic signals varies with respect to its frequencies. In order to gain information about these filter characteristics, the frequency spectrum of both the digital filter incorporated in the ultrasonic receiver and the UTs have been considered. Also the wires may act as filters but will be neglected in this analysis as they are assumed to be insignificant, and are not changed during the experiments. As a simplified model of the measuring system, the generated signal might be

considered as sequentially filtered through three different filters before ending up as an output signal, as shown in Figure 3.12.
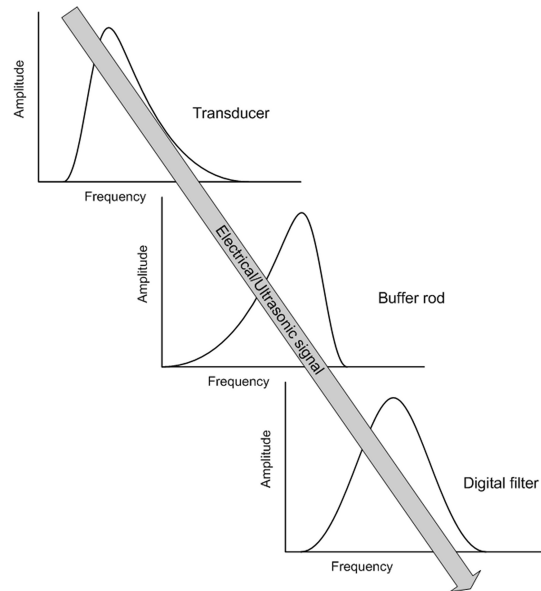
Figure 3.12:   The signal passes through three main "frequency filters" in the measuring system. Cascading all these modules reduces the ultrasonic signals in BR and media of propagation(electrolyte, molten metal, sludge etc.) as well as the electrical signals transmitted to various signal processing

Based on this approach, the highest relative amplitude of the reflected signal will be received when the frequency spectrum of the BR matches both the UT and the digital filter in the ultrasonic transceiver, i.e. the center frequencies should preferably be the same and the bandwidths of the UT and filter overlapping the bandwidth of the BR.

According to Table 3.2, UT4 has a center frequency of 9.35 MHz and a -6 dB bandwidth of 57.1 %, whereas UT3 has a center frequency of 9.27 MHz and a -6 dB bandwidth of 101.9 %. Hence, the ultrasonic energy is concentrated on a much smaller frequency bandwidth for UT4, which is beneficial to the signal amplitude if the center frequency is coincident with the filter settings of the transceiver and the filter properties of the BR itself. Hence, the results shown i Figure 3.11 indicate that the BRs with the smallest end diameters (group G1) has a narrow bandwidth with center frequency close to the center frequency of UT4.

The figure also indicates that the center frequencies of the medium thick BRs (group G2) are closer to the center frequency of UT6, which also is a UT with narrow bandwidth (36.7 %), but with lower center frequency (5.8 MHz). In group

G3, which are the thickest BRs, the highest amplitudes are gained with UT6 and UT10, both 5 MHz UTs with narrow bandwidths. The taper angle influences the filter characteristics of the BR in a similar but minor way, as will be discussed later in this chapter.

More information on the frequency properties of the BRs can be extracted from the test data, as variations in the signal amplitude is caused by four different bandpass filters with narrower bandwidth in the experiment. Figure 3.13 shows the frequency spectrum of the four bandpass filters (F1-F4) of the ultrasonic transceiver used during the experiments. The frequency spectrum of the four 6.35 mm UTs (UT1-UT4) are also drawn in the same figure.
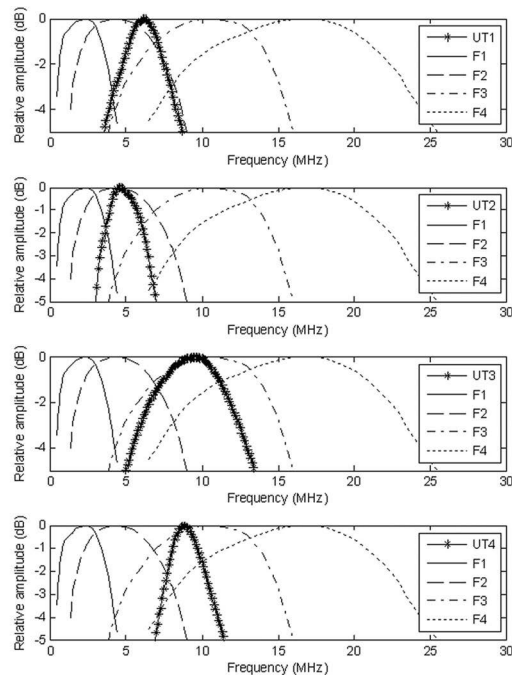
Figure 3.13: Comparison of peak frequency characteristics of UTs with in-built filters of EPOCH 1000i. The boldface curves represent frequency characteristics of the four 6.35 mm UTs, whereas the thinner curves represent the corresponding frequency characteristics for the internal filters of the ultrasonic transceiver. The graphs are merged and redrawn with data and images courtesy of Olympus NDT.

Considering the bandpass filters, an obvious expectation neglecting the filter properties of the BRs, follows; the signal generated by the 5 MHz UT (UT1 and UT2) would be least reduced by the filter F2, whereas the 10 MHz UT (UT3 and UT4) would be least reduced by the filter F3, and only fairly reduced by F2 and the high pass filter F4.

Figure 3.14 shows how the reflected amplitude varies with different built-in filters of the transceiver for BRs in group G1. The optimal bandpass filter frequencies to achieve a high reflected signal amplitude for BR R1 were F2 and F3, but also the high pass filter F4 did not reduce the signal strength considerably, indicating that this BR operates as a bandpass filter with center frequency close to 8 MHz, which is also supported by the fact that the UT with the best signal strength (UT4) had a peak frequency of 8.84 MHz.
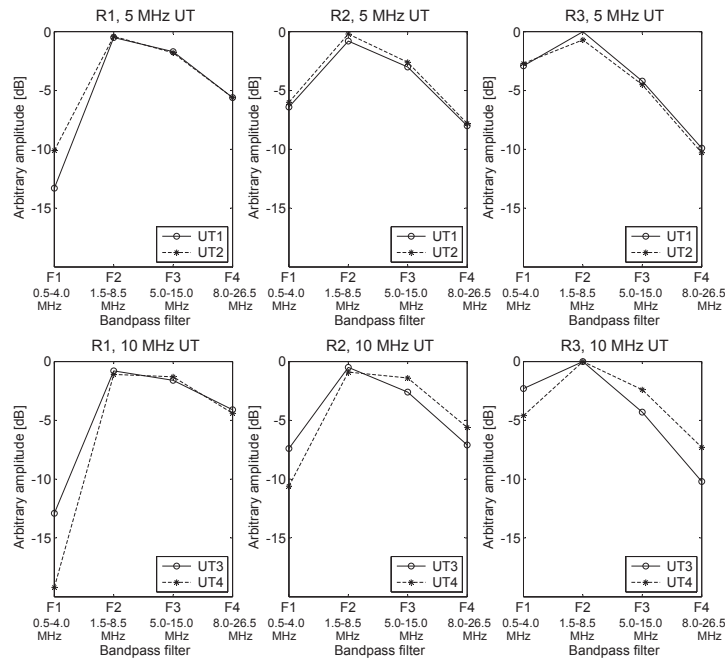
Figure 3.14: Bandpass filter index vs. the change in relative signal amplitude for the BRs in group G1, i.e. BRs with end diameter d_{Be}=8.9 mm. All the 4 UTs showed the highest reflected amplitude with filter F2, but for narrow-band 10 MHz (UT4) filter F3 gave almost similar results.

It should also be noted that a UT with a narrow bandwidth is beneficial if

the center frequency is close to the center frequency of the BR (considering the BR as a bandpass filter). The energy is then not spread out on a large range of frequencies, but gathered in a narrower BR matching range.

According to Figure 3.14, bandpass filter F1 provides very poor signal amplitudes with BR R1, i.e. taper angle $\alpha = 0.9°$, but as the taper angle α is increased for BR R2 and further for BR R3, this bandpass filter (F1) in the lower frequency range displays an increased signal amplitude, although the relative amplitudes are highest for filter F2. However, this indicates that the BRs with end diameter of 8.9 mm, displays a bandpass frequency with relatively high center frequency (close to 8 MHz), and the center frequency of the BR is to some extent reduced by an increased taper angle. The variation in bandpass filter properties are assumed to be related to the increased thickness of the middle part of the BR followed by an increased taper angle, more than a result of the increased taper angle per se.
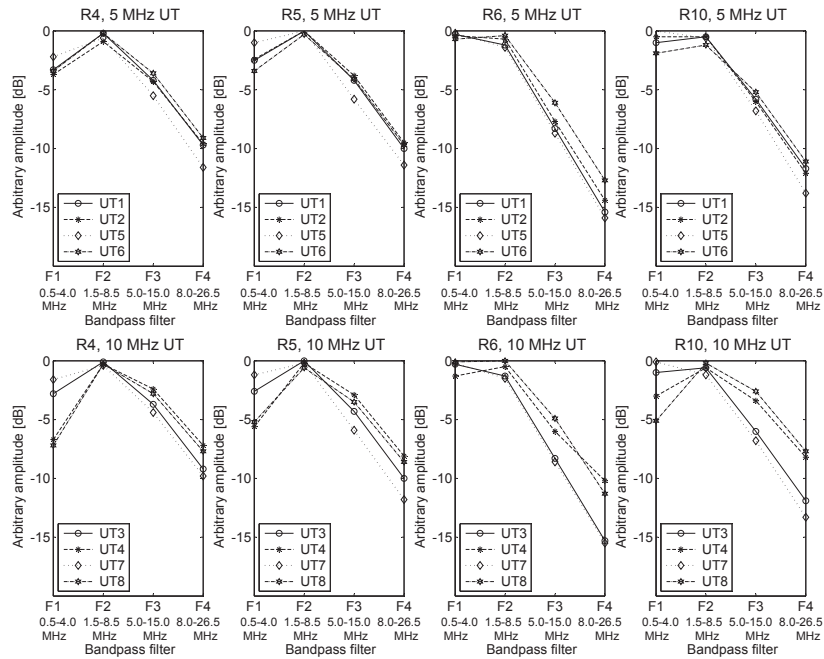
Figure 3.15: Bandpass filter index vs. the change in relative signal amplitude for the BRs in group G2, i.e. BRs with end diameter d_{Be}=17.8 mm. Most of the 8 UTs showed the highest reflected amplitude with filter F2, but for the thickest BR in this group, in general filter F1 gave the highest amplitude.

In Figure 3.15, similar but less significant changes are seen for the medium sized BRs in group G2. In general, the highest relative amplitudes are given by filter F2 for the BRs with smaller taper angles α, whereas the highest relative amplitudes for BR R6, which has the highest taper angle α, are with filter F1. Consequently, an increased taper angle α, and hence an increased maximum diameter of the BR d_{Bm}, will move the bandpass filter properties of the BR in the direction of lower frequencies. For the three thickest BRs (group G3), the highest amplitudes were achieved with both bandpass filter F1 and F2 (Figure 3.16). As the taper angle was increased, bandpass filter F1 provided slightly poorer results, which indicates that the center frequency of the BR increases slightly as the taper angle increases for group G3.
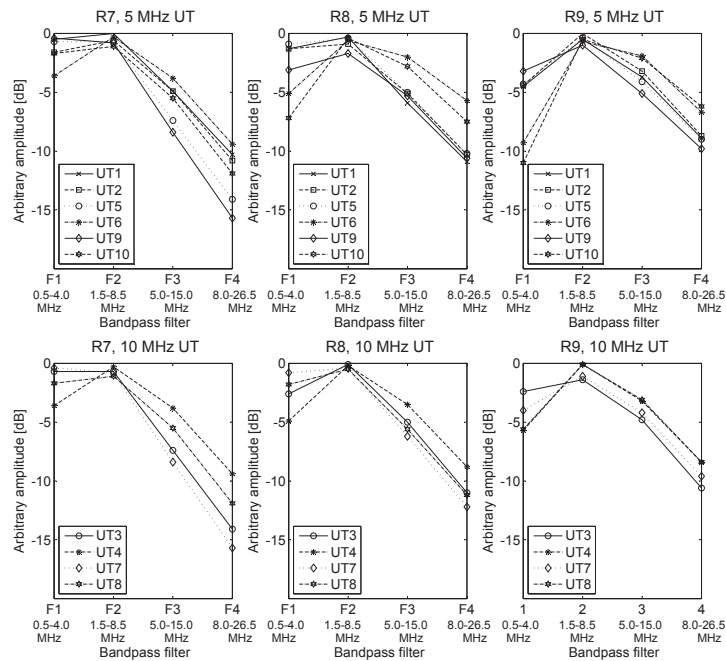
Figure 3.16: Bandpass filter index vs. the change in relative signal amplitude for the BRs in group G3, i.e. BRs with end diameter d_{Be}=25.4 mm. Most of the 10 UTs showed the highest reflected amplitude with filter F2, but for the BR with the smallest taper angle in this group, filter F1 and F2 gave approximately identical amplitudes.

3.3.6   Comparison of experimental and simulation results

Simulations of the BRs in group G3 with 5 MHz UTs were performed. The sizes of the three different simulated UTs were equal to the experimental UTs. The waveforms of the experimental and simulated waves for BR R7 are compared in Figure 3.17. In the graphs, the amplitudes of the reflection from the BR ends are scaled to unity size.
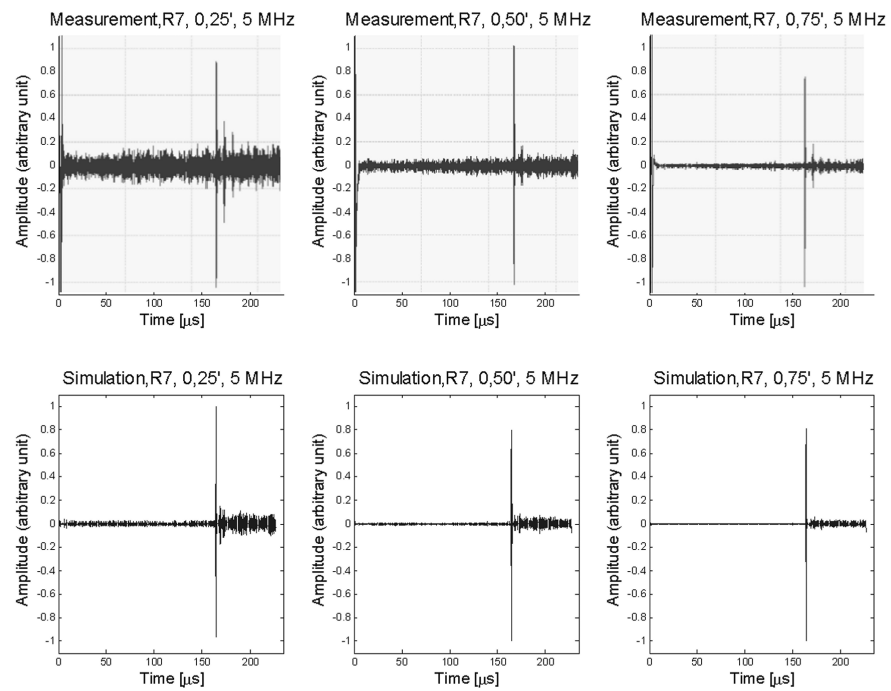
Figure 3.17:   Experimental and simulated waveforms at top and bottom, respectively. A 5 MHz UT is used with BR R7 . First column represents a 6.35 mm transducer (UT2), the second a 12.7 mm transducer (UT6), and the third a 19.1 mm transducer (UT10).

The trend of reduced trailing echoes as the UT size d_{UT} is increased, is supported by both the experimental and simulated waveforms. The overall noise contribution is larger for the experimental, but also noticeable variations occur in the simulated waveforms for R7, as the size of the UT is changed. The corre-

sponding waveforms of the experimental and simulated waves for R8 are depicted in Figure 3.18.
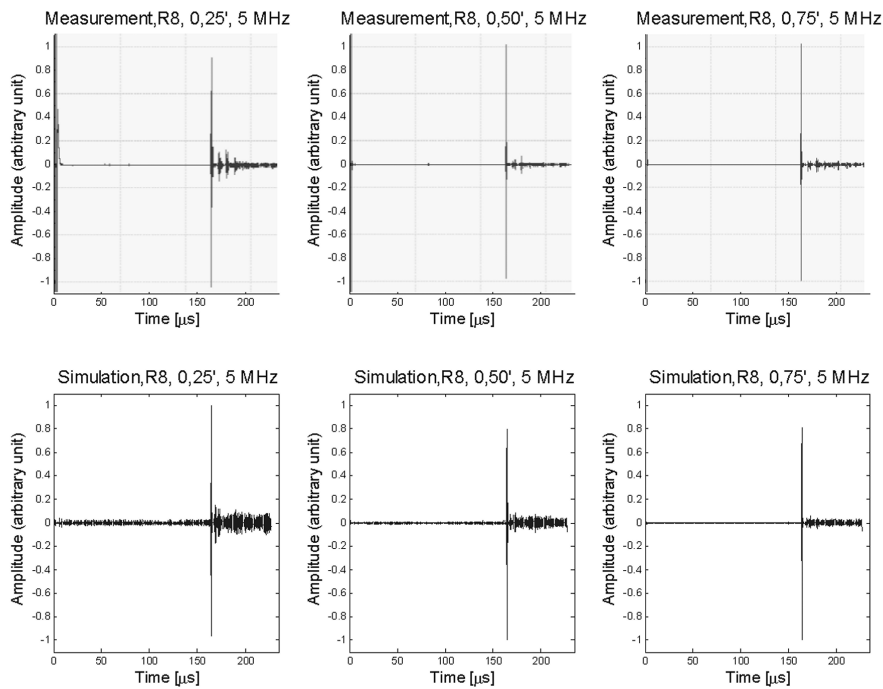
Figure 3.18: Experimental and simulated waveforms at top and bottom, respectively. A 5 MHz UT is used with BR R8 . First column represents a 6.35 mm transducer (UT2), the second a 12.7 mm transducer (UT6), and the third a 19.1 mm transducer (UT10).

Similar to the waveforms of BR R7, both the experimental and simulated waveforms of R8 indicate that by increasing the element size of the UT, the trailing echoes will be reduced. Although the shapes of the trailing echoes are different, in the sense that the experimental trailing echoes are more rapidly damped, the amplitudes, and hence the SNR are very similar. The corresponding waveforms of the experimental and simulated signals for BR R9 are given in Figure 3.19.
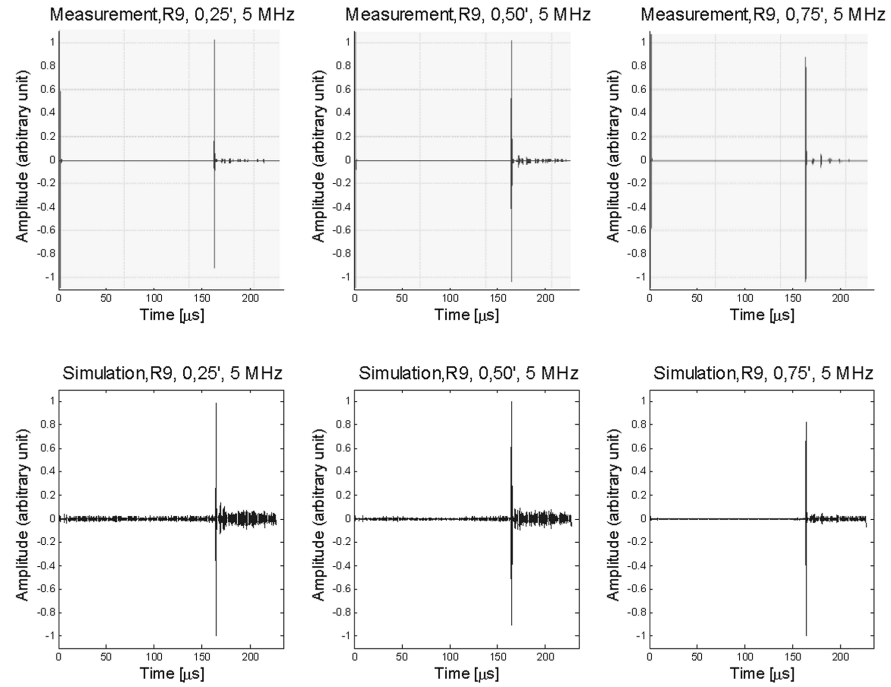
Figure 3.19: Experimental and simulated waveforms at top and bottom, respectively. A 5 MHz UT is used with BR R9 . First column represents a 6.35 mm transducer (UT2), the second a 12.7 mm transducer (UT6), and the third a 19.1 mm transducer (UT10).

In the experimental based waveforms of BR R9, the trailing echoed have almost been eliminated, and opposing to the waveforms of R7 and R8, the UT with the smallest d_{UT} is actually attaining the smallest trailing echoes. On the contrary the simulated waveforms are very similar for all the three BRs in group G3, although most noisy for the smallest UT. Considering the SNR of both the experimental and simulated waveforms for this group G3, there are very small variations among the simulated SNRs, varying between 18.8 dB and 22.9 dB, whereas the experimental based SNRs are in the range of 9.4 dB to 32.0 dB. Figure 3.20 shows the relation between the UT size d_{UT} and the taper angle α, with respect to the SNR, for both experimental and simulated waveforms.
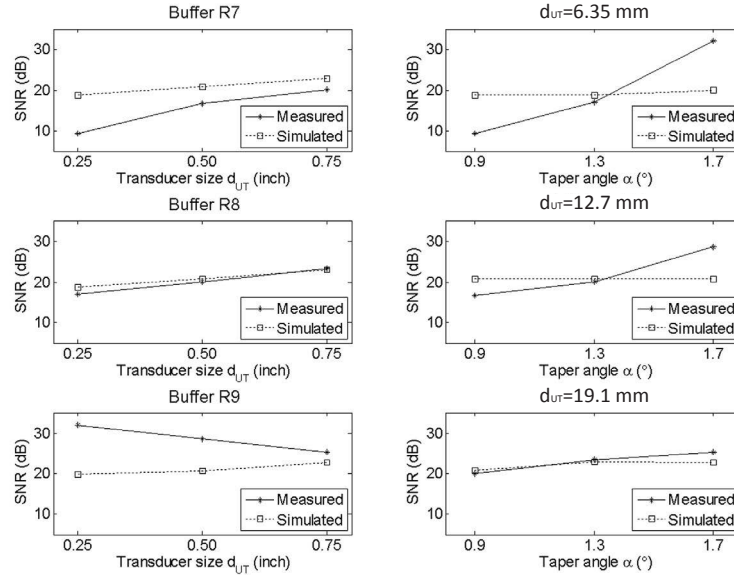
Figure 3.20:   Comparing the simulated and measured SNR results for the BRs in group G3. The simulated SNR shows very little variations, compared to the corresponding experimental SNR. The divergence is particularly distinct for the combinations with small UT sizes.

There is a slight tendency of increased SNR for increased UT size, regardless of the taper angle of the BRs, for the simulated waveforms. The curves of the simulated and experimental data are very similar for R8. There is also high agreement between simulations and measurements for all the BRs in combination with UT element size 19.1 mm, i.e. the UT and BR end have equal diameters. For R7 and R9, the simulated and experimental data diverge for smaller UT. The negative gradient of R9 based on the experimental data turns out to be positive gradient for the simulation. Generally, for the largest UT the simulated and experimental SNRs are close, although the variations are larger for the experimental data, i.e. the relation between increased taper angle and increased SNR is more persistent for the experimental data. The medium and especially the small UTs show a more clear difference between the simulated and experimental data. As an increased taper angle induces an increased SNR for the experimental results, no such trend is observed in the simulated results.

As the amplitudes attained in the simulations are not directly comparable with the amplitudes attained in the experiments, in the following figures, their mean values have been forced to be identical, hence the trends of relative amplitudes can be compared but not the absolute values. The relationship between the relative amplitude of the reflected wave A and the element size of the UT d_{UT}, as well as the taper angle α are shown in Figure 3.21. With respect to the taper angle, the simulated and experimental curves are following each trend quite well, although there are some large biases off-set. The taper angle seems to have only small influence on the amplitude of the reflected signal, for the simulated waveforms. For the experimental results, UT with $d_{UT} = 6.35$ mm, increased taper angle α, will increase the relative amplitude A, whereas α is of minor importance for the larger UTs. There is almost total agreement between simulated and measured results that larger d_{UT} provides increased amplitude A, although the difference in A between medium sized and large UTs are almost zero for the experimental results. However, for the experimental results, A is very much reduced, from $d_{UT} = 19.1$ mm to $d_{UT} = 6.35$ mm.
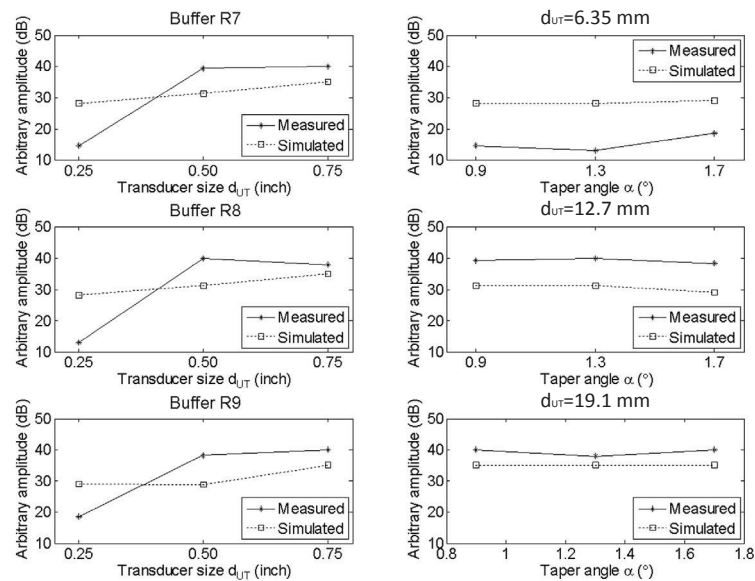
Figure 3.21: Comparing the simulation and measured results, both for the amplitude vs. the size of the UT, and for the amplitude vs. the taper angle.

Though the small UTs afford distinct smaller amplitudes, the smaller UTs might be the utmost choice in some BR applications, if the SNR are improved for these UT. Modern ultrasonic equipments do often have the possibility to amplify the signal to very high levels, so the signal amplitude is not always the most important parameter to consider, in selection of measurement setup. As for the SNR, the divergences between the simulated and experimental amplitudes are most distinct for the small UT.

3.4   Concluding remarks

The experiments performed with the ten titanium BRs confirmed that the geometric appearances of the BRs are most decisive with respect to their waveguiding properties (Figure 3.5 and Figure 3.6), which is also well documented in the literature, and here described in former sections. Most interesting is the non-linear relationship between the taper angle of the BR α, and the waveguiding properties, i.e. SNR and the amplitude. For "long" and "thin" BRs, "small" taper angles are preferred, whereas BRs with larger taper angles have a better waveguiding performance for thicker BRs.

Based on the experiments, larger UT size will in general only increase the size of the reflected amplitude, whereas the SNR will remain unchanged. There is also a tendency that thinner BRs and BRs with smaller taper angles α, operates as high pass filters, so that 10 MHz UT with narrow bandwidth are preferred, rather than 5 MHz UT. On contrary in combination with thicker BRs, or BRs with higher taper angles, 5 MHz UT provided best waveguiding results. Although the system is very sensitive to the alignment of the UT, validation tests have been performed with a correlation of 99 %. This confirms with a high certainty that the UT holders have been able to center the UTs on top of the BR, and that the pressure on top of the UTs have been firm and repetitive. However, there are uncertainties that are difficult to measure related to the manufacturing of the BRs. Optimal waveguiding performance requires that the ends of the BRs are total parallel, and even small angular deviations might be crucial. Also the smoothness of the surfaces is a factor that might cause undesired variations in the experiment. To minimize these uncertainties, the BRs have been manufactured by professionals.

There are some large variations between the experimental and simulated results of the UTDR. In general, there are smaller mutual variations for the simulated waveforms, as the taper angle α and UT element size d_{UT} are varied. Particularly, the largest divergence between experimental and simulated results appears for the smallest d_{UT}, i.e. the d_{UT} is $1/3$ of the end diameter of the BR. In the simulation, the SNR is almost not affected by the variation in taper angle α, whereas SNR is very much affected by α for the small d_{UT} in the experiment. Apparently,

the simulation model has limitations related to dispersions or mode conversions appearing on the BR sides. Even though the predicted errors might be very small at each step, the errors will be multiplied at each time step, and finally become critical for such long BRs.

More results, details and discussion related to the experiment with the ten titanium BRs are given in Paper C and D.

3.5   Abstract of Paper C

Buffer Rods (BR) as waveguides in ultrasonic time domain reflectometry (TDR) can somewhat extend the range of industrial applications of ultrasonics. Level, temperature and flow measurements involving elevated temperatures, corrosive fluids and generally harsh environments are some of the applications in which conventional ultrasonic transducers cannot be used directly in contact with the media. In such cases, BRs with some design modifications can make ultrasonic TDR measurements possible with limited success. This paper deals with TDR in conjunction with distance measurements in extremely hot fluids, using conventional ultrasonic transducers in combination with BRs. When using BRs in the ultrasonic measurement systems in extreme temperatures, problems associated with size and the material of the buffer, have to be addressed. The resonant frequency of the transducer and the relative size of the transducer with respect to the diameter of BR are also important parameters influencing the signal to noise ratio (SNR) of the signal processing system used in the ultrasonic TDR. This paper gives an overview of design aspects related to the BRs with special emphasis on tapers and cladding used on BRs. As protective cladding, Zirconium-Oxide Yttrium-Oxide composite was used, with its proven thermal stability in withstanding temperatures in rocket and jet engines up to 1650 °C.

In general a BR should guide the signals through to the medium and from and back to the transducer without excessive attenuation and at the same time not exacerbate the noise in the measurement system. The SNR is the decisive performance indicator to consider in the design of BR based ultrasonic TDR, along with appropriate transducer, with suitable size and operating frequency. This work presents and analyzes results from extensive experiments related to fine-tuning both geometry of and signals in cladded/uncladded BRs used in high temperature ultrasonic TDR with focus on overall performance based on measured values of SNR.

3.6   Abstract of Paper D

The use of waveguides or buffer rods (BR) is well known in performing Non-Destructive Testing (NDT) with ultrasonic or generally in high-temperature ultrasonic time domain reflectometry (TDR). However, determining optimal geometrical shapes of these buffers and parameters of the ultrasonic transducers are not straightforward. In this paper the signal to noise ratio (SNR) achieved with different combinations of buffer diameters and transducer diameters are considered based mainly on experiments and on some dedicated simulations. Experimental results show large variations of the SNR as the ratio between the transducer and the buffer rod diameter varies. Corresponding simulated results are less influenced by such variations in the ratio of diameters considered, showing possible limitations of these simulations.

Chapter 4

Some Aspects of Improving SNR in UTDR

In this chapter additional ultrasonic measurements performed in this study are presented. In this chapter we are interested in both reflected and transmitted signals at an interface, hence also in the incident and reflected angles.

Based on the experiments described in Chapter 3, BR8 that was one of the most optimal BR with respect to SNR was selected for tests in the aluminium electrolysis cell at Norsk Hydro, Årdal. The BR was cladded with the high temperature protective cladding, Zirconium-Oxide Yttrium-Oxide composite. The cladding had insignificant impact on the SNR. Further details are given in paper C. Also the utmost combinations of BRs and UTs from Table 2.1 were also selected for further experiments in the electrolysis cell. The upper part of the BRs were all wrapped with a copper pipe, that in combination with an air blower were used for cooling the upper part of the BRs. Hence, the UTs were protected from breakdown in spite of the extreme temperature.

Although the best combinations of BRs and UTs were selected to provide high wave-guiding performance, the reflected ultrasonic signal from the bath-metal interface was still difficult to distinguish from the rather high noise signals experienced in electrolysis cell. There are several possible explanations for this:

- Most of the ultrasonic pulse is transmitted through the bath-metal interface, hence not reflected, due to similar acoustic impedance in these two melts.

- Misalignment between the BR and bath-metal interface may reduce the reflection of the signal. This topic is studied using an adjustable plate of metal in water, to get an impression of how sensitive the measurement system is to misalignment of the BR and to waves on the interface of interest. The results are presented in the next section.

- The amplitude of the signal may be too small.

- The coupling between the BR and the bath, may be insufficient. The experiments showed that the bath would easily freeze at the BR tip, making the measurement fail. This is difficult to avoid as the bath temperature is just about 15 °C above the freezing temperature of the electrolyte. Due to our experiments, an immersion time of at least 10-15 minutes was needed to avoid extensive freezing at the tip of the BR.

4.1 Experimental study on the effects of axial misalignment of BRs

Several experiments with BRs in water, water/oil, molten Tin and Zinc were performed to simulate the application at an aluminium electrolysis cell. During these experiments and the experiments in the aluminium electrolysis cell, it was clear that this measurement concept was very sensitive to misalignment of the BRs. To validate this sensitivity an experiment in water was accomplished, and is presented in this section. Several different BRs were used to get a broader scope of this topic. The aim of this section is to consider the impact that BR shapes and UT selection have on the sensitivity of misalignment between the BRs and the reflected interface. The optimal situation is achieved if the BR is placed perpendicular to the interface where a desired reflection will appear. By adjusting the angular deviation from this position, hereafter called the reflector angle, a measure of the sensitivity to misalignment can be determined. Our experiment shows that misalignment between the BR and the reflector plate of only a few degrees may reduce the reflected signal to zero. This sensitivity to misalignment has been investigated by performing experiments with buffer rods of different shapes and sizes. The results are presented in this section.

4.1.1 The experimental setup

The aim of the experiment was to consider how sensitive the ultrasonic signals transmitted through acoustic buffer rods are to angle variations of a reflector. The measurements were performed in water using ultrasonic pulse-echo mode. A device with a steel-plate that can be adjusted in different degrees was constructed and utilized to extract fairly accurate measurements of the reflector angle. The device is called "the angular positioner", and is shown in Figure 4.1.

In the experiment 9 different double-taper titanium BRs with length approximately 50 cm were used to examine how much the reflected signal was reduced due to variations of the reflector angle. These BRs have different taper angles
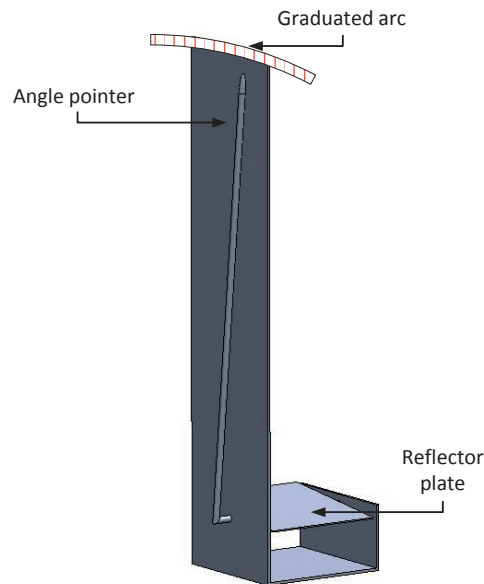
Figure 4.1:   The angular positioner. A device for adjusting and measuring the angle of the reflector plate.

and end diameters. Transducers with 5 and 10 MHz frequencies, with both narrow and broad bandwidth were tested out on most of the BRs using an Olympus Epoch 1000i ultrasonic transceiver. Measurements with two different distances between the buffer end and the reflector were performed and analyzed. A photo of the setup is shown in Figure 4.2.

At the end of the experiment some shorter buffer rods in other materials were tested out, to see if major differences in the sensitivity to reflector angle misalignment would appear.

4.1.2   Results and discussion

For the BR-UT combinations evaluated in Chapter 3 with a SNR of 20 or less, the interface between the water and metal reflector was really difficult and for some not possible to detect, even by a normal incident beam. Hence, only the BR-UT combinations with the best performance have been tested in this experiment.
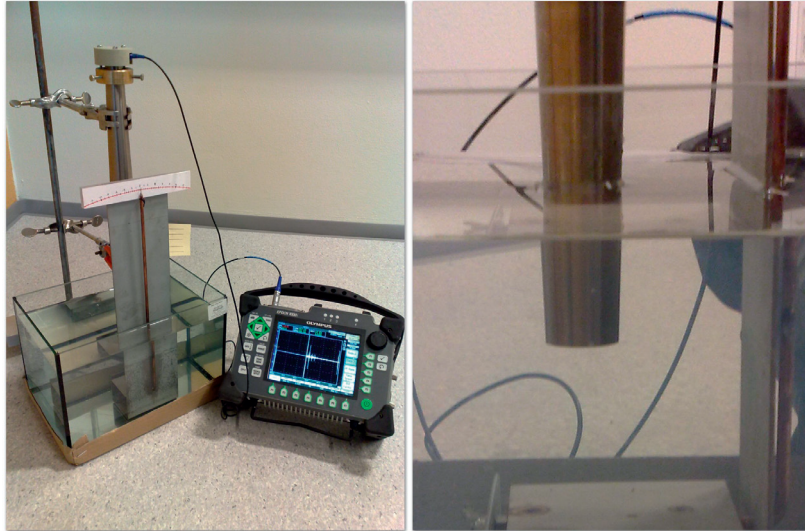
Figure 4.2:   Setup of the ultrasonic measurement with varying reflector angles, using the angular positioner.

Varying the diameter of BR end

The diameter of the BR end did not show any correlation with the amplitude of the reflected peak at the different angles of the reflector plate, i.e. the thin and thick buffer rods were almost equally sensitive to the misalignment of the reflector plate.

Varying the taper angle

Figure 4.3 shows how the relative amplitude of the reflected signal varies with variation of the reflector angle. Three different titanium BRs (R7, R8 and R9), all with end diameter 25.4 mm are compared in this graph. The distance between the BR and the reflector plate is approximately 15 mm for these measurements. The BR with taper angle $\alpha = 1.7°$ (R9) displays in general the widest and most smooth curves, whereas the curves based on measurements from the rod with the smallest taper angle (R7) are more irregular. By comparing these results with the SNR of the BRs given in Chapter 3, there is a distinct correlation between high SNR and the smoothness of curves of Figure 4.3. The higher the SNR, the more smooth is the curve.

Although the absolute amplitude of the reflected signal from the reflector is
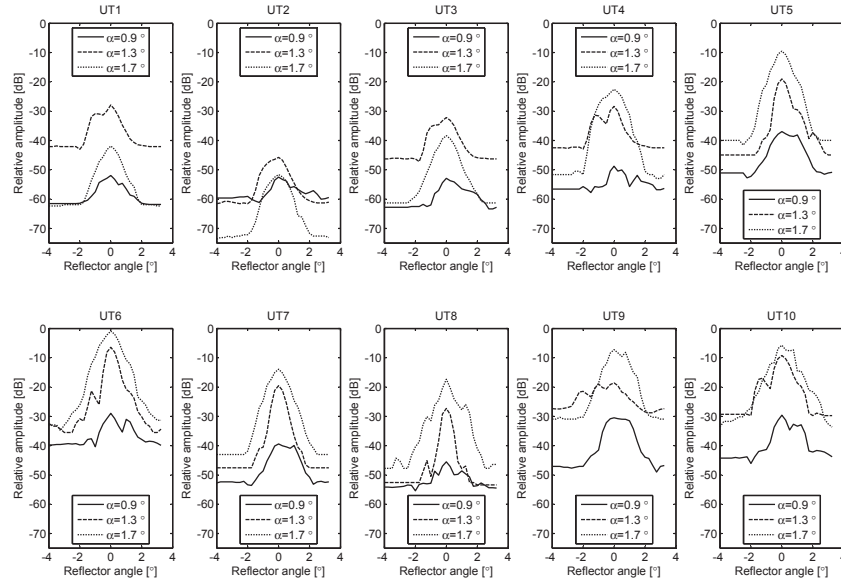
Figure 4.3: Amplitudes varying with the reflector angle for BRs with three different taper angles α. Measurements are perform with a BR-reflector distance of about 15 mm.

smaller for the small transducers (UT1-UT4), the height of the peaks are quite high and distinct for the large taper angle ($\alpha = 1.7°$) BRs. The curves seem to become irregular with increased transducer size (UT5-UT8), and gets quite flat at the top for the largest transducer size (UT9-UT10). Ultrasonic waves from the largest UTs will be more affected by the limited buffer boundaries compared to the smaller transducers, forcing more mode conversions at the buffer boundaries. Hence, more irregular curves for the largest transducers are reasonable. As the BR-reflector distance is increased from 15 mm to 98 mm the size of the peaks are reduced due to attenuation in water, whereas the shapes of the curves seem almost unchanged (Figure 4.4).

For all the ten titanium BRs, independent of end diameters, taper angles, or transducer specifications, even very small misalignment leads to considerable deterioration of signal amplitude and SNR in the pulse-echo mode. If the reflector is tilted more then about 2.0° in each direction from a normal incident ultrasonic beam, the reflection will not be detected, by any of the combinations due to their low critical reflection amplitude. Although they are all very sensitive to misalign-
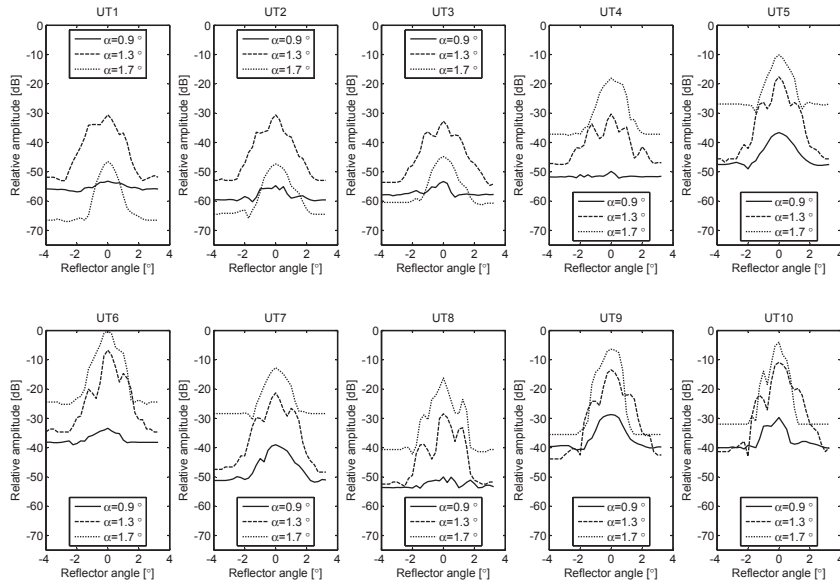
Figure 4.4:   Amplitudes varying with the reflector angle for BRs with three different taper angles α. Measurements are perform with a BR-reflector distance of about 98 mm.

ment, the curve of the reflected signal amplitude as a function of the reflector angle looks different for different combinations.

R1 which is a BR with an end diameter of 8.9 mm has also been tested (Figure 4.5). The results are quite similar for all the four transducer regarding the smooth curves. However, there are differences among the transducers according to the size of the peak related to the SNR. As the BR-reflector distance is increased from 15mm to 98 mm it is possible to see slightly more irregular shapes of the curves. The irregularity is most likely caused by disturbances in the water.

4.1.3 Estimating the angle between a BR and a reflecting plate

Some of the curves showing the results from the experiments with the variation of the reflector angle (Figure 4.4), were smooth. Particularly the curves for the applications where the transducer element is similar in size with the BR end, smooth peaks not influenced by noise, make them reliable also for angle measurements, as each angle is unique determined by the relative amplitude. This is a property
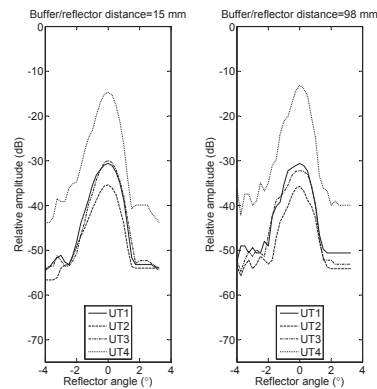
Figure 4.5:   Amplitudes varying with the reflector angle for the BR R1. *Left:* Measurements are perform with a buffer-reflector distance of about 15 mm. *Right:* Measurements are perform with a buffer-reflector distance of about 98 mm.

that could be utilized in different applications where small angle variations in an interface might be accurately detected by just measuring the amplitude of the reflected beam. On the other side the result with small critical reflector angles might limit the use of large buffer rods in industrial settings where the actual reflection surface, e.g. the interface between two separated liquids is uneven or wavy.

4.1.4   Tests with shorter BRs

Experiments with a smaller aluminium single taper rod, and a double-taper steel rod showed broader peak of amplitudes vs. reflector angle, i.e. it was possible to detect the reflection up to about 3 degrees of reflector angle misalignment, compared to about 2 for the long titanium rods (Figure 4.6).

4.1.5   Reduction of ultrasonic amplitude due to angle of incidence

It is a well known fact that the amplitude of an ultrasonic wave is reduced due to oblique incidence of the ultrasonic wave. To determine the influence of this relation the reflection coefficient is calculated. The reflection coefficient at oblique incident waves at the interface between two immiscible liquids can be calculated based upon the longitudinal wave reflection [41]:
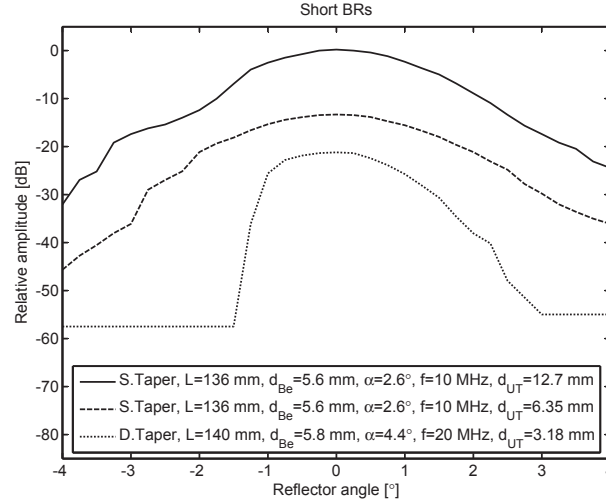
Figure 4.6: Amplitudes varying with the reflector angle for two shorter BRs. Measurements are perform with a BR-reflector distance of about 98 mm.

$$R = \frac{\cos\varphi_1 - \left(\frac{\rho_1 c_1}{\rho_2 c_2}\right)\sqrt{1 - \left(\frac{c_2}{c_1}\right)^2 \sin^2\varphi_1}}{\cos\varphi_1 + \left(\frac{\rho_1 c_1}{\rho_2 c_2}\right)\sqrt{1 - \left(\frac{c_2}{c_1}\right)^2 \sin^2\varphi_1}} \qquad (4.1)$$

φ_1 is the angle of incidence. Based on this formula the reflection constant and transmission constant does not change more than from $R = 0.9372$ at $\varphi_1 = 0°$ to $R = 0.9375$ at $\varphi_1 = 1.6°$. Hence the variation in reflected amplitude is only due to the misalignment of the reflected wave, as the amount of reflected wave from the steel surface is approximately identical for both cases.

4.2 Level measurements with two BRs using through transmission

Time domain reflectometry using the pulse echo method has been demonstrated to perform proper level measurements in several applications. However, this approach has some restrictions related to

- Wavy interfaces causing reflections

- Poor reflections due to low reflection coefficients

- High attenuating fluids with impurities and gas bubbles causing significant reduction in transmitted signals

In some applications the pulse echo method can be replaced by a through transmission setup as seen in Figure 4.7.
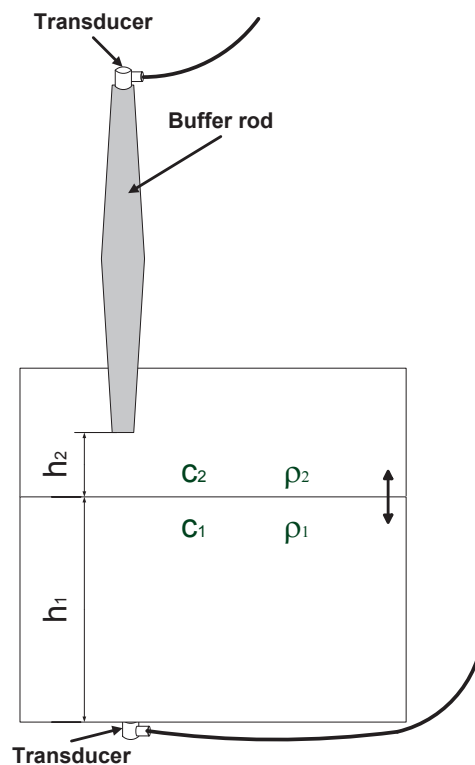
Figure 4.7:   Schematic drawing of a through transmission setup in combination with an acoustic buffer rod in a two-phase material, or with two separate fluids.

If the impedance between the two phases or liquids are close, the reflection coefficient will be approximately zero, and hence the major part of the acoustic wave is transmitted through their common interface. In such cases, an alternative approach to the pulse-echo method should be considered. Figure 4.7 shows a setup were one transducer is transmitting the pulse through a BR, into a tank containing to separate fluids. Underneath the tank another transducer is receiving the signal after a time period t. We define the distance between the buffer end and

the receiving transducer to be $h_3 = h_1 + h_2$, where h_1 is the distance between the interface and the bottom of the tank, and h_2 is the distance between the buffer end and the interface. Then we have the following relations;

$$h_1 = c_1 t_1 \tag{4.2}$$
$$h_2 = c_2 t_2 \tag{4.3}$$

where c_1 and c_2 are the sound velocity in medium 1 and 2, respectively, and t_1 and t_2 the transit time of the wave through medium 1 and 2, respectively.

Defining $t_3 = t_1 + t_2$, h_3 is given by;

$$h_3 = h_1 + c_2 t_2 \tag{4.4}$$
$$h_3 = h_1 + c_2(t_3 - t_1) \tag{4.5}$$
$$h_3 = h_1 + c_2(t_3 - \frac{h_1}{c_1}) \tag{4.6}$$
$$h_3 = h_1 + c_2 t_3 - h_1\frac{c_2}{c_1} \tag{4.7}$$
$$h_3 = h_1(1 - \frac{c_2}{c_1}) + c_2 t_3 \tag{4.8}$$

From this equation h_1 is derived;

$$h_1 = \frac{h_3 - c_2 t_3}{1 - \frac{c_2}{c_1}} \tag{4.9}$$
$$h_1 = c_1\frac{h_3 - c_2 t_3}{c_1 - c_2} \tag{4.10}$$

Hence, by subtracting the time-delay of the BR and the tank bottom, the interface level can be detected. This is in accordance to the method explained by Lynnworth [41]. We have tested this method for detecting a varying oil/water interface in a tank. The uncertainty in the results was about 15 %, but in this case the values of velocities of sound in oil and water are very close to each other. With interface layers in media with significantly different velocities of sounds, this method will probably lead to more reliable results.

In some applications, placing a transducer at the bottom of the tank is not an option, due to technical challenges. The through transmission method might still be an interesting option, utilizing an additional BR with a bend as illustrated in Figure 4.8. An initial experiment has successfully been tested out in a water tank, with a curved aluminum cylinder rod.
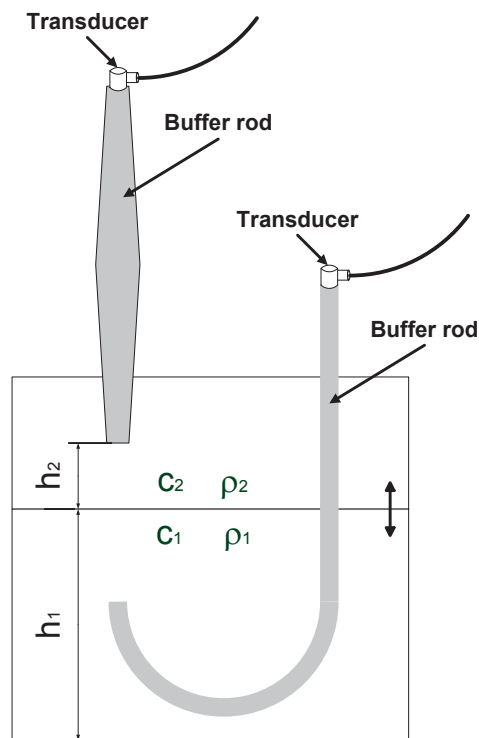
Figure 4.8: Schematic drawing of a through transmission setup in combination with two acoustic buffer rod in a two-phase material, or with two separate fluids. One of the buffer rods has a smooth curvature, bending the rod 180°.

4.3   Denoising ultrasonic waveforms using wavelets

Wavelets have been used in improving signal processing features in many applications especially in image processing applications involving compression of images and streaming videos. Wavelets can also be used to"denoise" [12, 43, 51].

In conjunction with UTDR signals, a study was performed to see the possibilities of exploiting the features offered by wavelets in denoising noisy signals and determining time differences between different sections of transmitted signals and the reflected signals from interfaces. The denoising techniques used in the study performed using UTDR techniques in a water-oil multilevel system is based on the signal decomposition and reconstruction schematically depicted in Figure 4.9. The crux of the technique is the employment of so called "mother wavelets" in the decomposition and reconstruction process executed offline using MATLAB Wavelet Toolbox. The palette of mother wavelets used in this study are db1, db3, coif1, sym3 and sym1 (names as used in MATLAB toolbox). Our focus is on the decomposition level and the reconstruction following this.
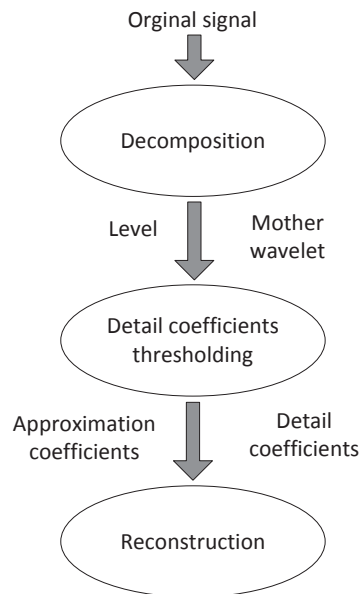
Figure 4.9:   Denoising procedure using selected mother wavelets. Results presented here are using the mother wavelets db1, db3, coif1, sym3 and sym1.

The original signal train for a typical UTDR measurement from the experimental set-up using water/oil multilevel system is shown in Figure 4.10 with con-

siderable amount of clutter. After performing the "denoising" operations using wavelets considerable improvement is found in the quality of signals using the five mother wavelets. The denoised waveforms are shown in Figure 4.11. The resulting SNR values as estimated from the signal trains of Figure 4.11 are shown in Figure 4.12. Although some details as to whether particular features related to propagational features of the ultrasonic wave within the BR and the media could be masked in this process have to be studied, this method does indicate good SNR improvement.
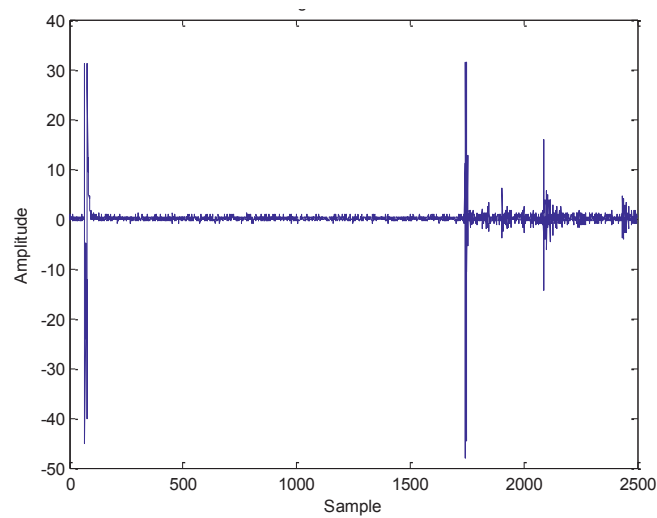
Figure 4.10:   Original signals with UTs in UTDR mode interrogating water oil multi-level system [12].

These wavelet based algorithms can be easily integrated as additional tools in verifying the results in UTDR applications.
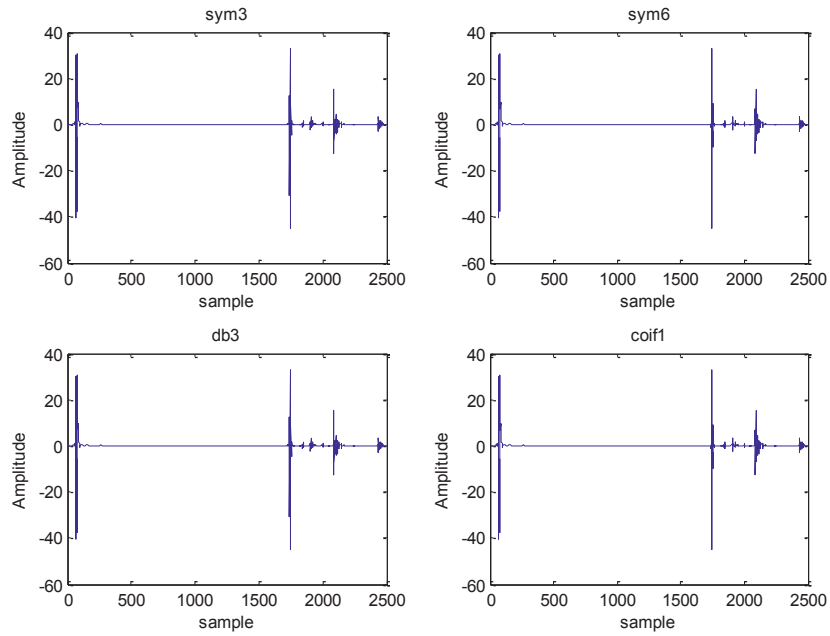
Figure 4.11: Signal of Figure 4.10 after denoising using different mother wavelets for decomposition and reconstruction according to Figure 4.9 [12]
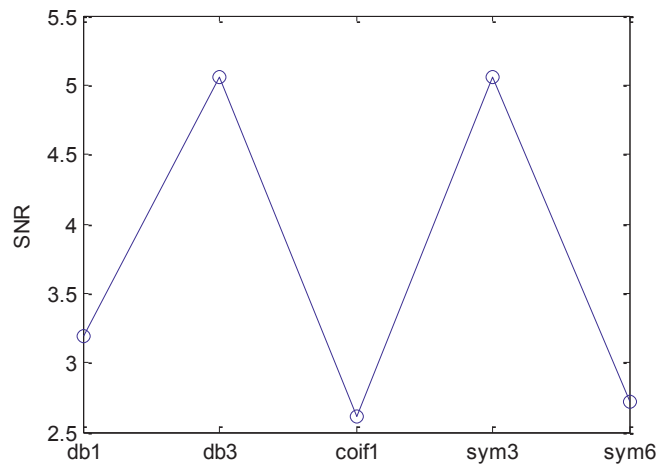
Figure 4.12: Overview of the SNR of the five denoised waveforms of Figure 4.11 [12]

Chapter 5

Measurements of Bath Fluctuations Using Laser Vibrometry

Lasers are in the category of non-contact measurement techniques, which make them well suited for distance measurements in harsh and hostile plant environments, as found for example in the aluminium electrolysis process. By using a properly oriented set of mirrors the laser can be easily placed at safe locations away from the cells. Due to the opaque cryolite, it is not possible to use a laser for measuring the metal level, but it could be a new approach of monitoring the cell performance. As a part of the PhD study, the vibrations on top of the cryolite bath in an aluminium electrolysis plant were monitored using a laser vibrometer [64, 65]. The vertical positions of all the anodes in the electrolysis cell were mutually adjusted step-wise, simultaneously with the laser vibrometer measurements. When the anodes were lowered their ACDs were reduced, and correspondingly the bath height in the cell increased, and vice versa.

5.1 System description

A laser vibrometer is used for measuring the motion of a mechanical system by laser measurements. A coherent laser beam is directed towards a point on the surface of the moving object. When the beam is reflected at the vibrating surface, a Doppler frequency shift in the reflected laser beam will be observed [44]. This Doppler frequency shift is proportional to the surface velocity. By measuring the shift in frequency, the surface velocity and displacement of the surface can be evaluated. The Fast Fourier Transform (FFT) can be used for determining the frequency of the vibrations. In this study an OMETRON portable laser vibrometer VH-1000-D was utilized in combination with a specially designed LabVIEW program installed on a industrial computer. A mirror was mounted on the same rig as

used for the ultrasonic measurements described in Chapter 2. To have access to the molten bath a hole in the crust was made to facilitate the measurement of vibrations of the molten electrolyte surface. Figure 5.1 shows a schematic drawing of the experimental set-up used at the aluminium electrolysis plant.
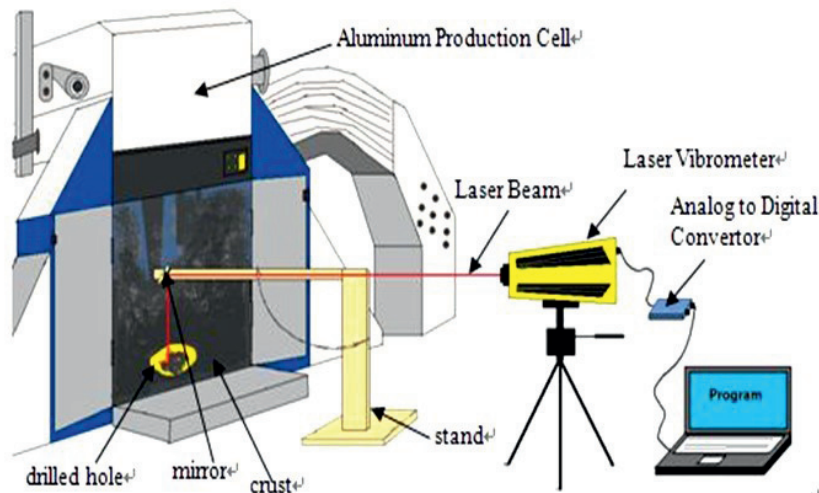
Figure 5.1:   Schematic drawing of the experimental setup for laser vibrometric measurements of the aluminium electrolysis cell, specially designed for this study in cooperation with our late colleague Talleiv Skredtvedt. This is a modified version of a figure in [65].

5.2   Results and discussion

During the laser measurements the vertical positions of all the anode blocks in the cell were mutually adjusted five times, resulting in six measurement sequences. After each sequence, the vertical position was adjusted by approximately 15 mm. Since the anodes covered a large part of the horizontal cell area, the bath level raised by approximately 10-13 mm, when the anodes were lowered by 15 mm, and vice versa. During the first two measurement sequences the anodes were lowered and they were raised for the next three measurement sequences. Hence, we find the sequence with the highest bath height and the smallest ACD at sequence No.3. The largest vibration amplitudes were achieved for this sequence, with a maximum peak to peak amplitude of 60 mm, as seen in the left part of Figure 5.2.

The high amplitudes in this sequence are indicating instability. This could be related to the smaller ACD, which have a tendency of generating more unstable cells.

The frequency of the bath fluctuations was also evaluated, by using a FFT within the LabVIEW program. The right part of Figure 5.2 shows the main frequency for each of the sequences. There are only small variations in the frequency values, but there is a tendency of decreasing frequency as the bath height is increased (and the ACD decreased) for the three first measurements. As the bath height is increased the pressure underneath the anodes will increase. That will increase the flow through the anodes of the CO_2-bubbles evolved under the anodes [34] . It is possible that larger pressure will lead to larger bubbles, but with reduced number of them. Hence the frequency of the bath fluctuation will be reduced, together with larger amplitudes of the fluctuations. Anyway, it is likely that the bath fluctuation is related to the bubbles formed under the anodes, as the frequency of these are given in the range of 0.5 to 2 Hz [39], which is close to our findings.
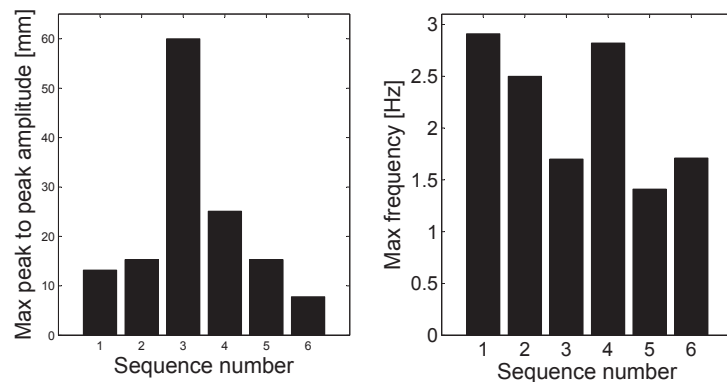
Figure 5.2: Amplitude and frequency of electrolyte surface vibration, based on Doppler frequency shift of the reflected laser beam. Tests performed using the system described in Figure 5.1. The sequences represent measurements made with six different anode positions.

Part III

SOFT SENSORS

Chapter 6

Using Inferential Methods to Estimate the Metal Height

As a substitute and/or supplement to the measurement techniques described in Part II, or the commonly used dip stick based manual measurements, inferential methods can be used for the height estimation. This approach often leads to a model giving additional parameter information of the system. Hence, it is often referred to as soft sensor, not involving any new hardware sensor. The soft sensor is based on a software algorithm for calculating the value of the process variable(s) of interest. Measurements from other hardware sensors and records of process operation are inputs to such algorithms. In this chapter we look into the possibility of developing soft sensors for estimation of the metal height in aluminium electrolysis cells. The software models can be developed by several different approaches. Using the "box system" [40], the models are organized in three main groups;

- *White box models.* These are pure mechanistic models, based upon well known physical and chemical insight of the process. Both the model structure and its parameters are derived from this mechanistic approach.

- *Black box models.* These are data driven models. The selection of the model structure is not based upon mechanistic insight of the process, but uses a predetermined model structure. Measurements of the actual process are used to determine the model parameters.

- *Gray box models.* These models are mixed variants of the two former modeling approaches, and are found in a variety of nuances. Thus, parameter estimation of a model with a mechanistic interpretation, using measurements from the actual process belongs to this group.

In this study the main focus is on the black and gray box models. More on this topic is given in Paper E.

As seen from the Table 1.3 and Table 1.4 and as described in Paper E, the measurements and control of the process operation in the aluminium electrolysis cells are based mainly on many manual measurements and operations. These are usually intermittent and with rare sampling. Using standard inferential techniques such as System Identification (SI), Multi Variate Data Analysis (MVDA) and Neural Networks (NN), some insight can be gained about the aluminium electrolysis process. The following list provides the reasons for not using these techniques directly with the process information available from plants:

- Most of the process variables are sampled with a sampling time much higher than 5 minutes [63].

- Most of the measurements are manual, inherently leading to intermittent sampling.

- For system identification purposes performing frequent measurements with fixed sampling rate is more demanding and expensive.

- Large variations in time constants for the different process variables.

- The saw-tooth-like variation of the metal and bath heights, due to the batch-wise tapping of aluminium.

- In real plant operations, many data points in the time series are frequently missing.

Because of these unavoidable limitations, developing models with a sampling rate less than 24 hours, based upon the available process data, is unrealistic. Performing dedicated measurements of all the relevant variables at a high sampling time for a longer period of time is a very expensive and demanding task. Therefore two different modeling approaches were selected in this study. The first was to use already sampled data from a electrolysis cell in normal operation. All the included variables were adjusted to fit a fixed sampling rate of 24 hours. This resulted in two black box models. The other approach was to develop a model that was able to estimate the metal height every 5 minutes. Both simulated data and real measurements were used in generating black and gray box models for the identification problem related to the estimation of the metal height.

6.1   Estimation using a 24 hour sampling rate

Time series from six input variables (Cell Voltage, Line Current, Bath Height, Anode Position, Feeding Frequency, Tapped Metal) and one output variable (Metal

Height) were collected over a time span of 300 days. The process variables are given in Figure 6.1. The samples were adjusted to a fixed sampling rate of 24 hours, by taking the mean value of each of the variables, every 24th hour. The time series of each process variable is shown in Figure 6.2.
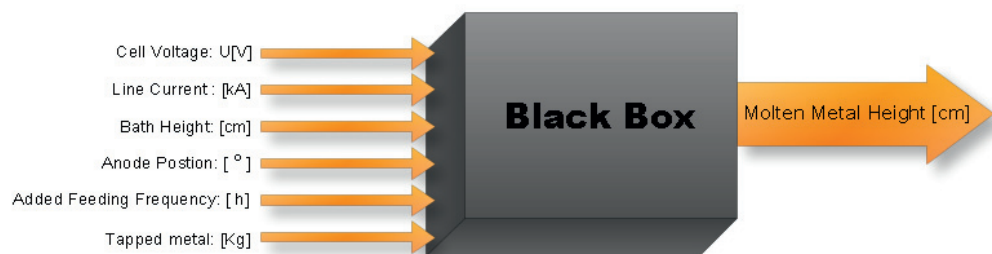
Figure 6.1: The six inputs and metal height as the single output in the black box approach to model with data at 24 hour sampling rate.

The data set representing the first 150 days were used for modeling purpose, and is called the identification data set, while the data set representing the next 150 days is used for validation purpose, and hence called the validation data set. The identification data set was utilized to generate both a NN model (*newlind* function in MATLAB) and a DSR model (subspace method) of the metal height. For more information on Neural Network and the DSR algorithm, the reader is referred to [24] and [10], respectively. The measurement of the metal height and the associated simulations using the identification data set are shown in the upper part of Figure 6.3.
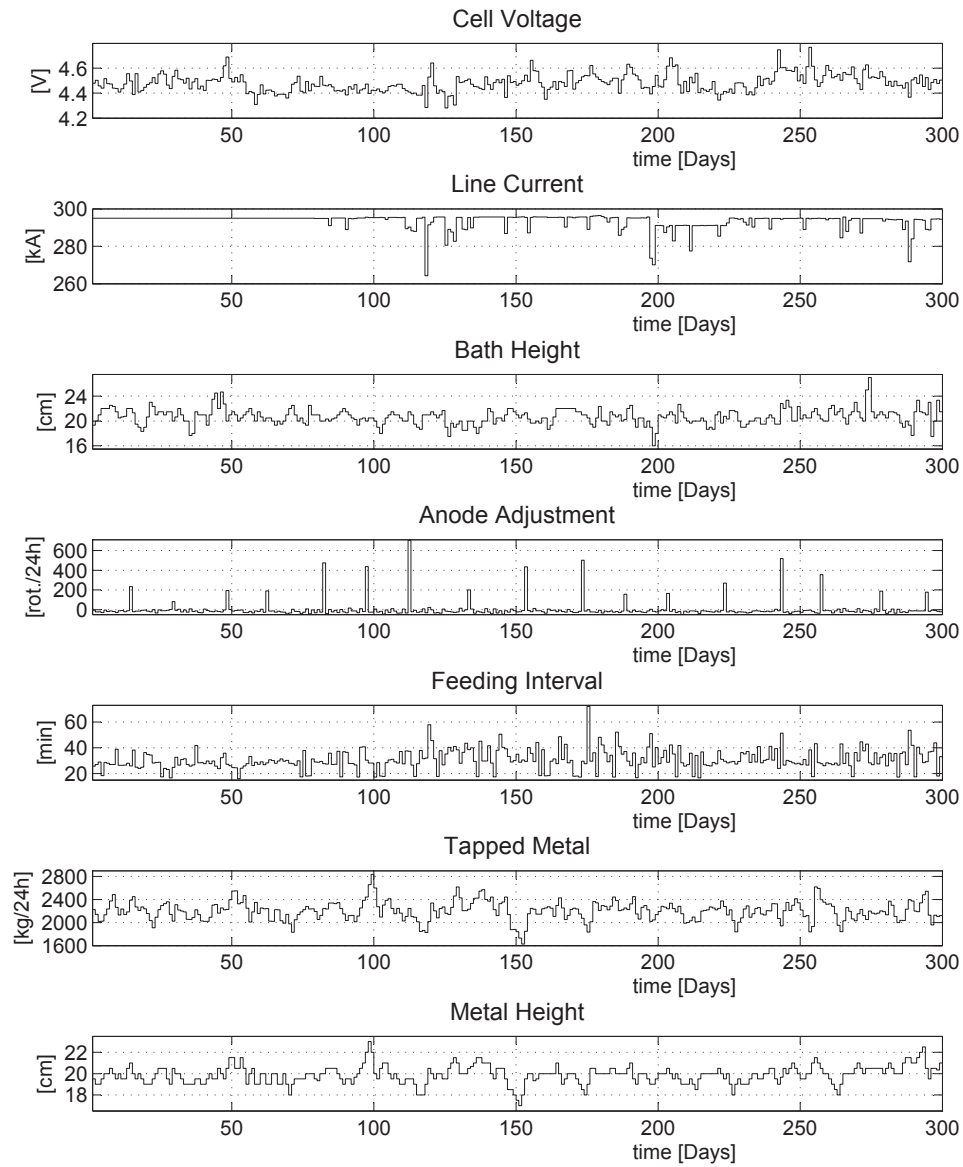
Figure 6.2: The time series of the six inputs and the single output (Metal Height) in the black box approach to model with data at 24 hour sampling rate.
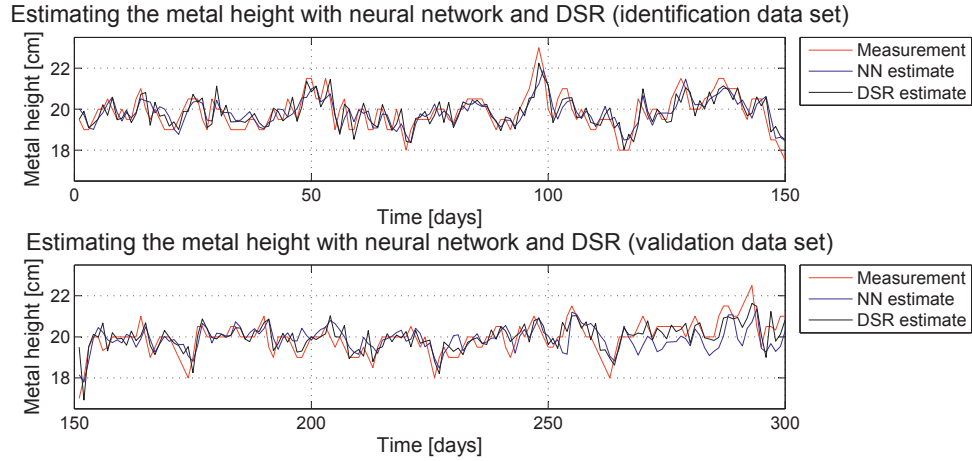
Figure 6.3: The estimated metal height using NN and DSR with data at 24 hour sampling rate. *Top:* Results from the identification data set. *Bottom:* Results from the validation data set.

Both the estimations of the NN and the DSR model seem to follow the measurements quite well. The corresponding plot using the validation data set is shown in the lower part of Figure 6.3. Although the validation data set has not been involved in generating the models, the estimations of the metal height, using this data set seem to follow the measurement well. Hence, the most important long term dynamic of the system has been adopted by the models. It is not possible to decide which of the estimations are better from the figure, hence the estimation errors are evaluated using statistical methods.

To validate the models Mean Square Error (MSE), Normalized Mean Square Error (NMSE), and Normalized Root Mean Square Error (NRMSE) where utilized. On contrary to the MSE, where the numerical value should be as small as possible, the numerical values of the NMSE and NRMSE are in the range $\langle-\infty, 1]$, where 1 is representing a perfect model. The numerical performance of these models are shown in Table 6.1.

The statistic results shown in Table 6.1, confirms that the performance of the DSR and NN based models are similar for the identification data set. For the validation data set there are larger variation. The DSR model display almost the same performance for both the identification and validation data set, while there are poorer performance using the validation data set with the NN model. This is in accordance with the deviation between the graph representing the NN based esti-

Table 6.1: Numerical validation of the black box models, used to estimate the metal height with a sampling rate of 24 hours. Ident. is the identification data-set, while Val. is the validation data-set

Algorithm	MSE		NMSE		NRMSE	
	Ident.	Val.	Ident.	Val.	Ident.	Val.
DSR	0.322	0.343	0.566	0.450	0.342	0.258
NN	0.342	0.519	0.539	0.167	0.321	0.0875

mation and the graph representing height measurements, from the last 50 days of the lower graph in Figure 6.3. The deviation between the measured and estimated values at the end of the validation set for the NN based model, might be reduced by including a Kalman filter in the estimation algorithm. This is already included in the DSR estimations.

6.2   Estimation using intermittent sampling rates

A simple mechanistic model of the metal height, based upon the geometrical parameters of an electrolysis cell, and physical and chemical insight of the electrolysis process, was developed. This model contains three input variables (Line Current, Metal Tap and Horizontal Metal Area) in addition to the output variable (Metal Height). This model was developed to simulate the actual process, with a sampling rate of 5 minutes. The generated simulation based results served as the substitute for real measurements, when developing the soft sensor algorithms. Both Prediction Error Methods (PEM) and subspace methods were used to identify models of the metal height. Two different PEM methods, Ordinary Least Square (OLS) method, and a Recursive OLS (ROLS) were both developed to be used with sets of intermittent metal height measurements. The structure of the mechanistic model were chosen as the model structure for both the OLS and the ROLS model. To have reliable substitutes of real measurements, white noise with a standard deviation of 0.75 cm was added to the simulated model. For the determination the OLS and ROLS models, measurements just before, and just after the metal tapping, were included.

The DSR algorithm, which is a subspace method was also used for determining a model for estimating the metal height. To utilize this method, another measurement scenario with fixed sample rate had to be included. A sampling rate of four hours was selected. In addition a variant of the DSR algorithm, called MDSR was also included in this project. The MDSR algorithm is developed to determine a model of a system, where multiple time series of the system are available. This is typical for batch processes and for processes where the measurement

series are interrupted for some reason. Hence, the algorithm determines a State Space Model (SSM) for the system, and initial states for each of the time series involved. With this approach another measurement scenario was selected, where the metal height was measured just before, and just after the metal tap, and with a sequence of new height measurements every 4 hour. Thus, a new time series was added for each new metal tap sequence.

The OLS and ROLS models were also tested on real data from an aluminium electrolysis cell. For a period of about 76 hours, the metal height was measured just before, and just after the metal tapping, and also every 4 hour between these measurements.

This approach is described in Paper E.

6.3   Abstract of Paper E

Standard system identification algorithms are usually designed to generate mathematical models with equidistant sampling instants, that are equal for both input variables and output variables. Unfortunately, real industrial data sets are often disrupted by missing samples, variations of sampling rates in the different variables (also known as multi-rate systems), and intermittent measurements. In industries with varying events based maintenance or manual operational measures, intermittent measurements are performed leading to uneven sampling rates. Such is the case with aluminium smelters, where in addition the materials fed into the cell create even more irregularity in sampling. Both measurements and feeding are mostly manually controlled. A simplified simulation of the metal level in an aluminium electrolysis cell is performed based on mass balance considerations. System identification methods based on Prediction Error Methods (PEM) such as Ordinary Least Squares (OLS), and the sub-space method combined Deterministic and Stochastic system identification and Realization (DSR), and its variants are applied to the model of a single electrolysis cell as found in the aluminium smelters. Aliasing phenomena due to large sampling intervals can be crucial in avoiding unsuitable models, but with knowledge about the system dynamics, it is easier to optimize the sampling performance, and hence achieve successful models. The results based on the simulation studies of molten aluminium height in the cells using the various algorithms give results which tally well with the synthetic data sets used. System identification on a smaller data set from a real plant is also implemented in this work. Finally, some concrete suggestions are made for using these models in the smelters.

Part IV

CONTROL STRATEGIES, CONCLUSIONS AND FUTURE WORK

Chapter 7

Control Strategies

In this thesis several potential approaches for determining the metal height in an aluminium electrolysis cell, along with some predictive modeling techniques for cell control and maintenance, are presented. Overall measurement and control strategies for implementing these will be outlined in this chapter.

Although further research on BR materials and cladding may lead to more sustainable BRs, continuous online measurements seem unlikely, due to the harsh and corrosive bath. Regular measurements of the metal height, e.g. every 4 hour, or intermittent measurements could be a more realistic measurement scenario. In this case, the immersion and elevation of the BR could be atomized, hence increasing the lifespan of the BR. This could be achieved by a device similar to a device designed by Pechiney, meant for measuring the temperature and bath height in an aluminium electrolysis cell [55]. The device is redrawn in Figure 7.1. The outer cylinder is first forced down to break the bath crust. Then the inner probe (in our case the BR) is immersed into the bath to perform the height measurement.

In combination with this hard sensor approach, a soft sensor approach as outlined in Paper E, can be used for estimating the metal height between the measurement instants. Soft sensors for other process variables can be developed in a similar way. It is also possible to use the soft sensor approach in combination with the existing dip stick measurement of the metal level. However, a common "sampling rate", identical to the "fast" sampling rate of the line current and cell voltage, can be achieved for more process variables. A control scenario for controlling the metal tapping, based on regular measurements of line current and voltage, and intermittent measurements of the metal height, is shown in Figure 7.2. The control scenario can be extended by more input variables, as the model of the metal height is improved.

Similar models could also be used for predicting the process variables several steps ahead, and hence be used for monitoring purpose as indicated in Figure 7.2.

In some cases it can be difficult to select an optimal estimator among several
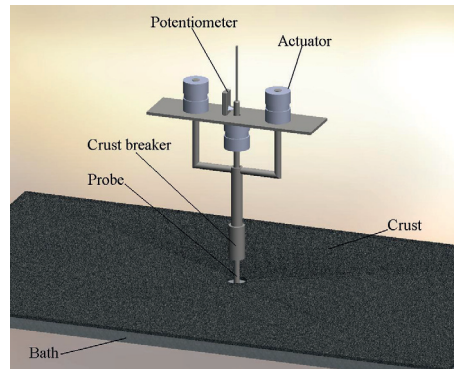
Figure 7.1: A schematic drawing of a device developed by Pechiney for measuring the temperature and the bath height in aluminium electrolysis cells.
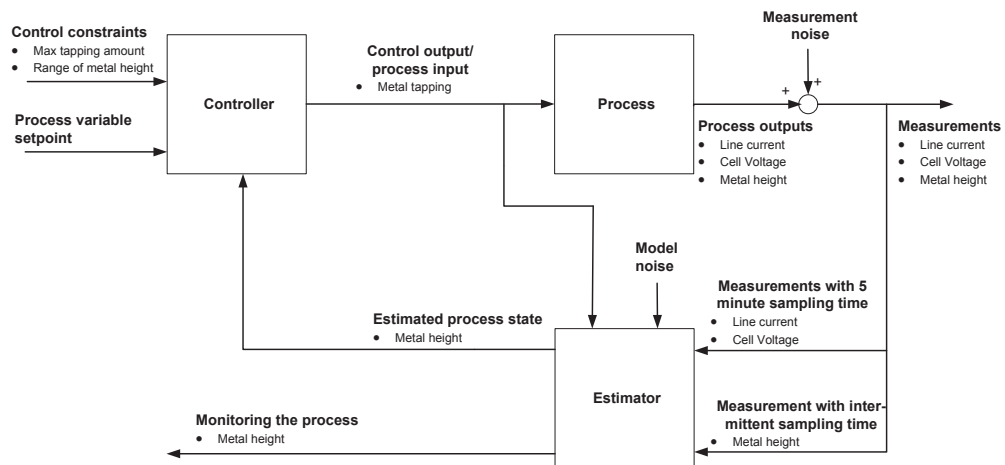
Figure 7.2: An example of a control scenario including an estimator of the intermediate time-steps between the height measurement in aluminium electrolysis cells.

different process models for estimating a process variable, like the metal height. Different models can be optimal at different parts of a process cycle, or in conjunction with different process events. Hybrid model where the most reliable model is selected based on the apriori criteria, can be included in the control loop. This is often called the switching model concept, and is illustrated in Figure 7.3. This concept could for instance be used to switch between different OLS models according to the bath temperature, if different models have been developed for different levels of bath temperatures. It is also possible to switch between different kinds of models structures, e.g. switching between white box and gray box models.
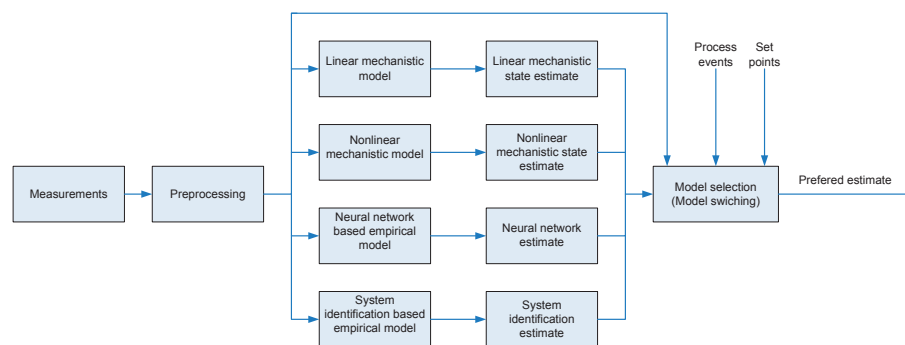
Figure 7.3: An example of an estimator where the switching model concept is utilized. The system select the most reasonable model by optimizing the performance using a cost function

Chapter 8

Conclusions

The Hall- Héroult process, which is the world wide common process of manufacturing aluminium today, was invented in 1886. Ever since a persistent work of optimizing the operation of the process has been on the agenda. Although there have been several improvements throughout the years, still the measurements and operation is dominated by manual intervention. Measuring the metal and bath height of an aluminium electrolysis cell is no exception. In this study an extensive literature study on potential measurement scenarios for detecting these measurands has been performed. The measuring procedures spanned from voltage and current based measurements within the electrolysis cell, to probes with thermocouples to be immersed into the operating cell. Some of the most promising measuring procedures found in the literature were related to ultrasonic measurements to determine the metal-bath interface. Although several measurement scenarios for determining the metal height were found in the literature, any of them seem to have been implemented in regular operation of aluminium electrolysis cells. All the different approaches have one common challenge; the harsh industrial environment displayed by high temperature, corrosive bath and extreme high magnetic fields.

Throughout this study the main objective has been on measurement scenarios for the metal height in the aluminium electrolysis process. Both direct measurements, involving physical sensors, and soft sensor approaches using inferential methods have been under scrutiny. Several different measurement and estimation scenarios have been considered, making this a truly multidisciplinary thesis. Hence, the thesis and the conclusion are to some extent structured in the same manner.

As wave phenomena based interrogation of the process is generally nonintrusive and non-invasive, techniques based on microwave, ultrasonic and optical techniques are worth pursuing for the measurement of process parameters in smelters. When the signals involved can be traced with sufficient SNR at different

layers, a solution for the measurement and control problem can be found for at least some parts of the process.

8.1   Hard sensors

From a plethora of potential hardware sensor approaches of measuring the metal height in aluminium electrolysis cells, the Ultrasonic Time Domain Reflectometry (UTDR) approach was selected for further research. This was a natural choice as the main impression from the literature survey was optimistic regarding this technique. In addition ultrasonic equipment and expertise were available at TUC. A literature survey on optimal selection of Buffer Rods (BR) in combination with Ultrasonic Transducers (UT) and transceiver settings was performed. Initial UTDR measurements with different BRs and UTs showed that the geometrical parameters of the BRs had a major impact on its wave guiding performance. This was further confirmed by literature survey, but very few guidelines for selecting the optimal geometry were found in the literature.

However, the literature study revealed that tapered BRs were most promising regarding high SNR. Hence, an extensive experiment including ten different tapered titanium BRs, all with length 50 cm, but with different taper angles and different diameters was performed. Nine BRs were double-taper BRs, whereas the last one was a multi-taper BR. Ten different UTs were utilized for examining the wave guiding characteristics of the ten BRs. With additional variations of the filter characteristics of the transceiver, 440 different combinations were examined with respect to the SNR and the amplitude of the reflected wave.

Only the results of the experiment using the BRs with the largest end diameters (d_{Be}=25.4 mm) were in accordance with the literature survey, confirming that an increased taper angle of a BR will increase the SNR of the ultrasonic signal. For the BRs with end diameters (d_{Be}=8.9 mm), the results showed the opposite. The SNR and the reflected amplitude are both reduced by increasing the taper angle from $0.9°$ to $1.3°$ and $1.7°$ for the BRs with this end diameter. For the BRs with d_{Be}=17.8 mm, only small variations in the SNR was observed for the different taper angles.

The overall two highest SNR were obtained for the thinnest BR with the smallest taper angle and the thickest BR with the largest taper angle. For these two cases both the experimental and the simulated waveforms provide SNRs above 30 dB. The test with the multi-tapered BR indicated that the multi-tapered BR and the double-tapered BRs have similar acoustic properties. More experiments with multi-tapered BRs have to be accomplished to verify this result, but the result is promising. By including multi-tapered BRs, the size of the BR might be more convenient in industrial settings.

The frequency characteristics of the built-in bandpass filters of the transceiver, and the frequency characteristics of the UTs was compared, and the SNR for different combinations of them were analyzed. The results showed a tendency of increased SNR by using UTs and filters in the higher frequency range, for the thinnest BRs. For the thicker BRs, improved SNR was found for slightly lower frequency ranges of the UT and the transceiver filters. Hence, the BRs can be considered as bandpass filters, where the BRs with the largest diameters are displaying filter properties with lower center frequency than the BRs with smaller diameters. The highest SNR were achieved with UTs with narrow bandwidth, where the pulse energy was not spread over a large spectrum of frequencies. In general, decent SNRs and high amplitudes were found using UTs where the diameter of the outer housing equals the diameter of the BR end, i.e. the element diameter is approximately 75 % of the BR end diameter.

Tests of one of the titanium BRs in molten zinc in about 15 minutes resulted in distinct corrosion of the BR. To withstand the high bath temperature and corrosive environment of an aluminium electrolysis cell, several claddings were considered for the BR. One of titanium BRs displaying the highest SNR was cladded with zirconium-oxide yttrium-oxide, which is a cladding used e.g. in high temperature engines. In spite of the cladding, after being immersed into a real aluminium electrolysis for about 30 minutes the cladded BR was severely corroded and had cracks.

In the experiment SNRs of more than 30 dB were achieved for some combinations of BR and UT. However, in practical applications of BR based height estimations in molten metal, the reflected signal from the interface of interest was often cumbersome to detect. The detection of the reflected signal was very sensitive to the alignment of the BR within the molten fluid. This impression was mutual for all our experiments in water, molten tin, molten zinc and in the aluminium electrolysis cell.

The sensitivity to misalignment of the BR was further investigated in water, by using a device with a metal plate that was tilted in different angles. The reflection from this plate was studied as the angle varied. Detectable peaks were only achieved for angles up to about $2°$. There were only small deviations in the results for the different UT-BR combinations for the 50 cm long titanium BRs, but a test with some shorter BRs, the maximum angle of detectable peaks increased to about $4°$. No significant difference in the angular range of detectable peaks was observed by varying the distance between the reflector plate and the BR. In the context of realizing BRs for industrial applications of ultrasonic TDR in the aluminium industry, this high sensitivity to misalignment between the BR and the interface of interest, has to be reduced.

An ultrasonic through transmission approach for measuring the height of an oil-water interface was successfully tested out in lab scale at TUC. In this setup

two UTs are utilized, each connected to a BR. One of the BRs is bend 180° to receive the ultrasonic signal from the straight BR. This concept seem to be less sensitive to the misalignment between the BR and the interface of interest, but has not been tested out in molten metal or the aluminium electrolysis.

Other ways of making ultrasonic height measurements more robust can be achieved by filtering the ultrasonic signal. This has been done by developing different programs and algorithms in Matlab and LabVIEW. By taking the mean values of several waveforms in a measurement sequence, more stable measurements was achieved. A fuzzy logic approach was developed to detect the reflection of interest from the waveform. Another concept used waveforms from measurements performed at two different heights. A new waveform was generated by subtracting the second waveform from the first. The new waveform was used to detect the height of the interface considered. Also wavelets have been tested with promising results for denoising the waveform of UTDR.

A measurement scenario in an aluminium electrolysis cell using a laser vibrometer, detected interesting relationships between both the frequency and displacement of the bath surface and the Anode Cathode Distance (ACD). For smaller values of the ACD, the bath surface vibrated with lower frequency but larger displacements. This is most likely related to the CO_2-bubbles evolved under the anodes and the overall instability observed for cells with too small ACD. Hence this could be a potential non-invasive measurement for monitoring the cell health conditions.

8.2   Soft sensors

The primary aluminium production is dominated by manual measurements and intervention, leading to a variety of sampling rates and intermittent measurements. Therefore, implementation of regular system identification methods for estimating the metal height was not straight forward. To take advantage of the huge records of measurements and process events from the aluminium production typically stored in a data base, the mean value of each day was calculated and used to create a Neural Network (NN) model and a subspace model of the metal height, with a sampling rate of 24 hours. Samples for 300 days were collected using six different input variables; cell voltage, line current, bath height, anode position, feeding frequency, tapped metal. The estimations from both models followed the measured metal height quite well.

For industrial utility a sampling rate of 24 hours is normally too large, as the short term dynamics of the process is not captured. A simple mechanistic model of the metal height with a sampling rate of 5 minutes was developed with two purposes; to simulate the metal height, serving as a substitute of lacking exper-

imental measurements, and to define the structure of both an OLS and a ROLS model used for estimating the metal height. The input of the OLS and ROLS models were the Line Current and the Tapped Metal. The regression parameters of these two models were calculated using intermittent sampling time of the metal height measurement corresponding to real measurements. The height measurements were sampled just before and just after the metal tapping, and added white noise with a standard deviation of 0.75 cm.

The model structures of two corresponding models with a fixed sampling rate of 5 minutes were also designed. It is shown that the regression parameters of these models are identical to the regression parameters of the corresponding models with intermittent sampling rate. Hence, the regression parameters are calculated by the models with intermittent sampling rate, but the metal height is estimated by the models with 5 minutes sampling rate. The estimated values of the metal height followed the simulated values quite well, in spite of large uncertainty put on the metal height measurements.

Two subspace methods for estimating the metal height were also tested with the simulated model. As intermittent sampling rate is not an option with these algorithms, different measurement scenarios were introduced. One of them was tested with a fixed sampling rate of 4 hours. The other was also tested with a sampling rate of 4 hours, but the data set was deviated into several data sequences, each sequence starting with a measurement just after the metal tapping. The estimated values of these two models followed the simulated metal height fairly well, but not as good as the OLS and ROLS models. The OLS model was also run with measurements from a real plant, showing optimistic results.

Chapter 9

Future Work

This thesis is to be considered as a small contribution to the work of improving the operation of aluminium electrolysis cells, although the results presented in this thesis could also be of interest for several other technological fields and applications. In this chapter related potential future work is outlined both for the height measurement of aluminium electrolysis cell, and for other applications.

One of the major concerns in developing equipments that are to be used in the aluminium electrolysis is related to the material properties capable of performing without deterioration in the harsh and demanding environment. Hence, further material research is required, but search for other measurement methods where physical contact with the molten electrolyte and molten metal is avoided should be considered.

It seems likely that a combination of hard sensor and soft sensor approach will be suitable making the process control more amenable for automation requiring less maintenance work and facilitating real time operational supervision and enabling modern data acquisition and processing as envisioned in the big data approach under discussion in the process industries.

With some of the experience gained during the process of this study, this section looks into the various scenarios involving the hard/soft sensor based monitoring and extrapolates these considerations into the imminent and evolving technologies in the aluminium industries in general.

9.1 Hard sensors

Although showing good wave guiding properties, the 50 cm long BRs used in this work were very sensitive to the misalignment between the BR and the interface of interest. The search for techniques of improving the robustness of the measurements may follow different approaches;

- *Shortening the length of BRs.* By using UTs with higher Curie temperature, i.e. the UT can withstand higher temperatures, shorter BRs can be accepted. According to our findings, this will make them less sensitive to misalignment between the BRs and the interface of interest. Integrated ultrasonic transducers, where the piezoelectric material is deposit onto one end of the BR, is one alternative where in addition exceptional coupling between the BR and the UT is provided.

- *Filtering the waveform combined with improved signal enhancement techniques.* Transforming and/or filtering the waveform from the UTDR, the peak representing the reflection of interest might be improved. E.g. Fourier transforms, wavelets, multivariate data analysis and neural network are potential methods of improving the signal.

- *Through transmission.* The through transmission approach with a BR with a 180° bend should be tested out in molten metal and in the aluminium electrolysis process. Also the sensitivity to misalignment of the BRs could be tested with this approach and the results compared to the results of the experiment with the pulse echo mode described in this thesis.

The concept of measuring the level of an interface using ultrasonic BRs could easily be tested out in other demanding, but preferably less corrosive environments.

More experiments with the laser vibrometer for monitoring the cell operation is a promising non-invasive measurement technique. By including more measurements and process events in the analysis of the cell condition, e.g. anode effects, instability in voltage and current measurements etc. unwanted events in the electrolysis cell could possibly be prevented.

9.2   Soft sensors

More research on different models for estimating the metal height, and other process variables is recommended, as hard sensors are difficult to implement in the aluminium electrolysis cell. A mechanistic model involving more process variables than the simplified can be developed and used for estimation of different process parameters. A parameter estimation of the different model parameters, in the derived model structure, could be calculated using system identification methods. Different Kalman filters could be tested out with the models for reducing the uncertainty of the measurements.

9.3 Alternative production methods of primary aluminium

Without going into details, an overview of ongoing research of improving the Hall- Héroult electrolysis cells, and of developing alternative candidates to this process is presented in the following, together with relevant research suggestions for each. There are two candidates that can be considered as modifications of the Hall- Héroult process, i.e. the wetted drained cathode and the inert anode. The carbothermic reduction and the kaolinite reductions represent alternative technologies of primary aluminium production [16]. Which concept, if any, that will be the successor of the Hall- Héroult process is still to early to predict.

Wettable drained cathodes

Research on inert wettable cathodes have gone on for decades, but have not yet reached a level of industrial relevance. With the wettable cathodes the approximately 20 cm high metal pad of unstable molten aluminium is replaced with a stable aluminium layer of 3-5 mm [38]. Hence, the disturbance of the magnetic field is reduced, making it possible to reduce the ACD without decreasing the CE. The wettable cathode technology is generally combined with the drained cathode technology, providing a steady thin layer of molten aluminium on top of the cathode. On contrary to the regular Hall- Héroult electrolysis cells where the molten aluminium is intermittently tapped from the cell, the produced aluminium is continuously drained [9]. The wettable drained cathode technology is expected to reduce the energy consumption of primary aluminium production with approximately 20 % [16]. The total reduction of CO_2 emission is only due to potential CO_2 emissions from electrical energy production. TiB_2 is the most promising coating material of the wettable cathodes, but still there are mechanical properties that have to be improved before implementing the technology into industrial production of aluminium [38].

Future perspective for the necessity of height measurements and associated techniques: With this approach there is no need for height measurement of the metal level, but monitoring cell performance by laser vibrometry on the surface of the electrolyte would still be a potential research candidate.

Inert anodes

With inert anodes the consumable carbon anodes of the Hall- Héroult process are replaced by inert anodes. Instead of CO_2 emission from the electrolysis cell, O_2 will evolve from the anode. This latent concept has been under consideration since the development of the aluminium electrolysis cell itself, but has since early 80's

become more highlighted [14]. The increased focus on this method is most likely related to the reduced CO_2 emissions in combination with reduced total energy consumption. Other major advantages is related to the discontinuation of producing and replacing the carbon anodes, and the simplification of controlling the ACD, due to the fixed position of the inert anode. With a successful implementation of this concept the local CO_2 emissions would vanish, in addition a reduction of approximately 21 % of the electrical energy consumption would reduce the environmental footprints dramatically [16]. Inert anode material requirements are high conductivity and high thermal and mechanical stability, without being dissolved or react with the cryolite. As for the other concepts, ideal material properties is extremely difficult to obtain in one single material, hence the concept is not industrially implemented.

Future perspective for the necessity of height measurements and associated techniques: With this approach there is still need for a metal height estimator.

Carbothermic reduction

Carbothermic reduction of alumina is an non-electro-chemical process of producing aluminium, on which research has been performed for more than 50 years [16]. The process in atmospheric pressure require temperatures above 2300 K [22]. By decreasing the operational pressure, the aluminium can be produced at lower temperatures, e.g. at 1 mbar the minimum required temperature is about 1700 K [23]. Although the alumina is reacting with carbon in this reaction, producing CO as a side product, the green house gasses emissions from the reaction would be reduced to about 50 % compared to the Hall- Héroult process [6]. In addition the energy consumption is reduced by about 20% for hydro electrical plants, and about 32% for coal burning electrical plants. This concept has much less demand on space requirements, but there are challenges connected to the high process temperature, e.g. the large amount of aluminium being in gas-phase [16]. The main challenge with this concept is related to the side and back reactions reducing the efficiency of aluminium production, but also a reduced purity of the produced aluminium [6].

Future perspective for the necessity of height measurements and associated techniques: With this approach the need for a metal height estimator is less evident, although an estimator indicating metal height might enhance the production process.

Kaolinite reduction

For more than 40 years, research for developing process technology for the kaolinite reduction has taken place. However, the electrolysis of aluminium chloride,

which is a part of this process, is an old concept developed before the Hall- Héroult process itself [16]. The kaolinite process is a two-step process. First the carbo-chlorination of kaolin clay , containing kaolinite (hydrated alumina silicate). The second step involves reduction of aluminium chloride in an electrolysis cell. With this process, the raw material is widely available, and conventional material of construction can be used for constructing the process equipment. Compared to the Hall- Héroult process, the total energy savings are estimated to about 16%. Although one of the side products is CO_2, the total emissions will be reduced by about 29% with the kaolinate reduction technology [16].

Future perspective for the necessity of height measurements and associated techniques: With this approach the need for a metal height estimator is likely, although the electrolysis process is quite different.

Bibliography

[1] M. M. Al-Jallaf, A. H. Mohamed, A. Kumar, and M. S Ali. Evolution of cd20 reduction cell technology towards higher amperage plan at dubal. *Light Metals*, pages 451–454, 2009. Proceedings at TMS (The Minerals, Metals & Materials Society) annual meeting and Exhibition 2009.

[2] D. G. Altenpohl. *Aluminum: Technology, Applications and Environment: A Profile of a Modern Metal Aluminum from Within*. Aluminum Series. Wiley, 1998.

[3] Z. S. Alterman and D. Loewenthal. Seismic waves in a quarter and three-quarter plane. *Geophysical Journal of the Royal Astronomical Society*, 20(2):101–126, 1970.

[4] H. H. Arbabi, Z. Wenjing, W. Xuecheng, and R. Xia. Estimating heights of molten metal using ultrasonic transducer with buffer rods. Master project, Telemark University College, 2009.

[5] G. H. Aylward and T. J. V. Findlay. *SI Chemical Data*. John Wiley & Sons Australia, Limited, 2002.

[6] E. Balomenos, D. Panais, I. Paspaliaris, B. Friedrich, B. Jaroni, A. Steinfled, E. Guglielmini, M. Halmann, M. Epstein, and I. Vishnevsky. Carbothermic reduction of alumina: a review of developed processes and novel concepts. In *Proceedings of EMC*, pages 729–743, 2011.

[7] C. Chen. *Ultrasonic and Advanced Methods for Nondestructive Testing and Material Characterization*. World Scientific, 2007.

[8] CyberLogic. About wave3000. `http://cyberlogic.org/about3000.html`.

[9] N. V. De and J. A. Sekhar. Drained cathode aluminium production cells, August 16 2001. EP Patent 0,892,085.

[10] D. Di Ruscio. Combined Deterministic and Stochastic System Identification and Realization: DSR - A Subspace Approach Based on Observations. *Modeling, Identification and Control*, 17(3):193–230, 1996.

[11] N. Dupas. Increasing electrolysis pot performances through new crustbreaking and feeding performance. *Light Metals*, pages 337–340, 2009. Proceedings at TMS (The Minerals, Metals & Materials Society) annual meeting and Exhibition 2009.

[12] Erihe. Fusing ultrasonic time domain reflectometric data for multi-level fluids in vessels. Master thesis, Telemark University College, 2014.

[13] K. H. Esbensen, D. Guyot, F. Westad, and L. P. Houmoller. *Multivariate Data Analysis: In Practice : an Introduction to Multivariate Data Analysis and Experimental Design*. Camo Process AS, 2002.

[14] I. Galasiu, R. Galasiu, and J. Thonstad. *Inert Anodes for Aluminium Electrolysis*. Aluminium-Verlag, 2007.

[15] E. Gran. A Multivariable Control in Aluminum Reduction Cells. *Modeling, Identification and Control (MIC)*, 1(4):247–258, 1980.

[16] J. A. S. Green. *Aluminum Recycling and Processing for Energy Conservation and Sustainability*. ASM International, 2007.

[17] K. Grjotheim. *Introduction to Aluminium Electrolysis: Understanding the Hall-Héroult Process*. Aluminium-Verlag, 1993.

[18] F. Habashi. *Handbook of extractive metallurgy: Primary metals; secondary metals; light metals*, volume I. VCH, 1997.

[19] F. Habashi. *Handbook of extractive metallurgy: Primary metals; secondary metals; light metals*, volume II. VCH, 1997.

[20] J. F. Hair and R. E. Anderson. *Multivariate data analysis*. Prentice Hall Higher Education, 2010.

[21] C. M. Hall. Process of reducing aluminium from its fluoride salts by electrolysis. Technical Report 400 664, US patent, 1889.

[22] M. Halmann, A. Frei, and A. Steinfeld. Carbothermal reduction of alumina: Thermochemical equilibrium calculations and experimental investigation. *Energy*, 32(12):2420 – 2427, 2007.

[23] M. Halmann, A. Steinfeld, M. Epstein, and I. Vishnevetsky. Vacuum carbothermic reduction of alumina. *Mineral Processing and Extractive Metallurgy Review*, 35(2):126–135, 2014.

[24] S. S. Haykin. *Neural networks: a comprehensive foundation*. Prentice Hall, 1999.

[25] W. Hoopes, J. D. Edwards, and B. T. Horsfield. Electrolytic cell and method of lining the same. Technical Report 1 534 322, US patent, 1925.

[26] C.-K. Jen. Acoustic waveguides having a varying velocity distribution with reduced trailing echoes, August 31 1993. US Patent 5,241,287.

[27] C.-K. Jen. Acoustic waveguides with reduced trailing echoes, May 30 1993. CA Patent App. CA 2,056,517.

[28] C.-K Jen, J.-Y. Chen, S. V. Hoa, K. T. Nguyen, J.-G. Legoux, and H. Hebert. Clad buffer rods for in-situ process monitoring. In *Ultrasonics Symposium, 1997. Proceedings., 1997 IEEE*, volume 1, pages 801–806 vol.1, 1997.

[29] C.-K. Jen and I. Ihara. Clad buffer rod sensors for liquid metals. In *Proceedings of the Advanced Sensors for Metals Processing Conference*, pages 275–285. Canadian Metal Society, Quebec, Canada, August 1999.

[30] C.-K. Jen and J.-G. Legoux. Clad ultrasonic waveguide with reduced trailing echoes. Technical Report 5 828 274, US patent, 1998.

[31] C.-K. Jen, K. T. Nguyen, J.-G. Legoux, I. Ihara, and Hébert H. Novel clad ultrasonic buffer rods for the monitoring of industrial materials processing. In *Proceedings of the 1ˢᵗ Pan American Conference for Nondestructive Testing, 1998*, volume 4. NDT.net, April 1999.

[32] C.-K. Jen, L. Piche, and J. F. Bussiere. Long isotropic buffer rods. *The Journal of the Acoustical Society of America*, 88(1):23–25, 1990.

[33] C.-K. Jen, H. Soda, Y. S. Liu, C. Neron, A. Ohno, and A. McLean. Acoustic characterization of metals with columnar grains. *Ultrasonics*, 33(3):181 – 186, 1995.

[34] K. Kalgraf, M. Jensen, and T. B. Pedersen. Multi sensor data fusion for aluminium cell health monitoring and control. In *TMS (The Minerals, Metals & Materials Society) Annual Meeting and Exhibition, Supplemental Proceedings*, volume 3, pages 149–159, 2010. ISBN Number 978-0-87339-753-7.

[35] J. J. Kaufman, L. Gangming, and R. S. Siffert. Ultrasound simulation in bone. *Ultrasonics, Ferroelectrics and Frequency Control, IEEE Transactions on*, 55(6):1205–1218, 2008.

[36] R. E. Kirk, D. F. Othmer, and M. Grayson. *Kirk-Othmer Encyclopedia of Chemical Technology*, volume II. Wiley, 3 edition, 1978.

[37] H. Kvande and W. Haupin. Cell voltage in aluminum electrolysis: A practical approach. *Light Metals*, 52(2):31–37, 2000.

[38] J. Li, X.-J. L*ü*, Y.-Q. Lai, Q.-Y. Li, and Y.-X. Liu. Research progress in titanium diboride wettable cathode for aluminum reduction. *JOM*, 60(8):32–37, 2008.

[39] J. Li, X. Lv, H. Zhang, and Y. Liu. Development of low-voltage energy-saving aluminum reduction technology. *Light Metals 2013*, 2013.

[40] L. Ljung. *System Identification -Theory for the User*. Prentice Hall, 2nd edition, 1999.

[41] L. C. Lynnworth. *Ultrasonic measurements for process control: theory, techniques, applications*. Academic Press, 1989.

[42] L. C. Lynnworth. *Ultrasonic Measurements for Process Control: Theory, Techniques, Applications*. Elsevier Science, 2013.

[43] L. Manganiello, C. Vega, A. Ríos, and M. Valcárcel. Use of wavelet transform to enhance piezoelectric signals for analytical purposes. *Analytica Chimica Acta*, 456(1):93–103, 2002.

[44] M. Martarelli, G. M. Revel, and C. Santolini. Automated modal analysis by scanning laser vibrometry: Problems and uncertainties associated with the scanning system calibration. *Mechanical Systems and Signal Processing*, 15(3):581 – 601, 2001.

[45] D. L Massart, B. G. M Vandeginste, L. M. C. Buydens, S. De Jong, P. J. Lewi, and J. Smeyers-Verbeke. *Handbook of Chemometrics and Qualimetrics*. Data handling in science and technology. Elsevier Science, 1997.

[46] P. A. Meyer and J. W. Anderson. Ultrasonic testing using phased arrays. In *Proceedings, 15th World Conference on Non-Destructive Testing*, 2000. Rome.

[47] C. Nappi. The global aluminium industry - 40 years from 1972. `http://www.world-aluminium.org/media/filer_public/2013/02/25/an_outlook_of_the_global_aluminium_industry_1972_-_present_day.pdf`.

[48] T. Norgate and S. Jahanshahi. Reducing the greenhouse gas footprint of primary metal production: Where should the focus be? *Minerals Engineering*, 24(14):1563 – 1570, 2011.

[49] O. G. H. Nygaard and S. Mylvaganam. Ultrasonic time-domain reflectometry for level measurement in molten metals. *Proceedings at Technishes Messen*, 60(1):4–14, 1993.

[50] Olympus. *Panametrics Ultrasonic Transducers UT product cataloge 920-041D-EN*, 2011.

[51] R. Paul and A Sengupta. Wavelet based noise reduction of liquid level system using minimum description length criterion. In *Communications, Devices and Intelligent Systems (CODIS), 2012 International Conference on*, pages 592–595, Dec 2012.

[52] K. A. Refsahl. Ultrasonic level measurements in smelters using buffer rods for thermal isolation. Master thesis, Telemark University College, 2009.

[53] M. Reverdy. Computer control of cells. *Proc. on the 28th International Course of Process Metallurgy Course of Aluminium, Department of Materials Science and Engineering, NTNU*, I:103–142, 2009.

[54] J. T. Staley. Aluminum processing. `http://www.britannica.com/EBchecked/topic/18071/aluminum-processing`.

[55] B. Sulmont, P. Homsi, and O. Granacher. Method and device for measuring the temperature and the level of the molten electrolysis bath in cells for aluminum production. Technical Report 6065867, US Patent 6,065,867, 2000.

[56] A. Tabereaux. Prebake cell technology: A global review. *JOM*, 52(2):23–29, 2000.

[57] The International Aluminium Institute. Primary aluminium production. `http://www.world-aluminium.org/statistics`.

[58] J. Thonstad. Electrolytic processes. Compendium in course no. 4295, The Norwegian University of Science and Technology (NTNU), 1998.

[59] J. Thonstad, P. Fellner, G. M. Haarberg, J. Hívés, H. Kvande, and Å Sterten. *Aluminium Electrolysis: Fundamentals of the Hall-Héroult Process*. Aluminium-Verlag, 3 edition, 2001.

[60] F. Ullmann, W. Gerhartz, Y. S. Yamamoto, F. T. Campbell, R. Pfefferkorn, and J. F. Rounsaville. *Ullmann's Encyclopedia of industrial chemistry*, volume A1. VCH, 1985.

[61] H. Viumdal and S. Mylvaganam. Beyond the dip stick: Level measurements in aluminum electrolysis. *JOM*, 62(11):18–25, 2010.

[62] H. Viumdal and S. Mylvaganam. Enhancing signal to noise ratio by fine-tuning tapers of cladded/uncladded buffer rods in ultrasonic time domain reflectometry in smelters. *Ultrasonics*, 54(3):894 – 904, 2014.

[63] H. Viumdal, S. Mylvaganam, and D. Di Ruscio. System Identification of a Non-Uniformly Sampled Multi-Rate System in Aluminium Electrolysis Cells. *Modeling, Identification and Control (MIC)*, 35(3):127–146, 2014.

[64] H Viumdal, R. Yan, M. Liane, B. Moxnes, and S. Mylvaganam. Multi sensor data fusion for aluminium cell health monitoring and control. In *TMS (The Minerals, Metals & Materials Society) Annual Meeting and Exhibition, Supplemental Proceedings*, volume 3, pages 149–159, 2010. ISBN Number 978-0-87339-753-7.

[65] R. Yan. Usage of laser vibrometry in monitoring surfaces and interfaces. Master thesis, Telemark University College, 2009.

[66] S. Zeng and J. Wang. System of height measurement for molten bath in alumina reduction cell. In *Fifth World Congress on Intelligent Control and Automation, WCICA 2004*, volume 4, pages 3675–3678, 2004.

Published and Submitted Work

Paper A

Multi Sensor Data Fusion for Aluminium Cell Health Monitoring and Control *

MULTI SENSOR DATA FUSION FOR ALUMINIUM CELL HEALTH MONITORING AND CONTROL

Håkon Viumdal[1], Ru Yan[2], Morten Liane[3], Bjørn Petter Moxnes[4], Saba Mylvaganam[1, 2]

[1]Tel-tek , Kjølnes ring 56, NO-3901 Porsgrunn, Norway
[2]Telemark University College, Faculty of Technology,Kjølnesring 56,
P.O. Box 203, NO-3901 Porsgrunn, Norway
[3]Hydro, Primary Metal Technology, P.O.Box 303, NO-6882 Øvre Årdal, Norway
[4]Hydro Aluminium, Sunndal, NO-6600 Sunndalsøra, Norway

Abstract

The prevailing aluminium electrolysis process demands steady-state conditions within narrow borders, to improve performance with respect to molten metal production per day, energy usage per kg of aluminium, current efficiency, CO_2 and flour-gas emissions etc. However, only the current and the cell voltage are obtained by on-line measurements. Many bath parameters are manually measured on a daily or even weekly basis. Innovating measurements of the bath temperature, the bath chemistry, the molten metal height and the height of the electrolyte would all be of substantial importance for the control regime. However, combining new measurements and soft sensors for estimating "unavailable" variables would improve both the monitoring and controlling tasks of the aluminium electrolysis process. This paper gives an overview of many online and off-line measurements and reports some new possible measurement scenarios with increasing potential for extensive, fast, efficient and even real-time data fusion. Finally some interesting examples of data fusion examples based on actual plant measurements covering many months are also included.

Introduction

A prolonged focus on increasing the productivity of aluminium electrolysis cells, has forced the cell current into extremely high levels, requiring enhanced monitoring and control facilities. On the contrary, few if any new sensors have been incorporated in the majority of cells worldwide, during the last decade. New measurement techniques and algorithms based on them have been developed and tested, but real breakthroughs in their actual implementation of these in actual industrial settings are still missing. There are several reasons for this conservatism:

1. Technical constraints due to prevailing harsh environment of the reduction cells
2. The maintenance and renewal costs of new invasive sensors are often very high due to the high temperature and corrosive environment in the cells.
3. The investment costs of new sensors should be kept low. Especially if more sensors are needed for each cell, the total costs for the whole plant could entail considerable investment burden for the plant.

Recently, in order to extract more information from the database of measurements and control system of aluminium electrolysis cells, researchers have started to show growing interest in neural networks and multivariate data analysis.

An Overview of Measurement Principles

The majority of measurements performed in the aluminium electrolysis cells are done manually, some on a daily basis and others occasionally. Only the cell voltage and the line current are measured automatically in regular cells. Table 1 displays the common measurements utilized in the operation of the aluminium electrolysis cells. Other measurements are mainly performed for research purposes or special cases, and not for routine day to day operations.

Table 1: Different Measurements Made in Aluminium Reduction Cells, [1, 2, and 3].

Class	Measured variable	Purpose	Frequency
Automatic	Cell voltage	Process control	Continuously
Automatic	Line current	Process control	Continuously
Manual	Bath temperature	Process control and cell monitoring	Daily to weekly
Manual	Bath composition/ chemistry	Process control and cell monitoring	Daily or several times a week
Manual	Bath height	Process control	Daily to every second day
Manual	Metal height	Process control	Daily to every second day
Manual	Tapped metal weight	Process monitoring	Daily to every second day
Manual	Metal purity	Quality indicator	Daily to weekly
Manual	Cathode voltage drop	Monitoring the cathode aging	Occasionally
Manual	Anode Current	Monitoring anode conditions	Daily or when pots are unstable
Manual	Cathode Current	Monitoring cathode conditions	Occasionally
Manual	Freeze profile	Monitoring the side ledge condition	Occasionally or at anode change

In addition to the measurements given in Table 1, visual inspection is used for observing the feeder system and ensuring the anode quality. It is usually performed every 8.th hour and seems to be a normal operational routine in many reduction cells [4].

The cell voltage and the line current are normally given as mean values every five minutes, and are utilized for deriving the pseudo resistance of the cell, which are used for controlling the point feeder. In addition to the line current, there seems to be a growing interest in measuring the individual anode currents, mainly for monitoring and diagnostic purposes, [5]. Continuous monitoring of the individual anode currents have been tested out and utilized already for some years in Elkem (now Alcoa), Mosjøen [6].

The frequency of bath temperature measurements vary from plant to plant depending on the different control strategies. These measurements are also manually performed by the operators. The prevailing techniques of measuring the bath and metal levels are based on immersing a metal rod into the bath, down to the carbon cathode, for some seconds. The rod is analysed after it has been withdrawn from the bath, to determine the position of electrolyte/metal interface and the electrolyte surface. This operation is normally done just ahead of a tapping procedure, in order to determine the amount of molten aluminium to be tapped.

A "method and device for measuring the temperature and the level of the molten electrolysis bath in cells for aluminium production" is reported in [7], however it has not yet been implemented in regular cells due to considerable technological challenges. A hole is made in the crust by a hollow cylinder, also called the crust-breaker (Figure 2). Then the temperature probe is immersed into the bath (Figure 3), until a certain temperature below the thermal equilibrium is attained (preferably 920ºC). The probe is then withdrawn from the bath after a predetermined period of time, and the temperature of the electrolyte is then calculated by extrapolation of the temperature measurements recorded in this particular period. The device is simultaneously measuring the voltage drop between the probe and the cathode block, in order to determine the bath height.
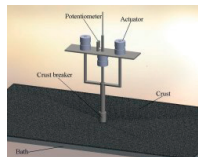
Figure 2. Mechanism for breaking the crust for enabling measurements, [7].
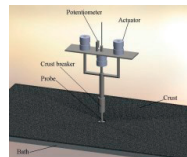
Figure 3. Measuring temperature and bath height with probe immersed in the bath,[7].

Chinese researchers have developed a system for bath height determination based on the temperature gradients of 15 thermocouples mounted on a vertical rod, [12]. As the rod is immersed into the bath and molten metal, the increase in temperature is recorded between 800 ºC and 900ºC. The temperature gradients of the molten metal and the molten bath are different, which makes it feasible to measure the interface between the two molten layers. Technical challenges, related to the endurance of the sensors and immersing mechanisms of the rod into the bath, are delaying this system from being implemented in industrial reduction cells.

A quartz pipe containing a tungsten wire (Figure 4) was used for determining the ACD (Anode Cathode Distance) [8]. The probe was immersed into the bath (Figure 5), and the tip brought to the lower anode surface and was its position was observed. As the probe was brought down to the molten metal area, a sudden change in the voltage potential between the probe and the cathode was detected, and hence the ACD derived.
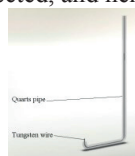
Figure 4. Tungsten probe embedded in a quartz pipe
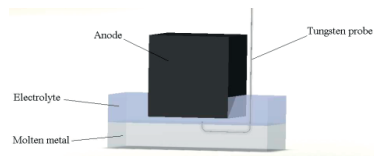
Figure 5. Measuring the ACD with the tungsten probe

Applications for determining the bath height has also been developed in combination with the point feeder device. Improved control of alumina content in the bath is reported by introducing intelligent crust breakers with the aim of reducing the number of feeder failures [4]. The pressure in the pneumatic cylinders for breaker operation are measured and utilized in controlling the breaker movements. A sensor for detecting the electrical contact with the molten bath is also discussed as an option for operating the cylinder. The main advantages of this kind of applications are less material build-up on the breaker and higher certainness that the added alumina is actually added into the bath and dissolved and not only added on top of the crust. The result is a more predictable alumina content leading to less anode effects [4]. Based on the literature survey, the bath height measurements performed by the crust breakers, are currently not utilized for other purposes in the control and monitoring system.

An ultrasonic transducer in combination with a thermal buffer rod for detecting the interface between molten aluminium and electrolyte was discussed and tested by Nygaard et al [10]. The basic principle is illustrated schematically in Figure 6. The buffer rod is placed between the ultrasonic transducer and the high temperature media of the electrolysis bath. In order to protect the piezoelectric materials inside the transducer, the buffer is cooled using some suitable medium.

A semi-automatic method of calculating the metal height based on measurements of the insertion height of the anodes and the anode beam position has been developed and applied to the regular process [11]. The algorithm of this system is mainly derived using the existing geometric relations of the cell, and the system requires occasionally calibration by manual measurements. More reliable metal height measurements led to improved stability of the cell temperature as the amount of tapped metal was stabilized.

Sensor Data Fusion in the Aluminium Reduction Cell

Data fusion is a process of associating, correlating, combining measured data and other relevant information from single and/or multiple sensors to achieve better estimates of observed parameters or even estimating parameters normally not amenable for direct measurements. Data fusion gives an added leverage to the measurement and control engineer in achieving more complete and timelier assessments of process status indicating simultaneously undesirable or dangerous situations, and their significance. The fusion process involves continuous refinements of its estimates and assessments, and by evaluation of the need for additional sources of information (i.e. possibly new sensors), leading very often to the modification of the process itself, leading thus to an overall improvement of the process and its performance indicators.
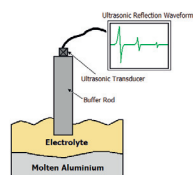
Figure 6. Ultrasonic time domain reflectrometry for bath height measurements, [10].
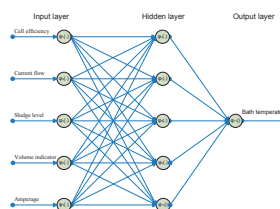
Figure 7. A 5x5x1 Back propagation network predicting the bath temperature

Data fusion is inherently associated with the concept of soft sensors. Soft sensor or virtual sensor is a common name for software based algorithms processing/fusing a plethora of measurements. The fusion of these measurements can be used in the estimation of new quantities that need not or cannot be measured. Strategies based on soft sensors are an essential part of modern data fusion and use among others the following:

- Artificial Neural Networks (ANN)
- System identification methods
- Fuzzy Logic
- Multivariate data analysis
- Markov Models
- Kalman filters

Approach based on data fusion and soft sensor is highly suitable for the supervision and control of electrolysis cells, and. Table 2 displays some of what has been found in resent literature. A main advantage of such models is that they do not need further measurements to be performed, just fetch more information from the data already recorded.

Table 1: Approaches using data fusion in aluminium electrolysis cells

Method	Inputs	Outputs	Sampling time	Purpose	Ref.
Feed forward neural network	8 Cell resistance etc.	Cell resistance 15 minutes ahead	5 minutes	Improve alumina feeding	[15]
Various neural networks	5-12 Se figure 7.	Needed bath additives Bath temperature Fault detection		Cell control Cell monitoring	[13, 14]
Back propagation neural network	10 Frequency components of the cell resistance	Normal condition Anode effect Metal roll	1 second	Predicting cell condition Monitoring	[16]
Neural network, including wavelets and fuzzy logic	8 Frequency components of the cell resistance	6 Normal behavior Faults	1 second	Predicting cell condition Monitoring	[17]
Fuzzy logic	Fluctuations in the cell voltage	Predicting anode effects		Predicting cell condition Monitoring	[18]
Neural network classifier	Fluctuations in the cell voltage	5 Normal behavior Faults		Predicting cell condition Monitoring	[22]
PCA (Principal Component Analysis)	17 Averaged values	Normal behavior Faults	24 hours	Predicting cell condition Monitoring	[20]
MPCA	11 Cell voltage, Line current, etc.	Detecting anode spikes	5 minutes	Predicting cell condition Monitoring	[21]

In aluminium electrolysis process neural networks has mainly been adopted for pattern recognition, particularly to determine failures in the process, and as a model for predicting different variables some time steps ahead. Multivariate data analysis is based on statistical methods, aiming to reduce large numbers of dependent (correlated) input variables to a minimum set of independent (uncorrelated) principal components, without losing relevant information from the system, [19]. The multivariate statistical technique PCA (Principal Component Analysis) seems to be of high interest for monitoring the aluminium electrolysis process.

Based on these overview of available measurement methods in the aluminium electrolysis cell, a possible sensor data fusion scenario can be visualized as shown in Figure 8, where the various measurements are stored at different times leading to a time series of available data, which can be processed in some cases on-line and in other cases off-line leading to possible improvements in cell performance, cell health and energy efficiency, all leading to better environmental record for the whole process. The fact that the time series may have different clock-times (shown as t_1 and t_2 in Figure 8), may entail some amount of algorithmic work in establishing temporal alignment, such as interpolation, extrapolation in the time domain.

Possible Sensor Networking Scenario for facilitating data fusion

Sensor networking is an efficient way of facilitating data fusion, as large number of sensors can be addressed thus extending the leverage available for fusion algorithms. Extending the concept of data fusion, by incorporating possible networked sensors, a modernized version of the cell supervision system can look like the one shown in Figure 9. Such sensor networking scenarios have been tested in different R&D projects, although to our knowledge, none has been implemented on a permanent basis in real operations on a continuous basis in the operation of aluminium electrolysis cells. In Telemark University College, a system is successfully implemented using Delta V of Emerson Process Management with wireless Hart protocols and dedicated gateway for networking with wireless sensors. Such a system can improve the quality of performance of the electrolysis cells of the aluminium industries world-wide.
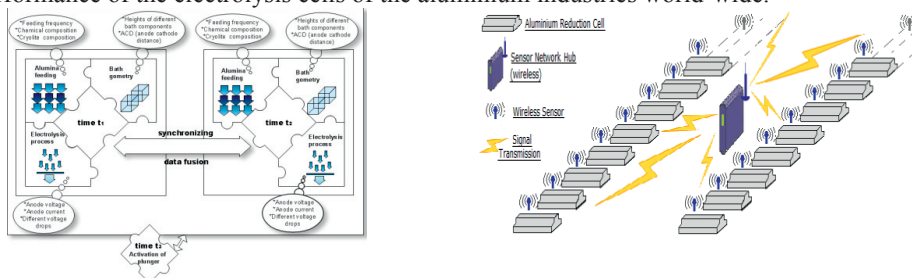
Figure 8. Data Fusion Scenario in aluminium reduction cells with data at times t_1 and t_2.

Figure 9. Possible sensor networking scenario

Some Experience with System Identification methods for data fusion

System identification methods are very often good tools for data fusion and are very useful in the estimations of the metal height. In this section we present a model based on already existing data

set of 6 different process variables from the measurement and control system (Figure 10). As shown in Figure 1, the data set is obtained manually, using automatic measurements or sampling methods with varying frequencies (hours, days or even weeks). Hence in the process of data fusion, the matter of time synchronization or alignment is an essential issue in discrete time events.

Because of the extreme difference and irregularity of the sampling intervals of the different variables, they were all averaged every 24 hours. Process data from 304 days were sampled. The first 200 of them were used to identify the system matrices of a 1st order discrete state space model including a Kalman filter, generated by DSR- algorithm (Deterministic and Stochastic system identification and Realization), [24, 25]. This can be represented by a black-box model shown schematically in Figure 11.

The 104 data sets that had not been involved in identifying the model parameters were utilized to compare the predicted and measured metal heights.
The model is given by,

$$\bar{x}_{k+1} = A\bar{x}_k + Bu_k + K(y_k - C\bar{x}_k)$$
$$\bar{y}_k = C\bar{x}_k$$

A, B and C are system matrices, K is the Kalman gain matrix, $\bar{x}_k$ the estimated state vector and $\bar{y}_k$ the estimated output at time step k. Figure 12 displays the normalized predicted metal height from day 210 to 258, exhibiting reliable prediction of the metal height.

The estimation error is also plotted in Figure 12, and shows only small variations in the predicted values. In Table 3 the mean value and standard deviation for the estimation/prediction error are given indicating good performance of the model.

Figure 10. Diverse measurements as observed in different Al-electrolysis cells
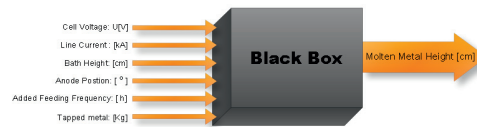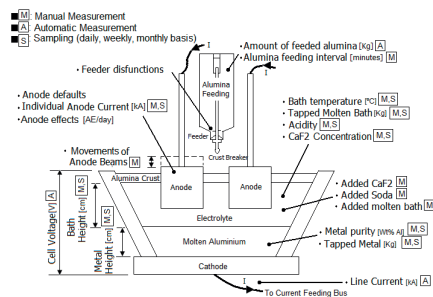
Figure 11. Black-box model using DSR algorithm in a modified Kalman filter used in the prediction

Table 3. Standard deviation and mean values of the prediction error

Estimated data		Predicted Values		Entire data set	
Mean	Std.	Mean	Std.	Mean	Std.
-0.033	7.78	-0.226	9.79	-0.163	9.17

155

Only small differences are shown in the error between the estimated data, i.e. data that are also used for identifying the model parameters, and the predicted data, i.e. data that has not been used for identifying the model parameters. That means that the method has detected general important dynamics of the system and not only relations between the variables of the actual training data set.
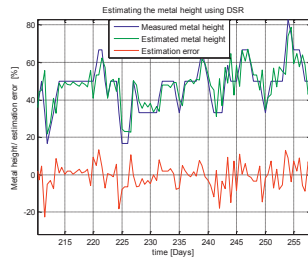
Figure 12. Estimation of the metal height based on a DSR-algorithm, with predicted values from sample 245 to 258.

.

By using raw data from an aluminium cell, a major challenge that we are faced with is the synchronizing of data. Data from 304 days were sampled in order to generate the model, i.e. for the voltage and current signal almost 80 000 data points had to be collected, but for other variables, whereas in the case of the bath height, only about 400 samples were extracted. Either we could decrease the number of current and voltage data, by averaging the values over a time window, or increasing the number of the other measurements by interpolation. By introducing interpolation, dynamics that may be totally wrong, may be included in the data set, and hence affecting the model. On the other side models based on too long sampling intervals will not be able to detect rapid dynamics of the system. Our choices should be based on the purpose of the predictor. Estimating the metal height just before the metal tapping could be accomplished using this model. Improved models can be developed, if the measurements can be synchronized reliably, and if better reference measurements could be performed, particularly in the process of identifying the model parameters.

Non-contact Measurements using LASER Vibrometry

Non-contact measurements using wave phenomena such as ultrasonics, electromagnetism, nuclear radiation seem to be good for the hostile environment of the electrolysis cells. Some recent tests using Laser vibrometry in aluminium electrolysis cells showed that non-contact measurements can be implemented to supervise some parameters of the electrolysis cells. In the study under discussion [24], the bath surface movements were measured to assess the displacement and frequency of molten electrolyte surface. Similar nonintrusive measurements may also be performed for estimating bath temperature.

The test set-up is shown in Figure 13. During these tests, the electrolyte height was changed in several sequences by adjusting the anode position, which gives rise to changes in ACD. When the anode was moved downwards, the electrolyte surface was pressed upwards thus creating various bath height scenarios for the LASER measurements performed. In each step, almost identical changes in anode position were implemented. When ACD changed, movements of the bath surface were observed in real-time results, which were almost equal to the changes in ACD.

156

It illustrates that this technique can work properly in assessing interface disturbances in spite of the intense magnetic field in the vicinity of electrolysis cells.

Measurement data, and processed data based on anode displacements led to results (shown in Figure 14) indicating the position of anode. When the anode was moved downwards, ACD decreased, and the amplitude of the displacement increased, indicating instability and disturbances in the electrolysis process.
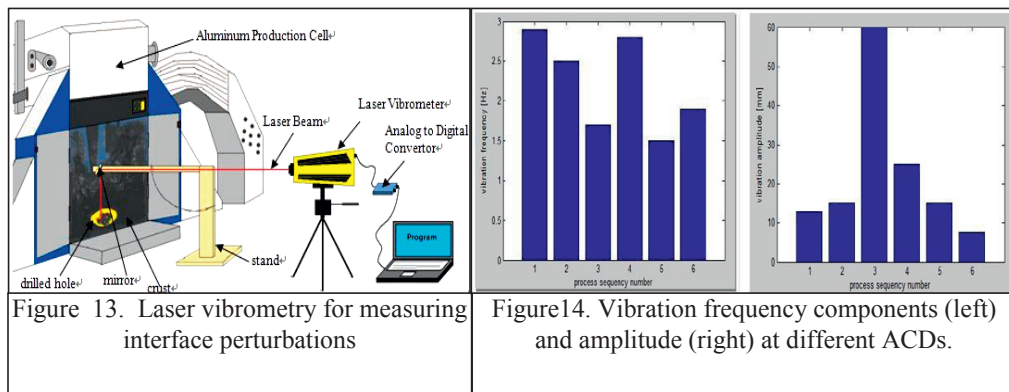
| Figure 13. Laser vibrometry for measuring interface perturbations | Figure14. Vibration frequency components (left) and amplitude (right) at different ACDs. |

Conclusions

This paper gives an overview of actual measurements made in the aluminium electrolysis cells and some new possible/feasible measurements. A dedicated sensor data fusion strategy will certainly help to improve system performance in all the sectors under focus in the modern process industry, viz. cost reduction, health and safety, energy efficiency and environmental protection. Some innovative strategies for sensor networking and data fusion can help to achieve these goals, as has been proven in test installations. It remains to be seen how these issues will be included in the process management by the aluminium electrolysis industries worldwide.

References
1. G.P. Bearne, "The development of Aluminium Reduction Cell Process Control", *JOM*, Volume 51, Number 5, 5(1999).
2. G. Lossman, "Utilistaion of Various Combined Measurements in Reduction Cells for Operational Improvements", *Light Metals*, (1992), 441-447.
3. V. Potocnik, "Measurement Techniques for Pot Analysis", (Paper presented at the 28th International Course on Process Metallurgy of Aluminium, Trondheim, Norway, 2009), 671-711.
4. R. M. Hvidsten and K. Å. Rye, ""Smart feeders" for Alumina in Hall-Heroult prebake cell", *Light Metals* (2007), 435-438.
5. J. Keniry and E. Shaidulin, "Anode Signal Analysis –The Next Generation in Reduction Cell Control", *Light Metals*, (2008), 287-292.

6. R. M. Hvidsten and K. Å. Rye, "Practical Applications of the Continuous Measurement of Individual Currents in Hall- Heroult Cells", *Light Metals* (2008), 329-331.

7. B. Sulmont et al., "Method and device for measuring the temperature and the level of the molten electrolysis bath in cells for aluminium production", *United States Patent* No. 6,065,867, May 23, (2000).

8. M. Jensen et al., "ACD Measurement and theory", *Light Metals,* (2009), 455-459.

9. N. Dupas, "Increasing Electrolysis Pot Performances Through new Crust Breaking and Feeding Solutions", *Light Metals*, (2009), 337-340.

10. O.G.H. Nygaard and K.S. Mylvaganam, "Ultrasonic time-domain reflectometry for level measurement in molten metals", *Technisches Messen*, 60 (1) (1993), Oldenburg Verlag, 4-14.

11. H. A. Gudmundsson, "Automatic determination of metal height in electrolysis cells", *Light Metals* (1999), 297-302.

12. S. Zeng and J. Wang, "System of Height Measurements for Molten Bath in Alumina Reduction Cell", *Proceedings of the 5.th World Congress on Intelligent Control and Automation-WCICA, IEEE*, (2004), 3675-3678.

13. V. Karri and F. Frost, "Need for Optimisation Techniques to select Neural Network Algorithms for Process Modelling of Reduction Cell", *PRICAI 2000*, Springer Verlag, (2000), 480-489.

14. Frost and V. Karri, "Productivity Improvements through Prediction of Electrolyte Temperature in Aluminium Reduction Cell Using BP Neural Network", *PRICAI 2000*, Springer Verlag, (2000), 490-499

15. A. Meghlaoui et al., "Neural networks for identification of the aluminium electrolysis process", *Computers Chemical Engineering*, 22 (10) (1998), 1419-1428.

16. S. Zeng, J. Li and L.Ding, "Fault Diagnosis System for 350kA Pre-baked Aluminium Reduction Cell Based on BP Neural Network", *Light Metals*, (2007), 583-587.

17. H. Li et al., "Diagnosis of working conditions of an aluminium reduction cell based on wavelet packets and fuzzy neural network", *Chemical Engineering and Processing* 45(2006), 1074-1080.

18. Renbijun et al., "Research of Fuzzy Control for Aluminium in Henan Hongkong Longquan Aluminium Co. Ltd., China", *Light Metals*, (2007), 439-442.

19. J. Tessier et al., "Analysis of Potroom Performance Drift, from a Multivariate point of view", *Light Metals*, (2008), 319-324.

20. J. Tessier et.al, "Multivariate Statistical Process Monitoring of Reduction cells", *Light Metals*, (2009), 305-310.

21. N. A. A. Majid et al., "Detecting Abnormalities in Aluminium Reduction Cells base on Process events using Multi-way Principal Component Analysis (MPCA)", *Light Metals*, (2009), 589-593.

22. A.I. Berezin et al., "Neural Network Qualifier of noises of Aluminium Reduction Cell", *Light Metals*, (2003).

23. R. Yan, "Usage of Laser Vibrometry in Monitoring Surfaces and Interfaces" (Master thesis, Telemark University College, 2009), 65-72.

24. D. Di Ruscio, "A method for identification of combined deterministic stochastic systems: robust implementation", The Third European Control Conference ECC95, September 1995, Rome, Italy.

25. O.A.Z. Sotomayor, S.W. Parka and C. Garcia, "Multivariable identification of an activated sludge process with subspace-based algorithms", Control Engineering Practice 11, 2003, pp. 961–969.

Paper B

Beyond the Dip Stick: Level Measurements in Aluminum Electrolysis [*]

Beyond the Dip Stick: Level Measurements in Aluminum Electrolysis

Håkon Viumdal and Saba Mylvaganam

The "old fashioned" and imprecise approach of using a dip stick is still employed to measure the crucial level information in electrolysis baths in the aluminum industry. The dip stick method is based on manually immersing a metal rod into the cell and observing the marks left by the molten bath components to estimate the metal/electrolyte interface and the bath level. However, methods to improve height estimation have been developed in recent years, although none has yet been introduced as part of the routine measurement procedure in the aluminum manufacturing industries. An attempt is made here to give an overview of the promising methods for measuring or estimating the different levels of the bath constituents in an electrolysis cell. Broadly, these methods can be classified into two categories: methods based on innovative physical equipment with the necessary sensors and transducers, and inferential methods which exploit existing measurement data. The first category encompasses many physical and chemical disciplines, whereas the second relies on inferential methods employing approaches sometimes called soft computing or soft sensors. Both approaches are presented and discussed in this paper.

INTRODUCTION

The common method for primary aluminum production is still based on the invention of the aluminum reduction cell introduced by Charles Hall and Paul Héroult in 1886. Although the process has undergone some improvements by incorporating new measurements and employing advanced control algorithms, the process with respect to the fundamental reactions and procedures is almost unchanged. Alterna-

---

How would you…

…describe the overall significance of this paper?

The manual dip stick method is still the prevailing procedure for measuring the electrolyte and molten aluminum levels in an aluminum electrolysis cell. This paper describes existing methods and novel measurement techniques for estimating these crucial parameters to optimize the cell operation. Possible alternative solutions involve both hardware measuring devices and inferential methods.

…describe this work to a materials science and engineering professional with no experience in your technical specialty?

The aluminum electrolysis cell has different interfaces involving cryolite crust, molten cryolite, and the molten aluminum. In addition the interfaces between the anode and the molten cryolite and the molten aluminum and the cathode also restrict the actual volume available for the cell. Having reliable and accurate information on these interfaces is important in optimizing the performance of the electrolysis cell. The paper provides an overview and gives some suggestions for implementing new measurement strategies.

…describe this work to a layperson?

The aluminum electrolysis cell operates around 970ºC and contains extremely corrosive materials. Aluminum electrolysis lacks a reliable method for estimating the level of molten aluminum produced. The harsh environment in the aluminum electrolysis process makes it impossible to insert any measuring device in the cell. This paper gives an overview of the prevailing level measurements in the aluminum electrolysis cells and describes some new methods based on ultrasound techniques similar to sonar echoing methods.

---

tive processes have been and are being investigated, but new plants are still established based on this process, as no other process seems to be able to replace the prebaked cells. The major modules and mechanical and electrical components in the Hall–Héroult process are schematically shown in Figure 1. Compared to the old methods of the last century, the modern cells have silo based automatic point feeding of alumina with synchronized crust breaking to facilitate such feeding into the electrolysis bath. The anodes are prebaked and are made of carbon, although a search for an inert anode material is still being pursued by almost all the major companies producing aluminum.

The major challenges faced by the operating engineer in an aluminum production plant are the extremely corrosive constituents in the bath, very high temperature environment with temperatures around 970°C, and the inevitable frozen cryolite at the top of the bath. As shown in Figure 1, only carbon, graphite, and titanium diboride seem to be able to withstand the hazardous conditions in a more or less satisfactory way.[1] The frozen cryolite, although making feeding of alumina much more difficult, helps to preserve the heat in the bath. The production rate of one single cell is rather low, usually only a few tons per day, so the investment costs should be kept at a low level, based on the prevailing market prices of aluminum and its products.[2]

Generally, improved control of a process can be achieved by improved measurements. However, the demanding conditions in the aluminum reduction cells and the high investment costs, due to the large number of new sensors that have to be incorporated in order to monitor each cell individually,

---

often make investment in new or extra measurement systems extravagant and not on the high priority list of the operators of such cells. Minimal investment in new sensors and implementation of enhanced control algorithms or inferential methods (also known as soft sensors) seem to be the path chosen in recent years.

The possible improvement strategies for the Hall–Héroult process have to address the following: the process, the control system, sensors, and sensor data fusion based on a sound system integration policy with synchronized data storage. Some of the recent process improvement strategies are related to the optimization of the stoichiometric contents of the electrolyte, so as to increase its conductivity and reduce its melting point, hence leading to a reduction in energy consumption. Other process-related improvements are the increased anode surfaces, making it possible to increase the line current (there have been tests on cells with currents up to 500 kA), and hence the production rate, without affecting the current density too much. There have also been improvements in the metal tapping process, but the implementation of the point feeder and crust breaker is considered as one of the most important breakthroughs in the aluminum industry, implying an arrangement involving both controls of the alumina content and incorporation of position sensors. Reduced anode effects and emissions, along with higher current efficiency, have been some of the benefits from this invention.

Controlling the aluminum reduction cell is more complicated now due to the process improvements and increased focus on environmental issues that demand the operation conditions to stay within much narrower constraints for the essential process parameters: bath temperature, alumina content, and acidity.[3] Enhanced control of the anode position has been decisive for achieving a reduced anode-cathode distance (ACD), and hence reduced energy costs. The computer-based controlling has also made it easier to control the whole reduction cell line and not only one single cell at a time.

There have been many attempts to incorporate different sensors, but the majority of measurements are still manually performed. Methods for determining the temperature, the bath height, the liquid metal height, and the electrolyte content have all been developed over the years and some of them successfully tested for their efficiency, but most of them are still facing technical challenges in the real production line. Bearne claims that the main contributions in the process improvements are not the inventions of new sensors, but the way they are used due to control algorithms.[2] In this paper we focus specifically on developments in the level measurements (i.e., measurements of the height of molten aluminum and liquid electrolyte) in the aluminum reduction cell of a prebaked cell.

WHY IS LEVEL ESTIMATION IMPORTANT?

Measurements or estimation of the bath height and the metal height are important seen both from the monitoring and controlling aspects of the alumina reduction process. During the last decades the production rate of aluminum has been improved by increasing the line current from about 100 kA to above 300 kA without increasing the current density in the same ratio, since the anode area has been increased as well, implying reduced electrolyte/bath volume. Simultaneously a lower ACD (see Figure 1) has been introduced, implying reduced energy consumption. Both of these modifications require improved control of the process.

The improved production rate and the smaller electrolyte volume, due to the enlarged anode volume, both increase the variation of the bath height, h_B defined as $h_B = h_3 - h_1$ (see Figure 1). Consequently, a small variation in the anode position will have a greater influence on the bath height than experienced earlier with smaller anodes. The increased production rate does also enlarge the variation of the metal height, h_M defined as $h_M = h_1 - h_0$ (see Figure 1). An increased production rate also involves increased alumina feeding frequency to the bath, which again requires improvements in the feeding procedures, where the detection of the bath height h_B may be of vital concern. If the point breaker or chisel is pulled too far into the bath, there will be a high degree of heat transfer from the bath to the point breaker causing reduced lifetime of the hydraulic cylinder that is moving the crust breaker, or the
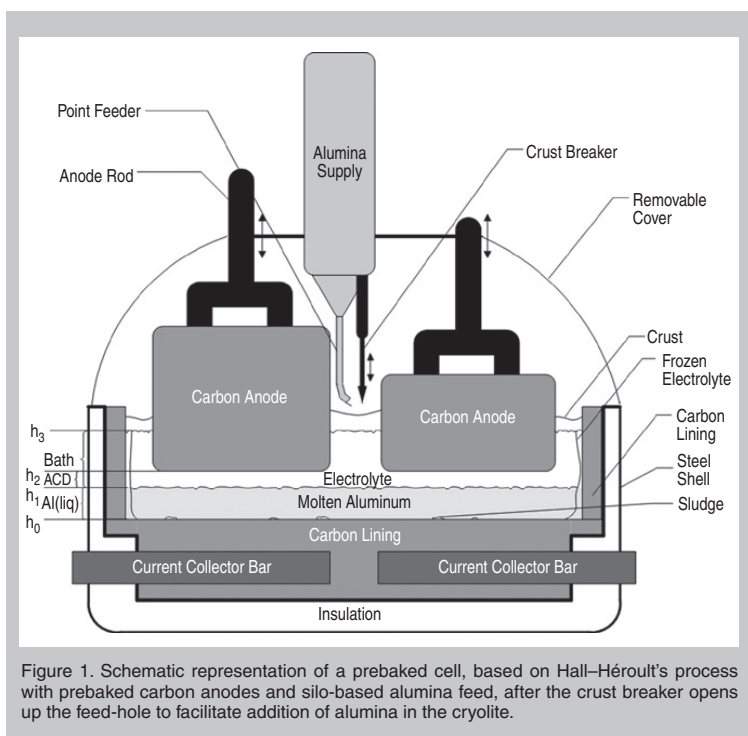
Figure 1. Schematic representation of a prebaked cell, based on Hall–Héroult's process with prebaked carbon anodes and silo-based alumina feed, after the crust breaker opens up the feed-hole to facilitate addition of alumina in the cryolite.

bath can attach to the crust breaker and cause corrosion.[4] In the worst case a short circuit may occur.

A good estimate or measurement of the bath height h_B may also prevent the steel anode stubs from being corroded by bath flowing over the anodes and the frequency of changing anode stubs may be reduced. Simultaneously, iron impurities from the corroded stubs may be reduced, implying aluminum of higher purity produced, as a result of improved bath monitoring.[5]

By implementing reliable on-line measurements or delivering estimates of the bath and metal height, manual work hours can be reduced to a minimum, and thus many man-hours per day can be saved. The exposure of operators to fluoride gases when opening the doors of the cell covers will be considerably reduced, too.

Summarized, the main benefits anticipated from improved on-line level measurements will be enhanced energy yield, reduced costs, and reduced fluoride emissions due to improved monitoring and control of the electrolytic process. In addition, significant improvements in health and safety for operators working in cell halls would result.

THE PREVAILING LEVEL ESTIMATION METHOD

Measurements of the levels of molten aluminum and the bath are of major concern in conjunction with the optimization of the operating conditions of the aluminum electrolysis process. Observing the marks left by molten materials on a steel dip rod, which is manually immersed into the cell, is the prevailing way of estimating the levels. This is a manual process and involves many man-hours and exposes the operators to a hazardous environment and to unhealthy gaseous by-products from the cells many hours a day. This measurement procedure has three main disadvantages: very inaccurate, requires manual operations, and the measurements are performed intermittently between long time intervals (e.g., once a day). To achieve better monitoring and control of the process, more accurate and frequent automated on-line measurements are desirable. This strategy would also reduce the number of expensive manual operations.

RECENT PROCEDURES FOR MEASURING OR ESTIMATING THE LEVELS

During recent decades several proposals and patents were developed, with diverse concepts describing techniques and devices to facilitate level measurements, but a real breakthrough accepted by the industry and included in routine measurements is still missing. The main challenges with implementing new sensors in the operating cell relates to the high temperature, the corrosive environment, the strong magnetic fields, and the opaqueness of the cell content. In this paper some of the proposed methods to address these challenges are presented. The methods can be organized into four groups: voltage and current measurements, temperature measurements, ultrasonic measurements (or generally wave-based measurements), and finally estimating the levels based on existing measurements of the process.

Voltage and Current Measurements

In a European patent from 1985,[6] a method of estimating the height of the molten electrolyte layer by measuring the change in the anode beam position, and the corresponding current reduction of one single anode, induced by elevating this single anode is presented (Figure 2). The measurements will be continuously sampled until the anode current reaches a predetermined level of about 5–10% of its initial values, indicating that the anode surface is about to separate from the molten electrolyte. The uppermost part of the bath height $(h_3 - h_2)$ is calculated from the sampled data after a correction is made regarding the change in the electrolyte level induced by raising the anode. By including an ACD (ACD = $h_2 - h_1$) estimation based on the pseudo-resistance of the electrolyte, the bath height, h_B, can be estimated. This method is based on the assumption of a highly homogeneous electrolyte, whereas in real cells the continuous local variations of alumina content and gaseous products in bath imply a continuous variation of electrolytic resistance.[7] Another and more severe drawback of this method is the process disturbance forced by a frequent anode rising, by bringing the process variables out of normal conditions. One alternative is to use this method only in connection with the anode changing procedure, but that would then not improve the number of level measurements compared to the now commonly used manual measurement using a steel dip stick.

Three years later a patent for a method of monitoring and controlling the additives of the cell, including an estimation method of the bath height was claimed.[8] A probe attached to the super structure of the cell connected to a level
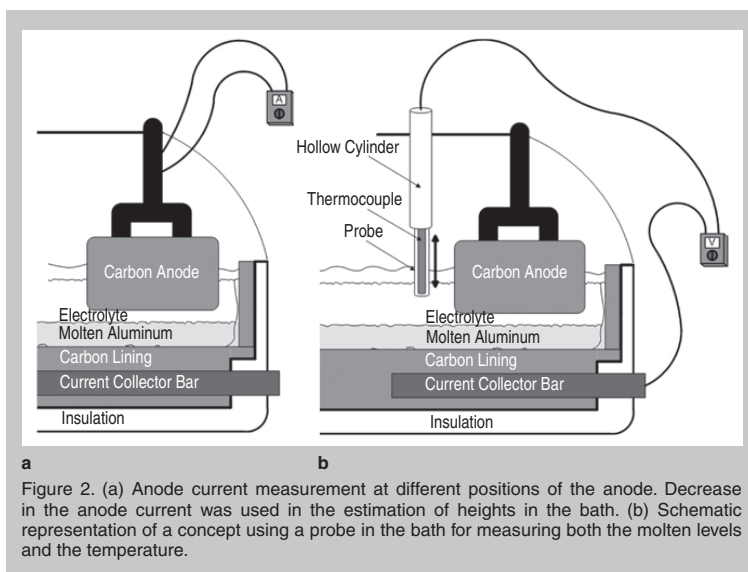
Figure 2. (a) Anode current measurement at different positions of the anode. Decrease in the anode current was used in the estimation of heights in the bath. (b) Schematic representation of a concept using a probe in the bath for measuring both the molten levels and the temperature.

sensor is immersed into the bath as the voltage drop between the probe and the cathode carbon is continuously measured. When the tip of the probe makes contact with the electrolyte the voltage experiences a sudden increase. No information is provided in the patent documents of Aluminum Pechiney as to the materials used in this method, how the hole in the crust is made, or how this probe is cleansed and maintained.

In 1998 a method for measuring both temperature and electrolyte level of aluminum electrolysis bath, by a single instrument was patented.[9] Two years later a slightly modified patent was published,[10] describing a cylindrical probe, located inside a hollow cylindrical crust breaker, that is immersed into the bath after the crust has been punctured by a crust breaker (Figure 2). Once the probe makes contact with the electrolyte bath, a sudden change in the voltage between the probe and the cathode is registered, and correlated with a level signal of the probe achieved by a potentiometer. During further immersion a gradual reduction in voltage is recorded, until the probe tip enters the metal-bath interface, due to the low resistance of molten aluminum. The immersion process duration for accomplishing the level measurements should not exceed 20 seconds due to the harsh environments.

The probe also includes thermocouples for temperature measurements. To avoid destruction of the probe due to the aggressive environment, the temperature of the probe does not reach the equilibrium temperature; instead the bath temperature is estimated by extrapolation. The inventor claims that the uncertainty of the level measurements is reduced from ±10 mm to ±5 mm by this method as compared with the results obtained using the manual method. In addition the higher frequency (every 30 minutes compared to 24 to 48 hours) of measurements make it possible to filter out outliers in a more efficient way, thus increasing the integrity of data obtained.

In *Light Metals 1999* this tool, labeled the CMD (semi-continuous and automatic measurement device) is presented, giving some technical results derived from three years of continuous operating in experimental pots.[11] Re-
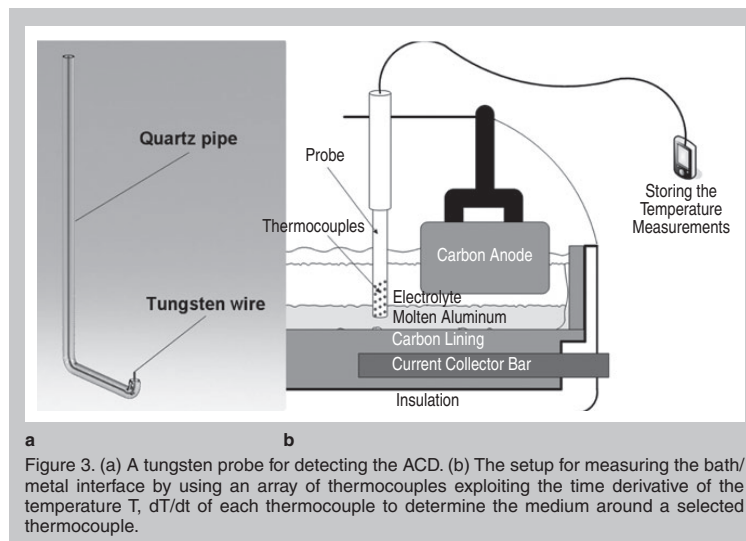
Figure 3. (a) A tungsten probe for detecting the ACD. (b) The setup for measuring the bath/metal interface by using an array of thermocouples exploiting the time derivative of the temperature T, dT/dt of each thermocouple to determine the medium around a selected thermocouple.

garding the bath height measurements, the standard deviation was reduced from 17.2 mm to 14.4 mm, and the current efficiency increased by 0.64%. In addition there were also noted improvements in the temperature measurements. The main economical benefits of this device relate to the gain in current efficiency and a potential extension of anode and anode beam life, due to improved bath height measurements. According to reliable sources, this system has not been included in the regular operating cells.

An invention in 2003 exhibits a method for monitoring the temperature and the quality of the cathode carbon in the electrolysis cell.[12] A metal rod with a built-in thermocouple and a bath electrode render possible a voltage measurement between the top of the carbon cathode and the electrode. A reduced voltage implies increased conductivity and cracks in the carbon.

A probe to measure the ACD for research purposes has been developed.[13] A J-shaped tungsten wire encapsulated by a quartz cylinder (Figure 3) is connected to the cathode by a voltage meter. After the crust has been broken, the probe is immersed into the bath and the position of the tungsten probe is recorded, both as the tip touches the lowest anode surface and the metal bath interface, indicated by a rapid voltage change. A short lifetime for the device is also the main challenge for this probe, although it is claimed to last for 40 measurements if

carefully used. It benefits from its uncomplicated construction and its relatively high accuracy. However, if such a device should be implemented in a regular cell, an automated system for determining the probe position should also be considered, instead of manually reading the levels using a ruler. At the moment there are no intentions of implementing this technique as a regular operation; it is only applied for research purposes.[14]

Level Determination Related to the Point Feeder System

In the latest versions of the point feeders, the so-called "smart feeders," different sensors have been incorporated to improve the alumina feeding procedure. One of the sensors is measuring the electrical contact between the crust breaker (chisel) and the cathode.[3] As the crust breaker penetrates the insulating crust, electrical contact is established and the crust breaker is withdrawn to reduce the time of contact with the bath. The method is successful, but could this measurement also improve other parts of the electrolysis process, if it was incorporated to other algorithms in the control system? The sampled data from the smart feeders could, for example, be beneficial to the metal-tapping procedure.

Thermocouple Measurements

Thermocouples have been used for determining the temperature in the

bath in aluminum electrolysis bath for many years,[15] but in 2004 a method using thermocouples for determining the temperature rising rate in both the electrolyte bath and the molten aluminum was published.[16] A sensor consisting of 15 vertically positioned thermocouples was immersed into the bath (Figure 3), and the temperature measurement from each thermocouple was sampled in order to establish the temperature rising rate for each of them. The different thermal characteristics, as the heat transfer coefficient, of molten electrolyte and molten aluminum were utilized so that the thermocouples that had the fastest temperature change were assumed to be located in the metal. The temperature measurements performed by the thermocouples located in the cryolite would change more slowly. If the temperature measured is T at the time instant t, the device described is tuned to estimate the time derivative dT/dt for the array of thermocouples to identify the medium in which each thermocouple was located. The temperature rising rate dT/dt from 800°C to 900°C was calculated to be 51.8°C /s for the cryolite and 62.8°C /s for the molten aluminum, respectively.

This method is claimed to increase the precision of the level measurements compared to the common manual measurements, but it has challenges due to the hazardous environments in the reduction cell. Obviously, the closer the thermocouples are positioned on the immersion rod, the better will be the accuracy obtained for the height estimates. The prevailing sensors of this method are only able to withstand the cell conditions for some few measurements. Another serious challenge is how the sensor can be immersed into the bath without affecting the measurements performed.

Ultrasound Measurements

Wave propagation in general, because of its nature, offers a contactless means of interrogating hazardous or high-temperature media. Electromagnetic waves generated by dedicated horn antennas, lasers, x-rays, etc. have been tested for different applications. Under these wave-propagation-based interrogation methods, ultrasonic measurements have also been considered by many studies. We present some recent attempts using ultrasonic waves in the monitoring of molten metals.

Attempts with ultrasonic measurements have been tried several times, with different modifications. They all utilize different kinds of thermal insulation or buffers shaped as long cylindrical rods to avoid the piezoelectric material of the ultrasonic transducer (Figures 4 and 5) reaching temperatures beyond the so-called Curie temperatures of the piezoelectric crystals used in such transducers, and hence lose their piezoelectric characteristics.

As the transmitted ultrasonic pulses propagate through the different media, the variations of their physical characteristics (e.g., acoustic impedances) will cause reflections to appear in their intersections. The ultrasonic transducer acts both as a transmitter and receiver, so as the reflected ultrasound reaches the ultrasonic transducer it appears as a pulse in the received signal, as seen in Figure 6. Both the reflection of the buffer rod end and the intersection between bath and molten metal will appear as separate pulses in the received time-domain signal. By utilizing the sound velocity of the different materi-
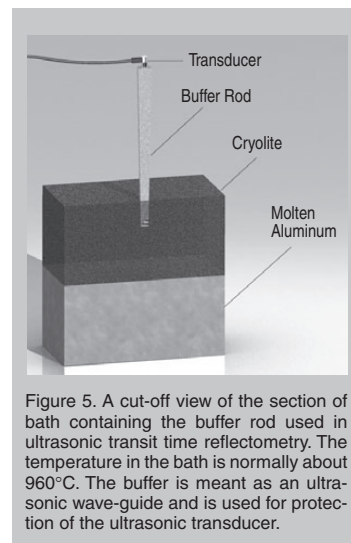
Figure 5. A cut-off view of the section of bath containing the buffer rod used in ultrasonic transit time reflectometry. The temperature in the bath is normally about 960°C. The buffer is meant as an ultrasonic wave-guide and is used for protection of the ultrasonic transducer.

als involved, the representative spatial distances between the intersections can be calculated, hence the level of the bath/metal interface.

In 1993 Nygaard and Mylvaganam presented a method using different buffer rods in combination with an ultrasonic transducer for measuring the molten metal height.[17] Diverse methods for cooling the buffer rods have been considered: a water- or air-based cooling system, temporary immersion of the buffer rod into the bath, or a combination of both of them. A buffer rod with grooves made of carbon, with a momentary bath immersion, seemed to be a good choice for the aluminum reduction cell since the carbon is already present in both anode and cathode and might possibly be incorporated into the anode. However, this method would probably have challenges due to the high attenuation in the large anode. Compared to metal buffer rods, the spurious signals produced by the ultrasonic propagation in the rod are smaller in a carbon buffer rod and the attenuation of mode converted signals at the wall of carbon rod is relatively high. Air- or nitrogen-based cooling will be the options accepted by the operators of aluminum electrolysis cells, as water near any cell is prohibited due to violent expansion of trapped steam in molten materials, leading to almost explosion-like spillage of bath contents.

In 1998 Ihara et al. presented experiments using a 1 m long buffer rod
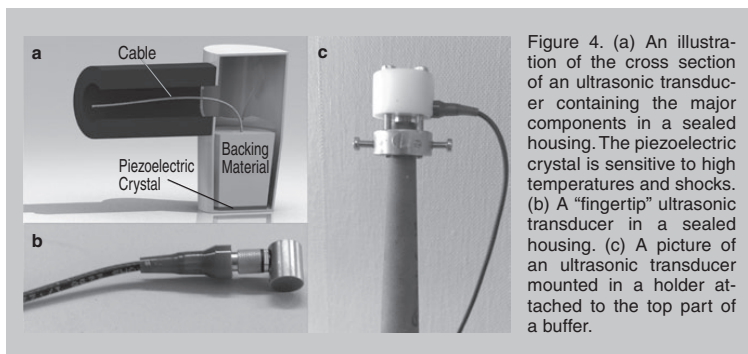
Figure 4. (a) An illustration of the cross section of an ultrasonic transducer containing the major components in a sealed housing. The piezoelectric crystal is sensitive to high temperatures and shocks. (b) A "fingertip" ultrasonic transducer in a sealed housing. (c) A picture of an ultrasonic transducer mounted in a holder attached to the top part of a buffer.

made of fine grain steel.[18] To reduce the spurious echoes the rod was thermal sprayed with a stainless steel cladding, and the rod was shaped to a taper design with a tapering angle of 1.1°, achieving a signal to noise ratio (SNR) better than 40 dB. A spherical acoustic lens was mounted at the buffer end to obtain high resolution imaging and the possibility of proper particle detection. To avoid superheating of the piezoelectric element an air-cooling system was implemented at the transducer end of the buffer rod. This buffer rod was not used for level estimation, but is mentioned here for a more complete picture of ultrasonic measurements using buffer rods in connection with molten aluminum.

Some years later Ihara et al. presented another experiment for monitoring the solidification process of aluminum alloys.[19] A tapered titanium buffer rod coated with a thermal sprayed titanium layer was connected to a conventional piezoelectric transducer. The buffer was then immersed into the molten aluminum alloy and an on-line registration of the height of the solid-molten interface was provided due to a large difference in longitudinal sound velocity in the molten and solid aluminum alloy. In this setup the temperature of the molten aluminum alloy was below 800°C and no corrosion from an electrolysis process was present. 5 or 2.25 MHz ultrasonic transducers were used for these experiments.

A 1 meter double-taper buffer rod (Figure 7) (i.e., a rod having a tapering shape from the middle in both directions), with thermal cladding, was utilized for measuring the height of the molten aluminum pad in an electrolytic

Figure 7. A double-taper buffer rod, including an ultrasonic transducer with housing.

cell at 960°C.[20] More than 30 cm of the buffer rod was immersed into the cryolite bath and molten aluminum. The immersion time of the steel clad buffer rod should, however, be reduced to a minimum, to avoid damages to the buffer due to the highly corrosive environment in the reduction cell. A similar but shorter (approximately 30 cm) double-taper steel buffer rod was described some years later, both for particle detection and ultrasonic imaging in molten aluminum at 780°C.[21] One buffer end had a spherical concave shape, included for improved focus abilities. The other end, connected to a 10 MHz conventional ultrasonic transducer, maintained a low temperature due to an air cooling system. Even though the aluminum was heated by an electric resistance furnace and not by electrolysis, the molten aluminum had a significant corrosive impact on the stainless steel rod, after 6 hours in the molten metal. In order to reduce this corrosion, the coating could be improved but the wettability of the buffer rod might then be reduced. An example of that is described by using an alumina rod in the molten aluminum, giving excellent resistance to corrosion but a very low wetting between the alumina rod and the molten aluminum, implying poor

coupling and waveguide for the ultrasonic signals.

None of these buffer rods has been applied for measurements in the aluminum electrolysis process, but could perhaps become feasible with a proper incorporation of technical apparatus and method.

Estimation of Bath and Metal Heights using Inferential Methods

Dynamic modeling of the energy and mass balance of aluminum reduction cells have been on the agenda for several decades, and in 1980 Erik Gran published a paper where a model with 26 different state variables and nine different controls was developed and used as a part of the control algorithms.[22] The bath and metal was estimated by nonlinear models of the aluminum electrolysis process like $\dot{x} = f(x, u, t)$ and $y = (x, u, t)$, where x is representing the state vector, u the control vector, y the measurement vector, and t the time. Depending on the application, the state vector x and the output y could be a selected set from those given in Figure 8.

One-step-ahead predictions of the process measurements, including bath and metal height, were predicted, but the system had a tendency to drift off after some time.[23] The researchers then developed a simpler but adaptive model for point fed cells. This system performed parameter estimations to be utilized in the control system, and could then be regarded as "an advanced measurement system, rather than an adaptive system in the usual sense." The estimator is based on an ARMAX model, including a forgetting factor, that forces the model to put more weight on recent measurements in order to track time varying parameters.

A rather new control scenario utilizes a nonlinear model predictive control
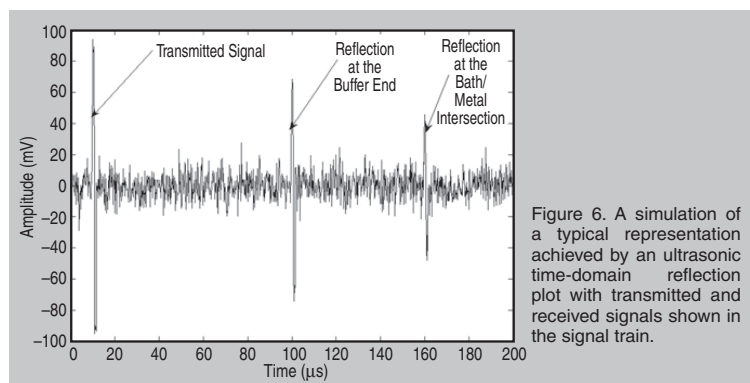
Figure 6. A simulation of a typical representation achieved by an ultrasonic time-domain reflection plot with transmitted and received signals shown in the signal train.

system (NMPC), where an estimator is included in the control loop to predict the future states of the process.[24] By including an estimator the bath and metal levels can be estimated for the intermediate time-steps between the level measurements, based on the controller output and the other measurements as depicted in Figure 8. Although information has been published about modeling of aluminum reduction cells, detailed information about estimation of bath and metal level and how they are utilized is hard to find. Such information is, to some extent, probably available in the monitoring and control system of the different plants.

In an attempt to achieve more precise estimation of the aluminum metal level in the reduction cell, measurements from an existing level sensor measuring the vertical anode rod position were utilized in another approach.[25] An improved version of the classic dip stick for level determination was also included in this method, reducing the influence caused by ridged or uneven carbon cathode by using the floor as the reference level. The main focus of this work relates to achieving a higher degree of precision of the metal level for the purpose of determining the metal tapping amount more optimal. Basically geometric relations in the bath in combination with the anode rod level,
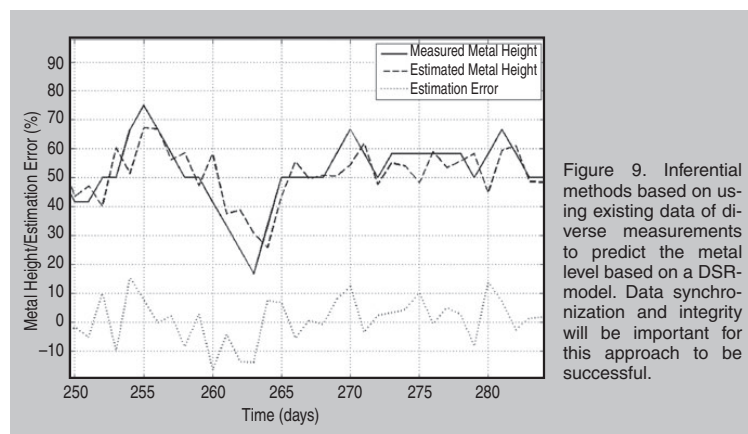
Figure 9. Inferential methods based on using existing data of diverse measurements to predict the metal level based on a DSR-model. Data synchronization and integrity will be important for this approach to be successful.

voltage, and current measurements constitute the main aspects of this method. Although this level estimation technique may improve the tapping process, it will be too inaccurate for the estimation of ACD and the manual measurements are still required since the bath height is not estimated. On the other side, this estimation reduced the variation of the metal level, and hence reduced the tapping variation.

Recently there has been an increased interest in data fusion methods for aluminum electrolysis. See, for example, the growing numbers of neural network related contributions in the recent *Light Metals* editions. The publications mainly consider fault de-

tections, but such methods could also be used effectively for developing mathematical models of the electrolysis process and finding correlations among process variables as a substitute or complement to the mass- and energy-balance-based mechanistic models already mentioned. These methods are commonly classified under inferential methods for monitoring and control.

The statistical relations between different process variables and the bath level have been recently investigated, expectedly indicating that the pot power input and anode cover material composition are influencing the bath height the most.[26] Such statistical data from the real process may serve as fundamental building blocks in the models based on multivariate data analysis.

A subspace system identification method has been utilized to develop a one-step-ahead predictor of the metal height.[27] The model is based on data from six process variables sampled over 200 days. The estimated metal level is following the measured level quite well (Figure 9). It should be noted that the uncertainty of the measured metal levels is large as they are measured by the regular manual method. By improving the accuracy of the measurements, the accuracy of the predictor would most likely also be improved. Although this model is at the research stage, it displays a perspective of the apparently sealed resource of correlated data in the control system. Anyway, the model should always be developed for a specific purpose, and adjusted to fit each cell's own characteristics. The model that has been demonstrated here
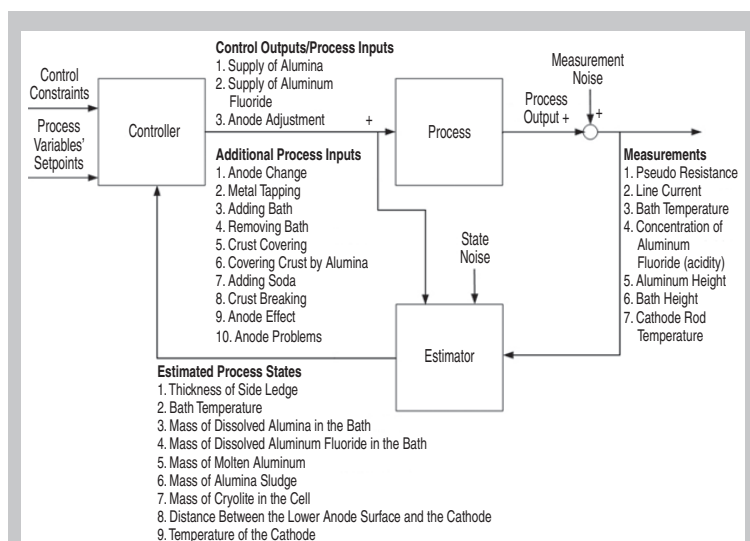
Figure 8. An example of a control scenario based on estimating future process states by applying a suitable process control model, which could be linear, nonlinear, inferential, or a combination of these. See Figure 10 for further details.
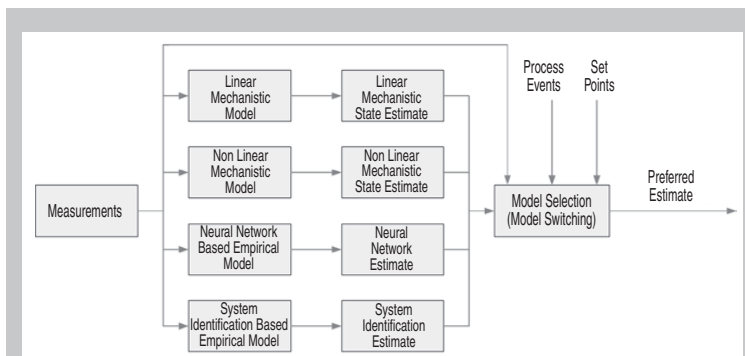
Figure 10. An estimator utilizing the switching model concept. From a set of well-proven models, the system tries out various models using a cost function to optimize performance.

has a sampling time of 24 hours and could be utilized in connection to the metal tapping procedure.

A third option regarding implementing an estimator to the control loop is hybrid models, often called "changing models" (also called model switching in some studies), where different models are applied simultaneously but only the best model is chosen at each time-step, by some criteria, posed a priori. Figure 10 illustrates how different mechanistic and empirical models may complement each other in a switching model scenario. Well-defined cost functions and high computing capacity are usually essential to be successful when employing this approach. No similar approaches are yet found in the literature for the aluminum electrolysis process, but might be included in the future, although different models from the set of models shown in Figure 10 have been successfully applied in solving some of the problems encountered in cell monitoring and management.

CONCLUSION

Improvements of the aluminum electrolysis process are considered continuously, both in the direction of alternative methods and in improvements of the old prebaked cells. In this paper we have been looking into contributions regarding improved height

measurements of the electrolytic bath/molten metal interface, and the bath height. A number of methods and devices have been developed so far, without the real breakthroughs, mostly due to technical challenges. Some of the most promising methods relate to the voltage measurements in the bath, and ultrasonic measurements in connection with a buffer rod. In addition, data-based models, employing inferential methods and model switching, for determining levels of the molten materials in the electrolysis cell have the great advantage of being versatile, cheap, and easy to be incorporated in an existing portfolio of algorithms. In addition, these may help to reduce maintenance costs.

References

1. S. Prasad, *Braz. J. Chem. Eng.,* 17 (2) (June 2000), pp. 211–218.
2. G.P. Bearne, *JOM,* 51 (5) (1999), pp. 16–22.
3. S. Kolås and S.O. Wasbø, *Light Metals 2010,* ed. John A. Johnson (Warrendale, PA: TMS, 2010), pp. 501–505.
4. L.-G. Sander, "Method and Device for Controlling the Movement of a Supply and Breaking Chisel in an Aluminum Production Cell," International application published under the patent cooperation treaty (PCT), PCT/SE00/01500 (January 2001).
5. S.J. Lindsay and P. Doiron, *Light Metals 2009,* ed. Geoff Bearne (Warrendale, PA: TMS, 2009), pp. 499–503.
6. J.S.S. Girard, "Controlling Aluminum Reduction Cell Operation," European patent 0,195,143 (18 March 1985).
7. B. Sulmont et al., "Method and Device for Measuring

the Temperature and the Level of the Molten Electrolysis Bath in Cells for Aluminum Production,, U.S. patent 6,065,867 (23 May 2000).
8. B. Sulmont, "Procédé et Dispositif de Contrôle des Additions d'électrolyte Solide dans les Cuves d'électrolyse pour la Production d'aluminum," European patent 0,288,397 (19 April 1988).
9. B. Sulmont et al., "Process and Apparatus for Measuring the Temperature and the Bath Level of Molten Electrolyte in Aluminum Winning Cells," European patent 07,160,165 (8 July 1998).
10. B. Sulmont et al., "Method and Device for Measuring the Temperature and the Level of the Molten Electrolysis Bath in Cells for Aluminum Production," U.S. patent 6,065,867 (23 May 2000).
11. O.P. Bonnardel and P. Homsi, *Light Metals 1999,* ed. C.E. Bickert (Warrendale, PA: TMS, 1999), pp. 303–309.
12. P. Verstreken, "Method for Monitoring Aluminum Electrolytic Cells," U.S. patent 6,620,309 B2 (September 2003).
13. M. Jensen, *Light Metals 2009,* ed. Geoff Bearne (Warrendale, PA: TMS, 2009), pp. 455–459.
14. M. Jensen, private communication (February 2010).
15. K. Grjotheim and H. Kvande, editors, *Introduction to Aluminum Electrolysis*, 2nd Edition (Düsseldorf, Germany: Aluminum Verlag, 1993).
16. Zeng Shuiping and Wang Junqing, *Proceedings of the 5th World Congress on Intelligent Control and Automation,* (Piscataway, NJ: IEEE, 2004), pp. 3675–3678.
17. O.G.H. Nygaard and K.S. Mylvaganam, "Ultrasonic Time-domain Reflectometry for Level Measurement in Molten Metals," *Technisches Messen 60-1* (Munich, Germany: Oldenburg Verlag, 1993), pp. 4–14.
18. I. Ihara et al., *Proceedings of IEEE Ultrasonic Symposium* (Piscataway, NJ: IEEE, 1998), pp. 803–807.
19. I. Ihara et al., *Proceedings of IEEE Ultrasonic Symposium* (Piscataway, NJ: IEEE, 2004), pp. 541–544.
20. C.-K. Jen, J.-G. Legoux, and L. Parent, *NDT & E International,* 33 (3) (2000), pp. 145–153.
21. Y. Ono et al., *IEEE Transactions on Ultrasonics, Ferroelectrics, and Frequency Control,* 50 (12) (2003), pp. 1711–1721.
22. E. Gran, *Modeling, Identification and Control,* 1 (4) (1980), pp. 247–258.
23. P. Borg et al., *Modeling, Identification and Control,* 7 (1) (1986), pp. 45–56.
24. S. Kolås, "Method and Means for Controlling an Electrolysis Cell," International patent WO 2009/067019 A1 (May 2009).
25. G.A. Gudmundsson, *Light Metals 1999,* ed. C.E. Bickert (Warrendale, PA: TMS, 1999), pp. 297–302.
26. J. Tessier and P. Doiron, *Light Metals 2010,* ed. John A. Johnson (Warrendale, PA: TMS, 2010), pp. 553–558.
27. H. Viumdal et al., "Multi Sensor Data Fusion for Aluminum Cell Health Monitoring and Control" (Paper presented at the TMS 2010 Annual Meeting, Seattle, Washington, February 14–18, 2010).

Håkon Viumdal, Ph.D. student, and Saba Mylvaganam, Professor, Process Measurements and Sensorics, are with Tel-Tek, Kjolnes Ring, Porsgrunn 3918, Norway. Mr. Viumdal can be reached at hakon.viumdal@tel-tek.no.

Paper C

Enhancing Signal to Noise Ratio by Fine-Tuning Tapers of Cladded/Uncladded Buffer Rods in Ultrasonic Time Domain Reflectometry in Smelters *

Enhancing signal to noise ratio by fine-tuning tapers of cladded/uncladded buffer rods in ultrasonic time domain reflectometry in smelters

Håkon Viumdal [a,b,*], Saba Mylvaganam [b]

[a] Tel-Tek, Kjølnes Ring 30, 3918 Porsgrunn, Norway
[b] Telemark University College, Faculty of Technology, Kjølnes Ring 56, 3918 Porsgrunn, Norway

ABSTRACT

Buffer rods (BR) as waveguides in ultrasonic time domain reflectometry (TDR) can somewhat extend the range of industrial applications of ultrasonics. Level, temperature and flow measurements involving elevated temperatures, corrosive fluids and generally harsh environments are some of the applications in which conventional ultrasonic transducers cannot be used directly in contact with the media. In such cases, BRs with some design modifications can make ultrasonic TDR measurements possible with limited success. This paper deals with TDR in conjunction with distance measurements in extremely hot fluids, using conventional ultrasonic transducers in combination with BRs. When using BRs in the ultrasonic measurement systems in extreme temperatures, problems associated with size and the material of the buffer, have to be addressed. The resonant frequency of the transducer and the relative size of the transducer with respect to the diameter of BR are also important parameters influencing the signal to noise ratio (SNR) of the signal processing system used in the ultrasonic TDR. This paper gives an overview of design aspects related to the BRs with special emphasis on tapers and cladding used on BRs. As protective cladding, zirconium oxide–yttrium oxide composite was used, with its proven thermal stability in withstanding temperatures in rocket and jet engines up to 1650 °C. In general a BR should guide the signals through to the medium and from and back to the transducer without excessive attenuation and at the same time not exacerbate the noise in the measurement system. The SNR is the decisive performance indicator to consider in the design of BR based ultrasonic TDR, along with appropriate transducer, with suitable size and operating frequency. This work presents and analyses results from extensive experiments related to fine-tuning both geometry of and signals in cladded/uncladded BRs used in high temperature ultrasonic TDR with focus on overall performance based on measured values of SNR.

© 2013 Elsevier B.V. All rights reserved.

1. Introduction

In several industrial applications, ultrasonic transducers (UT) cannot be directly placed in contact with the process media, due to harsh environments, high temperatures or rough surfaces. By utilizing ultrasonic waveguides in the form of buffer rods (BRs), such challenges may be overcome. In such applications, the BR functions simultaneously as a waveguide and protecting element for the UTs. Fig. 1 illustrates a simplified overview of transducer content, and demonstrates how the system can be arranged to determine interfaces in molten bath.

The demand, and hence the research on techniques for utilizing acoustic transducers in high-temperature environments arose in conjunction with non-destructive material testing in the period of extra-terrestrial travels involving rockets and airships, [1]. Acoustic BRs have successfully been utilized in the detection of small particles in molten metals, e.g. aluminium [2,3], and in detecting the solid–liquid interface in solidification of e.g. molten aluminium [4]. Acoustic BRs in longitudinal, shear and torsional modes, operating as delay lines [5], in staggering dead-bands and other applications are discussed in [6]. Level determination in industrial electrolysis processes using BRs, such as in magnesium and aluminium production facilities, have also been tested [7,8]. Ultrasonic online monitoring during polymer extrusion and curing processes of graphite/epoxy has been used with acoustic BRs [7]. Determination of reliable temperatures up to at least 3000 °C has also been possible by using BRs in combination with UT [1]. Methods for estimating liquid densities from reflection coefficients, using acoustic BRs are described in [9,10]. The BR used in [10] has a rather large diameter to avoid spurious reflections from its
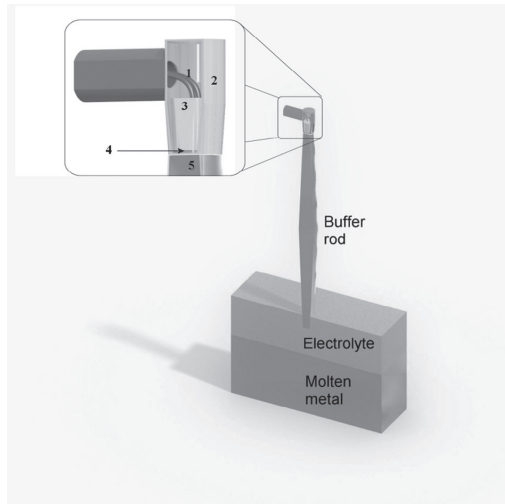

Fig. 1. Schematic drawing of a level measuring application with a transducer connected to a double taper BR immersed into a molten bath, consisting of two different materials or phases. 1 represents the cables, 2 the transducer housing, 3 the backing material, 4 the piezoelectric material and 5 the buffer rod.

Table 1
List of symbols and abbreviations.

Symbol	Quantity	Units
TDR	Time domain reflectometry	
NDT	Nondestructive testing	
UT	Ultrasonic transducer	
BR	Buffer rod	
SNR	Signal to noise ratio	dB
c	Sound velocity	m/s
z	Specific acoustic impedance	Ns/m^3
R	Reflection coefficient	
L	Length of buffer rod	mm
d_{Be}	Diameter of buffer rod end	mm
d_{Bm}	Maximum diameter of buffer rod	mm
θ	Taper angle	°
α	Ultrasonic beam spread angle	°
d_{UT}	Element diameter of transducer	mm
f	Frequency	Hz
A	Relative amplitude of reflected pulse	dB
d_N	Near field distance	m
κ	Thermal conductivity	W/(K m)
σ	Electrical conductivity	S/m
L_N	Lorentz number	Volt^2/K^2
T	Temperature	K

wall and the medium investigated is considerably small to the size of the BR, making this application more suitable for lab based sampling applications. An interesting overview of some of the first applications of ultrasonic BRs is given in [11], where the BR is used to evaluate Young's and Shear moduli and hence Poisson's ratio of materials based on longitudinal and shear wave velocity measurements. In 1965, in nuclear radiation environments, high temperature measurements were performed using BRs based on sound speed dependency on temperatures, [12].

Elasticity measurements in high-temperature applications using BRs for making resonant ultrasound spectroscopy have been reported in [13]. Simultaneous viscosity and temperature measurements in high temperature melts using ultrasonic transducers in combination with BRs is described in [14]. Dispersion phenomena are described in [15] and are exploited to possibly steer the launching direction of ultrasonic waves via a bundle of slender BRs of varying diameters. BRs are used in the measurement of reflection coefficient at interfaces of differing acoustic impedances, density of media, attenuation in the medium of ultrasonic propagation, and as delay lines for signal processing purposes.

The focus in this paper is on the design variations of straight and tapered BRs with and without cladding for improving signal to noise ratio in conjunction with estimating distances and interface levels.

There is a plethora of factors to be considered in the selection of an optimal ultrasonic waveguide for a particular application. The buffer material should match the material of the application, so that the signal is transmitted preferably intact into the actual material. The shape of the BR should match the transducer, and the material of BR should have low attenuation of ultrasonic signals, and facilitate reduction of spurious noise. Finally, the transducer should match the measurement requirements, such as propagation, temporal and not the least, accuracy requirements.

The intended use of the measurement system considered in this study relates to distance measurements and interface detection in conjunction with molten metals. In particular the BRs are designed to detect the level of the interface between two different materials or phases in metallurgical industry, as shown in Fig. 1. A list of symbols and abbreviations used in this paper is given in Table 1.

2. Buffer based ultrasonic TDR

BRs are ultrasonic waveguides used to protect the ultrasonic transducer from corrosive and/or high temperature environments, as in e.g. molten metals. Conventional piezoelectric UT can then be placed on top of the BR with appropriate bonding liquids/pastes, where the temperature is, or can be kept below the critical Curie temperature of the piezoelectric crystal used in the UT [16]. The transducer connected end of the BR might be cooled by cooling pipes wrapped around the BR or by dipping intermittently in the hot fluid, just before the measurements are taken. Nitrogen, water and air are typically used as cooling medium, but water is not allowed to be used in the vicinity of molten metals due to explosion hazard caused by expanding steam.

2.1. Material properties of BRs

In order to achieve consistent high-quality ultrasonic measurements and prevent equipment failure, several properties of the core material of the BR have to be considered, especially in the case of employing these BRs in corrosive environments. In the context of the present study, the physical properties of the BR have been divided into five main groups:

2.1.1. Acoustic properties

The basic acoustic properties to be considered are the acoustic attenuation, the sound velocity c, the specific acoustic impedance z, and the reflection coefficient R. The acoustic attenuation describes wave guiding property within a uniform material, whereas the reflection coefficient describes the reflection of acoustic waves, and hence indirectly the transmission between two materials. Both properties are important in choosing a proper acoustic BR.

As the attenuation of the ultrasonic signal increases with increasing transit distance, the attenuation could be a decisive factor, particularly for longer BRs. However, identifying the source of the attenuation and reducing it and hence the physical modelling of its causes, can be very complex and very often demanding tasks [17]. For metals, the attenuating properties are particularly dependent on the processing method used in the production of the material [18]. The grain size and the casting technique used are essential factors affecting the acoustic guidance property of the BR [19]. However, tabulated values of attenuations for different

metals are generally not readily available. Generally, the attenuation of the signals will increase with increasing frequency of the UT and with increasing grain size of metals. Heat treatment of metals has a great influence on the ultrasonic attenuation. For steel, the quenched material has lower attenuation, compared to the attenuation in overheated structures and the normally annealed structures [19]. Thus even the selection of the type a material within a known group is not trivial.

The VT14 titanium alloy shows an interesting behaviour in the ultrasonic attenuation properties, as its attenuation increases to a maximum about 8.5 dB/cm at ca. 850 °C and then decreases rapidly to about 4.0 dB/cm at ca. 950 °C [20]. Consequently, the attenuation profile as a function of the temperature and frequency should be studied before selecting the BR.

To be able to receive a well-defined reflection at the interface between the two materials or phases as shown in Fig. 1, their acoustic impedances should be different. Contrary to the requirement of difference of acoustic impedances at the interface between the two materials or phases, the specific acoustic impedances of the BR and liquid should have similar values, to reduce this undesired reflection from the tip of the BR to a minimum. Note, that the specific acoustic impedance is a function of temperature, as it is a function of material density and wave velocity, which varies with temperature [20]. Generally, the sound velocity, and hence also the acoustic impedance in metals decrease gradually, with a drop at the melting point, as the temperature is raised, [21]. The drop is due to changes in the bond of the metal structure in the transition process from solid metal to the molten phase.

2.1.2. Wettability and corrosion resistance

Wettability between a solid and a liquid is an indicator describing their mutual coupling property. This property is very much related to the surface tension between the media involved. In an interface between a BR and molten metal with poor wettability, a significant amount of the ultrasonic signals will be reflected. This might occur even though the reflection coefficient between the BR and the molten metal per se might be very low. The wetting performance is closely related to the contact angle [22]. Hence, a small contact angle will correspond to high wettability.

As a general rule, the higher the melting point of the molten metal, the higher the wettability, e.g. the wetting of mercury, lead and tin are very poor, whereas molten zinc and aluminium display increased wetting performance. Both the material properties of the BR and the fluid/molten metal are important to the wetting performance, so the buffer material should be selected so as to match the molten material of interest, regarding wettability [23]. However, there is a trade-off between high wetting properties and corrosion resistance. In corrosive liquids, good wetting of the BR will lead to better contact to the harmful liquid, thus promoting more corrosion.

Generally, applications involving high wetting and corrosion performance have the option of making the measurements very rapidly but intermittently (thus avoiding continuous contact of BR and liquid), whereas applications involving low wettability

materials, and low corrosion, the buffer rod might be used for continuous measurements, when signal amplitudes for TDR are of sufficient quality.

Good wettability implies that good acoustic coupling is established between the BR and a high temperature liquid. Good wettability leads to poor corrosion resistance due to the improved contact between the BR and the high temperature fluid, which is very often very corrosive. One method of alleviating the problem of contradicting performances of BR with respect to wettability and corrosion resistance is to polish the BR to extremely high level of smoothness, which may prevent wetting. The surface of the tip of BR in contact with the hot temperature fluid may additionally be protected by a diamond like carbon coating [24].

For example a clad steel BR, consisting of a steel core and a stainless steel cladding, shows high wettability in molten aluminium at 967 °C (about 300 °C above its melting point) [25]. The measurement duration is limited to less than 30 min due to both the corrosion and also high temperatures of the smelt. However, for acceptable performance of the BR in measurements, filing and machining operation on the BR may be mandatory between each measurement due to frozen metal clinging onto the surface of the BR.

Fig. 2 shows pictures of a titanium BR before and after being immersed into a molten zinc bath for about 15 min at approximately 600 °C. Only after a few minutes, the molten zinc shows good wetting performance, and sticks to the titanium rod. The excellent connection between the bath and the rod, results in a rapid corrosion of the buffer.

2.1.3. Thermal properties

The melting point of a BR should be above the temperature of the molten material. Although some studies refer to the usage of buffers made of the same material as the molten material in TDR measurements [26]. As already described, the temperature may affect the acoustic attenuation. Generally higher attenuation is observed at elevated temperatures particularly close to the melting point.

A BR should be resistant to thermal and mechanical shocks, as the temperature change from air temperature to the molten bath temperature often is huge. The thermal shock resistance is of special importance in applications where the rod is supposed to be intermittently immersed into a molten bath, inducing frequent and rapid temperature changes of the BRs. Ceramics like alumina will easily crack under demanding circumstances with high and rapid temperature variations. Fig. 3 shows an alumina BR that was immersed into a bath with molten zinc at approximately 600 °C. The fragile material structure was not able to withstand the temperature change, although it was preheated in the vicinity of the molten bath.

Regarding Curie temperature of the piezoelectric elements used in UTs, buffer materials with low thermal conductivity are preferable, and might eliminate the need for cumbersome cooling systems, predominantly employing gases such as nitrogen or helium, as water and molten metal comprise a very hazardous pair.
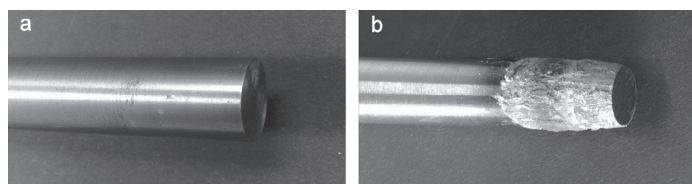

Fig. 2. A titanium buffer rod (a) before and (b) after being immersed into a molten zinc bath at approximately 600 °C for 15 min.
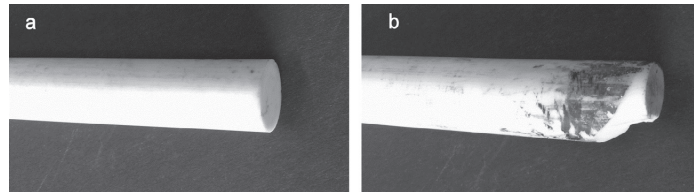
Fig. 3. An alumina buffer rod after (a) before and (b) being immersed into a molten zinc bath at approximately 600 °C.

The buffer geometry will also influence this issue, as BRs with thinner ends show higher thermal resistance than thicker BRs, giving tapered BRs (described in next section) advantages over straight BRs. According to Wiedemann–Franz–Lorenz equation, the thermal conductivity is proportional to the electrical conductivity for metals, [27].

$$\frac{\kappa}{\sigma} = L_N T \tag{1}$$

where κ is the thermal conductivity of the BR material and σ its electrical conductivity at temperature T with L_N being the Lorentz number. Hence, buffer materials with low electrical conductivity are desired for applications with high molten metal bath temperatures. Achieving all these in a single material will be difficult; however one can try to arrive at a compromise.

2.1.4. Microstructure

Any discontinuity in the BR material will lead to attenuation and dispersion and hence distortion of the signal from the UT as well as any reflected signal traversing the length BR. Therefore, the porosity of the core material of BRs should be as small as possible, i.e. small grain size and high homogeneity, in order to avoid trailing echoes (noise) and reduced SNR, [28]. Small grain size and elongated columnar grain structure of the metal achieved in certain processes are reported to reduce the longitudinal attenuation along the columnar grain direction [18,19]. In addition metallic BRs with elongated grain structures in the wave propagation direction have the advantage of enhanced mechanical strength, corrosion resistance and attenuate the shear wave propagation considerably [29], thus suppressing mode conversions too. This is similar and in accordance with results from research on buffer rods formed by a bundle of thin metal wires, where the acoustical signal is considered to be dispersion-free [30]. "The fibre", because of its extremely small diameter (d) to wavelength (λ) ratio ($d/\lambda \ll 1$) will support predominantly only the lowest order longitudinal $L(0,1)$ mode of propagation" [31].

2.1.5. Cladding

Spurious echoes will occur in BRs induced by the wave diffraction and their finite diameters [32]. According to several publications, these spurious echoes will be reduced, and hence the SNR will be improved by adding a cladding layer to metallic BR surfaces [33–35]. The general acoustic wave guidance in the buffer is also improved by the cladding. Especially, BRs with diffused boundaries between core and cladding will gain improved longitudinal wave guidance in the cores.

The microstructure of thermal sprayed cladding is porous, entailing higher ultrasonic loss, lower sound velocity and density. In other words the acoustic impedance is reduced but should be within one order of magnitude of the core material [36]. The thermal sprayed claddings are very dispersive and present attenuating media to ultrasonic waves [29], and thus can have a detrimental impact on the ultrasonic propagation characteristics [37].

Cladding is normally used at the sides of the buffer rods to improve the acoustic signal, but in one example the end of the buffer rod has been successfully coated with Ni, in order to improve the wettability between the stainless steel rod and the molten Pb/Bi alloy [38].

To protect the BR from harsh environments, an additional cladding preventing corrosion, could be added on top of the primary "signal improving" cladding. An environment with highly corrosive and high temperature is the molten cryolite in the aluminium electrolysis cell. In a research study conducted by us, we coated a 50 cm long double taper BR with a 1.5 mm thick zirconium oxide–yttrium oxide layer. The BR was immersed into an aluminium electrolysis cell, 3 times, lasting totally 30 min. Although zirconium oxide–yttrium oxide is a material used in high temperature engines of fighter planes, the zirconium oxide–yttrium oxide cladding on BR was severely corroded in the bath at 970 °C. The BR with the zirconium oxide–yttrium oxide cladding before and after being immersed in the aluminium electrolysis cell is shown in Fig. 4. The zirconium oxide–yttrium oxide cladding BR had damages due to both cracking and corrosion. This demonstrates an extreme industrial environment in which no material yet has been successfully used by immersion for measurement and control purposes. Ideally, a BR needs to have all the combinations of robustness to withstand the extreme demands of the harsh environments, surviving corrosion and extreme temperature swings, and at the same time enabling high SNR performance in conjunction with ultrasonic TDR measurements.

2.2. Transducer specifications

Proper design of a BR and selection of a UT depend on the existing application. Generally, high frequency UTs are best suited
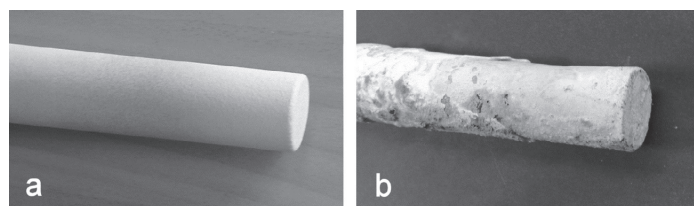

Fig. 4. Titanium buffer rod with zirconium oxide–yttrium oxide cladding before (a) and after (b) immersion into an aluminium electrolysis cell at 970 °C for 15 min.
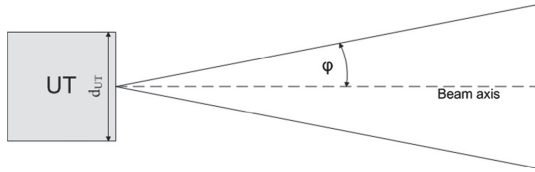
Fig. 5. The −6 dB ultrasonic beam spread angle φ for a flat ended transducer. φ is the beam spread angle.
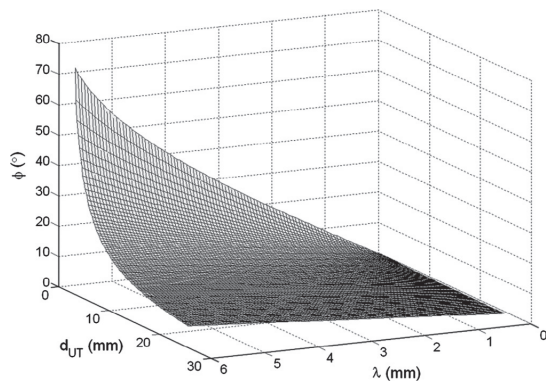

Fig. 6. Beam spread angle φ as functions of wavelength λ and transducer diameter d_{UT}.

for BRs with small diameters, providing mechanical flexibility and high spatial resolutions [26]. The diameter of the UT element, d_{UT}, should be about 75% of the diameter of the BR end connected to the UT, d_{Be}, i.e. buffer end diameter equals approximately the outer UT housing diameter [39]. For shorter BRs it is especially important to consider the extent of the near field, as the buffer end should be located in the far field region, and not in the noisy near field region. The near field distance d_N, which describes the extent of the near field is given by [40]:

$$d_N = \frac{d_{UT}^2 f}{4c} \qquad (2)$$

Ultrasonic beams diverge for all flat ended transducers in the far field. The – 6 dB ultrasonic beam spread angle φ in the far field region shown in Fig. 5 is given by [41]:

$$\varphi = \sin^{-1}\left(0.7\frac{c}{f \cdot d_{UT}}\right) = \sin^{-1}\left(0.7\frac{\lambda}{d_{UT}}\right) \qquad (3)$$

where c is the sound velocity in the medium, f the UT frequency and d_{UT} the diameter of the piezoelectric element.

Due to the relationship $c = f \lambda$, the above equation implies that the beam spread is proportional to λ, and hence small beam spread is achieved for UT with high frequency and large element diameters (Fig. 6). These characteristics are useful in reducing the trailing echoes, but on the other hand, using high frequency signals increase their attenuation in the BR, and large transducer diameters will need larger BR diameters.

A good acoustic coupling between the transducer and the BR is crucial to achieve good SNR of the received signal. Thin gold foils are also well suited for high temperature applications, [42–44]. Ordinary propylene glycol couplant can be used, but silicone oil is more suitable for high temperature applications as it evaporates less in hot environments. This is one of the major problems in high

temperature applications of BR based ultrasonic TDR. Diffusion bonding technology has been used successfully, e.g. with gold-to-gold diffusion technology to bond piezoelectric transducers to BR and/or backing [24].

The introduction of integrated ultrasonic transducers provides an exceptional coupling between the transducer and the BR, as the piezoelectric material has been coated or deposited directly onto one end of the BR [45].

Previous research has demonstrated improved SNR by increasing the UT frequency from 5 MHz to 20 MHz, but the geometrical properties of the BR was then not considered, [28]. Increased SNR is explained by reduced diffraction and mode conversion for high frequency UT, compared to low frequency UT, with reduced trailing echoes. According to our experience smaller BRs are more suitable for transducers with higher resonant frequencies, whereas for larger BRs it is beneficial to use transducers with lower resonant frequencies. Consequently, the BRs may be considered as band-pass filters. Selection of the operating frequency depends on the lateral and longitudinal dimensions of the buffer. Generally, increased frequencies will improve the accuracy of the distance measurements, at the expense of increased attenuation of the ultrasonic signal. Reducing the operating frequency will have the opposite effect.

The diameter to wavelength ratio in BRs has been studied in conjunction with BR based ultrasonic studies, according to which the value of d/λ at the launching end of the BR has significant effect on the propagation characteristics and mode conversions. As already described, small fibres show dispersion-free wave-guiding properties, because of its extremely small diameter (d) to wavelength (λ) ratio ($d/\lambda \ll 1$) will support predominantly only the lowest order longitudinal $L(0,1)$ mode of propagation" [31,46].

2.3. Geometry

The directly reflected echo at the buffer end, generated by the longitudinal wave along the cylinder shaped BR axis, is trailed by pulses, called trailing pulses or trailing echoes. Those echoes will always arrive later than the desired echoes. Fig. 7 shows an example of trailing echoes resulting from a measurement made with a 305 mm long cylindrical steel rod with diameter 19.6 mm, using a 10 MHz transducer with element diameter 12.7 mm. The rod had a 0.7 mm thick arc sprayed steel cladding, to increase the wave guiding performance.

Reduced noise can generally be achieved by increasing the diameter of the rod or shorten its length, as noise is generated at the solid/air interface at the sides of the BR. The thinner and longer the BR is, more will be the effects from wall reflections. The
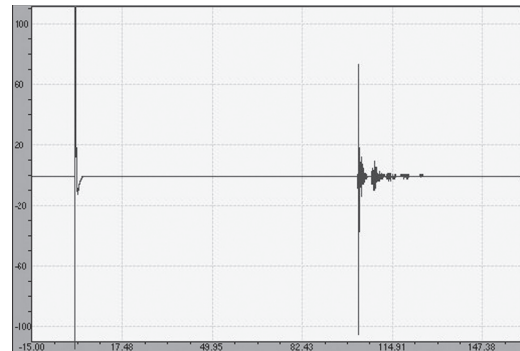
Fig. 7. Waveform from a cylindrical rod, illustrating trailing echoes.
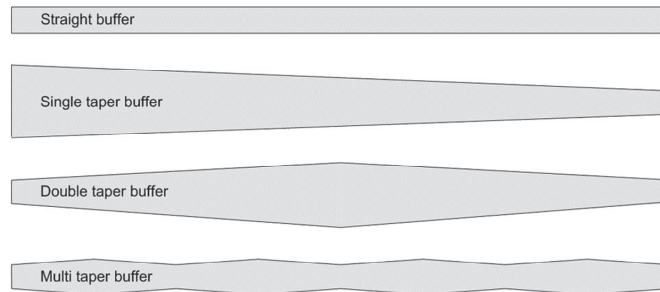
Fig. 8. BRs with straight, single and multi-tapers.
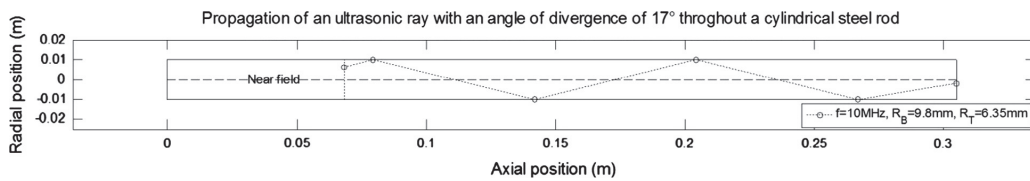
Fig. 9. Propagation of ultrasonic wave along cylindrical BR showing the path of a trailing pulse.

exception is the bundle of metal wires already described in Section 2.1.4, where the diameter of each wire is small compared to the wavelength of the acoustic wave. Hence, the dispersion of the internal wave will be minimised.

A screw thread groove along the rod axis has been reported to be an effective option to reduce the trailing echoes [47], predominantly generated at the buffer wall. Also rods with a graded velocity profile, ideally parabolic, through the cross section of the rod, are claimed to reduce the trailing echoes. The velocity along the centre line of the rod should have the smallest value [48]. This buffer design provides a more focused acoustic wave at the buffer end. The graded velocity profile is achieved by using different dopants.

Earlier studies have shown an improved SNR for tapered BRs compared to straight cylindrical BRs as shown in Fig. 8 [48]. The improvement is explained by an enhanced distribution of the trailing echoes, so that the mode converted waves from the buffer surface would not be in phase, as is the case in the straight cylindrical BRs.

Measurements for the cylindrical BR considered in Fig. 7 show that the total time of flight for the main pulse is 102.0 μs, whereas the 1st trailing pulse is returned to the transducer after 106.9 μs. Assuming a uniform material, this delay is due to the ultrasonic ray angle of divergence of the trailing pulse, as seen in Fig. 9. Neglecting the near field and the mode conversion, the length of its ray path is given by

$$l = \frac{x}{\cos \alpha},$$

where x is the distance traveled by the pulse traveling along the BR axis and α the angle of divergence of the trailing pulse.

Using this formula, the divergence angle of the trailing pulse is found to be approximately 17°. This is much higher than the divergence angle of the −6 dB ultrasonic beam calculated to be 1.9°, indicating that the trailing echo has its origin from a side lobe. This explanation is in accordance with the fact that the transducers with high diameter to wavelength ratios decreases the angle of divergence, and increases the side lobes [49]. In this application the ratio $\frac{d_{ut}}{\lambda} \approx 21$.

For a BR with length, $L = 65$ mm, increasing tapering angles θ shown in Fig. 10, are claimed to increase the SNR. Tapering angles up to 1.5° are recommended for convenience, to keep the rod diameter at an expedient size [37].

In our studies several different 50 cm long double tapered titanium BRs have been tested and compared. Table 2 shows the geometrical details of 3 of them, whereas Fig. 11 presents the signal waveforms in these BRs.

For this particular setup the SNR in the BR of the larger taper angle (1.7°), i.e. BR2, is poor compared to that of the BRs with smaller taper angle (0.9°), i.e. BR1 and BR3, which is the opposite of what has been reported in [37]. However, we have performed measurements of three other different 50 cm long double tapered titanium BRs, but with end diameter 25.4 mm, that are supporting the findings made in [37], indicating that other geometrical variables also have to be taken into account when selecting the taper angle to optimise the SNR.

Although all the measurements in Fig. 11 were made with the same transducer, and identical BR length and material, the waveforms are significantly different. The waveforms from BR1 and BR3 indicate wave-guiding performance with high SNR. The waveform from BR2 is much more distorted by noise. In order to understand why these variations between BRs occur, the buffer wall
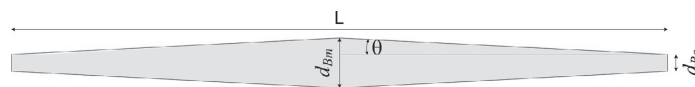
Fig. 10. Schematic drawing of a BR with symmetrical double taper with angle θ. Taper angle affects SNR of received signals.

Table 2
Tuning BR geometry: double tapered titanium BR used in the experiment.

Label	Length, L (mm)	End diameter, d_{Be} (mm)	Max. diameter, d_{Bm} (mm)	Taper angle, α (°)
BR1	500	8.9	16.8	0.9
BR2	500	8.9	23.7	1.7
BR3	500	17.8	25.7	0.9

reflections and the ensuing propagation of the −6 dB half-angle of divergence rays within the three BRs are shown in Fig. 12.

The initial −6 dB of divergence ray in these simulations are based upon the calculation of the diverging angle considered in the former subsection. With longitudinal velocity in titanium of 6100 m/s and the ultrasonic propagational characteristics given earlier, the initial beam angle of divergence in our simulations is about 7.7°.

Only the longitudinal waves are taken into consideration in these simulations. According to Arenberg [5] the amplitude of the mode converted rays are very small in these examples with angles of incidence close to 90°. Fig. 13 shows how the relative

amplitude of both the reflected longitudinal and the mode converted shear rays are affected by the angle of longitudinal incident rays. The calculations are based on the theory of Arenberg, with $\sigma = 0,323$ as the Poisson's ratio of titanium.

The double tapered BR can be considered as two parts as shown in Fig. 14, the 1st part with increasing diameter, and the 2nd part with decreasing diameter. It can be proven that the angle of ray divergence, due to the buffer wall reflections, for the 1st part and the 2nd part of the BR, respectively, are given by,

$$\alpha_{k+1} = \begin{cases} |\alpha_1 - 2k\theta| & k \in [1 \quad 2 \quad m] \\ |\alpha_{m+1} + 2k\theta| & k \in [1 \quad 2 \quad n] \end{cases} \quad \forall \; \theta > \alpha_i$$

θ is the taper angle of the BR, and α_i is the angle of divergence of the ultrasonic ray. m and n indicate the number of reflections in the 1st and 2nd part of the BR, respectively.

For taper angles $\theta > 0$, the ith angle of divergence of the ultrasonic ray will be reduced by twice the taper angle of the buffer rod at each wall reflection in the 1st part of the BR. In the 2nd part of the BR the diverging angle of the ultrasonic beam will increase by twice the taper angle of the buffer rod at each wall reflection. Hence, the taper angle possesses the characteristic of correcting
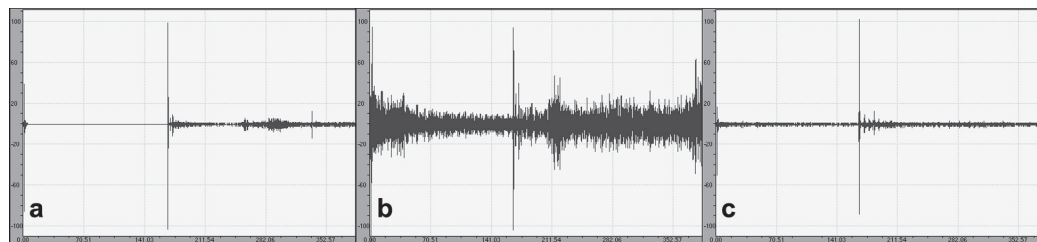
Fig. 11. Signal trains for three different 50 cm long titanium double taper BRs: (a) BR1, (b) BR2 and (c) BR3. Evident degradation of SNR due to internal reflections and possible mode conversions. Signal excitation at 5 MHz. Transducer diameter 6.35 mm.
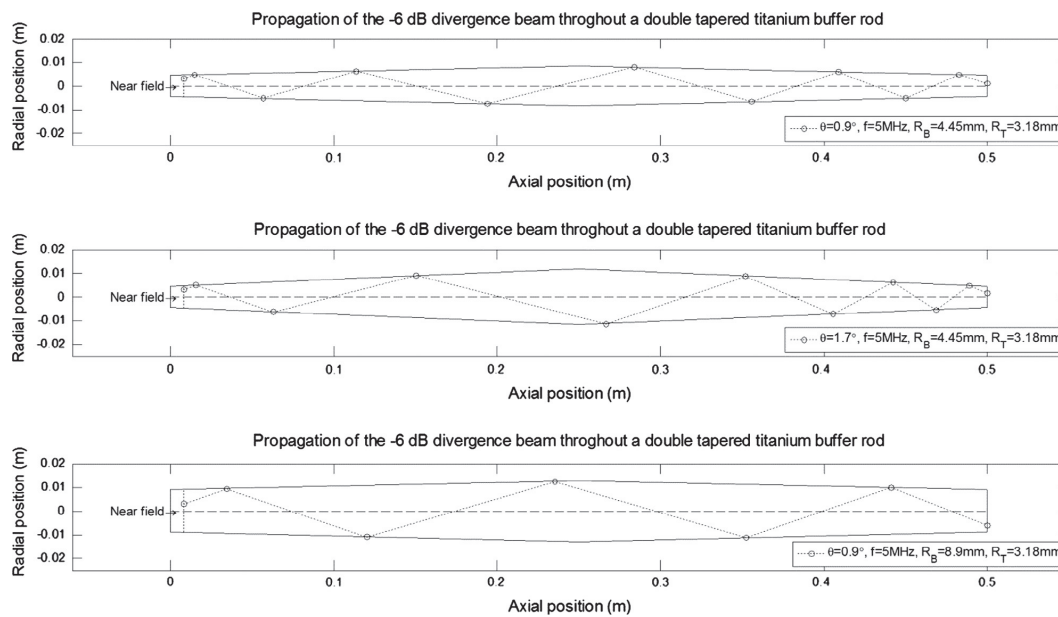
Fig. 12. The propagation of the −6 dB diverging ultrasonic ray in BR1, BR2 and BR3, respectively, all generated by the same 5 MHz transducer.
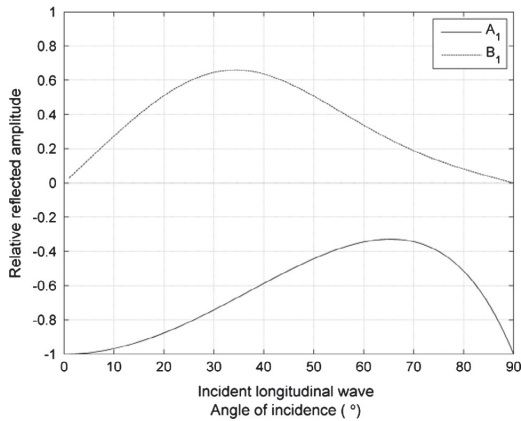
Fig. 13. Relative reflected amplitudes of both the reflected longitudinal (A_1) and the mode converted shear rays (B_1) as functions of the angle of incidence of the longitudinal ray.

the angle of divergence of the diverging ultrasonic ray. The larger the θ more rapidly the angle of divergence α_i is reduced at each reflection, but if the initial angle of divergence is small and the taper angle large, the correction of the divergence angle could be excessive, i.e. the divergence angle will not converge towards 0 in the 1st part of the BR. In such cases a smaller taper angle is more beneficial by tuning the diverging angle in smaller steps, making the diverging angle converge towards 0.

If the taper angle of the BR is zero, i.e. a cylindrical BR, the second angle of divergence will be equal to the first; $\alpha_2 = \alpha_1$, hence the divergence will never be reduced toward zero as with a tapered

BR. The reflections will then be in phase and give rise to the undesired trailing echoes.

Ideally the 1st part of the BR, should be able to reduce the diverging angle of the main part of the ultrasonic signal towards zero, or even provide a small converging angle toward the buffer end. In that case there would be no reflections in the 2nd part of the BR, and the ultrasonic wave would become more focused.

As the main part of the ultrasonic wave is propagating with an initial angle of divergence that is considerably smaller than the −6 dB half-angle of divergence, three additional plots from simulations are given in Fig. 15, all with an initial angle of divergence of 1.5°. The final diverging angles of the ultrasonic rays at the buffer end are then 2.1°, 8.3° and 3.3°, for BR1, BR2, and BR3, respectively. BR2 (with taper angle 1.7°) is not able to correct the ultrasonic ray in the first part of the BR, hence only the second part of the BR will affect the beam propagation, i.e. increasing the diverging angle of the ultrasonic beam. Also in BR3, no reflection is observed in the left part of BR for the particular ray given in Fig. 15, but as the taper angle is only 0.9°, the reflected ray is converging much less than the ray in BR2.

For these three long and thin BRs that have been compared here, smaller taper angles are preferred with respect to high SNR, although the opposite is the case for thicker versions of the same rods, particularly if simultaneously increasing the diameter of the UT.

Using multi-tapered BRs is an option, if long BRs with large taper angles are inconvenient [36]. The taper shape is then divided into smaller sections, avoiding very large and inconveniently large diameters of the rod, compared to single or double taper shaped rods. It can be compared to the advantage a Fresnel prism has over a convenient optical prism with respect to the physical size of the prism. Our experiments show that the SNRs are similar for a double tapered and a multi tapered titanium BR, with identical length (50 cm), taper angle (1.7°), end diameter (17.8 mm), and
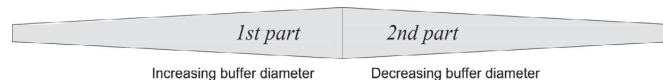
Fig. 14. The double tapered BR considered as two parts.
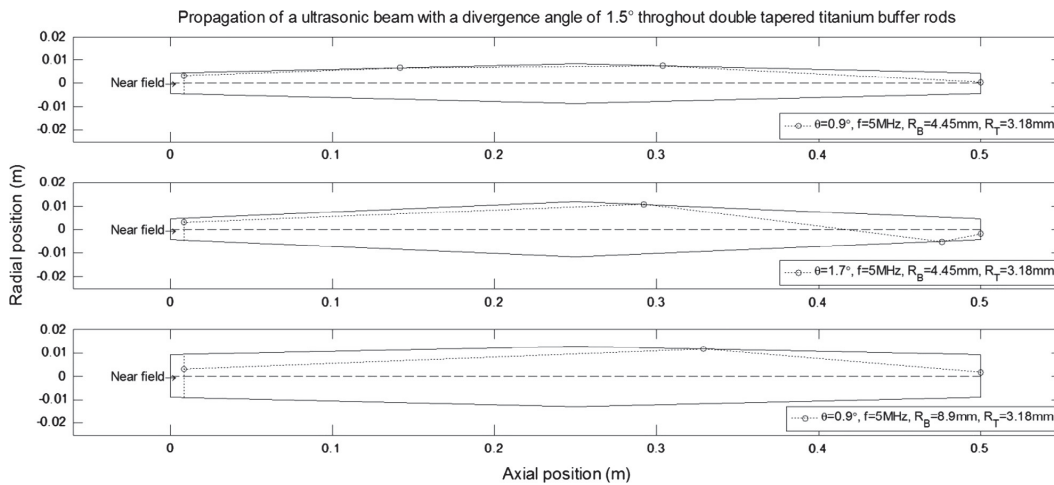
Fig. 15. The propagation of a diverging ultrasonic ray with initial angle of 1.5° in BR1, BR2 and BR3, respectively, all generated by the same 5 MHz transducer.

Table 3
A short overview of BR material considered in aluminium electrolysis cells.

Material	Corrosiveness	Wetting	Attenuation	Cracking ability
Steel[a]	Medium	Medium	Low	Low
Stainless steel	Medium	Medium	Low	Low
Steel with steel cladding	Medium	Medium	Low	Low
Titanium with zirconium oxide cladding	Medium	Medium	Low	Medium
Alumina	Low	Low	High	High

[a] Steel has a disadvantage due to the high magnetic field in and around the surroundings of aluminium electrolysis cells.
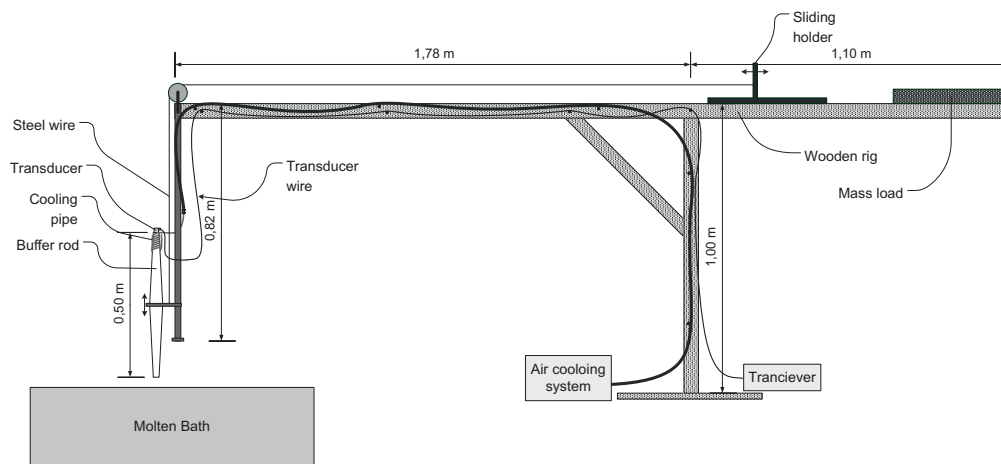
Fig. 16. The actual equipment setup with ultrasonic and laser sensors mounted on wooden rig used for measurements in aluminium smelters. Wooden rig mandatory for use in environment in and around electrolysis cells.

transducer specifications. To maximize the SNR, the diameter of the smaller end of the tapered BR is set to larger than or equal to 3 ultrasonic wavelengths [36].

3. Ideal BR for ultrasonic TDR in corrosive and high-temperature environments

From the studies conducted so far by many other researchers and us, a practically useful BR with long-life for ultrasonic TDR in corrosive and high-temperature environments is still elusive. Some aspects of the application environment limits its performance either by eroding the material of the BR (i.e. including any protective or signal enhancing cladding) or by exacerbating the SNR performance. Ideally, the BR should be able to withstand the environmental effects such as corrosion, temperature related material damages such as cracking, and non-homogenous expansions/contractions, and at the same time be able to guide the ultrasonic wave without much attenuation or distortion with sufficient SNR for detection purposes. This entails matching of acoustic characteristics for TDR performance, material characteristics to match the environmental impacts and of course all of these within acceptable price range. The BR based system should also be handy to use with no implications to the health and safety issues related to the industries. As an example, Table 3 shows some aspects related to these issues as applicable to aluminium smelters, based on our own experience. The actual setup used for measurements in aluminium smelters is shown in Fig. 16. Due to safety reasons, the rig was made of wood, and an air cooling system in combination with intermittent measurement provided sufficient low temperature for the UTs. Measurements of the SNR and the distance

were performed using Olympus epoch 1000i transceiver in combination with BRs as shown in Fig. 17. The figure entails an overview of the most essential steps in the signal path when studying the SNR.

Tables 4 and 5 gives an overview over titanium BRs and ultrasonic transducers used in our R&D work, which also looked into many other BRs made out of various materials. The frequencies
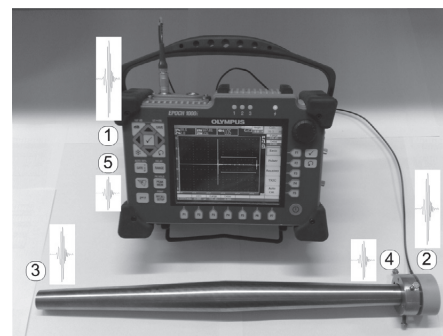
Fig. 17. The signal-path for the experimental set-up: (1) an electrical pulse is generated, (2) the electrical pulse is transformed into an acoustic pulse in the UT, (3) the acoustic pulse is reflected at the buffer/air interface, (4) the reflected acoustic pulse is transformed into an electrical pulse in the transducer, and (5) the electrical signal is received and displayed by the receiver. Equipment used is Olympus ECHO 1000i.

Table 4
Titanium BRS used in our research.

Label	Length, L (mm)	End diameter, d_{Be} (mm)	Max. diameter, d_{Bm} (mm)	Taper angle, α (°)
R1	500	8.9	16.8	0.9
R2	500	8.9	20.2	1.3
R3	500	8.9	23.7	1.7
R4	500	17.8	25.7	0.9
R5	500	17.8	29.1	1.3
R6	500	17.8	32.6	1.7
R7	500	25.4	33.3	0.9
R8	500	25.4	36.7	1.3
R9	500	25.4	40.2	1.7
R10	500	17.8	25.2	1.7

Table 5
Ultrasonic transducers used in the experiments. Based on data, courtesy of Olympus NDT.

Label	Type	Element diameter (mm)	Labeled frequency (MHz)	Peak frequency (MHz)	Centre frequency (MHz)	−6 dB bandwidth (%)
UT1	V	6.35	5	6.2	6.2	93.1
UT2	A	6.35	5	4.6	5.1	84.1
UT3	V	6.35	10	9.6	9.3	101.9
UT4	A	6.35	10	8.8	9.4	57.1
UT5	V	12.7	5	4.9	4.9	71.3
UT6	A	12.7	5	5.9	5.8	36.7
UT7	V	12.7	10	8.2	8.5	73.6
UT8	A	12.7	10	7.2	9.0	85.0
UT9	V	19.1	5	4.7	4.3	86.0
UT10	A	19.1	5	4.0	4.8	70.8

used are somewhat limited by the range of frequencies offered by the vendors.

Further improvement of the SNR and the accuracy of measurements can be achieved by cross-correlation function or other algorithms used to isolate the desired reflection from the noise. These matters will not be further treated in the present paper, but some of the related topics are covered in [8] and [50–53].

4. Conclusion

In this paper important aspects of characterization and selection of BRs for different industrial applications of ultrasonic TDR, including those with hot fluids such as molten metals, are discussed. The wave-guiding properties of the BR can be exploited by optimising the SNR at the receiver of the ultrasonic TDR measurement system used.

A cross-disciplinary approach addressing many factors has to be used in order to obtain sufficient amplitude level of the received signal. The transducer/BR interface has to be smooth and in good contact to each other, with a coupling medium (such as ultrasonic coupling gel or gold foil) between their surfaces. There should also be proper wetting between the BR and the hot fluid. The user has to trade-off between wetting ability and corrosion reduction, when operating the BR in corrosive fluids. The core material of BR and its microstructure have also considerable impact on both the signal amplitude and the SNR. Small grain size and elongated columnar grain structure along the wave direction reduce the longitudinal attenuation within the rod. These features have to be available in the BRs selected.

According to several publications, the geometrical parameters of the BRs have a decisive impact on the SNR. Straight cylindrical rods have a tendency of generating dispersion and mode conversion at the buffer wall, which are superimposed on what are often

called as trailing echoes, and hence distort the reflected signal. By introducing a small tapered angle of the rods, the mode conversions at the wall will not be in phase, hence the trailing echoes will be drastically reduced, and hence the SNR will be improved. By including double or multi- tapered BRs, the size of the BR can be kept to convenient level for usage in industrial settings. Further improvements in the SNR have been demonstrated by adding a cladding on the buffer rod wall.

To provide an efficient protection for the UT against high temperature, corrosion and harsh environments, the BRs need to have sufficient length thus making the attenuation an important variable to consider in the selection of BRs of right lengths and materials. If the internal attenuation in the BR makes long BRs difficult to use, a shorter BR in combination with a cooling device could be a suitable alternative. In very hot fluids, it could be necessary to install cooling features such as continuously flowing cool gases even on long BRs. The measurement system can be protected in addition by employing measurement cycles based on intermittent measurements.

The BRs can be considered as band-pass filters, where the BRs with the largest diameter have lower centre frequencies and the thinner variants of BRs work at a higher centre frequencies. By testing some BRs with potentially robust cladding materials and incorporating some design modifications in the formation of BR tapers, this paper gives a summary and overview of tackling some aspects of BR based ultrasonic TDR in interface detection and level measurements as encountered in industries dealing with molten metals.

References

[1] E.H. Carnevale, Acoustic techniques and applications at elevated temperatures, in Nasa, Electron. Res. Centre Aerospace Meas. Tech. (1967) 73–103.
[2] I. Ihara, H. Aso, D. Burhan, In-situ observation of alumina particles in molten aluminum using a focused ultrasonic sensor, JSME Int. J. Ser. A 47 (3) (2004) 280–286.
[3] Y. Ono, J.F. Moisan, C.K. Jen, Ultrasonic techniques for imaging and measurements in molten aluminium, IEEE Trans. Ultrason. Ferroelectr. Freq. Control 50 (2003) 1711–1721.
[4] I. Ihara, D. Burhan, Y. Seda, Ultrasonic sensing of solid-liquid interface during directional solidification of aluminum, in: 1st International Conf. on Sensing Technology, New Zealand, 2005, pp. 626–631.
[5] D.L. Arenberg, Ultrasonic solid delay lines, J. Acoust. Soc. Am. 20 (1) (1948) 1–26.
[6] L.C. Lynnworth, Slender Specimens in: Ultrasonic Measurements for Process Control – Theory Techniques, Applications, Academic Press, 1989. pp. 542–557.
[7] C.K. Jen, J.Y. Chen, S.V. Hoa, K.T. Nguyen, J.G. Legoux, H. Hebert, Clad buffer rods for in-situ process monitoring, in: IEEE Ultrasonics Symposium, Proceedings, 1997, pp. 801–806.

[8] O.G.H. Nygaard, K.S. Mylvaganam, Ultrasonic time-domain reflectometry for level measurements in molten metals, Tech. Mess. 60 (1993) 4–14.
[9] E. Bjørndal, K.E. Frøysa, S.A. Engseth, A novel approach to acoustic liquid density measurements using a buffer rod based measuring cell, IEEE Trans. Ultrason. Ferroelectr. Freq. Control 55 (8) (2008) 1794–1808.
[10] E. Bjørndal, K.E. Frøysa, Acoustic methods for obtaining the pressure reflection coefficient from a buffer rod based measurement cell, IEEE Trans. Ultrason. Ferroelectr. Freq. Control 55 (8) (2008) 1781–1793.
[11] L. Lynnworth, Bundle buffer measures flow at temperature extremes, Flow Control Mag. XIII (3) (2007) 36–43.
[12] E.H. Carnevale, L.C. Lynnworth, G.S. Larson, High temperature measuring device, NASA CR-54339, CONTRACT NAS 3–5201, February 1 1965.
[13] G. Li, J.R. Gladden, High temperature resonant ultrasound spectroscopy: a review, Int. J. Spectrosc. 2010 Article ID 206362 (2010) 1–13, http://dx.doi.org/10.1155/2010/206362.
[14] V.S.K. Prasada, Krishnan Balasubramaniama, Elankumaran Kannana, K.L. Geisingerb, Viscosity measurements of melts at high temperatures using ultrasonic guided waves, J. Mater. Process. Technol. 207 (2008) 315–320. 10.1016/j.jmatprotec.2008.06.049.
[15] L.C. Lynnworth, Y. Liu, J.A. Umina, Extensional bundle waveguide techniques for measuring flow of hot fluids, IEEE Trans. Ultrason. Ferroelectr. Freq. Control 52 (4) (2005) 538–544.
[16] A. McNab, K.J. Kirk, A. Cochran, Ultrasonic transducers for high temperature applications, IEE Proc. Sci., Meas. Technol. 145 (5) (1998) 229–236.
[17] L.W. Schmerr Jr., S.J. Song, Ultrasonic attenuation, in Ultrasonic Nondestructive Evaluation Systems, ISBN 978-0-387-49061-8, Springer Verlag, 2007, pp. 525–529.
[18] C.K. Jen, H. Soda, Y.S. Liu, C. Neron, A. Ohno, A. McLean, Acoustic characterization of metals with columnar grains, Ultrasonics 33 (3) (1995) 181–186.
[19] L.C. Lynnworth, Scope of applications, in Ultrasonic Measurements for Process Control – Theory, Techniques, Applications, Academic Press, Ch. 2 Sec. 6.3 (1989) 75–76.
[20] A. Kumar, T. Jayakumar, B. Raj, K.K. Ray, Characterization of solutionizing behavior in VT14 titanium alloy using ultrasonic velocity and attenuation measurements, Mater. Sci. Eng. 360 (2003) 58–64.
[21] R.L. Parker, J.R. Manning, N.C. Peterson, Application of pulse-echo ultrasonics to locate the solid/liquid interface during solidification and melting of steel and other metals, J. Appl. Phys. 58 (1985) 4150–4164.
[22] P. Atkins, J. De Paula, Molecular interactions, in Atkins' Physical Chemistry, 8th ed. Oxford University Press Part 2 Ch. 18 (2006) 620–645.
[23] M. Dionne, G. L'Espérance, A. Mirtchi, Wetting of TiB2-carbon material composite light metals (1999) 389–394.
[24] R. Kazys, A. Voleisis, R. Sliteris, B. Voleisiene, L. Mazeika, P.H. Kupschus, H. Aït Abderrahim, Development of ultrasonic sensors for operation in a heavy liquid metal, IEEE Sens. J. 6 (5) (2006) 1134–1143.
[25] C.K. Jen, K.T. Nguyen, J.G. Legoux, I. Ihara, H. Hébert, Novel clad ultrasonic buffer rods for the monitoring of industrial materials processing, in: 1st Pan American Conference for Nondestructive Testing, vol. 4, no. 4, 1999, pp. 16–20, <www.NDT.net>.
[26] N.D.G. Mountford, Testing of liquid melts and probes for use in such testing U.S. Patent 4 981045, 1991.
[27] R.B. Bird, W.E. Stewart, E.N. Lightfoot, Thermal conductivity of solids, in Transport Phenomena, 2nd ed., John Wiley & Sons (2007) 280–281.
[28] J. Voyer, B.R. Marple, C.K. Jen, Plasma-sprayed ceramic coatings for ultrasonic wave guidance in severe environments, in: Proceedings of the United Thermal Spray Conference, German Welding Society, Düsseldorf, Germany, 1999, pp. 630–635.
[29] J.G. Legoux, C.K. Jen, Ultrasonic applications of thick metallic coatings, The 9th Nat'l Thermal Spray Conf., 1996, pp. 65–72.
[30] L.C. Lynnworth, Y. Liu, J.A. Umina, Extensional bundle waveguide techniques for measuring flow of hot fluids, IEEE Trans. Ultrason. Ferroelectr. Freq. Control 52 (4) (2005) 538–544.
[31] I.L. Gelles, Optical-fiber ultrasonic delay lines, J. Acoust. Soc. Am. 39 (1966) 1111–1119.
[32] C.K. Jen, J.G. Legoux, High performance clad metallic buffer rods, Proc IEEE Ultrason. Symp. (1996) 771–776.
[33] C.K. Jen, Z. Wang, C. Neron, A. Miri, K. Abe, Tapered acoustic buffer rods, Electron. Lett. 27 (20) (1991) 1877–1879, http://dx.doi.org/10.1049/el:19911164.
[34] C.K. Jen, I. Ihara, Clad buffer rod sensors for liquid metals, Adv. Sens. Met. Proc. Conf. (1999) 275–285.
[35] C.K. Jen, K.T. Nguyen, J.G. Legoux, I. Ihara, H. Hébert, Novel clad ultrasonic buffer rods for the monitoring of industrial materials processing, in: Proceedings of the 1st Pan American Conference for Nondestructive Testing, 1998.
[36] C.K. Jen, J.G. Legoux, Clad ultrasonic waveguides with reduced trailing echoes, U.S. Patent 5828274, 1998.
[37] I. Ihara, C.K. Jen, D.R. Franca, Materials evaluation in molten metal using focused ultrasonic sensors: application to molten zinc, ATM 3 (2001) 45–50.
[38] R. Kažys, A. Voleišis, L. Mazeika, R. Sliteris, R. Van Nieuwenhove, P. Kupschus, H.A. Abderrabim, Investigation of ultrasonic properties of a liquid metal used as a coolant in accelerator driven reactors, Proc. IEEE Ultrason. Symp. 1 (2002) 815–818.
[39] H. Viumdal, K.-T. Wu, S. Mylvaganam, Dependency of signal to noise ratio on transducer diameter in guided wave time domain reflectometry, IEEE Int. Ultrason. Symp. (2011) 2142–2145.
[40] Olympus, Ultrasonic Transducers Technical Notes, 2011, pp. 41–49, <http://www.olympus-ims.com/en/panametrics-ndt-ultrasonic/pdf/>.
[41] P.A. Meyer and J.W. Anderson, Ultrasonic testing using phased arrays, in: Proceedings, 15th World Conference on, Non-Destructive Testing, October 2000 in Rome, pp. 15–21.
[42] R. Kažys, A. Voleišis, R. Sliteris, L. Mazeika, R. Van Nieuwenhove, P. Kupschus, Hamid Ait Abderrahim, High temperature ultrasonic transducers for imaging and measurements in a liquid Pb/Bi eutectic alloy, IEEE Trans. Ultrason. Ferroelectr. Freq. Control 52 (4) (2005) 525–537, http://dx.doi.org/10.1109/TUFFC.2005.1428033.
[43] J.R. Frederick, A study of the elastic properties of various solids by means of ultrasonic pulse techniques, Ph.D. Dissertation, University of Michigan, 1947.
[44] L.Y. Tu, J.N. Brennan, J.A. Sauer, Dispersion of ultrasonic pulse velocity in cylindrical rods', J. Acoust. Soc. Am. 27 (3) (1955) 550–555, http://dx.doi.org/10.1121/1.1907961.
[45] M. Kobayashi, C.-K. Jen, J.F. Bussiere, K.-T. Wu, High-temperature integrated and flexible ultrasonic transducers for nondestructive testing, NDTE Int. 42 (2009) 157–161.
[46] Lawrence C. Lynnworth, Marginally dispersive waveguides, United States Patent, Patent Nr. 5,159,838, Nov. 3, 1992.
[47] H.J. McSkimin, Measurement of ultrasonic wave velocities and elastic moduli for small solid speciemens at high temperatures, J. Acoust. Soc. Am. 31 (1959) 287–295, http://dx.doi.org/10.1121/1.1907714.
[48] C.K. Jen, Acoustic waveguides having a varying velocity distribution with reduced trailing echoes U.S. Patent 5 241 287, 1993.
[49] J.L. Rose, Ultrasonic waves in solid media, Cambridge University Press, 1999, pp. 346–354, ISBN 0 521 54889 6.
[50] S. Hirata, M.K. Kurosawa, T. Katagiri, Accuracy and resolution of ultrasonic distance measurement with high-time-resolution cross-correlation function obtained by single-bit signal processing, Acoust. Sci. Technol. 30 (2009) 429–438.
[51] J. Saniie, E. Oruklu, Analysis and synthesis of frequency diverse ultrasonic flaw detection system using order statistics and neural networks, in: Kentaro Nakamura, Sadayuki Ueha (Ed.), Ultrasonic Transducers: Materials Design and Applications, Woodhead Publishing Limited, ISBN: 9781845699895, October 2012.
[52] A. Kasaeifard, J. Saniie and E. Oruklu, A computationally efficient algorithm for ultrasonic signal decomposition and flaw detection, IEEE Ultrasonics Symposium, October 2011.
[53] R. Vicen, R. Gil, P. Jarabo, M. Rosa, F. López, D. Martínez, Non-linear filtering of ultrasonic signals using neural networks, Ultrasonics 42 (2004) 355–360.

Paper D

Dependency of Signal to Noise Ratio on Transducer Diameter and Buffer Diameter in Guided Wave Time Domain Reflectometry [*]

Dependency of Signal to Noise Ratio on Transducer Diameter and Buffer Diameter in Guided Wave Time Domain Reflectometry

Håkon Viumdal and Saba Mylvaganam
Faculty of Technology
Telemark University College and Tel-Tek
Porsgrunn, Norway

Kuo-Ting Wu
Industrial Materials Institute
National Research Council Canada
Montreal, Quebec, Canada

Abstract— **The use of waveguides or buffer rods (BR) is well known in performing Non-Destructive Testing (NDT) with ultrasonic or generally in high-temperature ultrasonic time domain reflectometry (TDR). However, determining optimal geometrical shapes of these buffers and parameters of the ultrasonic transducers are not straightforward. In this paper the signal to noise ratio (SNR) achieved with different combinations of buffer diameters and transducer diameters are considered based mainly on experiments and on some dedicated simulations. Experimental results show large variations of the SNR as the ratio between the transducer and the buffer rod diameter varies. Corresponding simulated results are less influenced by such variations in the ratio of diameters considered, showing possible limitations of these simulations.**

Keywords-component; Acoustic wave guides, Signal to noise ratio, Geometrical aspects, transducer, buffer/waveguide

I. INTRODUCTION

In hot and harsh industrial environments, commonly used ordinary ultrasonic transducers (UT) cannot be used and their applications in such environments are severely restricted. If the operating temperature is close to the Curie temperature of the UT, the lifetime of the UT is significantly reduced. During recent research new piezoelectric materials for high temperature application have been developed, e.g. as described in [1], but extreme temperatures and inherent corrosive media in some processes still render applications of these devices difficult or even impossible for direct contact measurements.

By using ultrasonic waveguides, also called buffer rods (BR), the operating temperature of the UT might be considerably reduced, compared to the temperature of the substance of interest, as the temperature at the BR end connected to the UT will be much lower than that of the buffer end in contact with the hot substance. UT in combination with BRs has been used for several industrial applications, in the areas of flow, liquid level and temperature [2]. The operating temperature of the UT might be further lowered by introducing cooling pipes or by performing intermittent measurements instead of continuous measurements, to reduce exposure of temperature sensitive components to critical temperatures, as suggested in [3].

Many factors have to be considered in selecting a measurement setup, both regarding the transducer, the buffer rod and the ultrasonic transceiver unit. This paper will focus on the geometrical aspects of the BRs, and in particular on how the diameter ratio of the BR and the UT affects the signal to noise ratio (SNR).

There are several software packages in the market for studying ultrasonic wave propagation phenomena in materials especially with focus on propagation or transit times. Ideally, the simulations of the ultrasonic measurement system should take into account the geometrical aspects of the BRs and the UTs. In this research, the experimental results of the SNR are compared to simulations of corresponding applications.

II. THE EXPERIMENT

The experiment was designed to see how small geometrical variations of BRs and UTs would influence the propagation time related performance of ultrasonic wave guides with focus on SNR. Therefore, only one geometrical or acoustic parameter was changed from one step to the other, during the experiments. Although high precision is used in the design of both BRs and UTs, experimental measurements with machined BRs will always have the inherent uncertainties in the manufacturing process itself in addition to other uncertainties. Details of both parts (i.e BRs and UTs) involved in the tests, and potential error contributions from each will be described in the following subsections.

A. The experimental setup

An Epoch 1000i in pulse echo mode was used to generate and receive ultrasonic signals, [4]. Longitudinal waveforms were utilized during the measurements based on TDR. The ultrasonic pulse was transmitted from the UT through a BR, and then reflected back to the transducer as shown in Fig. 1, *left*. A specially designed transducer holder helps to keep the UT firmly at a fixed and centered position at one end of the BR (Fig. 1, *right*). The other BR end was transmitting into free air, i.e. the ultrasonic pulse was assumed to be completely reflected at this BR end due to high impedance mismatch between buffer and air at this end.

B. The buffer rods

A sketch of a double tapered BR is shown in Fig. 2. Earlier publications report an improved SNR for BRs with tapered angle, α, compared to cylinder shaped BRs [5]. This relates to reduction or elimination of trailing echoes, as the mode converted reflections of the wave at the sidewalls of the BR are not in phase, as is the case in cylindrical BRs. By using double tapered BRs instead of single tapered BRs, the maximum diameter of the rod is halved, considering all the other parameters to be fixed. Therefore, all the BRs tested out in this experiment are double tapered. Nine BRs, all made of the same titanium grade 2 material, 50 cm long and with double taper were tested. The only differences between the BRs used, was the diameter of the buffer end, d_{Be}, their taper angles, α, and hence the middle diameter of the BRs, d_{Bm} (Fig. 2). The parameters of the BRs used in the experiments are shown in TABLE I.

To achieve optimal wave guiding properties of a particular BR, its two ends should be parallel. Tests have shown that even very small angle deviations of these two end surfaces will reduce the wave guiding properties considerably. Although the manufacturing of the BRs was performed with considerable precision, small deviations in the expected perfect parallelism of the end-planes of the buffer rods may still occur.

C. The ultrasonic transducers

Ten contact transducers (Olympus/Panametrics), enlisted in TABLE II, were used in different combinations with the BRs. Three different element diameters, d_{UT}, were used, i.e. 0.25", 0.50" and 0.75", with 5 or 10 MHz frequencies, with either
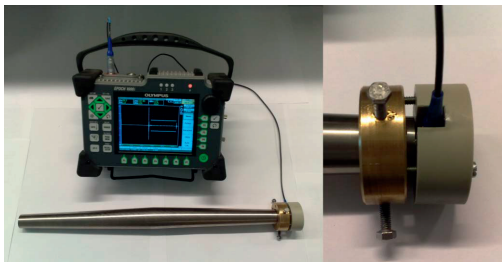
Fig. 1. *Left:* The measurement setup with the double tapered BR with the transducer. *Right:* The details of the transducer holder.
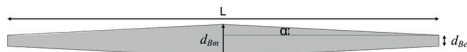
Fig. 2. Sketch of the geometrical aspects of the BRs

TABLE I.   TITANIUM BUFFER RODS

Parameters of the experimental titanium buffer rods			
Label	End diameter, d_{Be} (mm)	Middle diameter, d_{Bm} (mm)	Taper angle, α (°)
BR1	8.9	16.8	0.9
BR2	8.9	20.2	1.3
BR3	8.9	23.7	1.7
BR4	17.8	25.7	0.9
BR5	17.8	29.1	1.3
BR6	17.8	32.6	1.7
BR7	25.4	33.3	0.9
BR8	25.4	36.7	1.3
BR9	25.4	40.2	1.7

narrow or broad bandwidth type. For convenience, experiments were only performed with combinations where the UT element diameter was smaller than the corresponding BR end diameter. Although the UTs are grouped into two categories of bandwidths and frequencies, there will be always individual variations within these groups, which might influence the results of the experiments [6].

The ratio, κ, between the diameter of the UT element and diameter of the buffer end connected to the UT is defined as: $\kappa = d_{UT}/d_{Be}$. The following ratios are used in the experiment:

- $\kappa = d_{UT}/d_{Be} = 6.35mm/25.4mm = 0.25$
- $\kappa = d_{UT}/d_{Be} = 6.35mm/17.8mm = 0.36$
- $\kappa = d_{UT}/d_{Be} = 12.70mm/25.4mm = 0.50$
- $\kappa = d_{UT}/d_{Be} = 6.35mm/8.9mm = 0.71$
- $\kappa = d_{UT}/d_{Be} = 12.70mm/17.8mm = 0.71$
- $\kappa = d_{UT}/d_{Be} = 19.05mm/25.4mm = 0.75$

As shown, there are two different combinations that both give $\kappa = 0.71$. In the following plots their sequence are as given above.

III. RESULTS

Fig. 3 shows how the SNR changes with the d_{UT}/d_{Be}-ratio. The results are divided into four groups, based upon UT properties, i.e. bandwidth type and frequency.

A. Bandwidth

In general, there are only small differences in the SNR between the broad and narrow bandwidth UTs. The four curves

TABLE II.   ULTRASONIC TRANSDUCERS

Parameters of the experimental ultrasonic transducer			
Label	Element diameter, d_{UT} (mm)	Labeled frequency, f (MHz)	Bandwidth type
UT1	6.35	5	Broad-band
UT2	6.35	5	Narrow-band
UT3	6.35	10	Broad-band
UT4	6.35	10	Narrow-band
UT5	12.7	5	Broad-band
UT6	12.7	5	Narrow-band
UT7	12.7	10	Broad-band
UT8	12.7	10	Narrow-band
UT9	19.1	5	Broad-band
UT10	19.1	5	Narrow-band
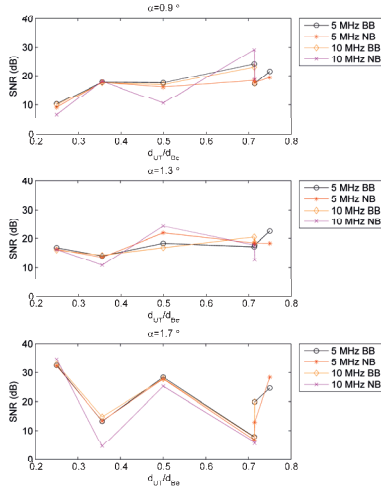
Fig. 3. SNR as a function of the diameter ratio between the UT and the BR end

are generally following each other quite well. However, the largest variations are seen for the UTs with the narrow band widths. This is reasonable as they are more sensitive to geometrical aspects of the BR, as the BR operates as a filter, and the wave energy of the narrow bandwidth UTs are concentrated within a smaller range of frequencies.

B. Taper angle of buffer rods

In general, the d_{UT}/d_{Be} -ratio seems to have positive influence on the SNR for the taper angles α=0.9° and α=1.3°, i.e. the SNR is generally increasing as κ increases. However, there are some large variations for the 10 MHz narrow band UT. As κ approaches 1, more of the BR end will be covered by the transducer, and therefore probably more wave energy will be received by the UT from the BR, with a high κ.

On the contrary, the other taper angle, α=1.7° has its maximum peak at the smallest diameter ratio; κ =0.25. This application involves the smallest UTs and the BR with the largest end diameter. Hence, there will be less reflections and mode conversions at the wall surface of the BR. In just reducing the taper angle and keeping κ =0.25, there is a clear reduction of the SNR as the taper angle is reduced and hence the middle diameter of the BR is reduced. The reduced SNR is best explained by more wave reflections at the BR's sidewall inducing mode conversions, and hence due to more trailing echoes. On the other side, according to the –6 dB ultrasonic beam spread angle φ in the far field region [7];

$$\varphi = \sin^{-1}\left(0.514\frac{c}{f \cdot d_{UT}}\right) = \sin^{-1}\left(0.514\frac{\lambda}{d_{UT}}\right) \quad (3)$$

where, c is the sound velocity in the medium, f the resonant frequency and d_{UT} the diameter of the piezoelectric element, the beam width angle should be smaller for larger UTs than

for smaller sized UTs. In titanium c= 6 100 m/s, and according to the parameters of UTs in Table II, the beam spread angle in this experiment will vary between approximately φ=0.9° and φ=5.7°

For α=1.7° the SNR curve has the shape of a "W". In this case, the d_{UT}/d_{Be} –ratio is probably not the most relevant parameter to explain why the SNR is varying that much. The peaks seen for α=1.7° in Fig. 3 are all representing SNR measurements with the thickest end diameter, d_{Be}, whereas the minimum values are representing the medium and small buffer ends. Hence, for the BRs with taper angle α=1.7°, the thickest BRs are reducing the trailing echoes the most. A larger α leads to a larger diameter and heavier buffer rod.

For all α's a high SNR may be obtained at κ =0.75. Two different combinations of BR and UT gives κ =0.71, where the thicker BR and UT provides better results for α=1.7°, whereas the combination of the thinner BR and UT provide the higher SNR for α=0.9°. As κ is identical in these two cases, other factors/variables are also contributing to the variations of the SNR.

C. Transducer frequency

There is no significant difference in the SNR as a function of the d_{UT}/d_{Be} –ratio, when comparing 5MHz and 10 MHz UTs. Using the signal processing terminology, the BRs may be considered as band pass filters. Based upon other results of this experiment, all the BRs seems to have a centre frequency of their pass band between 5 MHz and 10 MHz, although the thickest BRs has higher center frequency than the thinnest BR.

D. Signal amplitude

The main concern in this research has been on optimizing the geometrical aspects of the measurement system, i.e. the BR and UT, in order to improve the SNR. Another variable of interest is the amplitude of the reflected signal. With advanced ultrasonic transceiver systems, low signal amplitudes are often compensated by high sensitivity and wide ranged gain settings. However, higher reflected amplitude makes the measurement system more flexible to work at different applications, e.g. where the signal has to be transferred through longer distances of materials, or through materials with high attenuation.

In general, there is a high correlation between the relative signal amplitude and the SNR, as seen by comparing Fig. 3 and Fig. 4. There is a trend that the larger the dUT/dBe-ratio is, the higher is the signal amplitude, as shown in Fig. 4. This seems obvious as the UT covers more of the BR end as the dUT/dBe-ratio is approaching 1.

E. Simulations

The experimental results were compared with simulations performed with the Wave3000™ software (Fig. 5). In general, the SNR of the simulated results are higher than the experimental ones. This is probably due to the grain scattering within the BR material which generates spurious signals in the real measurements. These grain variations are not represented
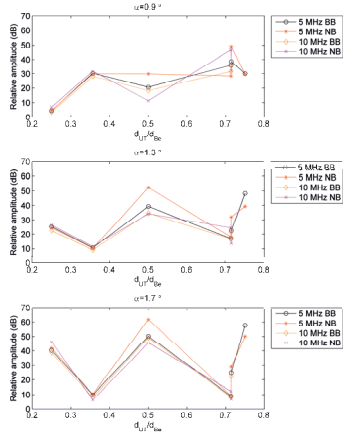
Fig. 4. Relative amplitude as a function of the diameter ratio between the UT and the BR

in any way in the Wave3000™ software. This phenomenon is not reflected in the results obtained from simulations.

Earlier publications have shown that the grain size of the metal buffer and also the elongated direction of the metal grains have a decisive influence on the grain scattering of the buffer, and hence the SNR [8],[9]. Fine grain size and columnar grains elongated in the propagation direction of the waves are most efficient to reduce the grain scattering.

There is a weak trend showing an increased SNR for increased d_{UT}/d_{Be} –ratio, in the results obtained from simulations, which is also supported by the experimental measurements for the two smallest taper angles. In contrary the W-curve for the largest taper angle seen for the real measurements, is not present in the results from simulations.
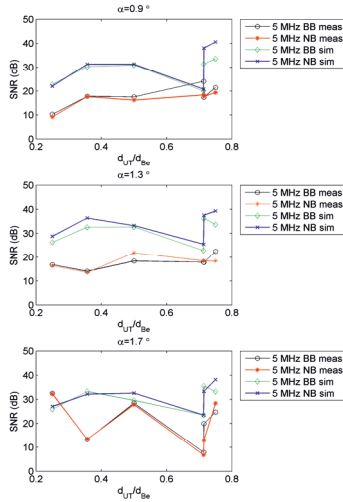
Fig. 5. Comparing the measured results with the simulated results with respect to the SNR

The three local maximum of the W-curve are representing the real measurements, and are very close to the results from simulations, whereas all the other measurements are considerably smaller than those obtained from simulations using Wave3000™ software. This confirms that the reflection and mode conversion from the side wall is very small for the BR with α=1.7° and d_{Be}=25.4 mm, especially for the smallest UT, i.e. d_{UT}/d_{Be}=0.25.

IV. CONCLUSION

Crisp general conclusions of how the SNR is affected by the ratio between the buffer end diameter and the UT diameter cannot be drawn for these experiments, but the experiments shows that small geometrical variations of the BRs and UTs may influence the performance of the measurement system *drastically. As a rule of thumb the SNR was high for all* combinations with d_{UT}/d_{Be}=0.75. For a robust design of an ultrasonic transducer system based on TDR, this aspect should be coupled to other parameters like taper angle and BR thickness.

REFERENCES

[1] C.-K. Jen, M. Kobayashi, "Integrated and flexible high temperature piezoelectric ultrasonic transducers", in Ultrasonic and Advanced methods for non destructive testing and material characterization, Editor: C.H Chen, World Scientific, 2007, pp.33-55.

[2] L. C. Lynnworth, "Waveguides in acoustic sensor systems", in Ultrasonic and Advanced methods for non destructive testing and material characterization, Editor: C.H Chen, World Scientific, 2007, pp.217-244.

[3] O. G. H. Nygaard and K. S. Mylvaganam, "Ultrasonic time-domain reflectometry for level measurements in molten metals," Proc. Technisches Messen 60, 1993, pp. 4-14.

[4] http://www.olympus-ims.com/en/ut-flaw/epoch1000/

[5] C.-K. Jen, L. Piche, and J. F. Bussiere, "Long isotropic buffer rods", J. Acoust. Soc. Am. Volume 88, Issue 1, 1990, pp. 23-25.

[6] R. C. Chivers, L. Bosselaar, and P. R. Filmore, "Effective area to be used in diffraction corrections", J. Acoust. Soc. Am. Volume 68, Issue 1, 1980, pp. 80-84.

[7] Olympus, "Ultrasonic Transducers Technical Notes," http://www.olympus-ims.com/en/panametrics-ndt-ultrasonic/pdf/, pp.41-49.

[8] C.-K. Jen, H. Soda, Y.S. Liu, C. Neron, A. Ohno and A. McLean, "Acoustic characterization of metals with columnar grains", Ultrasonics, vol. 33, No. 3, 1995, pp.181–186.

[9] L.C. Lynnworth, "Scope of Applications" in Ultrasonic Measurements for Process Control – Theory, Techniques, Applications, San Diego: Academic Press, 1989, Ch. 2, sec. 6.3, p. 75-76.

Paper E

System Identification of a Non-Uniformly Sampled Multi-Rate System in Aluminium Electrolysis Cells *

System Identification of a Non-Uniformly Sampled Multi-Rate System in Aluminium Electrolysis Cells

H. Viumdal [1] S. Mylvaganam [2] D. Di Ruscio [2]

[1] *Tel-Tek, N-3918 Porsgrunn, Norway and Telemark University College, Faculty of Technology, N-3918 Porsgrunn, Norway. E-mail:* hakon.viumdal@hit.no

[2] *Telemark University College, Faculty of Technology, N-3918 Porsgrunn, Norway. E-mail:* saba.mylvaganam@hit.no *and* david.di.ruscio@hit.no

Abstract

Standard system identification algorithms are usually designed to generate mathematical models with equidistant sampling instants, that are equal for both input variables and output variables. Unfortunately, real industrial data sets are often disrupted by missing samples, variations of sampling rates in the different variables (also known as multi-rate systems), and intermittent measurements. In industries with varying events based maintenance or manual operational measures, intermittent measurements are performed leading to uneven sampling rates. Such is the case with aluminium smelters, where in addition the materials fed into the cell create even more irregularity in sampling. Both measurements and feeding are mostly manually controlled. A simplified simulation of the metal level in an aluminium electrolysis cell is performed based on mass balance considerations. System identification methods based on Prediction Error Methods (PEM) such as Ordinary Least Squares (OLS), and the sub-space method combined Deterministic and Stochastic system identification and Realization (DSR), and its variants are applied to the model of a single electrolysis cell as found in the aluminium smelters. Aliasing phenomena due to large sampling intervals can be crucial in avoiding unsuitable models, but with knowledge about the system dynamics, it is easier to optimize the sampling performance, and hence achieve successful models. The results based on the simulation studies of molten aluminium height in the cells using the various algorithms give results which tally well with the synthetic data sets used. System identification on a smaller data set from a real plant is also implemented in this work. Finally, some concrete suggestions are made for using these models in the smelters.

Keywords: Height measurements, aluminium electrolysis, system identification

1 Introduction

Many industrial processes involve systems where two or more physical processes have strongly differing temporal characteristics, i.e large differences in time constants. Simulations of such systems may be solved without excessive use of small time steps, by using two different models, one for the rapid variations, assuming the slow varying process to be constant, and another model for the slow variations, where the rapid varying process is neglected. This is a possible way of attacking the system identification problem of such systems, also known as stiff systems. In some cases a model should be determined based upon already existing data from industrial processes. In such cases the researcher may be confronted with lacking data samples or outliers that should be deleted, hence making the system identification problem some more complicated. In addition multi-rate system widely exists in chemical process industries, typically with a slower sampling

Table 1: Nomenclature

Symbol	Quantity
A	Cross section of aluminium
CE	Current Efficiency
F	Faraday constant
I	Line current
K	Kalman gain matrix
M	Sampling difference factor between T_f and T_s
M_{Al}	Molecular mass of aluminium
N	Number of data samples
P	Covariance matrix
Q	Charge
T_f	Fast sampling time
T_s	Slow sampling time
V	Volume of aluminium
V_t	Criterion function
h	Height of molten aluminium
b_1 and b_2	Parameters in mechanistic model
f_s	Sampling frequency
f_m	System frequency
$\Delta \widehat{h}$	Predicted change of Aluminium height
$\bar{h}$	Aluminium height prediction
h	Aluminium height measurement
k	Discrete time
m	Mass of molten aluminium
n_i	Discrete sampling instant of the i-th output measurement
t	Continuous time
w_1	Weight put on the model
w_2	Weight put on the measurements
z	Charge number of an ion
α	Forgetting factor
Δt	Sampling time of input measurements
ϵ	Prediction error
θ	Parameter vector of OLS models
λ	Parameter weight in OLS model
ρ	Density
Φ	Measurement vector for fast sampling
ψ	Measurement vector for slow sampling
ACD	Anode Cathode Distance
CCA	Canonical Correlation Analysis
DSR	Deterministic and Stochastic system identification and Realization
MDSR	Multiple time series DSR
MSE	Mean Square Error
NMSE	Normalized Mean Square Error
NRMSE	Normalized Root Mean Square Error
NUSM	Non-Uniformly Sampled Multi-rate syst.
OLS	Ordinary Least Squares
PEM	Prediction Error Method
ROLS	Recursive Ordinary Least Squares
SNR	Signal to Noise Ratio
SSM	State Space Model

rate for the outputs, compared to the inputs of the system. Some of the measurements may also be manually performed, causing rare and intermittent sampling instants. All these factors complicate the system identification process. As the standard methods of system identifications are based upon equidistant sampling instants, these methods cannot be directly applied for such data sets.

During periods without measurement data, gathered data will consist of several data segments. Simply concatenating the data segments may lead to false transients in their connection points. A more consistent option is to calculate model parameters for each of the segments, using the identical model structure. Finally, the segment estimates should somehow be merged into the resulting model of the system. In Ljung (1999) the parameter estimates of the segments are given weight according to their estimated inverse covariance matrices. In 1957 Kranc introduced a method of replacing multi-rate sampled systems with single-rate models, using z transform methods (Kranc, 1957). In Kranc's approach the sampling and updating instants are synchronized but operate with different sampling periods. The sampling periods could all be expressed as unit fractions of an overall sampling rate T, later known as the frame period (Sheng et al., 2002). T is the least common multiple of the periods of the sampling and updating pattern of the system. Within each frame period T, there is one or more "sub"-sampling periods. The most common case is the system in which the inputs of the system are sampled on a higher rate than the output. The extracted single-rate model of the multi-rate system is designed with the sampling rate of the frame period T. This method is therefore known as the lifting technique (Sheng et al., 2002), as sampling periods are lifted to a higher and mutual level for all the variables. A dual-rate modeling case study on continuous catalytic reforming in the oil industry, using lifting technique, is presented in Li et al. (2003). A least squares method was used by Lu and Fisher to estimate the inter-sample outputs, for applications where the outputs are sampled at a slower rate, compared to the inputs (Lu and Grant Fisher, 1989). In Li et al. (1999) system identification of multi-rate systems, using subspace methods are discussed. In particular the systems considered are systems where the sampling rate of the input variables are n times faster than the sampling rate of the output variables, where n is an integer.

The lifting method has been used to generate a minimum variance predictor with the fast sampling rate of the input variables. This predictor shows enhanced performance compared to a similar predictor using the slow output sampling rate. The controllability and ob-

servability of lifted systems are discussed in Wang et al. (2004) and Ding et al. (2009), in addition to a recursive auxiliary least square model based upon a dual-rate system. A lifted state space model with an implemented Kalman filter for Non-Uniformly Sampled Multi-rate (NUSM) systems is presented in Li et al. (2008).

A simplified simulated model of the aluminium metal height in a pre-baked aluminium electrolysis process is used as a representative example throughout this paper. Aluminium electrolysis processes applying pre-baked anodes are the main procedure to manufacture primary aluminium to day. This is an old method heavily based upon frequent operator interventions involving a plethora of manual operations involving materials feeds, handling of measurands, removing crusts and excessive alumina of cryolite. Although there has been a considerable improvement by the introductions of the automated control system and some few automatically sampled measurements, the majority of the measurements are still manually performed. Regular sensor applications are normally not suitable for this electrolysis process due to the high temperature, the invasive corrosive environment of the bath and the generally harsh environment of the plants. In this paper the focus will be upon estimating the molten aluminium height, also called the metal height. By improving the monitoring of this vital variable, the process can be stabilized at more optimal conditions, which are beneficial to the environmental and economical performance of the whole plant. In other words undesired variations of the process should be reduced or eliminated.

The main focus in this paper is on using system identification methods on non-uniformly sampled multi-rate systems, and in particular on a simplified model of the aluminium electrolysis cell. The main contributions in this paper are as itemized in the following:

- Deriving a simplified model of the metal height in an aluminium electrolysis cell.

- Deriving and testing a Prediction Error Method (PEM) (Ljung, 1999) model for a non-uniformly sampled multi-rate system.

- Reducing the impact of the computer precision on updating the covariance matrix of the Multiple Input Single Output (MISO) system, in the Recursive Ordinary Least Square (ROLS) method (Di Ruscio, 2001), by rearranging the updating equation.

- Testing the combined Deterministic and Stochastic Realization (DSR) algorithm (Di Ruscio, 1996) on a data set with multi-rate sampling.

- Testing the Multiple time series Deterministic and Stochastic Realization (MDSR) algorithm (Di Ruscio, 1997) on a data set with multi-rate sampling and multiple time series.

- Comparing different system identification methods on the simplified discrete model of the metal height, showing saw-tooth-shaped behavior.

The rest of the paper is organized as follows. In Sec. 2 we derive a simplified discrete model of the metal height in an aluminium electrolysis cell, which represents the synthetic system that is to be identified throughout the rest of the paper. In Sec. 3 the black, white and gray model approaches in system identification are emphasized. Data sampling for system identification methods are discussed in Sec. 4. In Sec. 5 prediction error methods are described for use on the given synthetic system, assuming non-uniformly multi-rate sampling. In Sec. 6 the sub space method DSR and a corresponding version for multiple series are tested, assuming synchronous but multi-rate sampling. Sampled data from a real plant is utilized in Sec. 7. The results from the different methods are compared and analyzed in Sec. 8, whereas this paper is summarized and concluded in Sec. 9.

2 Simplified model of the metal height

There are several model approaches describing the level and shape of the metal/bath interface in aluminium electrolysis cells. The interface is not totally flat, but consists of gravitational standing waves, and unstable propagating waves (Kurenkov et al., 2004). The waves are generated by the high electrical and magnetic fields (Lorentz forces), and the Kelvin-Helmholtz instability of the mean flow. Under stable conditions, the interface waves are estimated to have an amplitude of about 0.5 mm, at fixed positions (for a 500 kA cell), but these waves can increase by variations in stability affecting parameters, like the Anode Cathode Distance (ACD) and the height of the liquid metal (Bojarevics and Pericleous, 2006, 2009). Larger deviations are present along the horizontal axis, due to the Lorentz forces. In this work we will consider a fixed horizontal position of the metal/bath interface, and are focusing on its mean value.

Consider the sketch of an aluminium electrolysis cell of Figure 1. A simplified model of the metal height, i.e. h, will be derived in this section, based upon the aluminium mass balance.

Due to the spatial mass balance of molten aluminium the time gradient of mass equals

129
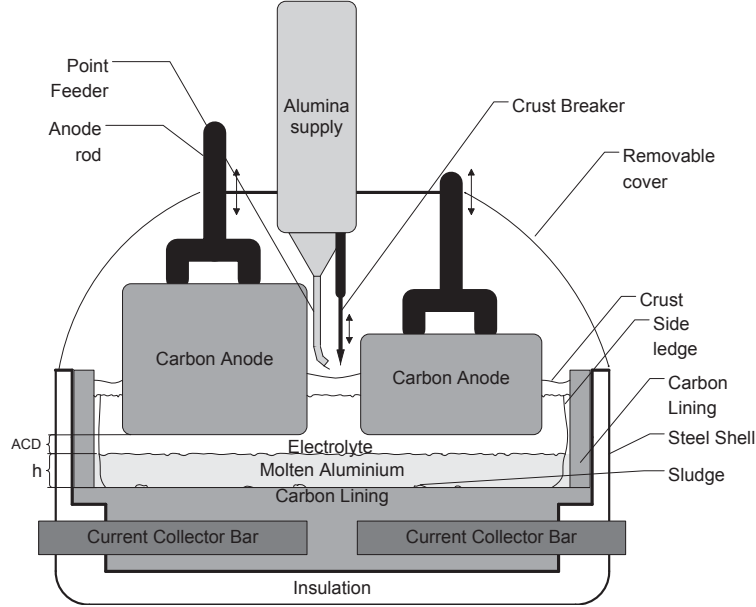
Figure 1: Schematic drawing of an aluminium electrolysis cell with the different structures in it forming the system under consideration. Our model focuses on temporal variations of molten metal height h.

$$\frac{dm}{dt} = \dot{m}_{gen}(t) + \dot{m}_{in}(t) - \dot{m}_{out}(t). \qquad (1)$$

where $\dot{m}_{gen}(t)$ is the instant mass rate of molten aluminium generated inside the cell, whereas $\dot{m}_{in}(t)$ and $\dot{m}_{out}(t)$ represents the mass flow of molten aluminium into and out of the electrolysis cell, respectively. For small values of Δt, a good approximation of the mass balance is the discrete model

$$\Delta m(k) = \Delta t(\dot{m}_{gen}(k) + \dot{m}_{in}(k) - \dot{m}_{out}(k)), \qquad (2)$$

where $k = \{1, 2, 3, \cdots\}$ represents the discrete time, whereas Δt is the sampling time. Normally, there are no inflow of molten aluminium to the system, as the aluminium is generated within the electrolysis cell, which is regarded as the system of interest.

The generated mass of aluminium per time unit is given by Faraday's laws of electrolysis (Grjotheim, 1993);

$$\dot{m}_{gen}(k) = \frac{\Delta Q(k) \cdot CE \cdot M_{Al}}{F \cdot z \cdot \Delta t} \qquad (3)$$

where CE is the current efficiency of the cell which in the following simulation is assumed to be constant for all t. $M_{Al} = 26.98 g/mol$ is the molecular mass of aluminium, F the Faraday constant, whereas z is

the number of electrons involved in the electrode reaction generating one single aluminium atom from a aluminium-ion. The charge transferred from time $k-1$ to k, i.e. $\Delta Q(k)$ is given by the time integral of the current

$$\Delta Q(k) = \int_{k-1}^{k} I(\tau) d\tau \qquad (4)$$

Assuming constant value of the current within each Δt, i.e. zero-order hold, the generated mass of aluminium per time unit equals

$$\dot{m}_{gen}(k) = \frac{CE \cdot M_{Al}}{F \cdot z} I(k), \qquad (5)$$

There is usually no inflow of molten aluminium to the process, hence

$$\dot{m}_{in}(k) = 0 \qquad (6)$$

The outflow of molten aluminium per time unit relates to the tapping proceeding. As the tapped mass of aluminium, and not its mass flow is measured in the tapping procedure, it is more convenient to put

$$m_{out}(k) = \Delta t \cdot \dot{m}_{out}(k), \qquad (7)$$

in Eq. (2), hence assuming a constant flow rate within each time step.

Assuming a crisp interface between the electrolyte and the molten aluminium, and that all the generated molten aluminium will be located at the bottom of the cell, i.e. assuming no time delay due to transportation of aluminium in the electrolyte, and no precipitations of other substances within this area, and assuming a homogeneous pure aluminium, $\Delta m(k)$ equals

$$\Delta m(k) = \rho \cdot \Delta V(k). \qquad (8)$$

Due to side ledge formation of frozen electrolyte at the side walls of the cell, the area of the horizontal section of molten aluminium varies with both height and time. Here the side ledge profile (Figure 1) is assumed to be straight vertical. Hence, the change in volume of the molten aluminium in one time step is, according to Figure 2, given by

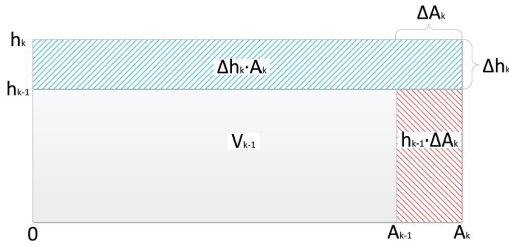$$\Delta V(k) = \Delta h(k) \cdot A(k) + h(k-1) \cdot \Delta A(k) \qquad (9)$$

Figure 2: Schematic figure of the volume of the metal pad, showing change in volume of the molten metal described by the variables A and h.

Consequently, in one time step, the net mass aluminium accumulated is

$$\Delta m(k) = \rho \left(\Delta h(k) \cdot A(k) + h(k-1) \cdot \Delta A(k) \right). \qquad (10)$$

Based upon Eq. 10, the change in metal height in one time step is given by

$$\Delta h(k) = \frac{\Delta m(k)}{\rho \cdot A(k)} - \frac{h(k-1) \cdot \Delta A(k)}{A(k)}. \qquad (11)$$

Inserting Eq. (2), (5), (7) into Eq. (11), leads to this simplified model of the height of aluminium in the cell:

$$\Delta h(k) = \frac{1}{\rho \cdot A(k)} [\Delta t \frac{CE \cdot M_{Al}}{F \cdot z} I(k) - m_{out}(k)] \\ - \frac{h(k-1) \cdot \Delta A(k)}{A(k)}, \qquad (12)$$

The model in Eq. (12) is used for generating the synthetic data set simulating the aluminium height throughout this paper.

An even simpler model of the metal height is derived, by assuming that the area A is constant. Hence, the last term in Eq. (12) will disappear. By further collecting the constants into two constants, a very simple finite impulse response (FIR) model is formed

$$\Delta h(k) = b_1 \cdot \Delta t \cdot I(k) - b_2 \cdot m_{out}(k), \qquad (13)$$

where

$$b_1 = \frac{CE \cdot M_{Al}}{\rho \cdot A(k) \cdot F \cdot z}, \qquad (14)$$

and

$$b_2 = \frac{1}{\rho \cdot A(k)}. \qquad (15)$$

This model is the basis of the PEM models used for the system identification problem in Sec. 5.

The assumptions used in this model are:

1. Homogeneous layers of molten cryolite (electrolyte) and molten aluminium.

2. Perfect crisp interface between the layers. No mixing of the materials in the different layers.

3. No transportation delay for any of the materials in the system.

4. The process variables are fixed for each sampling interval Δt.

5. A straight vertical side ledge profile.

6. Constant current efficiency.

7. No precipitates or impurities in the aluminium volume, only pure aluminium.

8. Constant density of the molten aluminium.

The aluminium electrolysis process requires a very stable energy balance, as the operation temperature of the electrolyte within the cell is close to its freezing point, so that the top surface of the bath is covered with frozen electrolyte, as well as the side ledges. The frozen electrolyte has a desired heat insulating effect, as well as it protects the side shell of the cell from corrosion. Simultaneously it is important that the active electrolyte is in molten condition. To maintain these steady conditions of the heat transfer, and hence the side ledge profiles, the variation of the metal height varies with only about some centimeters between maximum and minimum position of the interface. However, the total height of the aluminium layer is normally close to 20 cm.

2.1 Simulation of the molten metal height

A simulation of the aluminium height was performed using the simplified model derived in Eq. (12). Normal distributed noise with mean value $\mu = 0$ and standard deviation $\sigma = 0.75$ cm was added to the height measurement, and rounded to nearest half centimeter. This is a very high, but a realistic measurement uncertainty of the manually performed height measurements in aluminium electrolysis plants. The time of the daily performed tapping procedure is randomly varied from day to day, as seen in in Figure 3. In the simulation typical variations of the variables I and m_{out} are included. To make the simulation more dynamic, a variation of the horizontal cross sectional area A has been implemented as a sine-curve. The simplified model is simulated with $\Delta t = 5min$. This simulation approach will be used throughout this paper, examining different system identification methods.

3 Black, white and gray box models

There are several ways of categorizing different system identification methods. In this paper we use the box system to categorize the utilized algorithms, to have a better overview of the benefits and drawbacks of each method.

3.1 Introduction to model types

There are two main approaches to generate mathematical models of industrial processes. Mechanistic models, also called white box models, are merging several well-know physical relations between the different variables of concern to achieve a reasonable model of the process. With set of mechanistic model variables that are assumed to influence the total system, the outputs may be calculated with these models. Although the basic models are well established and may work excellent for small processes, the many assumptions and uncertainties induced by the often huge number of relations integrated in the model, the final simulation of the variables may not be satisfying. The deviations of the simulated variables from the real values, regarded as random noise is normally not white noise, and some of the noise might be eliminated by improving the models.

The optional approach of creating mechanistic models is a conglomerate of different empirical methods that all depend on sampled data from the particular system of interest. In that sense such systems are more individually calibrated to the actual system, whereas the mechanistic approach induces more general models. System identification, neural networks, multivariate data analysis are all groups of algorithms that
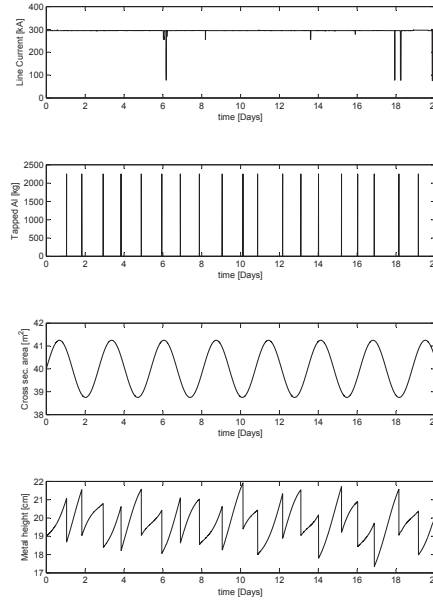
Figure 3: Simulations of the three input variables (Line current, Tapped Aluminium, and The horizontal Cross sectional area of the metal pad) and the output variable (Metal height) considered in the simplified model of an aluminium electrolysis cell.

are belonging to algorithms based on empirical reasoning/analysis. Models where the model structure is not influenced by physical relations is often called black box models (Ljung, 1999), because parameters are adjusted to fit the input and output data-sets, without reflecting physical considerations of the system. The model structure inside is not reflecting the structure of the real system, whereas the mechanistic models attempt to have identical structure to the real systems, and hence called white models.

It is also possible to take advantage of the empirical methods in conjunction with the mechanistic models, by utilizing the well known physical relations and calibrate the physical parameters by empirical methods, called parameter estimation. With this approach, all the variables are still easily available as the model structure is identical or similar to the mechanistic

model, but simultaneously more individually fitted, due to the empirical methods. There is a large range of such gray models,varying from models with almost any physically based model structures to mechanistic models where some parameters are estimated. Hence, gray model is a collective term of such mixed models.

The main focus in this approach will be parameter estimation using least square methods, which can be considered as a gray box, as the structure is designed based on physical insight, and the parameters calibrated according to empirical data.

Many testing techniques of different processes have been developed over the years based on functional, process and system modeling (among a plethora of other possibilities), aiming at testing, verifying and predicting system behavior robustly and as accurately as possible. The different modeling approaches display diverse characteristics as shown in Table 2. Naturally, some solutions may involve a series of white box, black box, and gray box in tandem depending on the system architecture and the needed set of outputs.

3.2 White Box Models

White box models are based on knowledge of the internal behavior of the system. The available form of knowledge can be in terms of equations, coherent data with the related temporal and spatial associations etc. This approach may increase effectiveness, reveal internal structures, but is essentially a general approach, that is not calibrated to the actual process. White box modeling is widely performed in simulation purposes, as no measurement of the process has to be performed, to generate the model. The process does not need to exist at all, which makes this modeling approach ideal for designing and modifying systems. The simplified model of the metal height, derived in Sec. 2 is an example of a white box model.

3.3 Black Box Models

Black box models are based on the insurmountable fact of not having any knowledge about the internal behavior of the system under scrutiny. Black box model does not have any information of the system architecture or any underlying equations describing the internal behavior of the variables involved. A typical black box model is based on the study of a set of inputs provided by the user to the system and outputs from the system oblivious to where, when and how these inputs were operated inside the system to deliver the observed outputs. In other words, how these outputs are generated or what is inside the black box representing the system are not important or unknown to the user of the black box model. The main advantages may be in the ease of the usage and implementation of the model, and the process specific approach. On the other side, generating the model requires consistent measurement of the system, measurements that can both be cumbersome and expensive. The DSR and MDSR model of the metal height, that will be presented in Sec. 6 are examples of black box models.

3.4 Gray Box Models

Gray box models address systems with limited knowledge of the internal behavior of the system under scrutiny. As the name implies, the model will have the strategies of white box and black box models in analyzing a given system. This method may have the advantage of harvesting from both white box and black box analysis of a given system. For complicated systems like the one we have in the case of aluminium electrolysis cell, this method may be an unavoidable option, as models addressing all the phenomena in the cells are not available or incomplete. The OLS and ROLS model of the metal height, that will be presented in Sec. 5 are examples of gray box models.

4 Data sampling

Table 3 provides a set of the most common variables that are measured in the aluminium electrolysis process.

In the aluminium electrolysis process, there is a large variety in sampling intervals for the different variables. The online measurements; line current and cell voltage are the most regular performed measurements often given as mean values every 5 minutes. The tapping procedure is intermittently performed typically once a day. The height of the molten aluminium in industrial plants is only measured just before the tapping proceeding, and may influence the amount of aluminium to be tapped. In case of generating a model of this process, if just implementing these few measurements into a black box model, without adding any additional information of the system, a complete unfeasible model of the aluminium height will be the result. A black box model will "see" a folded version of the system as the dynamic of the saw-tooth shaped periodic oscillation is not sampled. By further including a realistic normal distributed measurement error with mean $\mu = 0$, and standard deviation $\sigma = 0.75$ cm, the identification process will become even worse, as can be seen in Figure 4. The uncertainty of the metal height measurements will add random dynamics to the already poor folded measurements.

Tests with real data from the industry show that the simple prediction model;

133

Table 2: Different "Box" Systems in conjunction with modeling and their overall characteristics

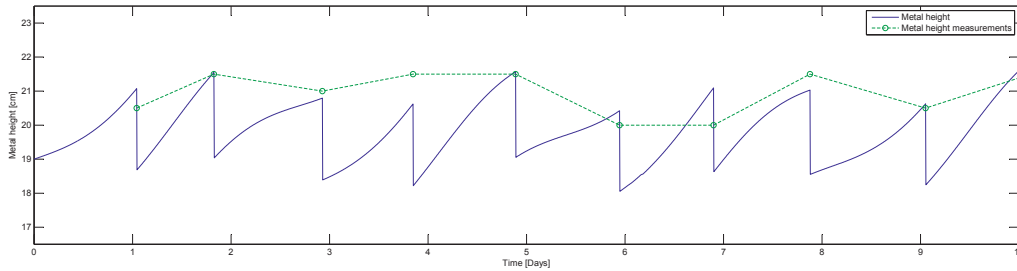| Model Type	Physical insight	Model structure	Validity
White Box	Crucial	Rigid	General
Black Box	Less important	Flexible	Specific
Gray Box	Important	Adjustable	Fairly Specific

Figure 4: Synthetic data set showing metal height steadily increasing with sudden drops in its values, due to tapping, over a period of time, in this case about 10 days. It is common to measure the metal height just before the metal tapping, once a day.

$$\bar{h}(k+1) = h(k), \qquad (16)$$

provides smaller error predictions than many advanced system identification models, because of the lack of information of the dynamic system the few sampling instants gives. To overcome these challenges both more physical insight of the system and more measurements have to be considered.

In cases where the output variables make stepwise jumps, like the saw-tooth jumps of the aluminium height, making the measurements at the right time instants is even more important than just increasing the number of measurements in general. The Nyquist theorem states that the sampling frequency f_s should at least be twice the frequency of the variable to be measured (Shannon, 1949, 1998);

$$f_s > 2f_m \qquad (17)$$

In many reel applications it is more common to sample with a sample frequency about 10 times the system frequency. In the aluminium electrolysis example $f_s = f_m$, which according to both the Nyquist theorem and simulations provides a too poor sampling rate for system identification purposes. At the other side, increased number of manually performed metal height measurements might be to time demanding, and hence expensive for the plant, as the sampling range might span some weeks. Especially in cases where recursive models are considered, as few manual measurements as possible should be included.

A more cost efficient solution to the high sampling rate is to use knowledge of the system to decide crucial measurement instants, i.e. including more information on the physical and chemical connections between the variables to establish a more realistic model with improved predictability. Based on sensible reasoning of the system, or if a mechanistic model of the system is available, it is possible to set up decisive intermittent measurement instants without performing a lot of measurements with a high sampling frequency. One measurement just before, and one just after the tapping procedure would have been a reasonable minimum requirement for detecting the model of the aluminium height. If the mechanistic model structure is assumed to be of high accuracy, a prediction-error-method (PEM) would be the first choice, to estimate its parameters (Ljung, 1999).

When deciding the crucial measurement instants, variables with rapid short term variations are isolated from variables with long term slow variations. After this segregation of variables, it is possible to utilize different system identification methods for each of the two variable groups. This will be considered in the following example from the aluminium electrolysis cell.

5 Prediction Error Methods (PEM)

In this section different PEMs are used to predict the metal height, based on the synthetic data set described in Sec. 2. To make it realistic, the input variables are assumed sampled with a "fast" sampling rate T_f, while the output is sampled with a "slow" variable sampling rate $T_s(i)$. $T_s(i)$ will vary with time, due to manual intervention in performing the measurements. For convenience $T_s(i)$ is adjusted to fit a multiple of T_f, as shown in Figure 5. n_i is the discrete time of output measurement number i, while the inputs are sampled at each k.

The Ordinary Least Square (OLS) algorithm is designed for both these sampling rates, entailing two OLS-models. The model with sampling rate $T_s(t)$ is used for determining the parameter vector θ, while the model with sampling rate T_f is used for predicting the inter-sample outputs. It is utilized that the identified parameter vector θ is identical for both models.

5.1 Ordinary Least Square (OLS)

Based upon the simple discrete model in Eq. (13), a linear regression model is constructed;

$$\Delta\widehat{h}(k|\theta) = \overbrace{\left[\begin{array}{cc} \Delta t \cdot I(k) & m_{out}(k) \end{array}\right]}^{\Phi^T(k)} \overbrace{\left[\begin{array}{c} \theta_1 \\ \theta_2 \end{array}\right]}^{\theta} \quad (18)$$

where $\Delta\widehat{h}(k|\theta)$ is the predicted change of the metal height from time step $k-1$ to k, given the parameter vector θ. The parameters are estimated by the least square method, where the optimal θ, given the defined model structure and a specific data set with N input and output samples, is the parameter vector $\widehat{\theta}_N^{LS}$ that minimizes the least square criterion for the linear regression

$$V_N(\theta) = \frac{1}{N}\sum_{k=1}^{N}\epsilon^T(k)\lambda\epsilon(k), \quad (19)$$

where $\epsilon(k) = \Delta h(k) - \Delta\widehat{h}(k|\theta)$ describes the prediction error at time step k.

Table 3: Common measured variables in aluminium electrolysis plants. The statistics are based upon process data from one single aluminium electrolysis cell generated over one year. The measurements can be categorized into two main categories; on-line measurements ($\oplus$) and measurements performed with manual interactions ($\ominus$).

| Index	Variable	Unit	Category	Average sample time	Average	Standard deviation	Minimum value	Maximum value
1	Metal height	cm	$\ominus$	24 h	20.1	1.2	17	28
2	Cell Voltage	V	$\oplus$	5 min	4.49	0.29	0.44	28.3
3	Line current	A	$\oplus$	5 min	293.4	3.7	0	315.6
4	Bath height	cm	$\ominus$	24 h	20.7	1.5	14	32
5	Anode position 1	$\frac{rotations}{day}$	$\oplus$	78 min	0.0	1679	150	2569
6	Anode position 2	$\frac{rotations}{day}$	$\oplus$	78 min	0.0	1677	112	2634
7	Alumina feeding	$\frac{kg}{day}$	$\oplus$	15 min	4137	323	3044	5121
8	Tapped aluminium	$\frac{kg}{day}$	$\ominus$	24 h	2182	301	0	3125
9	Acidity	%	$\ominus$	48 h	10.7	1.7	6.3	15.2
10	Added bath	$\frac{kg}{day}$	$\ominus$	10 days	590	264	350	1750
11	Tapped bath	$\frac{kg}{day}$	$\ominus$	7 days	665	354	150	2100
12	Bath temperature	C	$\ominus$	7.5 h	962	9.0	939	998
13	Added CaF2	$\frac{kg}{day}$	$\ominus$	24 days	35	12.7	25	50
14	CaF2 concentration	%	$\ominus$	56 h	5.1	0.2	4.3	5.7
15	Anode effects	$\frac{1}{day}$	$\ominus$	24 hours	0.19	0.6	0	5
16	Feeder defects	$\frac{1}{day}$	$\ominus$	13 days	0.080	0.31	0	2
17	Superheat	C	$\ominus$	4 days	7.58	5.19	1.9	36
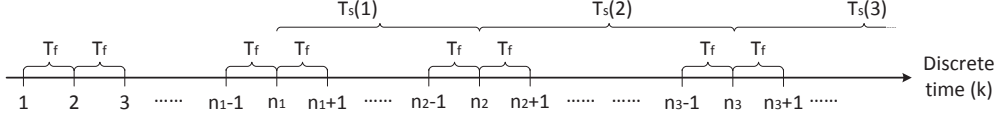
Figure 5: Time line showing the fast sampling rate T_f used for the input variables, and the slow sampling rate $T_s(i)$ used for the output measurement (the aluminium height). As indicated $T_s(i)$ will vary with time, due to manual intervention, but it is adjusted to fit a variable multiple of T_f. i indicates the i-th element of the output measurements sequence, while the inputs are sampled at each k.

The analytical solution of the optimal $\widehat{\theta}_N^{LS}$ is given by

$$\widehat{\theta}_N^{LS} = \left(\sum_{k=1}^{N} \Phi(k)\Phi^T(k) \right)^{-1} \sum_{k=1}^{N} \Phi(k)\Delta h(k), \quad (20)$$

if the inverse of the indicated matrix exists. As this is a MISO (multiple input, single output) system, the weight λ is a scalar, hence $\lambda^{-1}\lambda = 1$, and λ is therefore not included in Eq. (20);

Consider a data set of input and output variables describing a period of 20 days. Assuming a regular consistent measurement regime, the number of metal height measurements will be $N_h = 20$, whereas the number of line current measurements are $N_I = 5760$. Although the tapping is performed 20 times, the number of samples in the "tapping" vector is for convenience set to $N_t = 5760$ to match N_h, where the sample values between the tapping incidents are zero. Due to the manual intervention of the height measurements and tapping procedure, variations in both the number and time instants are common. The LS-model of Eq. (18) has to incorporate these properties, hence become more flexible in utilizing intermittent measurements from real plants.

The elements of the regression vector $\Phi(k)$ are defined as $\phi_1(k) = \Delta t \cdot I(k)$ and $\phi_2(k) = m_{out}(k)$. The predicted change of the metal height between two metal height measurements, i.e. from time step n_i to n_{i+1} are due to the LS-model in Eq. (18), given by

$$\sum_{k=n_i+1}^{n_{i+1}} \Delta\widehat{h}(k|\widehat{\theta}_N^{LS}) =$$
$$\theta_1[\phi_1(n_i+1) + \phi_1(n_i+2) + \cdots$$
$$+\phi_1(n_{i+1}-1) + \phi_1(n_{i+1})]$$
$$+\theta_2[\phi_2(n_i+1) + \phi_2(n_i+2) + \cdots$$
$$+\phi_2(n_{i+1}-1) + \phi_2(n_{i+1})] \quad (21)$$

To simplify the notation, we write

$$\Delta\widehat{h}(n_{i+1}|\widehat{\theta}_N^{LS}) = \sum_{k=n_i+1}^{n_{i+1}} \Delta\widehat{h}(k|\widehat{\theta}_N^{LS}) \quad (22)$$

By summing up the right-hand side of Eq.(21), a prediction model with linear regression structure is achieved;

$$\Delta\widehat{h}(n_{i+1}|\widehat{\theta}_N^{LS}) = \quad (23)$$
$$\underbrace{\left[\sum_{k=n_i+1}^{n_{i+1}} \phi_1(k) \quad \sum_{k=n_i+1}^{n_{i+1}} \phi_2(k) \right]}_{\Psi_{n_{i+1}}^T} \left[\begin{array}{c} \theta_1 \\ \theta_2 \end{array} \right]$$

Although the linear regression model of Eq. (23) is used for estimating the least square parameter vector θ, this parameter vector is mutual for both Eq. (23) and Eq. (18), hence it can be used to predict the metal height by Eq. (18).

5.1.1 Simulation of the metal height

As the tapping proceeding is a rapid process compared to the slow electrolysis process where molten aluminium is generated, height measurements should ideally be made both just before and immediately after the metal tapping. Hence, the top and at the bottom level of the metal height would be measured in each cycle. In that way, the rapid changes of the metal height, due to metal tapping, is isolated into a small temporal regression vector Ψ_{n_i}. The next regression vector $\Psi_{n_{i+1}}$ will isolate the influence of the slower electrolysis process. However, the second measurement instant should be carefully chosen due to an eventually time lag. With this approach every second Ψ-vector in the considered simulation, the last element of this vector, representing the amount of tapped metal, is zero.

5.1.2 The prediction algorithm

With the predictor model of Eq. (18), the measurement based update of the predicted metal height is very rare. Hence, the predictions of $\Delta h(k)$ will be updated only by the predictor model for all the time instants between two metal height measurements. The estimated height of the metal height is given by;

$$\overline{h}(k+1) = \overline{h}(k) + \Delta\widehat{h}(k+1) \qquad (24)$$

Although the parameter estimation may be good, noise and uncertainties in the model may cause the predicted output of the aluminium height to drift away from the real value of the aluminium height. On the other side the manually performed metal height measurements are likely to be corrupted by decisive noise. Therefore, a weighting algorithm has been incorporated in the predictor at each time step a new metal height measurement is performed;

$$\overline{h}(k+1) = w_1\overline{h}(k) + w_2\tilde{h}(k) + \Delta\widehat{h}(k+1), \qquad (25)$$

where $\tilde{h}(k)$ is the metal height measurement at time step k. The weights w_1 and w_2 are related so that $w_1 + w_2 = 1$. The weights are adjusted by trial and error. Generally w_1 should be close to 1, if the model is assumed to be of proper quality and simultaneously the measurements having large uncertainties. w_1 should be reduced if the model seems unreliable or the measurements more reliable. In the following example $w_1 = 0.75$.

The data sets given in Figure 3, were used to generate the θ-parameters of the OLS-algorithm. The predictions are compared to the results of simulated model and measurements in Figure 6. The predicted metal height is following the real metal height quite well, in spite of large uncertainties in the metal height measurements.

5.2 Recursive Ordinary Least Square (ROLS)

Variations in the cell performance may cause a need for updating the parameters of the model. In this case where the measurements are both rare and displaying low accuracy, updating the model has to be very slow, in order to avoid rapid variations of the model parameters, due to measurement uncertainties. Hence, short term variations of the plant will have minor influence on the model, but prospective seasonal and aging variations will have impact on the parameter variations of the model. In an OLS or a recursive ordinary least square (ROLS) method, by increasing the number of

samples, each sample will have less influence on the estimated parameters. In systems where it is likely that there will be long term variations of the model parameters, a forgetting factor α could be included (Ljung, 1999). The criterion function at time t will then obtain the following form;

$$V_t(\theta) = \frac{1}{t}\sum_{k=1}^{t} \alpha^{t-k}\epsilon^T(k)\lambda\epsilon(k), \qquad (26)$$

Hence, the newest measurements are weighted more than the older ones. The choice of α is a trade off between reducing the sensitivity of the model regarding measurement noise, and simultaneously be able to adopt to time variations of the system parameters. Values between 0.95 and 0.99 are common choices. For a given forgetting factor, e.g. $\alpha = 0.95$, the weight assigned to a sample-value 30 samples before the current sample, is reduced to approximately 21% ($0.95^{30} \approx 0.21$) of the weight put on the current sample-value, whereas defining $\alpha = 0.99$, the representative weight is reduced to approximately 74% ($0.99^{30} \approx 0.74$).

According to Eq. (20), an optimal parameter vector given a data sample with discrete time $[1, 2, \cdots, t-2, t-1]$ is given by

$$\widehat{\theta}_t = \underbrace{(\sum_{k=1}^{t} \Phi(k)\lambda\Phi^T(k))^{-1}}_{P_t} \sum_{k=1}^{t} \Phi(k)\lambda\Delta h(k), \qquad (27)$$

if the inverse of P_t exists.

A recursive ordinary least square (ROLS) method with a forgetting factor is possible to include in the parameter estimation in the following way (Di Ruscio, 2001):

1. Initial values of the covariance matrix P_t and the parameter vector θ_t are defined. It is common to let

$$P_0 = \delta\begin{bmatrix} 1 & 0 \\ 0 & 1 \end{bmatrix} = \delta I$$

$$\theta_0 = \begin{bmatrix} 0 \\ 0 \end{bmatrix},$$

where δ is a "large" number, e.g. 10 000.

2. The regression vector Ψ is updated at each metal height measurement:

$$\Psi_{n_{i+1}} = \begin{bmatrix} \sum_{k=n_i+1}^{n_{i+1}} \phi_1(k) & \sum_{k=n_i+1}^{n_{i+1}} \phi_2(k) \end{bmatrix}^T \qquad (28)$$

3. Updating the inverse of the covariance matrix

$$P_{n_{i+1}}^{-1} = \alpha P_{n_i}^{-1} + \Psi_{n_{i+1}}\lambda\Psi_{n_{i+1}}^T \qquad (29)$$
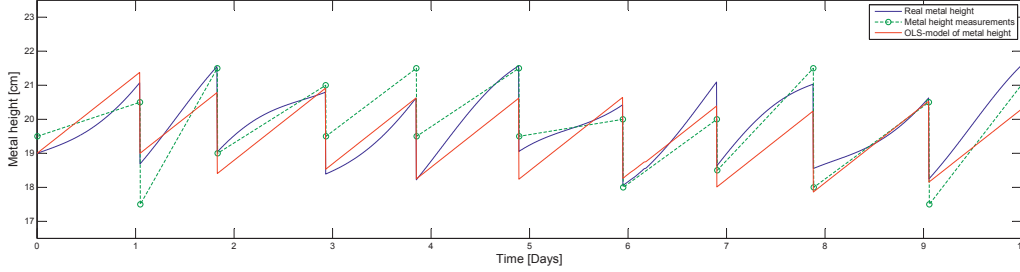
Figure 6: Prediction of metal height for the earlier presented synthetic data set showing fairly well correlation between the simulated and predicted values. The prediction model is based on the OLS algorithm and the noisy metal height measurements, just before and just after metal tapping, shown with the green circles in the figure.

and the "Kalman" gain matrix

$$K_{n_{i+1}} = P_{n_{i+1}} \Psi_{n_{i+1}} \lambda \qquad (30)$$

after each metal height measurement.

4. Updating the present parameter vector at each metal height measurement

$$\theta_{n_{i+1}} = \theta_{n_i} + K_{n_{i+1}} \left(\Delta h n_{i+1} - \Psi_{n_{i+1}} \theta_{n_i} \right) \quad (31)$$

where $\Delta h n_{i+1} = h(n_{i+1}) - h(n_i)$

5. Computing the covariance matrix after each metal height measurement:

$$P_{n_{i+1}} = \left(\alpha P_{n_i}^{-1} + \Psi_{n_{i+1}} \lambda \Psi_{n_{i+1}}^T \right)^{-1} \qquad (32)$$

6. At each time instant k the predicted change of metal height is given by

$$\Delta h(k) = \Phi(k) \theta^T \qquad (33)$$

5.2.1 Matrix inversion lemma

An equivalent form of Eq. (29) and Eq. (32) that is more suited for rapid computation is given by the Sherman-Morrison-Woodbury formula (Golub and Loan, 1996), also called the matrix inversion lemma;

$$(A + UV^T)^{-1} = A^{-1} - A^{-1}U(I + V^T A^{-1} U)^{-1} V^T A^{-1} \qquad (34)$$

Applying Eq. (34) to Eq. (32), where

$$
\begin{aligned}
A &= \alpha P_{n_i}^{-1} \\
U &= \Psi_{n_{i+1}} \\
V^T &= \Psi_{n_{i+1}}^T
\end{aligned}
$$

gives

$$P_{n_{i+1}} = \qquad (35)$$
$$\frac{1}{\alpha} P_{n_i} - \left(\frac{1}{\alpha} P_{n_i} \Psi_{n_{i+1}} \right) \cdot$$
$$\left(\left(\left(I + \Psi_{n_{i+1}}^T \frac{1}{\alpha} P_{n_i} \Psi_{n_{i+1}} \right) \right)^{-1} \Psi_{n_{i+1}}^T \frac{1}{\alpha} P_{n_i} \right)$$

The matrix inversion in Eq. (32) is modified using Eq. (34), hence the inversion of a matrix is now replaced by a inversion of a scalar, i.e. the denominator in the following deducted equation:

$$P_{n_{i+1}} = \qquad (36)$$
$$\frac{1}{\alpha} P_{n_i} \left(I - \frac{\Psi_{n_{i+1}} \Psi_{n_{i+1}}^T P_{n_i}}{\alpha + \Psi_{n_{i+1}}^T P_{n_i} \Psi_{n_{i+1}}} \right)$$

Note that this way of calculating $P_{n_{i+1}}$ is more sensitive regarding selection of initial values of P_0 when working with regression vectors where one element is zero, and the other is "large". In the simulated system that is considered, only proper parameter estimation is achieved for values of $\delta \leq 10^{-4}$. For larger values of δ, the first element of the P-matrix will become zero, and hence θ_1 will also remain at zero throughout the whole estimation period. For values of $\delta \leq 10^{-8}$, P and hence θ will converge very slowly towards its proper values.

If the normal routine of letting the initial value of P_{11} be "large" is followed, and in addition ψ_1 is "large", the impact of $\alpha \in< 0, 1]$, will easily be neglected due to the limitations of the computer precision. Assuming that $\alpha << \Psi_1^T P_0 \Psi_1$, the first estimate of P will become a lower triangular matrix due to the computer precision;

$$
\begin{aligned}
P_1 &= \frac{1}{\alpha}P_0\left(I - \frac{\Psi_1\Psi_1^T P}{\alpha + \Psi_1^T P_0 \Psi_1}\right) \\
&= \frac{1}{\alpha}P_0\begin{bmatrix} 1 & 0 \\ 0 & 1 \end{bmatrix} - \frac{1}{\alpha}P_0\begin{bmatrix} 1 & 0 \\ 0 & 0 \end{bmatrix} \\
&= \frac{1}{\alpha}P_0\begin{bmatrix} 0 & 0 \\ 0 & 1 \end{bmatrix}
\end{aligned}
\tag{37}
$$

However, by rearranging Eq. (36) in the following way, proper values of θ will be estimated also for larger values of δ:

$$
\begin{aligned}
P_1 &= \frac{1}{\alpha}P_0\left(\frac{\alpha}{\alpha + \Psi_1^T P_0 \Psi_1}I + \frac{\Psi_1^T P_0 \Psi_1 I - \Psi_1\Psi_1^T P}{\alpha + \Psi_1^T P_0 \Psi_1}\right) \\
&= \frac{1}{\alpha}P_0\left(\begin{bmatrix} \frac{\alpha}{\Psi_1^T P_0 \Psi_1} & 0 \\ 0 & \frac{\alpha}{\Psi_1^T P_0 \Psi_1} \end{bmatrix} + \begin{bmatrix} 0 & 0 \\ 0 & 1 \end{bmatrix}\right) \\
&= \frac{1}{\alpha}P_0\begin{bmatrix} \frac{\alpha}{\Psi_1^T P_0 \Psi_1} & 0 \\ 0 & 1 \end{bmatrix}
\end{aligned}
\tag{38}
$$

$$\tag{39}$$

P_1 will in this case remain a diagonal matrix, which is crucial. The reason why, the matrix inversion lemma had to be rearranged is that displaying $\frac{\Psi_1\Psi_1^T P}{\alpha + \Psi_1^T P_0 \Psi_1}$ requires higher computer precision than displaying $\frac{\alpha}{\alpha + \Psi_1^T P_0 \Psi_1}$, since the former has a very small perturbation from 1, whereas the other has a small perturbation from 0.

Given a realistic example from the system considered in this paper, where $\Psi_1^T = \begin{bmatrix} 2.5 \cdot 10^{10} & 0 \end{bmatrix}$ and $P_0 = 10^4 I$. Computing P_1 will then involve computation with numbers close to the precision limits of the computer. By using the ordinary matrix inversion lemma, only values where $10^{-7} < \delta < 10^{-4}$ caused reasonable results. Model predictions outside this area where unstable as one of the parameters maintained zero throughout the regression. For larger values P_{11} and θ_1 became zero for the ordinary matrix inversion lemma, whereas the modified inversion lemma performed proper estimations for all larger values of P_{11}.

5.2.2 Prediction of the metal height

The data sets given in Figure 3, were used to generate the θ-parameters of the ROLS-algorithm. The prediction is compared to the simulated model and measurements in Figure 7. The predicted metal height is following the real metal height quite well, in spite of large uncertainties in the metal height measurements.

In Figure 8 the temporal variation of the regression parameters is shown. For this simulation the recursive variant of the OLS is superfluous, as these parameters are not following the constant system parameters very well.
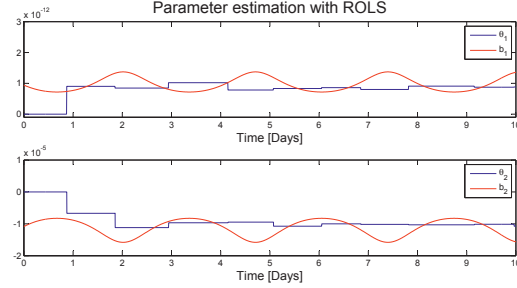

Figure 8: Simulating the values of the estimated parameters, calculated in the ROLS model, using the earlier presented synthetic data set. The "'rapid"' oscillation of the parameters is not detected by the ROLS-model. The estimated parameters are close to the mean value of the parameters, and will only follow long term variations of the parameters.

6 System Identification using DSR

Assume that there are dynamics within the system that are not detected by the strict mechanistic model used with PEM, as how the temperature is influencing the area A. An alternative is to identify black box models, like the DSR (Deterministic and Stochastic Realization) model. The DSR method is based upon a linear discrete time invariant State Space Model (SSM)

$$
x_{k+1} = Ax_k + Bu_k + Ce_k \tag{40}
$$
$$
y_k = Dx_k + Eu_k + Fe_k, \tag{41}
$$

and is explained in Di Ruscio (1996).

6.1 Regular DSR

The sample scenario used with the OLS and ROLS algorithms in the former section is not consistent with the SSM in Eq. (40). Further the number of measurements has to be increased to extract information on the short term system dynamics between the tapping instants. Hence, a new measurement regime has been set up for the identification of a DSR model, as described in the following.

Assume that the system of interest might be described by the linear SSM, and that the inputs are sampled with one fast sampling rate, T_f, whereas the output is known at a slow sampling rate, T_s. Contrary to Sec. 5, T_s is constant in this section. The input sampling rate is M times faster than the output sampling rate, hence $T_s = MT_f$. If it is not possible to increase T_s, the *modus operandi* is to consider only the
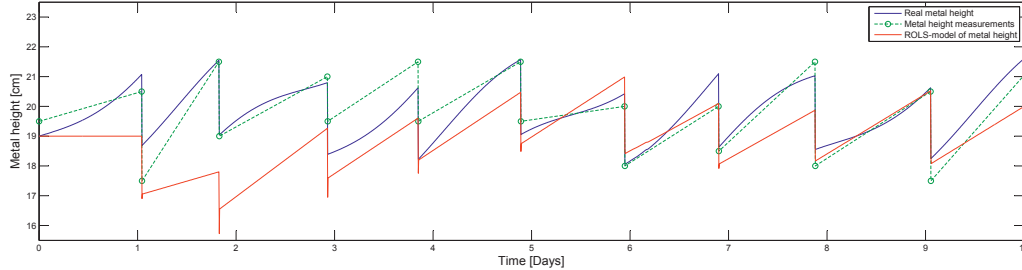
139

Figure 7: Simulating the predicted metal height using ROLS. Prediction of metal height for the earlier presented synthetic data set showing good correlation between the simulated and predicted values. The prediction model is based on the ROLS algorithm and the noisy metal height measurements shown with the green circles in the figure. Although the initial value is set to high, the predicted values "'soon"' reaches the desirable level. ROLS needs some time to adjust its model parameters and hence the variations in its initial phase.

inputs at a sampling rate of T_s, in order to achieve a common sampling rate, which is required to use the standard DSR-method (Di Ruscio, 2000). Then, to get a discrete SSM with the fast sampling rate, T_f, the generated discrete SSM is first transformed into a continuous SSM, utilizing e.g. the MATLAB function $[A_c, B_c] = d2c(A, B, T_s)$. Next the continuous model is transformed back to a discrete model, but now with another sampling rate by the MATLAB function $[A_d, B_d] = c2d(A_c, B_c, T_f)$. A periodical variation in the cell temperature introducing a variation in the width of the metal bath has been introduced in the following simulations. Hence, in addition to the sawtooth variation, already explained, the metal height will fluctuate with a period of about 10 hours. Assuming that the three input variables I, m_{out} and T (bath temperature) are sampled every 5 minutes, and the metal height measured every 3rd hour. To be able to utilize the DSR algorithm the mean values every third hour are used as inputs, to generate the state space model. The model is then transformed from a sampling time of 3 hours to 5 minutes as already described. Figure 9 shows the result of a simulation of the metal height in the aluminium electrolysis cell, using this method. The simulation shows a fairly good estimation, in spite of the poor metal height measurements also shown in the figure. By running several additional simulations with random generated measurement noise, some of the concomitant predictions had a tendency of drifting away from the real metal height. This could be compensated by including measurement in the prediction algorithm, e.g. including a Kalman filter, when running the prediction model online. This could be a useful estimation technique if implementing automatic metal height

measurements as discussed in (Viumdal et al., 2010; Viumdal and Mylvaganam, 2010). To be able to utilize the DSR algorithm the mean values every 3rd hour are used as inputs, to generate the state space model. The model is then transformed from a sampling time of 3 hours to 5 minutes as already described. This transformation of the model unfortunately more often involves less robust models.

6.2 DSR in case of multiple time series

Another approach to identify a model of the metal height is to use the MDSR, as addressed in (Di Ruscio, 1997). MDSR is designed to handle multiple time series, e.g. an industrial process where the time series are interrupted by shutdowns in the production line, or where each time series represents a batch process. By just placing measurements from different time series successively in a large data matrix, the initial states of each time series is not computed when using ordinary DSR algorithm. By using MDSR, initial state values are calculated for each time series, in addition to the overall state space model. In the aluminium electrolysis example, the increase in metal height is "interrupted" by the metal taps. Instead of measuring the metal height every 3rd hour, as assumed with the DSR-algorithm, another measurement scenario is applied for the MDSR approach. These measurement series are divided into several sub time series, each starting immediately after the metal tapping. As the tapping has an intermittent sampling interval, there will be a shift in the sampling incidents between each of the time series. Within each sub time series, new metal height measurements are sampled each 3rd hour. The mean value
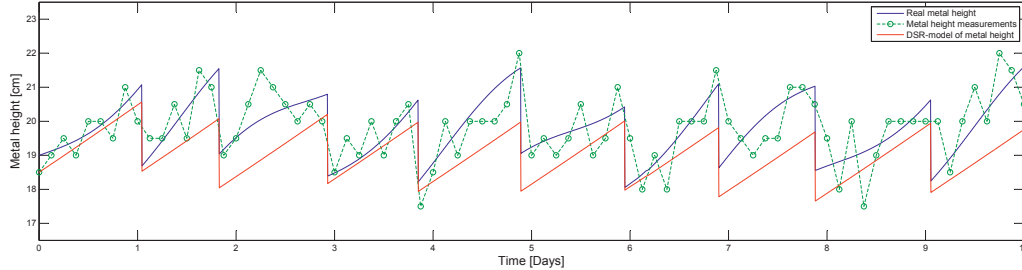
Figure 9: Prediction of the metal height, using DSR on the earlier synthetic data set. Unlike the assumed measurement regime for the OLS and ROLS models, the metal height is here assumed to be measured every 3rd hour. The noisy metal height measurements are shown with the green circles in the figure. In general, the simulated values are closer to the predicted than the measured values.

of the input variables are taken for each time step as done with the DSR model. The result is a new model, with as many initial states as there are sub time series. Figure 10 shows an example where MDSR is used, still with a sampling time between each metal height measurement of 3 hour, but here with sampling occurrence according to the latest metal tap instance. Attempts of transforming the MDSR model with a sampling rate of 3 hours to a sampling rate of 5 minutes failed, therefore the graph in Figure 10 is marked with dots, at the locations where model has calculated the predictions.

However, in a real aluminium electrolysis process, the metal height is still measured manually in an intermittent manner, and normally only just before the tapping proceeding. Hence, the PEM-algorithms seem to be the most realistic approach at the moment. Using MDSR online is not straightforward, one alternative is to use any PEM-algorithm to predict the drop in metal height due to the metal tapping, and using the MDSR as the model describing the metal height between the tapping proceeding.

7 System identification using real measurements

A measurement sequence from an Aluminium reduction cell in Norsk Hydro, Årdal, was performed with a time span of 76 hours. The metal height was measured just before, and just after the tapping instants, and then approximately every 4th hour. The input variables "Line current" and "Tapped bath" were sampled each 5 minute. Two different OLS models of the process was generated for this data set. The first model was only based on the metal height measurements performed in conjunction with the metal tapping, while

the inter sampled measurements are included in the second OLS model. Figure 11 shows the predictions of the two OLS models, the measurements, and a simulation of the mechanistic model. The mechanistic model is based upon geometrical parameters of the aluminium reduction cell, and the initial value is adjusted to fit the measurements. The element values of the parameter vector θ are about 36% to 50% less than the corresponding parameter values in the mechanistic model. The parameter vector of the two OLS models are similar, but as the first model is based on fewer measurements than the second model, the former is expected to be less reliable. However, the main difference between these two models, is that the second OLS model is updated more often by new measurements. It is difficult to verify which model is closest to the real system based of these few measurements, particularly as the measurements are corrupted with so much noise. More reliable models can be achieved by extending the time span of the sampling, and by introducing improved measurement systems, which are beyond the scope of this paper.

8 Comparing performance of the models in metal height predictions

In addition to the methods already described, the problem was also organized as a lifted model approach, using the same data set, as used for the DSR approach, i.e. the sampling time for the three input variables were every 5 minute, whereas the sampling time of the output was every 3rd hour. Hence, the inputs were sampled 36 times as often as the output, resulting in an input matrix with 72 (2x36) variables. Due to the
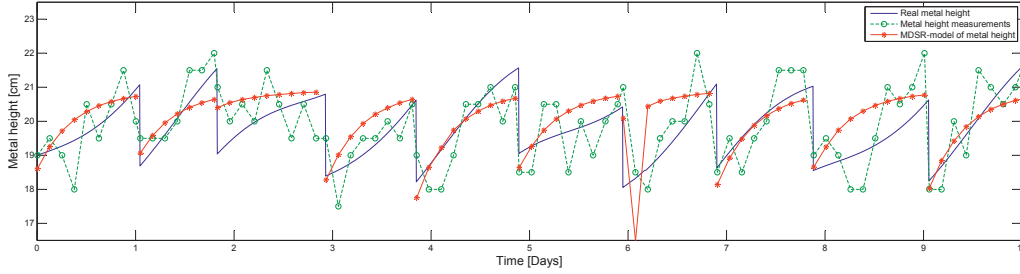
Figure 10: Prediction of the metal height, using MDSR on the earlier synthetic data set. Unlike the assumed measurement regime for the OLS and ROLS models, the metal height is here assumed to be measured every 3rd hour, but as opposed to the measurement regime using the DSR, here the measurements are considered as multiple time series, each starting just after the tapping proceeding. The noisy metal height measurements are shown with the green circles in the figure. In general, the simulated values are closer to the predicted than the measured values.
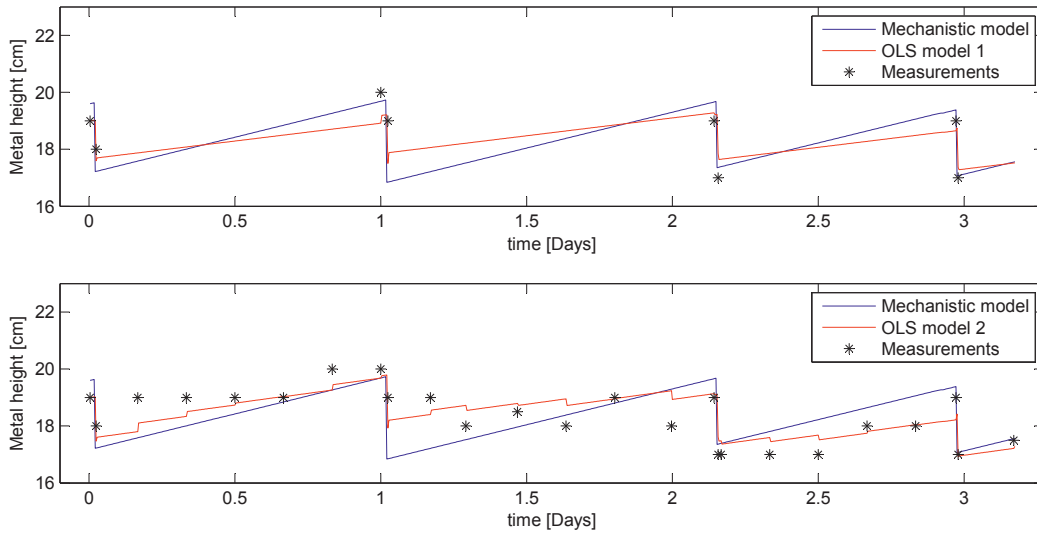

Figure 11: Predictions of the metal height, using two different OLS models based on the data from a real aluminium plant. OLS model 1 is based upon the measurements just before and just after the metal tap instants. OLS model 2 is in addition based on inter sampled measurements every 4 hour as indicated in the figure. The mechanistic model is based upon the physical parameters of the aluminium reduction cell, and the initial value is adjusted to fit the measurements.

rare tapping operations, 21 variables having no variance, were deleted from the input matrix. They were all representing the original metal tap variable. As proposed by Li et al. (2003), the Canonical Correlation Analysis (CCA) initially developed by Hotelling was applied, to reduce the number of variables with poor correlation to the output. Running this test, all the 25 best correlation results were representing the

line current. Hence, a model built on this approach would not include the impact of the metal tapping. The main problems related to the lifted model in this approach is most likely related to the poor variance of the input matrix, that is even poorer in the lifted input matrix. In addition the saw tooth like metal height graph, is difficult to identify, as the tap proceedings are not synchronized, and the noise level was rather high. Of that reason, the lifted model was not further considered in this work. For the other models considered in this work, a new data set was generated for validation purpose. In addition to the mechanistic model, predictions of the system identification models were simulated. The selected results from the simulations are shown in Figure 12. The validation of the models was analyzed using Mean Square Error (MSE), Normalized Mean Square Error (NMSE), and Normalized Root Mean Square Error (NRMSE). On contrary to the MSE, where the numerical value should be as small as possible, the numerical values of the NMSE and NRMSE are in the range $\langle -\infty, 1]$, where 1 is representing a perfect model. The numerical performance of these models are shown in Table 4. The validation data set has been extract for the period after the ROLS model has stabilized.

The results show that the OLS model and ROLS model are following the mechanistic model quite well. So are also the results based on DSR, but the DSR model fails in the validation data set. In contrast to the OLS model and ROLS model, where the predictions are updated by new measurements, only the initial state vector is calculated in the DSR model. Thus, the states are not updated by new measurements in the DSR model, inducing a tendency of drifting away. By utilizing new measurements of the metal height in a implemented state estimator, an online version of the DSR, will enhance the performance, by reducing the drift of the model. The MDSR predictions are updated by the new measurements, but the model does not recreate the dynamics in a proper way. In systems where the main dynamics is well known, and the variations in the measurement instant make subspace methods difficult, an OLS approach seems to be the optimal choice of system identification algorithm.

In real applications the DSR model often has the advantage to include more input variables to the model, with the intention of improving the model. The need for looking for such "lurking" input variables can be revealed by analyzing an error prediction plot or residual plot. The prediction errors for the OLS model is plotted in Figure 13, together with a sine curve with identical periodicity of the not measured input variable "Cross section area". As this is a "lurking"variable, indicating that it has not been involved in the identi-

fication problem (as it is not measured), it will not be detected by the OLS model. Similar error predictions are seen by the other models, but as mentioned a DSR model will easily include new input measurements of the system. Although the variable "Cross section area" is difficult to measure on a regular basis, some of the "lost" dynamics can perhaps be detected by the other variables that are more easily available. It would then be possible to identify a model describing this additional dynamic by eg. a DSR model. Finally, the OLS and the new DSR model could be merged to a gray box model, hence gaining advantage of both model types. This will not be treated in the present paper, as it is beyond the scope of this work, but the reader is referred to Draper and Smith (1998) for more details for utilizing the error prediction or residual plots.

9 Conclusion

This paper addresses challenges using ordinary system identification methods in applications with rare and intermittent sampling frequencies, and if the sampling frequencies are different for the input and output variables. In particular the challenge with identifying a robust predictor of the metal height in aluminium electrolysis cells is under scrutiny. When dealing with so few regularly performed measurements as in the electrolysis process, using historical data to model the metal height is insufficient. With measurements just before, and just after the tapping of metal, it is possible to achieve quite good predictors, by just using the two main inputs; line current I and the amount of tapped aluminium m_{out}. This can be achieved in spite of the intermittent tapping instants, by defining two linear models with common parameter vector θ. The first with a slow sampling rate, that is consistent with the metal height measurement, where the input variables are summed between each metal height measurements. This regression model is used for determining θ. The other linear model should have a sampling rate identical to the input variables, and serves as a predictor of the metal height between the measurements. To determine more complex dynamic between the tapping, more measurements have to be taken, in particular metal height measurements, but also more input variables with regularly performed measurements. If measuring the metal height every 3rd hour throughout 20 days, some acceptable predictions of the metal height was achieved using ordinary DSR-algorithms, although it often created rater unstable models, due to the transformation from models with 3 hours sampling time to 5 minutes sampling time. If instead considering metal height measurements every 3rd hour, but now adjusted in time after each metal tapping procedure,
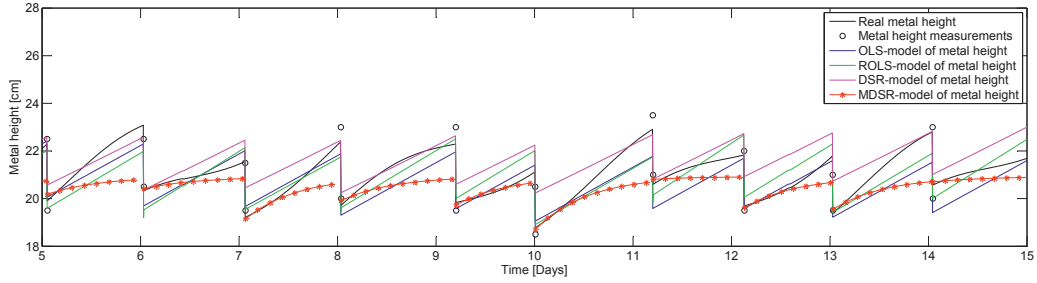
Figure 12: Simulations of the different models, based on the validation data set. The OLS and ROLS predictions are following the "real" metal height quite well, in spite of the large measurement uncertainty. The DSR has a tendency of drifting away as it is not updated by the new metal height measurements, as in the case of the former models. The MDSR has problems in reproducing the system dynamic, but updates the predicted metal height very well at each new measurement.

Table 4: Numerical validation of the models

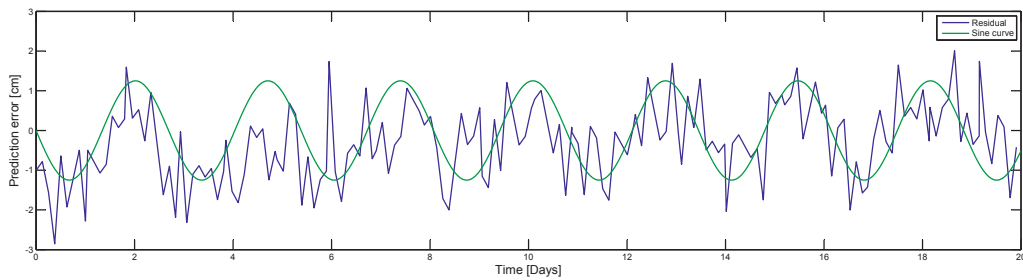| Algorithm	MSE		NMSE		NRMSE	
	Identification	Validation	Identification	Validation	Identification	Validation
OLS	$6.52 \cdot e^{-5}$	$5.03 \cdot e^{-5}$	0.16	0.49	0.83	0.29
ROLS	$3.59 \cdot e^{-5}$	$3.79 \cdot e^{-5}$	0.54	0.62	0.32	0.38
DSR	$12.8 \cdot e^{-5}$	$9.97 \cdot e^{-5}$	-0.65	-0.0054	-0.28	0.0027
MDSR	$5.33 \cdot e^{-5}$	$7.93 \cdot e^{-5}$	0.37	0.080	0.21	0.041

Figure 13: The prediction errors of the OLS prediction shows a periodic tendency as indicated by the sine function plotted with identical periodicity of the not measured input variable "Cross section area". This indicate that there are dynamics in the data set not identified by the OLS model. This is related to a "lurking" variable, that is not included in the data set used for identification.

the DSR did not work, due to the time-lag. In this case MDSR, which is the DSR for multiple time series provided acceptable predictions. As far as there are so few regularly performed measurements in the aluminium electrolysis process, parameter estimation approaches using PEM-algorithms seem to be the most satisfying and reliable approach to predict the metal height in the aluminium electrolysis process. This conclusion is mainly based on the experience with this simplified mechanistic model given in Eq. (12), as the real measurements are few in their numbers and have considerable uncertainties.

Acknowledgments

References

Bojarevics, V. and Pericleous, K. Comparison of MHD models for aluminium reduction cells. In *TMS annual meeting and exhibition*. pages 347–352, 2006.

Bojarevics, V. and Pericleous, K. Solutions for the metal-bath interface in aluminium electrolysis cells. In *TMS annual meeting and exhibition*, volume 1. pages 569–574, 2009.

Di Ruscio, D. Combined Deterministic and Stochastic System Identification and Realization: DSR - A Subspace Approach Based on Observations. *Modeling, Identification and Control*, 1996. 17(3):193–230. doi:10.4173/mic.1996.3.3.

Di Ruscio, D. A Three Dimensional DSR Algorithm. Technical report, Telemark University College, Faculty of Technology, 1997.

Di Ruscio, D. Subspace system identification of multiple time series and different sampling rates. *Unpublished report*, 2000. pages 1–18.

Di Ruscio, D. Model Predictive Control and Optimization. Technical report, Telemark University College, Faculty of Technology, 2001. Lecture Notes.

Ding, F., Qiu, L., and Chen, T. Reconstruction of continuous-time systems from their non-uniformly sampled discrete-time systems. *Automatica*, 2009. 45(2):324 – 332. doi:10.1016/j.automatica.2008.08.007.

Draper, N. and Smith, H. *Applied regression analysis*. Wiley series in probability and mathematical statistics. Applied probability and statistics. Wiley, 3rd edition, 1998.

Golub, G. H. and Loan, C. F. V. *Matrix Computations*. The John Hopkins University Press, 3rd edition, 1996.

Grjotheim, K. *Introduction to Aluminium Electrolysis: Understanding the Hall-Héroult Process*. Aluminium-Verlag, 1993. URL http://www.beuth.de/en/publication/introduction-to-aluminium-electrolysis/143079846.

Kranc, G. Input-output analysis of multirate feedback systems. *Automatic Control, IRE Transactions on*, 1957. 3(1):21–28. doi:10.1109/TAC.1957.1104783.

Kurenkov, A., Thess, A., Zikanov, O., Segatz, M., Droste, C., and Vogelsang, D. Stability of aluminium reduction cells with mean flow. *Magnetohydrodynamics*, 2004. 40(2):203–212.

Li, D., Shah, S., Chen, T., and Patwardhan, R. System identification and long-range predictive control of multi-rate systems. In *American Control Conference, 1999. Proceedings of the 1999*, volume 1. pages 336–340 vol.1, 1999. doi:10.1109/ACC.1999.782796.

Li, D., Shah, S., Chen, T., and Qi, K. Application of dual-rate modeling to CCR octane quality inferential control. *Control Systems Technology, IEEE Transactions on*, 2003. 11(1):43–51. doi:10.1109/TCST.2002.806433.

Li, W., Shah, S. L., and Xiao, D. Kalman filters in non-uniformly sampled multirate systems: For FDI and beyond. *Automatica*, 2008. 44(1):199 – 208. doi:10.1016/j.automatica.2007.05.009.

Ljung, L. *System Identification -Theory for the User*. Prentice Hall, 2nd edition, 1999.

Lu, W. and Grant Fisher, D. Least-squares output estimation with multirate sampling. *Automatic Control, IEEE Transactions on*, 1989. 34(6):669–672. doi:10.1109/9.24247.

Shannon, C. Communication in the presence of noise. *Proceedings of the IRE*, 1949. 37(1):10–21. doi:10.1109/JRPROC.1949.232969.

Shannon, C. Communication in the presence of noise. *Proceedings of the IEEE*, 1998. 86(2):447–457. doi:10.1109/JPROC.1998.659497.

Sheng, J., Chen, T., and Shah, S. L. Generalized predictive control for non-uniformly sampled systems. *Journal of Process Control*, 2002. 12(8):875 – 885. doi:10.1016/S0959-1524(02)00009-4.

Viumdal, H. and Mylvaganam, S. Beyond the dip stick: Level measurements in aluminum electrolysis. *JOM*, 2010. 62(11):18–25. doi:10.1007/s11837-010-0161-0.

Viumdal, H., Yan, R., Liane, M., Moxnes, B., and Mylvaganam, S. Multi sensor data fusion for aluminium cell health monitoring and control. In *TMS annual meeting and exhibition supplemental proceedings*, volume 3. pages 149–159, 2010. ISBN Number 978-0-87339-753-7.

Wang, J., Chen, T., and Huang, B. Multirate sampled-data systems: computing fast-rate models. *Journal of Process Control*, 2004. 14(1):79 – 88. doi:10.1016/S0959-1524(03)00033-7.